Advances in Polymer Science 283

Maria Laura Di Lorenzo
René Androsch *Editors*

Thermal Properties of Bio-based Polymers

Springer

283
Advances in Polymer Science

Aims and Scope

The series Advances in Polymer Science presents critical reviews of the present and future trends in polymer and biopolymer science. It covers all areas of research in polymer and biopolymer science including chemistry, physical chemistry, physics, and material science.

The thematic volumes are addressed to scientists, whether at universities or in industry, who wish to keep abreast of the important advances in the covered topics.

Advances in Polymer Science enjoys a longstanding tradition and good reputation in its community. Each volume is dedicated to a current topic, and each review critically surveys one aspect of that topic, to place it within the context of the volume. The volumes typically summarize the significant developments of the last 5 to 10 years and discuss them critically, presenting selected examples, explaining and illustrating the important principles, and bringing together many important references of primary literature. On that basis, future research directions in the area can be discussed. Advances in Polymer Science volumes thus are important references for every polymer scientist, as well as for other scientists interested in polymer science - as an introduction to a neighboring field, or as a compilation of detailed information for the specialist.

Review articles for the individual volumes are invited by the volume editors. Single contributions can be specially commissioned.

Readership: Polymer scientists, or scientists in related fields interested in polymer and biopolymer science, at universities or in industry, graduate students.

More information about this series at http://www.springer.com/series/12

Maria Laura Di Lorenzo • René Androsch
Editors

Thermal Properties of Bio-based Polymers

With contributions by

R. Androsch · D. Cavallo · M. L. Di Lorenzo · S. E. Fenni · W. Focke · E. Forestier · N. Guigo · K. Jariyavidyanont · A. J. Müller · R. Pantani · E. Piorkowska · A. Rhoades · N. Sbirrazzuoli · H. Tsuji

Springer

Editors
Maria Laura Di Lorenzo
Institute of Polymers, Composites and Biomaterials
National Research Council
Pozzuoli, Italy

René Androsch
Interdisciplinary Center for Transfer-Oriented Research in Natural Sciences
Martin Luther University Halle-Wittenberg
Halle/Saale, Germany

ISSN 0065-3195 ISSN 1436-5030 (electronic)
Advances in Polymer Science
ISBN 978-3-030-39961-0 ISBN 978-3-030-39962-7 (eBook)
https://doi.org/10.1007/978-3-030-39962-7

This Springer imprint is published by the registered company Springer Nature Switzerland AG.
The registered company address is: Gewerbestrasse 11, 6330 Cham, Switzerland

Preface

Industrial production of thermoplastics is mostly based on the use of fossil sources. Due to serious environmental concerns, in the past years a number of environmental friendly polymers, produced from short-term renewable resources and often addressed as bio-based polymers or biopolymers, have been developed. Their expected large-scale commercialization will preserve mineral resources for future generations, which also contributes to an increased worldwide interest in this class of materials.

Polymers synthesized from short-term renewable resources exhibit a variety of properties, which make them amenable to production of different types of final products, such as films, sheets, molded articles, and fibers. Their commercial development is linked to the final application, which in turn is strongly affected by the property profile. In order to tailor specific properties, the relationship between chemical architecture, processing behavior, physical structure, and the resulting property profile needs to be known. The key to proper design of industrial processing is a thorough knowledge of polymer melting, crystallization, and vitrification. For this reason, in this volume focus is given to these main thermal properties of bio-based polymers.

Bio-based polymers formally include also long known/traditional polymers that are typically made from fossil resources, such as bio-polyethylene, bio-polypropylene, or bio-poly(ethylene terephthalate). The latter bio-based "classical" polymers have the same properties as the petrochemical-based analogues, and are therefore not treated in this volume.

Three main types of bio-based polymers have been identified: (1) natural polymers directly derived from biomass, such as starches, chitin, chitosan, cellulose and its derivatives, or natural rubber; (2) bio-engineered polymers, synthesized by microorganisms and plants like poly(hydroxyalkanoates); and (3) polymers synthesized from monomers obtained from short-term renewable resources, like poly (L-lactic acid) or poly(butylene succinate). Their thermal properties are summarized

in the introductory chapter, where an overview of the commercially available bio-based polymers is presented, together with the main features of each class of material.

The next two chapters are devoted to quiescent and flow-induced crystallization of poly(L-lactic acid) (PLLA), which is the bio-based polymer that has received the largest attention in recent years. PLLA is not only bio-based, but it is also biodegradable, compostable, and biocompatible. Despite its ability to degrade after disposal, PLLA is extremely robust when used for applications like food packaging, parts in electronic industry, automotive, or in the biomedical sector, with global suppliers now able to produce several kilotons per year.

Crystallization of poly[(R)-3-hydroxybutyrate] (PHB) is discussed in the next chapter. PHB is the first produced and most studied poly(hydroxyalkanoate). It represents a class of polymers that is synthesized by a variety of bacteria through fermentation, which leads to a number of special features. These include a perfect isotactic configuration with all chiral carbon atoms in (R)-position, or the absence of catalyst residues and other impurities typically present in the majority of synthetic polymers, often promoting crystallization. These peculiarities make PHB a model compound for the study of polymer crystallization, and therefore its crystallization behavior has received considerable attention over the years.

The following chapter focuses on thermal properties of polyamide 11, a semi-crystalline high-performance thermoplastic engineering polymer produced from castor oil, with many specific applications in all fields of engineering, including bio-engineering. Its main feature is the balanced property profile in terms of thermal stability, mechanical behavior, and resistance to media, which all led to increasing production volumes in recent years.

Last but not least, bio-sourced polymers based on 2,5-furandicarboxylic acid (FDCA) are discussed. These materials have the potential to replace oil-based polyesters, such as PET, in a wide range of applications, including bottles and carpets. Major attention is given to thermal properties of poly(ethylene 2,5-furanoate) (PEF), which is by far the most studied FDCA polyester due to its structural analogy with PET, even foreseen to compete with PET in the near future regarding price and performance, with the added value of sustainability.

The volume ends with a chapter on crystallization of bio-based polyester blends. Polymer blending has extensively been used to develop novel bio-based polymer formulations with an attractive combination of properties that combine those of the pure components, with some of them that have already found specific industrial applications.

As Editors, we truly thank all the chapter authors for sharing their scientific points of view on the thermal properties of the different bio-based polymers. We would like to express our sincere gratitude also to the many colleagues who actively participated in the review process and invested time and efforts to revise, comment, and improve each contribution.

We hope that we have reached the goal to provide an overview of the main thermal transitions (crystallization, melting, and glass transition) of bio-based polymers, as these are essential for their current and future development. We also hope that this volume helps to promote further development of bio-based polymers, with the aim to preserve a sustainable environment for the future generations.

Pozzuoli, Italy — Maria Laura Di Lorenzo
Halle/Saale, Germany — René Androsch

Contents

Overview of Biobased Polymers 1
Ewa Piorkowska

Quiescent Crystallization of Poly(Lactic Acid) and Its Copolymers-Based Materials 37
Hideto Tsuji

Poly(Lactic Acid): Flow-Induced Crystallization 87
Alicyn Rhoades and Roberto Pantani

Crystallization of Poly[(R)-3-hydroxybutyrate] 119
Maria Laura Di Lorenzo and René Androsch

Thermal Properties of Biobased Polyamide 11 143
Katalee Jariyavidyanont, Walter Focke, and René Androsch

Thermal Properties of Biobased Polymers: Furandicarboxylic Acid (FDCA)-Based Polyesters 189
Nathanael Guigo, Emilie Forestier, and Nicolas Sbirrazzuoli

Nucleation and Crystallization in Bio-Based Immiscible Polyester Blends 219
Seif Eddine Fenni, Dario Cavallo, and Alejandro J. Müller

Index 257

Adv Polym Sci (2019) 283: 1–36
https://doi.org/10.1007/12_2019_52

Published online: 17 December 2019

Overview of Biobased Polymers

Ewa Piorkowska

Contents

1 Introduction 2
2 Cellulose 3
3 Starch 5
4 Lignin 7
5 Chitin and Chitosan 8
6 Natural Rubber 10
7 Other Natural Polymers 12
7.1 Collagen 12
7.2 Alginates 12
7.3 Pullulan 13
7.4 Pectin 14
7.5 Galactomannan 14
8 Polyhydroxyalkanoates 15
9 Poly(Butylene Succinate) 17
10 Polylactide 18
11 Bio-polyethylene 21
12 Bio-poly(Ethylene Terephthalate) 21
13 Bio-polyamides 22
14 Thermosetting Bio-materials 23
15 Other Polymers 24
16 Concluding Remarks 25
References 25

Abstract Awareness of the environmental issues results in increasing attention paid to biobased polymers as their development and commercialization can help to limit exploitation of fossil resources and global warming. The article presents an overview of biobased polymers comprising most abundant natural polymers, bio-engineered polymers, and polymers synthesized fully or partially from biobased substrates,

E. Piorkowska (✉)
Centre of Molecular and Macromolecular Studies, Polish Academy of Sciences, Lodz, Poland
e-mail: epiorkow@cbmm.lodz.pl

including analogs of petrochemical resins. The structure, important properties, synthesis, and applications are addressed.

Keywords Biobased polymers · Biodegradability · Properties · Structure

1 Introduction

The term "biobased" is used to describe polymers produced from natural renewable resources, that is, biomass, which is the only source of available renewable carbon. The regeneration time of biomass carbon is measured in decades, whereas that from fossil resources reaches several million years [1]. Humankind has been using biomass since Stone Age, but converting it into substrates used for production of "biobased" polymers started in the nineteenth century. In fact, early technologically important discoveries in the field of polymer materials concerned biobased polymers. Goodyear empirically discovered the vulcanization of natural rubber in 1839, Schönbein obtained nitrocellulose in 1845, and the Hyatt brothers produced celluloid as a substitute for ivory in 1869 [2]. At the end of the nineteenth century, many polymers were available on the market including fully synthetic ones, and this period is considered as the beginning of polymer science and technology. Since that time tremendous development in both polymer science and technology resulted in a huge increase of production and broadening of polymer applications. Nowadays, it is difficult to imagine everyday life without polymer products. However, durability of polymer materials, which contributed to their success, created a serious impact on the environment as they can remain in water, soil, and landfill for many years. Nevertheless, many waste problems in agriculture, marine fishery, and construction industries, among others, were solved by the development of biodegradable polymers, driven by an increasing awareness of environmental issues [3, 4]. "Biodegradable" polymers, which include both naturally derived polymers and artificially synthesized ones, are degraded by microorganisms to biomass, water, and, depending on aerobic or anaerobic conditions, carbon dioxide or methane, respectively. It must be noted that biodegradable polymers are sometimes defined as biocompostable polymers, that is, those intended to be decomposed in industrial and municipal composts after their service life.

Biobased polymers are either biodegradable (e.g., polyhydroxyalkanoates) or non-biodegradable (e.g., bio-polyolefins). Although not all biobased polymers are biodegradable, biodegradability was an important motivation for their progress. Nowadays, the development of biobased polymers is a subject of intensive research [e.g., 5–10] as it plays a vital role in struggling with carbon dioxide emissions causing global warming and in diminishing still growing dependence on fossil resources. Initially, many biobased polymers were derived from agricultural products such as corn, potatoes, and other carbohydrate-containing resources. However,

in recent years, the focus moved away from food-based feedstocks, due to desire to save the land for food production but also because of biotechnology development. In 2016, the worldwide production capacity for biobased polymers amounted to 2% of the global polymer market and was expected to increase further [11].

Nowadays biobased polymers are classified into three groups:

- The first class: natural polymers directly derived from biomass, including those modified chemically, such as starches, modified starches, chitin, chitosan, cellulose, cellulose acetate, and natural rubber
- The second class: bio-engineered polymers, synthesized by microorganism and plants like polyhydroxyalkanoates
- The third class: polymers synthesized from monomers obtained from renewable resources, like polylactide, poly(butylene succinate), bio-poly(ethylene terephthalate), and bio-polyolefins [12, 13]

The polymers of the first and second group, with defined chemical structures, are directly used, which enables their efficient production but limits versatility. Monomers for the polymers of the third group are obtained from naturally synthesized molecules. Due to diversity of those bio-substrates, the third group comprises numerous polymers differing in structure and properties. It includes biodegradable and non-biodegradable polymers, like bio-polyolefins and bio-poly(ethylene terephthalate). The third group of polymers is in fact the most promising. The main advantage of their production and use is reduction of exploitation of the fossil resources and limiting atmospheric carbon dioxide.

In the review the most abundant natural polymers are briefly described. However, extensive research on natural polymers like cellulose, native starch, or natural rubber has been going on for a long time and led to accumulation of vast knowledge, easily accessible. Therefore, the review recalls only the most important features and applications of those materials. In more detail, the most promising polymers, bio-engineered or synthesized from monomers of natural origin, especially biodegradable polyesters, are presented. Routes to obtain biobased analogs of fossil-based commercial polymers are also briefly described.

2 Cellulose

Numerous natural biodegradable polymers occur in living organisms on Earth: proteins, DNA, natural rubber, cellulose, lignin, chitin, pectin, etc. The most abundant natural polymer on Earth is cellulose – a biodegradable polysaccharide present in plant cell walls (15–50% of the dry weight of plant biomass) [14]. Natural cellulose-based materials, including wood, cotton, hemp, and also cellulose derivatives, are widely used. Cellulose is a linear polymer composed of D-glucose (β-D-glucopyranose) units linked through covalent β(1 → 4) glycosidic bonds, as shown in Scheme 1.

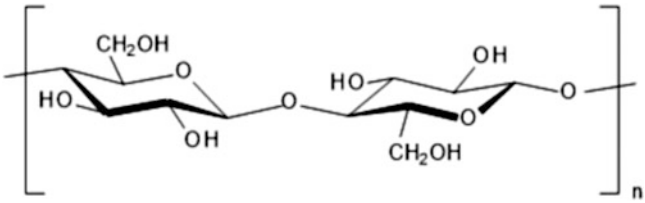

Scheme 1 Chemical structure of cellulose repeating unit: two β-D-glucopyranose units linked through covalent β(1 → 4) glycosidic bond

The intramolecular hydrogen bonds between hydroxyl groups and oxygens of neighboring rings stabilize the structure and result in linear configuration of cellulose macromolecule [15, 16]. Van der Waals and inter-chain hydrogen bonds between hydroxyl groups and oxygens of adjacent chains stimulate formation of cellulose elementary microfibrils having 2–20 nm in diameter [15–17]. In the fibrils there are differently ordered regions: highly ordered crystalline, low order, and amorphous regions. The intra- and inter-chain hydrogen bonding network is a reason of stability and axial stiffness [17]. The physical and chemical properties of cellulose depend on the number of inter- and intramolecular hydrogen bonds, the chain lengths, the chain length distribution, the crystallinity, and also the distribution of functional groups within the repeating units and along the polymer chains as well as on the isolation process employed [17–19]. The number of D-glucose rings in the chain varies in a broad range and depends on cellulose source, production process, and treatment; it is in the 800–10,000 range for cellulose in plant fibers [17]. Native cellulose generally exhibits higher molar mass than regenerated cellulose or cellulose processed by pulping. Cellulose exhibits high tensile strength of 63–500 MPa and elongation of 4% [20, 21]. The glass transition temperature (T_g) of cellulose derivatives ranges from 53 to 180°C [22]. Four principal cellulose polymorphs have been identified: I, II, III, and IV. Native cellulose I with parallel chain ordering is composed of triclinic Iα and monoclinic Iβ forms, and irreversibly transforms into stable monoclinic cellulose II with antiparallel chain arrangement upon regeneration or alkali treatment [15, 16, 23].

Although insoluble in water, cellulose is hydrophilic. Because of its high energy of cohesion, cellulose does not melt but decomposes at elevated temperatures. The cellulose has to be dissolved or chemically modified to obtain it in the liquid state. Its derivatives, cellulose xanthogenate and carbamate, are soluble in aqueous sodium hydroxide, and pure cellulose is regenerated in a wet spinning step forming viscose fibers or cellophane. The direct solvents, e.g., N-methylmorpholine N-oxide, are also used for that purpose. Owing to its thermal stability and modulus, regenerated cellulose is the largest biobased polymer produced for fibers and films widely used in numerous applications [7, 24]. In addition to pure cellulose, cellulose derivatives like cellulose acetate, cellulose nitrate, and carboxymethyl, methyl, ethyl, hydroxyethyl, and carboxyethyl cellulose are commercially important and used [25]. Cellulose esters, acetate and nitrate, are applied as films and fibers. Functional thermoplastic derivatives of cellulose were reviewed recently in [26]. A certain type of aerobic bacteria (mostly studied is *Gluconacetobacter xylinus*) produces

high-purity and high-strength bacterial cellulose [16, 27], which is mainly used in food and biomedical applications.

Numerous reports on using cellulose-containing fibers as reinforcement for other polymers were published, both natural fibers and regenerated cellulose fibers [28, 29]. Recently, cellulose nanomaterials, including net-forming nanofibers and rod-shaped nanocrystals, isolated from native cellulose, draw increasing attention. Due to their abundance, low weight, high strength and stiffness, and renewability, numerous studies have been reported on the isolation of nano-cellulose nanomaterials from different sources, their morphology and properties, as well as their use in high-performance applications, including polymer nanocomposites [16, 30, 31].

3 Starch

Starch, a natural polysaccharide, consisting of D-glucose (α-D-glucopyranose) units predominantly linked by α(1 → 4) glycosidic bonds (Scheme 2), is present in many food feedstock like potato and wheat seeds, as green plants produce starch by photosynthesis.

Native starch forms small granules of various shapes, with size ranging from 0.5 to 175 μm, consisting of amylose and amylopectin [32]. Amylose, of a molar mass of 10^2–10^3 kg/mol, is sparsely branched, whereas amylopectin is a highly multiple-branched polymer of a molar mass of 10^4–10^6 kg/mol [33]; the branches in amylopectin constitute about 5% of the molecule [34]. Moreover, starch can contain traces of lipids, gluten, or phosphate after industrial isolation and processing. The composition and structure of starch depend on its origin; starch can contain 20–25 wt.% of amylose and 75–80 wt.% of amylopectin. The starch granule is composed of alternating concentric amorphous and crystalline zones; crystallinity varies in the range of 17–50 wt.% [34]. Amylopectin is the dominating component of crystalline phase in the form of thin lamellae, whereas amylose and the branching regions of amylopectin form the amorphous phase. The crystals are formed by short, external chain segments of amylopectin with a degree of polymerization (DP) approx. 10–20 [34]. Different starch crystallographic forms exist: monoclinic A, hexagonal B, and C being a combination of A and B [34, 35]. In both A and B polymorphs, macromolecules are in a double helix conformation with six glucose monomers per turn. The monoclinic A form is synthesized in cereals in dry and warm

Scheme 2 Repeating unit of starch

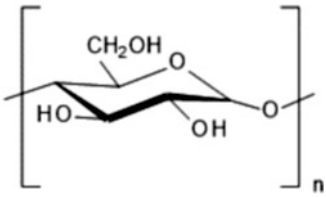

conditions, whereas the hexagonal B form in tubers, and occurs in starch with high amylose content. The A and B unit cells contain 8 and 36 water molecules per cell, respectively. The C form is synthesized in some vegetables [34, 35].

In food or noon-food applications, usually chemically and/or physically destructured starch is used, with the exception of the application as a filler for other polymers [35, 36]. T_m of neat dry starch is in the 220–240°C range, whereas starch decomposition begins at 220°C [35, 37]. Gelatinization with water and heat treatment disrupt most of inter-macromolecular hydrogen bonds and reduces both the melting temperature (T_m) and T_g. At a high level of destructuring and low water content, plasticized starch, also called "thermoplastic starch" (TPS), is obtained, which is processed using conventional plastic processing equipment. At water content decreasing below 20 wt.%, T_m approaches the degradation temperature. To overcome this problem, plasticizers, like glycerol or other polyols, like sorbitol or poly(ethylene glycol) or their mixtures, are added to decrease both T_m and processing temperature. Other compounds can also be utilized like those containing nitrogen (urea, ammonium derived, amines) [35].

TPS exhibits reduced crystallinity, composed of residual crystallinity from the native state (A, B, and C types) and processing-induced crystallinity, the latter influenced by processing parameters. During processing, amylose single helices recrystallize into crystals with orthorhombic or hexagonal unit cells (V and E types) with different levels of hydration [38].

Being dependent on its formulation, TPS thermal and mechanical properties can vary in a wide range. T_g of TPS is between −50 and 110°C, and its elastic modulus can be similar to that of polyolefins [39]. For instance, TPS with 10 wt.% of glycerol and 10 wt.% of water exhibits T_g of 43°C and elastic modulus of 1,144 MPa, whereas for TPS with 35 wt.% of glycerol, the respective values are −20°C and 11 MPa [33]. However, after processing, TPS exhibits aging, which leads to increased brittleness and stiffness [35]. Below T_g it undergoes physical aging accompanied with densification, whereas above T_g retrogradation occurs with crystallinity increasing over time. Van Soest [38] proposed a complex mechanism of such post-processing crystallization, involving both amylose and amylopectin.

Although exhibiting water permeability, TPS is less permeable to oxygen than most polyesters. To alter its properties, starch can be chemically modified, for instance, by esterification. Moreover, to improve its mechanical performance, TPS was reinforced with various types of natural cellulose fibers, lignins, mineral microfillers, and nanofillers, like cellulose whiskers, starch nanocrystals, or nanoclays. The different starch-based formulations are suitable for a range of short-lived applications, for instance, packaging [40, 41]. However, starch is still mostly used in paper, cardboard, cosmetics, pharmaceuticals, and paints [7].

4 Lignin

The second most abundant natural polymer in plant biomass is lignin – the main renewable source of aromatic structures on Earth. It is found in plant cell walls and binds cells together imparting rigidity and impact resistance. Lignin is amorphous, relatively hydrophobic, and rich in aromatic units. It is a complex cross-linked phenolic polymer built of heterogeneous phenylpropane units, so-called monolignols, p-coumaryl (p-hydroxyphenyl), coniferyl, and sinapyl alkohols (Scheme 3), differing by the degree of substitution by methoxyl groups on the aromatic ring. The structure of lignin depends on its source and is a product of radical polymerization of monolignols, which results in a variety of inter-unit linkages [42]. The proportions of the three monoligols determine the type of inter-unit bonds, which is decisive for the degree of branching and also reactivity [42–45]. Softwood lignins are almost entirely built of coniferyl units, hardwood lignin of coniferyl and sinapyl units, and grass lignins of all three types [42]. Lignin decomposes slower than cellulose and in a broader temperature range, 200–500°C [46].

Traditionally, lignin is obtained as a by-product of cellulose in the paper production. The main lignin derivatives are kraft lignins, lignosulfates, soda lignins, and organosolv lignins.

Lignin has rather low added-value applications, primary as biofuel, and only 1–2% is used for more demanding applications, although the high carbon content makes it an interesting precursor for all kinds of carbon materials, including carbon fibers. Promising opportunities are also in the field of adsorbing materials [42]. Lignin phenol groups are well-known antioxidants acting as hydrogen donors [47, 48]. Moreover, different possibilities have been investigated to blend unmodified lignins with other polymers [42, 49], although they are chemically modified to increase their potential applications in polymeric materials. In addition

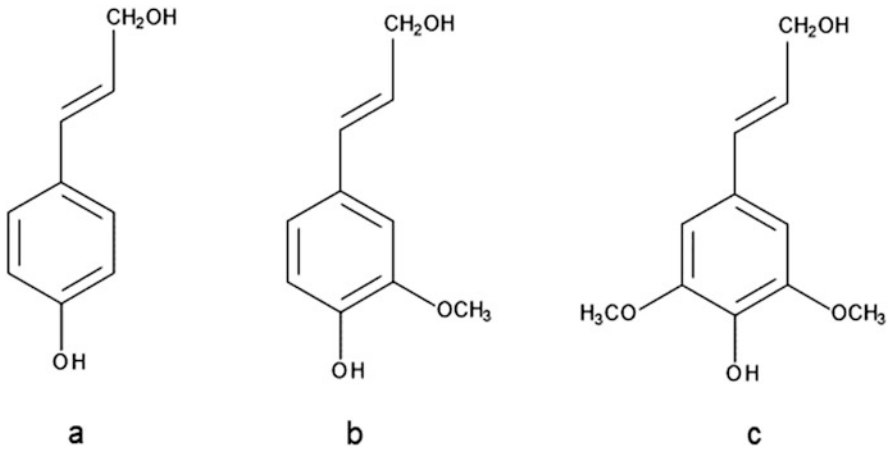

Scheme 3 Monolignols: (**a**) p-coumaryl alcohol, (**b**) coniferyl alcohol, and (**c**) sinapyl alcohol

to molar mass and functionality, T_g of lignin is of importance for its properties. Depending on lignin source and processing, its T_g varies in a broad temperature range, 113–174°C [49].

Lignin nano- and microstructures include aerogels, functionalized lignin beads, nanoparticles, and also lignin-based micro- and nanocapsules for encapsulation [42].

Due to their chemical structure, lignins are a potential source of renewable phenolic groups to replace phenol in thermoset resins, such as phenol-formaldehyde resins, and also as a source of hydroxyl groups to react with diisocyanates to form polyurethanes (PUs) [42]. The synthesis and properties of thermosets and thermoplastic polymers obtained from biobased aromatic compounds potentially derived from lignins were recently reviewed [10].

5 Chitin and Chitosan

Chitin is an abundant natural amino polysaccharide mainly present in the exoskeleton and internal structure of invertebrates. It is a biodegradable polymer of N-acetylglucosamine (2-acetamido-2-deoxy-β-D-glucopyranose) units linked with β(1 → 4) glycosidic bonds [9, 50, 51] (Scheme 4), although some of the glucopyranose residues are in the deacetylated form, as 2-amino-2-deoxy-β-D-glucopyranose.

The potential applications of chitin are related to its crystalline structure and thermal properties [51, 52]. Natural chitin forms ordered crystalline microfibrils [9, 53]. As a result of the differences in the inter- and intra-molecular hydrogen bonds in the structure, natural chitin occurs in three crystalline forms: α-, β-, and γ-chitin [54–56]. Chains in the α-chitin and the β-chitin are aligned antiparallel and parallel, respectively [57–59]. The γ-chitin is a combination of the α- and β-chitin [60], although it was also claimed to be a different form of the α-crystals [9, 61]. Chitin is highly hydrophobic and insoluble in water and most organic solvents [51, 62]. T_g of chitin is very high. It was estimated to be at 236°C [63], although recently a value of 165°C for Antarctic krill chitin was reported [54]. The weight-average molar mass of chitin is 10^3–2.5×10^3 kg/mol, but the deacetylation decreases it to 5×10^2 kg/mol [9]. On an industrial scale, chitin and chitosan are

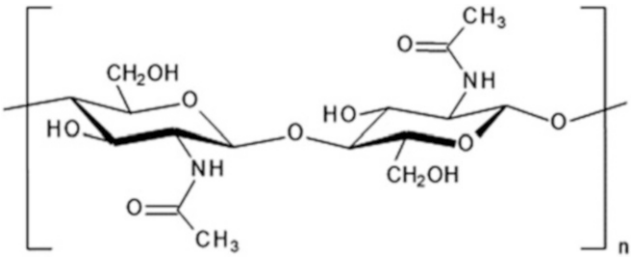

Scheme 4 Repeating unit of chitin, polymer of N-acetylglucosamine (2-acetamido-2-deoxy-β-D-glucopyranose) units linked with β (1 → 4) glycosidic bonds

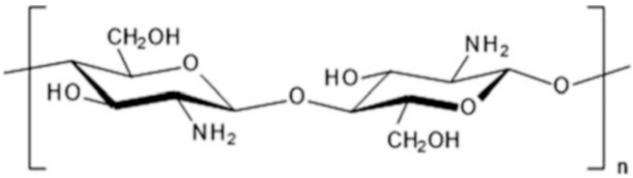

Scheme 5 Chemical structure of polymer of 2-amino-2-deoxy-β-D-glucopyranose units linked with β(1 → 4) glycosidic bonds

derived from waste of shrimps, prawns, and crabs by chemical extraction based on demineralization by acid, deproteination by alkali, and finally deacetylation into chitosan [7]. It is also possible to produce chitin by enzymatic processes or fermentation, but these methods are not economically viable on a large scale [7, 64]. Chitosan is a deacetylated derivative of chitin, in which acetamide groups are replaced with amino groups as shown in Scheme 5. In fact, the degree of deacetylation (DD) usually ranges from 50 to 95%, and glucopyranose residues with amido and amino groups are present in the same chain.

The presence of amino groups in chitosan modifies properties of this polymer compared with chitin. Chitosan is more soluble in diluted acids, and it can form complexes with metal ions, acids, and polyanions. Characteristics of films, fibers, and chitosan-based materials differ depending on their composition, solvents used for preparation, and conditions of formation. The physical properties of chitosan depend on its molar mass, DD, purity, and sequence of the amino and the acetamide groups [9, 65]. Chitosan is a semicrystalline polymer exhibiting polymorphism, described in detail in a recent review [66]. Orthorhombic unit cell was reported for hydrated chitosan (known also as tendon chitosan) from lobster or crab tendon (DD of 100%) and also for dehydrated chitosan, whereas films of chitosan obtained from solutions exhibited orthorhombic or monoclinic unit cells [66]. The orthorhombic polymorph of hydrated chitosan [67] is formed by chains in helical conformation with intramolecular hydrogen bonds, directed parallel to the b axis. The neighboring chains are antiparallel and connected by hydrogen bonds. Water molecules, one per polymer repeating unit, form interlayers between the chains and contribute to stability of the structure linking the chains through hydrogen bonds. The transformation to anhydrous form by removing the stabilizing water molecules occurs above 200°C due to destabilization of hydrogen bonds [68]. Motions of chains to the regions previously inhabited by water molecules result in the decrease of orthorhombic unit cell parameters, a and especially b, which is reduced by half [66]. T_g of amorphous phase of chitosan (DD 96%) was found at 203°C [69].

Owing to the presence of reactive amino side groups, a variety of beneficial chitosan derivatives can be created, as described in [9]. The advantages of chitosan include not only biodegradability, biocompatibility, and bioactivity, including antimicrobial activity, but also chemical inertness, low toxicity, high mechanical strength, good film-forming properties, and low cost [7]. Pharmaceutical and biomedical applications include treating burns, tissue engineering, preparation of

artificial skin, contact lenses, artificial blood vessels and blood dialysis membranes, dental therapy, and also gene and drug delivery [9]. It is also applied in cosmetic products for hair and skin care [70]. In agriculture chitosan is used as a coating fertilizer and fungicide [71, 72]. Water engineering takes advantage of its adsorbing ability to recover different elements and compounds from wastewater [9]. Chitosan is also applied in the food industry as a preservative and an antioxidant, and emulsifying as well as stabilizing and thickening additive, and also to reduce lipid adsorption [9].

6 Natural Rubber

Natural rubber (NR), also called India rubber or caoutchouc, is the most abundantly used biopolymer, together with cellulose and starch, because of its valuable characteristics combining very large elastic strain with high tensile strength and crack growth resistance. It is the most important raw material used in the production of elastomers. Although more than 2 500 plant species are known to produce NR, currently, the tropical *Hevea brasiliensis* is its main commercial source (99% of the world market) [73–75]. NR latex is collected from the trunks, coagulated, and dried. Dried NR consists mainly of poly(1,4-cis-isoprene) (Scheme 6) with a molar mass of 10^2–10^3 kg/mol and contains a few percent of other substances, such as proteins, fatty acids, resins, and inorganic materials [73–77].

NR obtained from the *Hevea* species contains two trans-isoprene units in the terminal region of the macromolecule followed by several hundred to a few thousand cis-isoprene units and long-chain fatty acid groups linked to the rubber molecule through phospholipids [74–76]. The Guayule rubber of *Parthenium argentatum* (1% of the world market) [75] is important because of its hypoallergenic properties as it does not contain proteins causing allergy. Only a few species synthesize poly (1,4-trans-isoprene) (Scheme 6), a structural isomer that has similar but not identical properties [75, 76].

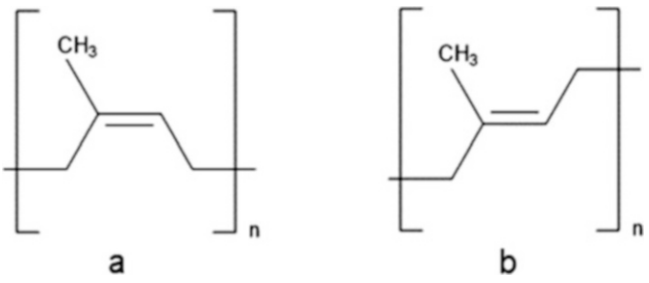

Scheme 6 Repeating unit of (**a**) poly(1,4-cis-isoprene) and (**b**) poly(1,4-trans-isoprene)

Macromolecules of NR are long, flexible, and practically linear. T_g of NR is near −70°C, whereas maximum crystallization rate is approx. at −25°C [78–80]. Various lattice parameters for either monoclinic or orthorhombic structure of NR crystals were proposed with the value of β angle being the only difference between these two systems [79]. The outstanding properties of NR are partly attributed to its strain-induced crystallization (SIC) as the strain-induced crystallites are supposed to slow down, deviate, and even stop crack growth [81]. The SIC of NR was reviewed recently in [78]. When stretch ratio exceeds four, SIC starts almost instantaneously and can continue for days. The thus-formed crystallites are aligned in the stretching directions. Crystallization rate increases with the maximum stretch ratio. SIC is accompanied by a stress decrease due to the relaxation of amorphous chains. SIC of NR is not very sensitive to a strain rate, although its hardening effect decreases at very small strain rates $<10^{-3}$/s. Moreover, SIC diminishes with temperature increase and disappears above 80°C [79].

In 1839, Goodyear empirically discovered the vulcanization of NR with sulfur, which could dramatically improve properties. During the vulcanization, the macromolecules are cross-linked by bridges containing one to several sulfur atoms; the number of atoms in the cross-link strongly affects the physical properties of the final material. Although NR can be vulcanized also with organic peroxides or radiation [82], those vulcanized NRs exhibit worse long-term stability because the polymer chains are cross-linked solely by carbon bonds [74]. The basic vulcanizing ingredients include not only vulcanizing agents but also accelerators, activators, antidegradants, fillers such as carbon black, and processing aids [73].

The ability of NR to crystallize is not affected by vulcanization [79]. The diffraction patterns of vulcanized and unvulcanized NR are very similar, and the crystal structure is not changed in NR vulcanizates containing carbon black fillers [83, 84]. The influence of cross-linking and carbon black fillers on SIC of NR is addressed in [7]. In general, the number of crystallites increases, whereas their size decreases with increasing cross-link density. There exists an intermediate cross-link density, at which the volume crystallinity reaches a maximum value. However, the stretch ratio inducing the onset of SIC is roughly independent of the cross-link density. Contrary to that, carbon black fillers decrease macroscopic stretch ratio inducing SIC because they enhance the local stretch [79].

Nowadays numerous applications of rubbers take advantage of their flexibility, relative gas impermeability, resistance to water and most chemicals, as well as electrical resistance. Besides NR, various types of synthetic rubber are produced: polyisoprene, styrene-butadiene rubber, acrylonitrile-butadiene copolymers, ethylene-vinyl chloride copolymers, polybutadiene, and polychloroprene [73, 75]. Nevertheless, about 40% of rubber is of natural origin, and most of NR (75%) is used for automobile tires [73, 75, 76]. It is worth noting that the so-called isoprene rubber (IR) is a polymer with molecular structure similar to NR, with predominant cis-isoprene units bonded by 1,4-linkages although it can contain up to 10% trans-isoprene units [73].

Biodegradation of NR was recently reviewed, e.g., in [73, 75, 76]. It can be degraded by bacteria and fungi although the process is slow. Examination of the

biodegradation products of NR and synthetic rubbers indicates oxidative cleavage of the double bond in the polymer backbone [75, 76]. Degradation of vulcanized rubber by microorganisms is also possible, although more difficult due to cross-linked structure, and is also influenced by additives present in the rubber [73, 75].

7 Other Natural Polymers

7.1 Collagen

Collagen, insoluble and fibrous, is the most abundant protein present in connective tissue and extracellular matrix in the animal kingdom. Although 27 different types of collagen have been identified, type I prevails in the connective tissue. Collagen macromolecules are composed of three α-chains forming the triple helix mainly stabilized by intra- and inter-chain hydrogen bonds [85]. The sources of collagen for industrial purposes are pig skin, bovine hide, and pork and cattle bones, although the use of non-mammal collagen increases in importance [7, 85]. Biocompatibility, biodegradability, and weak antigenicity [86] make collagen a very useful biomaterial, applied for drug delivery and tissue engineering [87]. Chemical pretreatment and warm-water extraction of collagen permits to obtain gelatin [85], which applications take advantage of its gel-forming ability, mainly in the food industry. It is worth noting that a range of applications of gelatin broadens with increasing tendency to use natural substances and includes also foaming, emulsifying, and stabilizing agents, as well as microencapsulating and biodegradable film-forming materials [7, 85].

7.2 Alginates

Alginates, linear polysaccharides, are anionic heterogeneous copolymers built of blocks of (1 → 4) linked α-L-guluronate (G) and β-D-mannuronate (M) residues (Scheme 7) and also blocks comprising alternating GM residues. They are synthesized by bacteria, for instance, *Azotobacter* and *Pseudomonas*, and brown algae [88]. Alginates are mainly obtained by alkali solution treatment of algae, although bacterial biosynthesis may be a source of these polymers with more defined chemical structures and physical properties than the alga-derived alginates. Commercially available are sodium alginates [88].

The content and length of G and M blocks, as well as molar mass, vary depending on the source of extraction. These factors are responsible for properties of alginates and alginate-based hydrogels [89]. Only the G-blocks participate in intermolecular cross-linking with divalent cations resulting in the formation of hydrogels [88]. The mechanical properties of alginate gels are enhanced by increasing the G-block length and molar mass. Molar mass of commercial alginates ranges from 32 to 400 kg/mol.

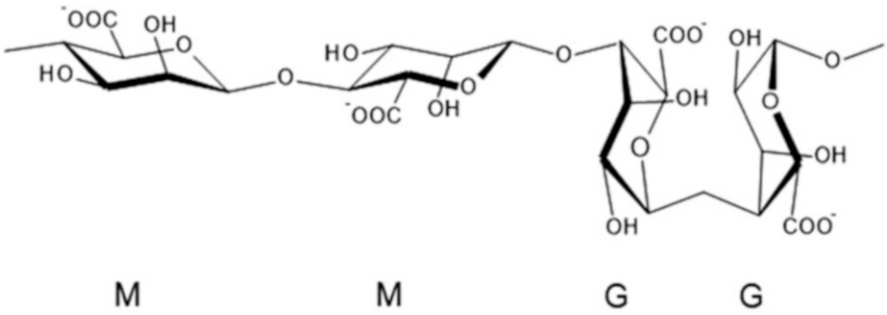

Scheme 7 MMGG sequence of alginate

However, solutions of high molar mass alginates polymer are highly viscous, which is often a disadvantage for processing [90]. Upon heating alginates decompose, alginic acid above 150°C, whereas sodium alginate above 175°C [91]. Nowadays, more than 200 different alginates are produced with different chemical structures. Alginates have some unique properties such as non-toxicity, biocompatibility, biodegradability, and hydrophilicity and have a relatively low cost. They are used as viscosifiers and stabilizing, gel-forming, film-forming, and water-binding agents in various industrial applications [7]. Owing to their biocompatibility and good gelation ability, alginates are attractive for pharmaceutical and food applications [92].

Alginates are typically used in biomedicine in hydrogels, that is, cross-linked three-dimensional networks built of hydrophilic polymers with high water content. The most common method to prepare alginate-based hydrogels is to combine an aqueous alginate solution with ionic cross-linking agents, such as divalent cations, for instance, Ca^{2+} from $CaCl_2$. They bind to G-blocks and connect the G-blocks of neighboring alginate chains. Another way is covalent cross-linking, interesting because of its inability to dissociate. However, unreacted reagents, if toxic, have to be removed from the gels [89]. The other possible ways, being explored, are thermal gelation and cell cross-linking [93, 94].

7.3 Pullulan

Pullulan, first isolated in 1958 [95], is a linear polysaccharide, with structure being a succession of α(1 → 6)-connected (1 → 4)-α-D-triglucosides, i.e., maltotrioses (Scheme 8).

Pullulan is produced extracellulary by a yeast-like fungus *Aureobasidium pullulans* and other microorganisms by fermentation of feedstocks containing sugars as an amorphous slime on the surface of microbial cells [96]. Owing to the presence of hydroxyl groups, it can be chemically modified to induce pH sensitivity by introducing functional reactive groups, to decrease solubility in water or to obtain

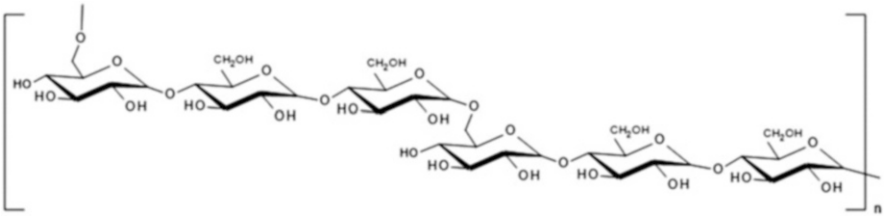

Scheme 8 Structure of pullulan repeating unit: two maltotrioses linked with α(1 → 6) bond

water-insoluble polymer [7]. Pullulan can be molded into articles with transparency, strength, and toughness [97] similar to those made of conventional polymers such as polystyrene. Although pullulan is brittle, it is odorless and tasteless and exhibits good moisture retention and barrier property for oxygen. Owing to these features, it is an interesting material for food preservation [98]. Its commercial and industrial applications include healthcare, pharmaceutical, food, and cosmetic industries and even lithography. In recent years, pullulan has also been examined for various biomedical applications [99].

7.4 Pectin

Pectins, known also as pectin polysaccharides, are a group of hetero-polysaccharides abundant in cell walls of terrestrial plants. Pectin macromolecule is very complex as it can be composed of 17 different monosaccharides containing more than 20 different linkages [100]. However, all pectins are built of the same repeating units, although their amount and chemical structures differ, being dependent on pectin origin. Pectins mainly contain galacturonic acid residues, in which carboxyl groups are mostly esterified to methoxyl esters. In addition, in pectin macromolecule, certain amount of neutral sugars might be present as side chains [101]. Main applications of pectin polysaccharides are in the food industry, primarily as gelling, stabilizing, or thickening agents. Most of the pectin used in food products is obtained from citrus peel and apple pomace [100].

7.5 Galactomannan

Galactomannans are natural polysaccharides having β-(1–4)-D-mannan backbone with single α-(1–6)-linked D-galactose branches [102], which are able to form stable viscous solutions in water. The main sources of those polysaccharides are locust bean gum, guar, tara plant, and fenugreek [103]. The physicochemical properties of galactomannans depend to a great extent on the mannose/galactose ratio (M/G) and on the distribution of D-galactose groups along the main chain. For instance, the

galactomannans with M/G from 1.3 to 5.6 exhibited T_g ranging from −70 to −65°C, tensile strength from 1.4 to 6.9 MPa, and elongation at break of 37–70% [104]. The structural features responsible for properties are related to galactomannan origin and extraction method used [104, 105]. Their capability to moisture retention as well as thickening, binding, gelling, emulsifying, suspending, and film-forming ability makes galactomannans useful in food, paper, textile, pharmaceutical, biomedical, and cosmetics industries [106].

8 Polyhydroxyalkanoates

Polyhydroxyalkanoates (PHAs) are thermoplastic semicrystalline polyesters of 3-, 4-, 5-, and 6-hydroxyalkanoic acids, which are synthesized by microorganisms, and are materials with a potential to replace conventional fossil-hydrocarbon-based polymers. PHAs are biocompatible and biodegradable; it is worth noting that they are able to biodegrade in the environment [107, 108]. More than 150 PHA monomers have been identified [109]. The repeating unit of PHA polymers is –O–CHR–$(CH_2)_m$–CO–. For $m = 1$ and R being hydrogen, methyl, ethyl, propyl group the polymer is called poly(3-hydroxypropionate), poly(3-hydroxybutyrate) (P3HB), poly(3-hydroxyvalerate) (P3HV), poly (3-hydroxyhexanoate), respectively. Examples of PHAs structure are shown in Scheme 9.

Depending on the number of carbon atoms in the repeating unit, PHAs are classified as short-chain-length (scl-PHA), medium-chain-length (mcl-PHA), and long-chain-length (lcl-PHA) with up to 5, 6–14, or more than 14 carbon atoms, respectively, the latter uncommon and least studied. P3HB and P3HV are scl-PHA, whereas mcl-PHA include poly(3-hydroxyhexanoate), poly(3-hydroxyoctanoate), and poly(3-hydroxydecanoate). Due to the presence of chiral carbon atom in the repeating unit, PHA polymers can exhibit different chirality, but naturally obtained PHAs are stereospecific with the carbons in the backbone in the R configuration. The first discovered PHA was P3HB. The French scientist Lemoigne extracted it from *Bacillus megaterium* in 1927 [110].

Microorganisms synthesize PHA for energy storage in the form of granular submicron inclusions, with the average size approx. 0.2–0.5 μm. To collect PHA it is necessary to destroy the bacterial cell and remove the protein layer on the granules. PHA production involves synthesis of the polymer by bacteria, requiring minimum

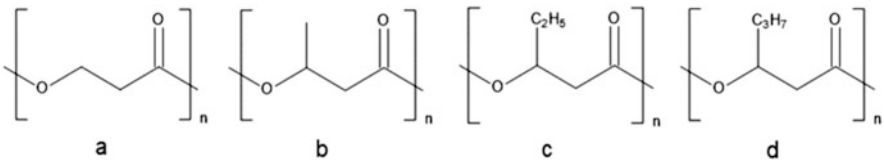

Scheme 9 Repeating units of (**a**) poly(3-hydroxypropionate), (**b**) poly(3-hydroxybutyrate), (**c**) poly(3-hydroxyvalerate), and (**d**) poly (3-hydroxyhexanoate)

of 48 h, followed by its isolation and purification. Depending on the PHA required, feedstocks include cellulosics, sugars, starch, alcohols, vegetable and other plant oils, fatty acids, organic waste, and even municipal solid waste [7, 111]. The recovery methods for the isolation and purification of PHA from the cells were recently reviewed in [112]. The methods include solvent extraction, mechanical disruption, and chemical and enzymatic digestion. Research on PHA production and optimization was recently reviewed in [113]; the academic studies focused on seeking cost-efficient carbon sources and also on improving productivity by genetic engineering. More than 300 different microorganisms synthesize PHAs, but only a few are sufficiently effective for large-scale production [113]. Some bacteria are able to synthesize PHA as much as 90 wt.% of dry cells when the feedstock is depleted of essential nutrients such as nitrogen, phosphorus, or magnesium [113, 114]. Different PHAs are produced by different bacteria. Typically, copolymers of 3-hydroxybutyrate with other comonomers contain 80–95% of the first comonomer [7]. The molar mass of PHAs depends on the type of microorganism and its growth conditions and may range from 200 to 3,000 kg/mol [114].

In general, PHAs are insoluble in water and relatively resistant to hydrolysis. They exhibit good resistance to UV but poor to acids and bases [115]. PHAs are thermoplastics with T_g from −50 to 4°C and T_m from 40 to 180°C [7, 111]. Similarly to T_g and T_m, other features of PHAs like thermodegradation temperature, crystallinity, mechanical properties, and barrier properties for vapor and oxygen depend on their chemical structure [115]. Exemplary mechanical and thermal properties of PHAs are shown in Table 1. P3HB is brittle, with tensile strength of 30–40 MPa, and elongation at break of a few percent. T_m of P3HB is high, near 177°C [108, 116, 117]. P3HB crystallizes from melt in the orthorhombic α-form, whereas metastable

Table 1 Examples of thermal and mechanical properties of biodegradable biobased polyesters

Polymer	Glass transition temperature (°C)	Melting temperature (°C)	Tensile strength (MPa)	Tensile strain at break (%)	Tensile modulus (MPa)	References
P3HB	10	177	40	4	3,500	[113]
	5–9	173–180	40	3–8	3,500–4,000	[116]
PHBV						
(15.5)	−1	140	34	12	2,500	[117]
(20.1)	−5	114	26	27	1,900	[117]
(24)	−6	138	Nr	Nr	Nr	[137]
(25)	Nr	Nr	70	30	1,370	[137]
(28.4)	−8	102	30	700	1,400	[117]
PBS	−32	114	62–59	660–710	470–540	[126]
	−32	115	31	24	337	[129]
PLA	59	154	56	13	3,740	[168]
	55	165	59	7	3,500	[169]

Numbers in brackets indicate mol% content of 3HV in PHBV. *Nr* not reported

orthorhombic β-form is strain-induced [117]. Crystallization from melt is slow, in the form of large spherulites, whose size can be decreased using nucleating agents. A relatively low thermal decomposition temperature of PH3B is also a problem as well as ageing at room temperature [115]. To overcome those disadvantages, research efforts focused on finding effective nucleating agents and plasticizers to shorten crystallization, to improve flexibility and drawability, and to reduce T_m. Also biosynthesized copolymers of 3-hydroxybutyrate with other hydroxyalkanoate comonomers can exhibit improved mechanical performance and decreased T_m, which permits to avoid degradation during processing. For instance, copolymers of 3-hydroxybutyrate and 3-hydroxyvalerate (PHBV) are less crystalline, less stiff, and brittle and can exhibit increased tensile strength and toughness compared to P3HB [113, 116], as exemplified in Table 1, although their properties and structure are related to their chemical composition. Moreover, PHBV melt viscosity is higher, which is advantageous for extrusion and blow molding. Nowadays, besides P3HB, PHBV, and poly(4-hydroxybutyrate) (P4HB), copolymers of 3-hydroxybutyrate and 4-hydroxybutyrate, as well as copolymers of 3-hydroxybutyrate and 3-hydroxyhexanoate, are produced on a large scale [117, 118]. It is worth noting that also modification by blending with other biodegradable polymers and fillers, including those based on cellulose and lignin, can modify PHAs [115–117, 119, 120]. Moreover, different methods such as epoxidation, carboxylation, chlorination, hydroxylation, and pyrolysis were used to alter the properties [121]. PHA applications include biomedical uses (drug delivery, development of scaffolds, implants, and biosensors) but also food coating, paper coating, packing, agriculture, molded goods, non-wovens, fabrics and other textiles, performance additives [108, 121]. Owing to PHA biocompatibility and biodegradability, their medical uses were recently extensively investigated [122].

9 Poly(Butylene Succinate)

Poly(butylene succinate) (PBS) is a thermoplastic polyester synthesized from succinic acid (SA) and 1,4-butanediol (BDO), named also as poly(tetramethylene succinate), with chemical structure shown in Scheme 10.

SA is obtained through hydrogenation of maleic anhydride, derived from oxidation of butane or benzene, followed by hydration. However, SA can be also

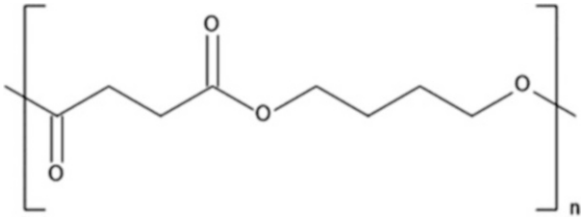

Scheme 10 Repeating unit of poly(butylene succinate)

produced by bacterial fermentation of renewable feedstock, like starch or glucose. Several bacterial strains are able to produce SA [123]. BDO can be obtained via different chemical processes but also by catalytic reduction of purified SA, obtained by fermentation of corn-derived glucose [124, 125]. In addition, genetically modified *Escherichia coli* is able to ferment sugar into BDO [124]. Synthesis of PBS involves esterification of SA and BDO or transesterification of dimethyl succinate and BDO to obtain oligomers, which are subjected to polycondensation yielding high molar mass PBS [126].

PBS is a semicrystalline polymer with crystallinity level of 35–45 wt.% [126, 127], although higher values were also reported, 65 wt.% for raw PBS, and nearly 72 wt.% for extruded fibers [128]. Exemplary properties of PBS are shown in Table 1. T_m of PBS is near 115°C, heat distortion temperature near 95°C, and T_g below −30°C [124, 126, 129]. Crystallization of PBS occurs in the monoclinic α-form [130, 131]. The transition of α-form to monoclinic β-form occurs reversibly upon stress application and removal [132, 133]. In both polymorphs hydrogen bonds were revealed by Raman spectroscopy [134]. Crystallization of PBS from the melt is spherulitic, and its temperature depends on a cooling rate; a decrease of crystallization peak temperature from 80°C at 5°C/min to 62°C at 25°C/min was reported [135]. PBS is featured by good thermal stability; significant weight loss during TGA experiment occurs above 300°C [136, 137]. PBS exhibits similar mechanical properties to polyethylene. Its elastic modulus is approx. 0.4–0.5 GPa, and it can exhibit relatively high tensile strength and large elongation at break, as shown in Table 1. PBS is hydrophilic but insoluble in water. PBS can be processed using extrusion, injection molding, and thermoforming [126]. To tailor physical properties, random copolymerization with different types of comonomer units has been studied, including adipic, terephthalic, methyl succinic, 2,2-dimetyl succinic and benzyl succinic acids, ethylene glycol, and 1,3-propanediol [124]. It is also worth noting that PBS and its copolymers are biodegradable in soil, water, and compost, also in lipase solution and activated sludge [124].

Linear structure of PBS may result in low melt strength and viscosity, which might be disadvantageous during processing, for instance, foaming; chain extenders and also branching enable to overcome this drawback [138]. Improvement of PBS properties can be also achieved by modification with other biodegradable polymers [7, 124, 139–142], fillers, and nanofillers [140, 143–147]. PBS and its blends have found commercial uses in many fields like agriculture, fishery, forestry, and construction, for instance, as mulch film, packaging, foaming, and flushable hygiene products [7]. The biomedical applications of PBS were recently reviewed in [126].

10 Polylactide

The most promising biobased polyester for replacement of conventional thermoplastics is polylactide (PLA), termed also as poly(lactic acid). The repeating unit of polylactide is $CHCH_3$–CO–O– (Scheme 11).

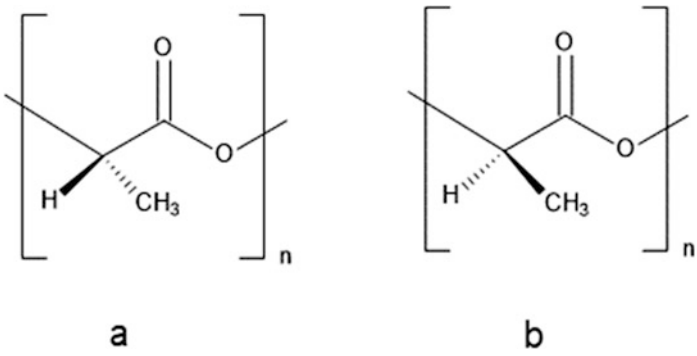

Scheme 11 Repeating units of (**a**) poly(L-lactide) and (**b**) poly(D-lactide)

PLA can be synthesized through polycondensation of lactic acid (2-hydroxypropanoic acid), which results in polymer with secondary alcohol and carboxylic end groups. Depolymerization of lactic acid oligomers leads to cyclic dimers of lactic acid called lactide (LA). Ring-opening polymerization (ROP) of LA permits to obtain PLA with secondary alcohol and ester end groups, and allows to reach high molar mass [148, 149]. In industrial processes, the latter method of synthesis is mostly used. Lactic acid can be obtained through fermentation of hexoses by a group of lactic acid bacteria, other bacteria, fungi, or yeasts. Sugarcane, beet, and corn have been used for industrial production of lactic acid. However, there is a growing demand for low-cost and non-food sources for production, including starchy wastes, molasses, and lignocellulose [150].

Lactic acid is optically active, and lactic acid bacteria can produce either or both L and D (S and R) stereoisomers [148, 150]. This results in a diversity of chemical structures of PLAs, which can be optically pure poly(L-lactide) (PLLA) or poly(D-lactide) (PDLA), or copolymers containing repeating units of both chiralities [151].

Rheological properties of PLA melt were recently reviewed in [152]. PLA can be cooled to the glassy state without crystallization; in this way wholly amorphous glassy material is obtained [153, 154]. Examples of thermal and mechanical properties of amorphous PLA are shown in Table 1. T_g of amorphous PLLA and PDLA with high molar mass is similar, at around 60°C [153]. Both the enantiomeric composition of PLA and its molar mass influence T_g. T_g increases with increasing molar mass in accordance with the Flory-Fox equation and becomes nearly constant for PLA with molar mass exceeding 100 kg/mol [153, 154]. The presence of comonomers of different chirality decreases T_g; for a copolymer with equal contents of L-lactide and D-lactide, T_g decreases by about 10°C [154].

Crystallization and crystal structures of PLA were recently a subject of extensive reviews [154–157]. Ability of PLA to crystallize strongly depends in its enantiomeric composition. Optically pure PDLA and PLLA exhibit the best ability to crystallize reflected in the fastest spherulite growth rate and high crystallinity, even 60–70 wt.% [154, 156], although dependent on crystallization conditions and molar

mass. Also T_m of optically pure PLA is higher, up to approx. 180°C. The presence of comonomers of different chirality decreases the spherulite growth rate, diminishes crystallinity, and lowers T_m; the highest the content, the stronger the decrease [154]. For the copolymers, T_m decreases linearly with increasing minor fraction content; at 10% content T_m can be lowered even by approx. 25 K. T_m of PLA increases with increasing molar mass but levels off for molar masses above 50 kg/mol [154]. The crystallization is spherulitic. The spherulite growth rate dependence on temperature is bell-shaped with a maximum in the 115–130°C range [154]. However, an additional maximum is visible near 110°C, as the plot diverges from the typical bell-shaped curve below 120°C [158], which is most possibly related to crystallization in a different crystallographic modification. The orthorhombic phase of PLA crystallizes in two variants: the ordered α-phase (termed also as the δ-phase) and the less ordered α′-phase that form at high and at low crystallization temperature, respectively [157, 159, 160]. It was observed [157] that the α-form crystallized at 120°C and above, the α′-form below 100°C, whereas both modifications formed in the intermediate temperature range. The orthorhombic γ-phase was found in PLLA crystallized epitaxially on hexamethylbenzene [157, 161]. The frustrated trigonal β-phase of PLLA was first observed in stretched fibers, but recently also in thin films [157]. Moreover, the mesophase formed during strain-induced crystallization of PLA [162].

In semi-crystalline PLLA, two distinct mobile amorphous fractions exist: a bulk-like totally mobile fraction and a slightly constrained mobile fraction, which vitrify/devitrify in the region of the bulk T_g, whereas at the crystal–amorphous interface, a rigid amorphous fraction is located, which vitrifies/devitrifies above the bulk T_g [153, 163]. The thermal properties of PLLA were extensively described in recent reviews [153, 154]. Because of slow crystallization, cooling of PLA, even optically pure, may result in fully amorphous glass, which can cold-crystallize above T_g during subsequent heating. The crystallinity developed during cooling and/or heating depends on molecular characteristics of PLA, cooling rate and/or heating rate, and thermomechanical history. Shearing of PLA melt can induce crystallization during cooling even in slowly crystallizing PLA containing a significant fraction of D-lactide [164]. The enantiomeric PDLA and PLLA form stereocomplex (scPLA) due to weak multicentered hydrogen bonds [165, 166], which significantly improves PLA properties [5, 167]. T_m of scPLA is in the range of 220–230°C.

Barrier properties of PLA have been recently reviewed in [152]. Oxygen permeability of PLA, 1.3–2 $\times$ 10^{-18} m^3 m/(m^2 s Pa) at 30°C, is similar to that of polystyrene but higher than in the case of poly(ethylene terephthalate). However, the barrier property of PLA for water vapor is worse than that of many polymers including polyolefins, PS polystyrene, poly(ethylene terephthalate), and PHBV.

Owing to its T_g, amorphous PLA is stiff and brittle at room temperature, with modulus of elasticity of about 3.5 GPa, yield strength near 60 MPa, and strain at break of few percent [152, 168, 169]. Examples of tensile properties of amorphous PLA are given in Table 1. In the amorphous PLA, crazing and shear banding are observed during drawing. Crystallinity increases the modulus but further decreases the strain at break; specimens frequently fracture before the yield. For instance, PLA

with 43 wt.% of crystallinity fractured during tensile test before the yield at the stress of 43 MPa and strain of 6%, and exhibited the modulus of 4,250 MPa [168]. With increasing temperature the drawability of PLA improves. Strain-induced crystallization during tensile drawing leads to the formation of the mesophase or α′-crystals, depending on temperature and strain rate [162].

Recently star-shaped polymers attract increasing attention. The syntheses, properties, and selected applications of star-shaped polymers with arms composed of homo- or copolymers of polylactide were recently reviewed [170]. Crystallization of 6-arm PLLAs with high molar mas was compared with their linear counterparts in [171].

After their service life, PLA products can degrade in compost under appropriate conditions via hydrolysis and enzymatic biodegradation. The hydrolytic degradation is the most important stage of biodegradation. Degradation processes occurring during processing and also in compost are comprehensively reviewed in [172].

In order to improve properties of PLA polymers, including crystallizability; mechanical performance; rheological, electrical, and barrier properties as well as stability and inflammability, various modification routes are applied, including copolymerization, chain extension, plasticization, and blending with other polymers, fillers, nanofillers, fibers, and nucleating agents [151, 152, 168, 173–181].

PLA is suitable for processing by various techniques, and nowadays PLA products are widely used, from biomedical applications to packaging, daily appliances including textiles, items used in agriculture and engineering, water treatment, car parts, electric appliances, etc. [7, 151].

11 Bio-polyethylene

Polyethylene (PE) is obtained by catalytic polymerization of ethylene under appropriate temperature and pressure conditions. Bio-PE is produced from bio-ethylene. Ethanol can be obtained by anaerobic fermentation of extracted sugarcane juice with high sucrose content and distilled to remove water and to yield azeotropic mixture of anhydrous ethanol. Although industrial-scale production is based on sugarcane, other feedstocks including sugar beet, starch crops, wood, and plant wastes can be also used. Bio-ethylene is obtained by dehydration of ethanol at high temperatures over a solid catalyst followed by polymerization [182, 183]. Bio-PE has the same properties as PE produced from petrochemical sources.

12 Bio-poly(Ethylene Terephthalate)

Poly(ethylene terephthalate) (PET) production is normally carried out through prepolymer synthesis which is mainly bis(2-hydroxyethyl) terephthalate (BHET) followed by polycondensation. The first step is the esterification of terephthalic acid

(TPA) and ethylene glycol (EG) or the transesterification of dimethyl terephthalate and EG. The synthesis of bio-PET requires biobased monomers. One of them, bio-EG, is obtained by oxidation of biobased ethylene or through hydrogenation of products of sugar pyrolysis [184]. Use of bio-EG allows to synthesize 30% biobased PET. Fully biobased PET can theoretically be produced from bio-EG and bio-TPA. Synthesis of the latter was recently reviewed in [5, 185]. Bio-TPA is a product of oxidation of *p*-xylene, resulting from cyclization of two molecules of isooctane, the latter obtained from iso-butanol produced by dehydration of sugars. Another way leading to bio-TPA is a series of reactions beginning with muconic acid produced by chemical processes and biorefinery; from the muconic acid, tetrahydroterephthalic acid is obtained and dehydrogenated to bio-TPA. Bio-TPA can also be produced from limonene-derived building blocks or from furan derivatives, especially the furan derivative such as 2,5-furandicarboxylic acid. In addition, fermentation of sugar and starches yield biobased 1,3-propane diol (bio-PDO) [186], which is used to produce biobased poly(trimethylene terephthalate) [187]. Development of the production of biobased butanediol will lead to biobased poly(butylene terephthalate) [188].

13 Bio-polyamides

Biobased polyamides (bio-PAs) include PA4, PA4.4, PA4.10, PA6.10, PA10.10, PA11, and PA12 [5, 189]. Some of them, for instance PA11 used for high-performance applications, synthesized from castor oil, are known for decades. Triglycerides in castor oils are subjected to a transesterification or a saponification to give ricinoleic acid or the corresponding methyl ester, respectively. Pyrolysis of the acid yields undecanoic acid and then 11-aminoundecanoic acid. Polycondensation of the latter with water extraction results in PA11. Another route of synthesis of bio-PAs utilizes sebacic acid derived from ricinoleic acid. PA6.10, PA10.10, and PA10.12 are polymerized from sebacic acid and hexamethylene diamine (HDMA) obtained petrochemically from butadiene. However, decamethylene diamine can be produced from bio-sebacic acid and used to synthesize bio-PAs. Besides polycondensation of dicarboxylic acids and diamines, another way of synthesis of PAs is ROP of lactams. Although starting materials to obtain bio-PAs by polycondensation are castor oil, fatty acids, carbohydrates, terpenes, and roisin acids, it is also possible to use terpenes and fatty acids to derive lactams and synthesize bio-PAs by ROP. Recent advances in biobased PAs and their synthesis are comprehensively reviewed in [189]. Properties of biobased and petrochemically obtained PAs are compared in [5]. Although bio-PAs occupy only 5% of the current biopolymer market, they are becoming increasingly important as they are applied as high-performance polymers [189].

14 Thermosetting Bio-materials

Thermosetting materials are highly cross-linked polymers that are cured at elevated temperature, also under elevated pressure, and/or by irradiation. Owing to their high cross-linking density, thermosets are high-performance materials featured by high elastic modulus, strength, durability, and resistance to thermal stresses and chemicals. The potential opportunities and drawbacks of the use of renewable feedstock in the design of some commonly used thermosets including phenolics, epoxy, polyester, and polyurethane resins were extensively reviewed in [190].

Phenolic resins, synthesized from phenol and formaldehyde, are widely applied because of superior mechanical strength, dimensional stability, heat and flame resistance, as well as high resistance against various solvents, acids, and water. Alternatively, hexamethylenetetramine can be used as a replacement for formaldehyde. A range of phenolic resins, more flexible than the conventional ones, can be obtained by reactions of cardanol with formaldehyde. The source of bio-cardanol is a cashew shell liquid, which is an agricultural by-product [190].

Owing to its structure and abundance, lignin is considered as a potential source of phenol for phenol-formaldehyde-based thermosets [10, 190]. However, because of steric hindrances, lignin reactivity with formaldehyde is limited, and in order to enhance it, lignin has to be chemically modified through acid hydrolysis and acetosolv and organosolv processes [191, 192]; recently environmentally friendly enzymatic approaches have been also developed [193]. Other raw bio-materials considered in the design of phenolic resins are tannins and pyrogallol derived from hydrolysable tannins.

Epoxy resins are formed from precursors having epoxy groups. The reaction between bisphenol A (2,2-bis(4′-hydroxyphenyl)propane) and epichlorohydrin, resulting in diglycidyl ether of bisphenol A (DGEBA), is a basis for nearly 90% of the world production of epoxy resins [190]. The so-called curing agents, reacting with epoxy groups, include amines, anhydrides, and amides; in some cases catalysts are required. To obtain bio-epoxy resins, epoxidized plant oils and fatty acids have been used [194, 195]. Depending on the oil type, the comonomers (divinylbenzene or styrene), and the stoichiometry, a range of thermosets, from elastomers to rigid materials, can be obtained by thermal or cationic copolymerization. Some of them are potentially (bio)degradable in soil. Moreover, the use of novel phosphorous-containing derivatives of fatty acids permitted to obtain epoxy thermosets with good flame-retardant properties [196]. Co-reactants (or hardeners) of natural origin are also expected to be valuable in epoxy thermosetting materials, for example, cis-9,10-epoxy-18-hydroxyoctadecanoic acid present in birch tree [197]. Another example is alcoholysis lignin that has been used as hard and hydrophilic segments in epoxy resins [198]. To reinforce oil plant-based epoxy resins, different inorganic or organic fillers were used, including glass, carbon, mineral fibers, and various nanofillers [190, 199–202].

An important class of versatile materials for flexible and rigid foams, and thermoplastics, with variety of applications, are polyurethanes (PUs). PUs, with

marked contents of urethane groups, are obtained through reactions of various polyols and isocyanates, usually catalyzed with tin derivatives [203], which permits to alter the product properties. Biopitches, soy flours, and castor oil have directly been applied as raw polyols in synthesis of bio-PUs; while isocyanate is mainly petroleum-based, recent development in biotechnology should allow to obtain biobased isocyanate compounds in the near future [190]. Among other renewable resources, plant oils, other than castor oil, have a potential to be a source of polyols for polyurethanes [204]. Other ways were also explored, for instance, oxypropylation of natural cork [205] or the use of cardanol derivatives [206].

Polycondensation of a polyol and a polyvalent acid or acid anhydride yields unsaturated polyester resins, which can be cured in the presence of unsaturated monomers, for instance, styrene. Acid anhydrides, phthalic or maleic anhydrides, are usually used, while polyols are (di)pentaerythritol, glycerol, ethylene glycol, trimethylolpropane, and neopentylglycol [207]. Polyester resins are used in decorative coating and also composites having a broad range of applications. In the design of bio-polyester resins, isosorbide, sorbitol derivative obtained from starch, can be used as a polyol, whereas fatty acids or oils are used as polyacids [190]. The design of polyester thermosetting resins was reviewed recently in [208].

15 Other Polymers

It must be noted that besides the biobased polymers described above, there are others being studied and developed. Biodegradable poly(ethylene succinate) is synthesized from SA and EG and could also be produced from biobased substrates [5]. Owing to the good barrier properties for oxygen, and elongation, it can be used in film applications. Other succinic polymers include copolymers of SA and other dicarboxylic acids, such as poly(butylene succinate-co-butylene adipate), poly(butylene succinate-co-butylene terephthalate), and poly(butylene succinate-co-butylene furandicarboxylate) [209–211] with relatively long aliphatic sequences, suitable for packaging applications. As mentioned above, bio-PDO is used to produce biobased poly(trimethylene terephthalate), and it is envisaged that biobased poly (butylene terephthalate) will also be available [5]. Other examples are biobased poly (ethylene 2,5-furandicarboxylate), with high oxygen barrier properties, and terpene-derived polymers [5, 212]. Synthesis of biobased poly(ether-ether-ketone) was also described [213]. Performance of certain recently developed biobased polymers can surpass that of conventional fossil-based materials; for instance, biobased liquid crystalline polymer derived from natural phenol, 4-hydrocinnamic acid, exhibits the mechanical strength of 63 MPa and elastic modulus of 16 GPa, and high softening temperature [214, 215]. Superstrong transparent bio-PAs with phenylenecyclobutane repeating backbone [216] and esters of poly(α-glucan) [217, 218] with outstanding thermal properties were recently reported.

16 Concluding Remarks

In the review biobased polymers were described including natural polymers, bio-engineered polymers produced by microorganisms, and those synthesized from biobased monomers. The increasing interest in biobased polymers is driven by awareness of environmental issues, that is, struggle with carbon dioxide emissions causing global warming and with still increasing dependence on fossil resources. However, it must be remembered that production of plastics consumes only a few percent of oil, whereas the rest is mainly used for fuels and asphalt. It is important that many biobased polymers are able to degrade in the environment or in compost, which is helpful in solving the plastic waste problem. It must be noted, however, that biodegradation results in irreversible loss of material, which otherwise could be re-used through recycling or burn to recover energy. Moreover, although biodegradability in the environment or compost can be helpful in decreasing the impact of the plastic waste on the environment, it is not always desirable, for instance, in the case of applications demanding durability in water or soil.

Naturally occurring polymers are abundant and can be directly used, but they are not versatile, and bio-engineered polymers also have this disadvantage to some extent. However, chemical and physical modifications of those polymers allow to obtain materials with improved properties and a broad range of applications. It must be noted that the development of biotechnology plays an important role in increasing diversity of bio-engineered polymers. Nevertheless, the most versatile are polymers synthesized from bio-substrates. It is worth noting that naturally occurring polymers also serve as a source of substrates for synthesis of other biobased polymers. For example, lignin is a potential source of phenol for phenol-formaldehyde-based thermosets. Polymers synthesized from bio-substrates are a broad range of materials including thermoplastic polyesters, polyolefins, PAs, and thermosetting resins, differing in properties and applications. This group of polymers comprises resins produced currently on industrial scale, like PLA, PBS, bio-PE, bio-PET, and some bio-PAs. Not all of them are fully biobased, like 30% biobased PET, although there is a perspective of substitution of non-biobased substrates used so far with biobased ones. Other materials, for instance, thermosets, are being developed and studied. It is worth noting that some of the newly synthesized biobased polymers exhibit better properties than the conventional fossil-based ones. Nevertheless, it is rather obvious that expansion of production of biobased polymers and increase of their share in the global plastics production require further efforts focused on improvement of their performance and also economic viability.

References

1. Okkerse C, van Bekkum H (1999) From fossil to green. Green Chem 1:107–114
2. Kausch-Blecken von Schmeling HH (2011) Eighty years of macromolecular science: from birth to nano-, bio- and self-assembling polymers – with slight emphasis on European contributions. Colloid Polym Sci 289:1407–1427

3. Steinbuechel A (2001) Biopolymers. Wiley, Weinheim
4. Domb AJ, Kost J, Wiseman DM (1997) Handbook of biodegradable polymers. Harwood Academic Publishers, London. ISBN 90-5702-153-6
5. Nakajima H, Dijkstra P, Loos K (2017) The recent developments in biobased polymers toward general and engineering applications: polymers that are upgraded from biodegradable polymers, analogous to petroleum-derived polymers, and newly developed. Polymers 9:523
6. Jiang Y, Loos K (2016) Enzymatic synthesis of biobased polyesters and polyamides. Polymers 8:243
7. Babu RP, O'Connor K, Seeram R (2013) Current progress on bio-based polymers and their future trends. Prog Biomater 2:8
8. Wróblewska AA, Lingier S, Noordijk J, Du Prez FE, De Wildeman SMA, Bernaerts KV (2017) Polyamides based on a partially bio-based spirodiamine. Eur Polym J 96:221–231
9. Zargar V, Asghari M, Dashti A (2015) A review on chitin and chitosan polymers: structure, chemistry, solubility, derivatives, and applications. ChemBioEng Rev 2:204–226
10. Llevot A, Grau E, Carlotti S, Grelier S, Cramail H (2016) From lignin-derived aromatic compounds to novel biobased polymers. Macromol Rapid Commun 37:9–28
11. http://news.bio-based.eu/bio-based-polymers-worldwide-ongoing-growth-despite-difficult-market-environment/. Accessed 4 June 2019
12. Kimura Y (2009) Molecular, structural, and material design of bio-based polymers. Polym J 41:797–807
13. Nakajima H, Kimura Y (2013) Chapter 1, General introduction: overview of the current development of biobased polymers. In: Kimura Y (ed) Bio-based polymers 1st edn. CMC Publishing, Tokyo, pp 1–23
14. Pauly M, Keegstra K (2008) Cell-wall carbohydrates and their modification as a resource for biofuels. Plant J 54:559–568
15. Poletto M, Pistor V, Zattera AJ (2013) Chapter 2, Structural characteristics and thermal properties of native cellulose. In: van de Ven T, Godbout L (eds) Cellulose – fundamental aspects. InTech, Rijeka, pp 45–68
16. Moon RJ, Martini A, Nairn J, Simonsen J, Youngblood J (2011) Cellulose nanomaterials review: structure, properties and nanocomposites. Chem Soc Rev 40:3941–3994
17. Klemm D, Heublein B, Fink HP, Bohn A (2005) Cellulose: fascinating biopolymer and sustainable raw material. Angew Chem Int Ed 44:3358–3393
18. Åkerholm M, Hinterstoisser B, Salmén L (2004) Characterization of the crystalline structure of cellulose using static and dynamic FT-IR spectroscopy. Carbohydr Res 339:569–578
19. Oh SY, Yoo DI, Shin Y, Kim HC, Kim HY, Chung YS, Park WH, Youk JH (2005) Crystalline structure analysis of cellulose treated with sodium hydroxide and carbon dioxide by means of X-ray diffraction and FTIR spectroscopy. Carbohydr Res 340:2376–2391
20. Bisanda ETN, Ansell MP (1992) Properties of sisal-CNSL composites. J Mater Sci 27:1690–1700
21. Eichhorn SJ, Baillie CA, Zafeiropoulos N, Mwaikambo LY, Ansell MP, Dufresne A, Entwistle KM, Herrera-Franco PJ, Escamilla GC, Groom L, Hughes M, Hill C, Rials TG, Wild PM (2001) Review: current international research into cellulosic fibres and composites. J Mater Sci 36:2107–2131
22. Picker KM, Hoag SW (2002) Characterization of the thermal properties of microcrystalline cellulose by modulated temperature differential scanning calorimetry. J Pharm Sci 91:342–349
23. Atalla RH, Vanderhart DL (1984) Native cellulose: a composite of two distinct crystalline forms. Science 223:283–285
24. Edgar KJ, Buchanan CM, Debenham JS, Rundquist PA, Seiler BD, Shelton MC, Tindall D (2001) Advances in cellulose ester performance and applications. Prog Polym Sci 26:1605–1688
25. Jedvert K, Heinze T (2017) Cellulose modification and shaping - a review. J Polym Eng 37:845–860

26. Teramoto Y (2015) Functional thermoplastic materials from derivatives of cellulose and related structural polysaccharides. Molecules 20:5487–5527
27. Esa F, Tasirin SM, Rahman NA (2014) Overview of bacterial cellulose production and application. Agric Agric Sci Procedia 2:113–119
28. Faruk O, Bledzki AK, Fink HP, Sain M (2012) Biocomposites reinforced with natural fibers: 2000–2010. Prog Polym Sci 37:1552–1596
29. Faruk O, Bledzki AK, Fink HP, Sain M (2014) Progress report on natural fiber reinforced composites. Macromol Mater Eng 299:9–26
30. Jonoobi M, Oladi R, Davoudpour Y, Oksman K, Dufresne A, Hamzeh Y, Davoodi R (2015) Different preparation methods and properties of nanostructured cellulose from various natural resources and residues: a review. Cellulose 22:935–969
31. Oksman K, Aitomaki Y, Mathew AP, Siqueira G, Zhou Q, Butylina S, Tanpichai S, Zhou X, Hooshmand S (2016) Review of the recent developments in cellulose nanocomposite processing. Compos Part A 83:2–18
32. Donald AM (2004) Understanding starch structure and functionality. In: Eliasson AC (ed) Starch in food: structure, function and applications. Woodhead Publishing, Cambridge, pp 156–184
33. Averous L (2004) Biodegradable multiphase systems based on plasticized starch: a review. J Macromol Sci Part C 44:231–274
34. Bertoft E (2017) Understanding starch structure: recent progress. Agronomy 7:56
35. Avérous L, Halley PJ (2009) Biocomposites based on plasticized starch. Biofuels Bioprod Biorefin 3:329–343
36. Shah PB, Bandopadhyay S, Bellare JR (1995) Environmentally degradable starch filled low-density polyethylene. Polym Degrad Stabil 47:165–173
37. Russell PL (1987) Gelatinization of starches of different amylose amylopectin content – a study by differential scanning calorimetry. J Cereal Sci 6:133–145
38. van Soest JJG, Hulleman SHD, de Wit D, Vliegenthart JFG (1996) Crystallinity in starch bioplastics. Ind Crop Prod 5:11–22
39. Jane J (1995) Starch properties, modifications and applications. J Macromol Sci Part A 32:751–757
40. Avella M, De Vlieger JJ, Errico ME, Fischer S, Vacca P, Volpe MG (2005) Biodegradable starch/clay nanocomposite films for food packaging applications. Food Chem 93:467–474
41. Lu DR, Xiao CM, Xu SJ (2009) Starch-based completely biodegradable polymer materials. eXPRESS Polym Lett 3:366–375
42. Duval A, Lawoko M (2014) A review on lignin-based polymeric, micro- and nano-structured materials. React Funct Polym 85:78–96
43. Boerjan W, Ralph J, Baucher M (2003) Lignin biosynthesis. Annu Rev Plant Biol 54:519–546
44. Nanayakkara B, Manley-Harris M, Suckling ID, Donaldson LA (2009) Quantitative chemical indicators to assess the gradation of compression wood. Holzforschung 63:431–439
45. Wagner A, Donaldson L, Ralph J (2012) Lignification and lignin manipulations in conifers. Adv Bot Res 61:37–76
46. Brebu M, Vasile C (2010) Thermal degradation of lignin – a review. Cell Chem Technol 44:353–363
47. Gregorova A, Kosikova B, Stasko A (2007) Radical scavenging capacity of lignin and its effect on processing stabilization of virgin and recycled polypropylene. J Appl Polym Sci 106:1626–1631
48. Kirschweng B, Tatraaljai D, Foldes E, Pukanszky B (2017) Natural antioxidants as stabilizers for polymers. Polym Degrad Stab 145:25–40
49. Thakur VK, Thakur MK, Raghavan P, Kessler MR (2014) Progress in green polymer composites from lignin for multifunctional applications: a review. ACS Sustain Chem Eng 2:1072–1092
50. Hu X, Du Y, Tang Y, Wang Q, Feng T, Yang J, Kennedy JF (2007) Solubility and property of chitin in NaOH/urea aqueous solution. Carbohydr Polym 70:451–458

51. Rinaudo M (2006) Chitin and chitosan: properties and applications. Prog Polym Sci 31:603–632
52. Villetti MA, Crespo JS, Soldi MS, Pires ATN, Borsali R, Soldi V (2002) Thermal degradation of natural polymers. J Therm Anal Calorim 67:295–303
53. Raabe D, Al-Sawalmih A, Yi S, Fabritius H (2007) Preferred crystallographic texture of α-chitin as a microscopic and macroscopic design principle of the exoskeleton of the lobster Homarus americanus. Acta Biomater 3:882–895
54. Wang Y, Chang Y, Yu L, Zhang C, Xu X, Xue Y, Li Z, Xue C (2013) Crystalline structure and thermal property characterization of chitin from Antarctic krill (Euphausia superba). Carbohydr Polym 92:90–97
55. Cabib E (1981) Chitin: structure, metabolism and regulation of biosynthesis. In: Tanner W, Loewus FA (eds) Plant carbohydrates II. Encyclopedia of plant physiology (New series), vol 13 B. Springer, Berlin, Heidelberg, pp 395–415
56. Cabib E, Bowers B, Sburlati A, Silverman SJ (1988) Fungal cell wall synthesis: the construction of a biological structure. Microbiol Sci 5:370–375
57. Blackwell J (1969) Structure of β-chitin or parallel chain systems of poly-β-(1-4)-N-acetyl-D-glucosamine. Biopolymers 7:281–298
58. Minke R, Blackwell J (1978) The structure of α-chitin. J Mol Biol 120:167–181
59. Rudall KM (1963) The chitin/protein complexes of insect cuticles. Adv Insect Physiol 1:257–313
60. Rudall KM, Kenchington W (1973) The chitin system. Biol Rev 48:597–633
61. Atkins E (1985) Conformations in polysaccharides and complex carbohydrates. J Biosci 8:375–387
62. Kurita K (1998) Chemistry and application of chitin and chitosan. Polym Degrad Stab 59:117–120
63. Kim SS, Kim SJ, Moon YD, Lee YM (1994) Thermal characteristics of chitin and hydroxypropyl chitin. Polymer 35:3212–3216
64. Kaczmarek MB, Struszczyk-Swita K, Li X, Szczesna-Antczak M, Daroch M (2019) Enzymatic modifications of chitin, chitosan, and chitooligosaccharides. Front Bioeng Biotechnol 7:243
65. Rinaudo M (2008) Main properties and current applications of some polysaccharides as biomaterials. Polym Int 57:397–430
66. Baklagina YG, Klechkovskaya VV, Kononowa SV, Petrova VA, Poshina DN, Orekhov AS, Skorik YA (2018) Polymorphic modifications of chitosan. Crystallogr Rep 63:303–313
67. Okuyama K, Noguchi K, Miyazawa T, Yui T, Ogawa K (1997) Molecular and crystal structure of hydrated chitosan. Macromolecules 30:5849–5855
68. Naito PK, Ogawa Y, Kimura S, Iwata T, Wada M (2015) Crystal transition from hydrated chitosan and chitosan/monocarboxylic acid complex to anhydrous chitosan investigated by X-ray diffraction. J Polym Sci B Polym Phys 53:1065–1069
69. Sakurai T, Maegawa T, Takahashi T (2000) Glass transition temperature of chitosan and miscibility of chitosan/poly(N-vinyl pyrrolidone) blends. Polymer 41:7051–7056
70. Hirano S (1996) Chitin biotechnology applications. Biotechnol Annu Rev 2:237–258
71. Illum L (1998) Chitosan and its use as a pharmaceutical excipient. Pharm Res 15:1326–1331
72. Mormile P, Petti L, Rippa M, Immirzi B, Malinconico M, Santagata G (2007) Monitoring of the degradation dynamics of agricultural films by IR thermography. Polym Degrad Stab 92:777–784
73. Shah AA, Hasan F, Shah Z, Kanwal N, Zeb S (2013) Biodegradation of natural and synthetic rubbers: a review. Int Biodeter Biodegr 83:145–157
74. Tanaka Y, Sakdapipanich JT (2001) Chemical structure and occurrence of natural polyisoprenes. In: Koyama T, Steinbüchel A (eds) Biopolymers. Polyisoprenoids, vol 2. Wiley, Weinheim, pp 1–25
75. Rose K, Steinbuchel A (2005) Biodegradation of natural rubber and related compounds: recent insights into a hardly understood catabolic capability of microorganisms. Appl Environ Microbiol 71:2803–2812

76. Yikmis M, Steinbuchel A (2012) Historical and recent achievements in the field of microbial degradation of natural and synthetic rubber. Appl Environ Microbiol 78:4543–4551
77. Subramaniam A (1995) The chemistry of natural rubber latex. Immunol Allergy Clin North Am 15:1–20
78. Wood LA, Bekkedahl N (1946) Crystallization of unvulcanized rubber at different temperatures. J Appl Phys 17:362–375
79. Huneau B (2011) Strain-induced crystallization of natural rubber: a review of X-ray diffraction investigations. Rubber Chem Technol 84:425–452
80. Loadman MJR (1985) The glass transition temperature of natural rubber. J Therm Anal 30:929–941
81. Hamed GR, Kim HJ, Gent AN (1996) Cut growth in vulcanizates of natural rubber, cis-polybutadiene, and a 50/50 blend during single and repeated extension. Rubber Chem Technol 69:807–818
82. Coran AY (1978) Vulcanization. In: Eirich FR (ed) Science and technology of rubber. Academic Press, New York, pp 291–338
83. Gehman SD, Field JE (1939) An X-ray investigation of crystallinity in rubber. J Appl Phys 10:564–572
84. Gehman SD, Field JE (1940) X-ray structure of rubber-carbon black mixtures. Ind Eng Chem 32:1401–1407
85. Gomez-Guillen MC, Gimenez B, Lopez-Caballero ME, Montero MP (2011) Functional and bioactive properties of collagen and gelatin from alternative sources: a review. Food Hydrocoll 25:1813–1827
86. Maeda M, Tani S, Sano A, Fujioka K (1999) Microstructure and release characteristics of the minipellet, a collagen based drug delivery system for controlled release of protein drugs. J Control Release 62:313–324
87. Lee CH, Singla A, Lee Y (2001) Biomedical applications of collagen. Int J Pharm 221:1–22
88. Lee KY, Mooney DJ (2012) Alginate: properties and biomedical applications. Prog Polym Sci 37:106–126
89. George M, Abraham TE (2006) Polyionic hydrocolloids for the intestinal delivery of protein drugs: alginate and chitosan – a review. J Control Release 114:1–14
90. LeRoux MA, Guilak F, Setton LA (1999) Compressive and shear properties of alginate gel: effects of sodium ions and alginate concentration. J Biomed Mater Res 47:46–53
91. Soares JP, Santos JE, Chierice GO, Cavalheiro ETG (2004) Thermal behavior of alginic acid and its sodium salt. Ecl Quim J 29:57–63
92. Nesic A, Onjia A, Davidovic S, Dimitrijevic S, Errico ME, Santagata G, Malinconico M (2017) Design of pectin-sodium alginate based films for potential healthcare application: study of chemico-physical interactions between the components of films and assessment of their antimicrobial activity. Carbohydr Polym 157:981–990
93. Zhao SP, Cao MJ, Li H, Li LY, Xu WL (2010) Synthesis and characterization of thermosensitive semi-IPN hydrogels based on poly(ethylene glycol)-co-poly(epsilon-caprolactone) macromer, N-isopropylacrylamide, and sodium alginate. Carbohydr Res 345:425–431
94. Lee KY, Kong HJ, Larson RG, Mooney DJ (2003) Hydrogel formation via cell crosslinking. Adv Mater 15:1828–1832
95. Bernier B (1958) The production of polysaccharide by fungi active in the decomposition of wood and forest litter. Can J Microbiol 4:195–204
96. Singh RS, Saini GK, Kennedy JF (2008) Pullulan: microbial sources, production and applications. Carbohydr Polym 73:515–531
97. Leathers TD (2003) Biotechnological production and applications of pullulan. Appl Microbiol Biotechnol 62:468–473
98. Chen CT, Chen KI, Chiang HH, Chen YK, Cheng KC (2017) Improvement on physical properties of pullulan films by novel cross-linking strategy. J Food Sci 82:108–117
99. Singh RS, Kaur N, Rana V, Kennedy JF (2017) Pullulan: a novel molecule for biomedical applications. Carbohydr Polym 171:102–121

100. Voragen AGJ, Coenen GJ, Verhoef RP, Schols HA (2009) Pectin, a versatile polysaccharide present in plant cell walls. Struct Chem 20:263–275
101. Thakur BR, Singh RK, Handa AK (1997) Chemistry and uses of pectin – a review. Crit Rev Food Sci Nutr 37:47–73
102. Blibech M, Maktouf S, Chaari F, Zouari S, Neifar M, Besbes S, Ellouze-Ghorbel R (2015) Functionality of galactomannan extracted from Tunisian carob seed in bread dough. J Food Sci Technol 52:423–429
103. Prajapati VD, Jani GK, Moradiya NG, Randeria NP, Nagar BJ, Naikwadi NN, Variya BC (2013) Galactomannan: a versatile biodegradable seed polysaccharide. Int J Biol Macromol 60:83–92
104. Dos Santos VRF, Souza BWS, Teixeira JA, Vicente AA, Cerqueira MA (2015) Relationship between galactomannan structure and physicochemical properties of films produced thereof. J Food Sci Technol 52:8292–8299
105. Cerqueira MA, Pinheiro AC, Souza BWS, Lima AMP, Ribeiro C, Miranda C, Teixeira JA, Moreira RA, Coimbra MA, Goncalves MP, Vincente AA (2009) Extraction, purification and characterization of galactomannans from non-traditional sources. Carbohydr Polym 75:408–414
106. Srivastava M, Kapoor VP (2005) Seed galactomannans: an overview. Chem Biodivers 2:295–317
107. Doi Y, Kasuya K, Abe H, Koyama N, Ishiwatari S, Takagi K, Yoshida Y (1996) Evaluation of biodegradabilities of biosynthetic and chemosynthetic polyesters in river water. Polym Degrad Stab 51:281–286
108. Philip S, Keshavarz T, Roy I (2007) Polyhydroxyalkanoates: biodegradable polymers with a range of applications. J Chem Technol Biotechnol 82:233–247
109. Steinbüchel A, Valentin HE (1995) Diversity of bacterial polyhydroxyalkanoic acids. FEMS Microbiol Lett 128:219–228
110. Macrae RM, Wilkinson JF (1958) Poly-β-hydroxybutyrate metabolism in washed suspensions of Bacillus cereus and Bacillus megaterium. J Gen Microbiol 19:210–222
111. Raza ZA, Abid S, Banat IM (2018) Polyhydroxyalkanoates: characteristics, production, recent developments and applications. Int Biodeter Biodegr 126:45–56
112. Kunasundari B, Sudesh K (2011) Isolation and recovery of microbial polyhydroxyalkanoates. Express Polym Lett 5:620–634
113. Chanprateep S (2010) Current trends in biodegradable polyhydroxyalkanoates. J Biosci Bioeng 6:621–632
114. Varsha YM, Savitha R (2011) Overview on polyhydroxyalkanoates: a promising biopol. J Microb Biochem Technol 3:99–105
115. Bugnicourt E, Cinelli P, Lazzeri A, Alvarez V (2014) Polyhydroxyalkanoate (PHA): review of synthesis, characteristics, processing and potential applications in packaging. Express Polym Lett 8:791–808
116. Anjum A, Zuber M, Zia KM, Noreen A, Anjum MN, Tabasum S (2016) Microbial production of polyhydroxyalkanoates (PHAs) and its copolymers: a review of recent advancements. Int J Biol Macromol 89:161–174
117. Laycock B, Halley P, Pratt S, Werker A, Lant P (2013) The chemomechanical properties of microbial polyhydroxyalkanoates. Prog Polym Sci 38:536–583
118. Chen GQ (2010) Industrial production of PHA. In: Plastics from bacteria: natural functions and applications. Microbiology monographs, vol 14. Springer, Berlin, pp 121–132
119. Singh S, Mohanty AK (2007) Wood fiber reinforced bacterial bioplastic composites: fabrication and performance evaluation. Compos Sci Technol 67:1753–1763
120. Avérous L, Le Digabel F (2006) Properties of biocomposites based on lignocellulosic fillers. Carbohyd Polym 66:480–493
121. Gadgil BST, Killi N, Rathna GVN (2017) Polyhydroxyalkanoates as biomaterials. MedChemComm 8:1774–1787

122. Hazer DB, Kilicay E, Hazer B (2012) Poly(3-hydroxyalkanoate)s: diversification and biomedical applications. A state of the art review. Mater Sci Eng C 32:637–647
123. Bechthold I, Bretz K, Kabasci S, Kopitzky R, Springer A (2008) Succinic acid: a new platform chemical for biobased polymers from renewable resources. Chem Eng Technol 31:647–654
124. Xu J, Guo BH (2010) Poly(butylene succinate) and its copolymers: research, development and industrialization. Biotechnol J 5:1149–1163
125. Cooper JS, Vigon B (2001) Life cycle engineering guidelines. Chapter 5: new design. National Risk Management Research Laboratory. Office of Research and Development, U.S. EPA, Cincinnati, EPA/600/R-01/101, pp 50–52
126. Gigli M, Fabbri M, Lotti N, Gamberini R, Rimini B, Munari A (2016) Poly(butylene succinate)-based polyesters for biomedical applications: a review. Eur Polym J 75:431–460
127. Soccio M, Lotti N, Finelli L, Gazzano M, Munari A (2008) Influence of transesterification reactions on the miscibility and thermal properties of poly (butylene/diethylene succinate) copolymers. Eur Polym J 44:1722–1732
128. Almeida LR, Martins AR, Fernandes EM, Oliveira MB, Correlo VM, Pashkuleva I, Marques AP, Ribeiro AS, Duraes NF, Silva CJ, Bonifacio G, Sousa RA, Oliveira AL, Reis RL (2013) New biotextiles for tissue engineering: development, characterization and in vitro cellular viability. Acta Biomater 9:8167–8181
129. Gigli M, Lotti N, Gazzano M, Finelli L, Munari A (2013) Synthesis and characterization of novel poly(butylene succinate)-based copolyesters designed as potential candidates for soft tissue engineering. Polym Eng Sci 53:491–501
130. Liu G, Zheng L, Zhang X, Li C, Jiang S, Wang D (2012) Reversible lamellar thickening induced by crystal transition in poly(butylene succinate). Macromolecules 45:5487–5493
131. Ihn KJ, Yoo ES, Im SS (1995) Structure and morphology of poly(tetramethylene succinate) crystals. Macromolecules 28:2460–2464
132. Ichikawa Y, Suzuki J, Washiyama J, Moteki Y, Noguchi K, Okuyama K (1994) Strain-induced crystal modification in poly(tetramethylene succinate). Polymer 35:3338–3339
133. Ichikawa Y, Kondo H, Igarashi Y, Noguchi K, Okuyama K, Washiyama J (2000) Crystal structures of α and β forms of poly(tetramethylene succinate). Polymer 41:4719–4727
134. Tatsuoka S, Sato H (2018) Stress-induced crystal transition of poly(butylene succinate) studied by terahertz and low-frequency Raman spectroscopy and quantum chemical calculation. Spectrochim Acta A Mol Biomol Spectrosc 197:95–102
135. Yarici T, Kodal M, Ozkoc G (2018) Non-isothermal crystallization kinetics of poly(butylene succinate) (PBS) nanocomposites with different modified carbon nanotubes. Polymer 146:361–377
136. Chrissafis K, Paraskevopoulos KM, Bikiaris DN (2005) Thermal degradation mechanism of poly(ethylene succinate) and poly(butylene succinate): comparative study. Thermochim Acta 435:142–150
137. Hemsri S, Thongpin C, Moradokpermpoon N, Niramon P, Suppaso M (2015) Mechanical properties and thermal stability of poly(butylene succinate)/acrylonitrile butadiene rubber blend. Macromol Symp 354:145–154
138. Diaz A, Katsarava R, Puiggali J (2014) Synthesis, properties and applications of biodegradable polymers derived from diols and dicarboxylic acids: from polyesters to poly(ester amide)s. Int J Mol Sci 15:7064–7123
139. Deng Y, Thomas NJ (2015) Blending poly(butylene succinate) with poly(lactic acid): ductility and phase inversion effects. Eur Polym J 71:534–546
140. Gumede TP, Luyt AS, Müller AJ (2018) Review on PCL, PBS, and PCL/PBS blends containing carbon nanotubes. eXPRESS Polym Lett 12:505–529
141. Li J, Luo X, Lin X, Zhou Y (2013) Comparative study on the blends of PBS/thermoplastic starch prepared from waxy and normal corn starches. Starch 65:831–839
142. Qiu Z, Ikehara T, Nishi T (2003) Poly(hydroxybutyrate)/poly(butylene succinate) blends: miscibility and nonisothermal crystallization. Polymer 44:2503–2508

143. Hwang SY, You ES, Im SS (2012) The synthesis of copolymers, blends and composites based on poly(butylene succinate). Polym J 44:1179–1190
144. Calabia BP, Ninomiya F, Yagi H, Oishi A, Taguchi K, Kunioka M, Funabashi M (2013) Biodegradable poly(butylene succinate) composites reinforced by cotton fiber with silane coupling agent. Polymers 5:128–141
145. Kurokawa N, Kimura S, Hotta A (2018) Mechanical properties of poly(butylene succinate) composites with aligned cellulose-acetate nanofibers. J Appl Polym Sci 135:45429
146. Wang XW, Zhang CA, Wang PL, Zhao J, Zhang W, Ji JH, Hua K, Zhou J, Yang XB, Li XP (2012) Enhanced performance of biodegradable poly(butylene succinate)/graphene oxide nanocomposites via in situ polymerization. Langmuir 28:7091–7095
147. Lin N, Yu JH, Chang PR, Li JL, Huang J (2011) Poly(butylene succinate)-based biocomposites filled with polysaccharide nanocrystals: structure and properties. Polym Compos 32:472–482
148. Sodergard A, Stolt M (2002) Properties of lactic acid polymers and their correlation with composition. Prog Polym Sci 27:1123–1163
149. Byers JA, Biernesser AB, Delle Chiaie KR, Kaur A, Kehl JA (2018) Catalytic systems for the production of poly(lactic acid). Adv Polym Sci 279:67–118
150. Tan J, Abdel-Rahman MA, Sonomoto K (2018) Biorefinery-based lactic acid fermentation: microbial production of pure monomer product. Adv Polym Sci 279:27–66
151. Masutani K, Kimura Y (2018) Present situation and future perspectives of poly(lactic acid). Adv Polym Sci 279:1–25
152. Domenek S, Fernandes-Nassar S, Ducruet V (2018) Rheology, mechanical properties, and barrier properties of poly(lactic acid). Adv Polym Sci 279:303–341
153. Righetti MC (2018) Amorphous fractions of poly(lactic acid). Adv Polym Sci 279:195–234
154. Saeidlou S, Huneault MA, Li HB, Park CB (2012) Poly(lactic acid) crystallization. Prog Polym Sci 37:1657–1677
155. Muller AJ, Avila M, Saenz G, Salazar J (2015) Crystallization of PLA-based materials. In: Jimenez A, Peltzer M, Ruseckaite R (eds) Poly(lactic acid) science and technology: processing, properties, additives and applications. RSC polymer chemistry series. Royal Society of Chemistry, Cambridge, pp 66–98
156. Androsch R, Schick C, Di Lorenzo ML (2018) Kinetics of nucleation and growth of crystals of poly(L-lactic acid). Adv Polym Sci 279:235–272
157. Lotz B (2018) Crystal polymorphism and morphology of polylactides. Adv Polym Sci 279:273–302
158. Di Lorenzo ML (2005) Crystallization behavior of poly(L-lactic acid). Eur Polym J 41:569–575
159. Zhang J, Tashiro K, Tsuji H, Domb AJ (2008) Disorder-to-order phase transition and multiple melting behavior of poly(L-lactide) investigated by simultaneous measurements of WAXD and DSC. Macromolecules 41:1352–1357
160. Wasanasuk K, Tashiro K (2011) Crystal structure and disorder in poly(L-lactic acid) δ form (α′ form) and the phase transition mechanism to the ordered α form. Polymer 52:6097–6109
161. Cartier L, Okihara T, Ikada Y, Tsuji H, Puiggali J, Lotz B (2000) Epitaxial crystallization and crystalline polymorphism of polylactides. Polymer 41:8909–8919
162. Stoclet G, Seguela R, Lefebvre JM, Elkoun S, Vanmansart C (2010) Strain-induced molecular ordering in polylactide upon uniaxial stretching. Macromolecules 43:1488–1498
163. Pyda M, Czerniecka-Kubicka A (2018) Thermal properties and thermodynamics of poly (L-lactic acid). Adv Polym Sci 279:153–194
164. Bojda J, Piorkowska E (2016) Shear-induced nonisothermal crystallization of two grades of PLA. Polym Test 50:172–181
165. Sarasua JR, Rodríguez NL, Arraiza AL, Meaurio E (2005) Stereoselective crystallization and specific interactions in polylactides. Macromolecules 38:8362–8371

166. Zhang J, Sato H, Tsuji H, Noda I, Ozaki Y (2005) Infrared spectroscopic study of $CH_3 \cdots O{=}C$ interaction during poly(L-lactide)/poly(D-lactide) stereocomplex formation. Macromolecules 38:1822–1828
167. Tsuji H (2005) Poly(lactide) stereocomplexes: formation, structure, properties, degradation, and applications. Macromol Biosci 5:569–597
168. Lezak E, Kulinski Z, Masirek R, Piorkowska E, Pracella M, Gadzinowska K (2008) Mechanical and thermal properties of green polylactide composites with natural fillers. Macromol Biosci 8:1190–1200
169. Farah S, Anderson DG, Langer R (2016) Physical and mechanical properties of PLA, and their functions in widespread applications – a comprehensive review. Adv Drug Deliv Rev 107:367–392
170. Michalski A, Brzezinski M, Lapienis G, Biela T (2019) Star-shaped and branched polylactides: synthesis, characterization, and properties. Prog Polym Sci 89:159–212
171. Bojda J, Piorkowska E, Lapienis G, Michalski A (2018) Crystallization of star-shaped and linear poly(L-lactide)s. Eur Polym J 105:126–134
172. Gorrasi G, Pantani R (2018) Hydrolysis and biodegradation of poly(lactic acid). Adv Polym Sci 279:119–151
173. Liu H, Zhang J (2011) Research progress in toughening modification of poly(lactic acid). J Polym Sci B Polym Phys 49:1051–1083
174. Zubrowska A, Piorkowska E, Bojda J (2018) Novel tough crystalline blends of polylactide with ethylene glycol derivative of POSS. J Polym Environ 26:145–151
175. Kowalczyk M, Piorkowska E, Dutkiewicz S, Sowinski P (2014) Toughening of polylactide by blending with a novel random aliphatic-aromatic copolyester. Eur Polym J 59:59–68
176. Siakeng R, Jawaid M, Ariffin H, Sapuan SM, Asim M, Saba N (2019) Natural fiber reinforced polylactic acid composites: a review. Polym Compos 40:446–463
177. Piekarska K, Sowinski P, Piorkowska E, Ul Haque MM, Pracella M (2016) Structure and properties of hybrid PLA nanocomposites with inorganic nanofillers and cellulose fibers. Compos Part A Appl Sci Manuf 82:34–41
178. Goncalves C, Goncalves IC, Magalhaes FD, Pinto AM (2017) Poly(lactic acid) composites containing carbon-based nanomaterials: a review. Polymers 9:269
179. Piekarska K, Piorkowska E, Bojda J (2017) The influence of matrix crystallinity, filler grain size and modification on properties of PLA/calcium carbonate composites. Polym Test 62:203–209
180. Pluta M, Bojda J, Piorkowska E, Murariu M, Bonnaud L, Dubois P (2017) The effect of halloysite nanotubes and N,N′-ethylenebis(stearamide) on morphology and properties of polylactide nanocomposites with crystalline matrix. Polym Test 64:83–91
181. Murariu M, Dubois P (2016) PLA composites: from production to properties. Adv Drug Deliv Rev 107:17–46
182. Chen GW, Li SL, Jiao FJ, Yuan Q (2007) Catalytic dehydration of bioethanol to ethylene over $TiO_2/\gamma\text{-}Al_2O_3$ catalyst in microchannel reactors. Catal Today 125:111–119
183. Morschbacker A (2009) Bio-ethanol based ethylene. J Macromol Sci Part C Polym Rev 49:79–84
184. Tullo A (2017) New route planned to biobased ethylene glycol. C&EN Glob Enterp 95:10–10. https://doi.org/10.1021/cen-09546-notw6
185. Collias DI, Harris AM, Nagpal V, Cottrell IW, Schultheis MW (2014) Biobased terephthalic acid technologies: a literature review. Ind Biotechnol 10:91–105
186. DuPont Tate & Lyle BioProducts Report. http://www.cosmoschemicals.com/uploads/products/pdf/technical/susterra-propanediol-89.pdf. Accessed 3 Dec 2018
187. Xie Q, Hu X, Hu T, Xiao P, Xu Y, Leffew KW (2015) Polytrimethylene terephthalate: an example of an industrial polymer platform development in China. Macromol React Eng 9:401–408
188. Bio-BasedWorld News Report. https://www.biobasedworldnews.com/novamont-opensworlds-first-plant-for-the-production-of-bio-based-butanediol-on-industrial-scale. Accessed 3 Dec 2018

189. Winnacker M, Rieger B (2016) Biobased polyamides: recent advances in basic and applied research. Macromol Rapid Commun 37:1391–1413
190. Raquez J-M, Deléglise M, Lacrampe M-F, Krawczak P (2010) Thermosetting (bio)materials derived from renewable resources: a critical review. Prog Polym Sci 35:487–509
191. Vazquez G, Rodriguez-Bona C, Freire S, Gonzalez-Alvarez J, Antorrena G (1999) Acetosolv pine lignin as copolymer in resins for manufacture of exterior grade plywoods. Bioresour Technol 70:209–214
192. Cetin NS, Ozmen N (2002) Use of organosolv lignin in phenol–formaldehyde resins for particleboard production. I. Organosolv lignin modified resins. Int J Adhes Adhes 22:477–480
193. Sena-Martins G, Almeida-Vara E, Duarte JC (2008) Eco-friendly new products from enzymatically modified industrial lignins. Ind Crop Prod 27:189–195
194. Meier MAR, Metzger JO, Schubert US (2007) Plant oil renewable resources as green alternatives in polymer science. Chem Soc Rev 36:1788–1802
195. Guner FS, Yagci Y, Erciyes AT (2006) Polymers from triglyceride oils. Prog Polym Sci 31:633–670
196. Lligadas G, Ronda JC, Galia M, Cadiz V (2006) Development of novel phosphorus-containing epoxy resins from renewable resources. J Polym Sci Part A Polym Chem 44:6717–6727
197. Olsson A, Lindstrom M, Iversen T (2007) Lipase-catalyzed synthesis of an epoxy-functionalized polyester from the suberin monomer cis-9,10-epoxy-18-hydroxyoctadecanoic acid. Biomacromolecules 8:757–760
198. Hirose S, Hatakeyama T, Hatakeyama H (2003) Synthesis and thermal properties of epoxy resins from ester-carboxylic acid derivative of alcoholysis lignin. Macromol Symp 197:157–169
199. Boquillon N (2006) Use of an epoxidized oil-based resin as matrix in vegetable fibers-reinforced composites. J Appl Polym Sci 101:4037–4043
200. Miyagawa H, Misra M, Drzal LT, Mohanty AK (2005) Biobased epoxy/layered silicate nanocomposites: thermophysical properties and fracture behavior evaluation. J Polym Environ 13:87–96
201. Uyama H, Kuwabara M, Tsujimoto T, Nakano M, Usuki A, Kobayashi S (2003) Green nanocomposites from renewable resources: plant oil–clay hybrid materials. Chem Mater 15:2492–2494
202. Lligadas G, Ronda JC, Galia M, Cadiz V (2006) Bionanocomposites from renewable resources: epoxidized linseed oil-polyhedral oligomeric silsesquioxanes hybrid materials. Biomacromolecules 7:3521–3526
203. Caraculacu AA, Coseri S (2001) Isocyanates in polyaddition processes, structure and reaction mechanisms. Prog Polym Sci 26:799–851
204. Petrovic ZS (2008) Polyurethanes from vegetable oils. Polym Rev 48:109–155
205. Evtiouguina M, Barros-Timmons A, Cruz-Pinto JJ, Pascoal Neto C, Belgacem MN, Gandini A (2002) Oxypropylation of cork and the use of the ensuing polyols in polyurethane formulations. Biomacromolecules 3:57–62
206. Suresh KI, Kishanprasad VS (2005) Synthesis, structure, and properties of novel polyols from cardanol and developed polyurethanes. Ind Eng Chem Res 44:4504–4512
207. Penczek P, Czub P, Pielichowski J (2005) Unsaturated polyester resins: chemistry and technology. Adv Polym Sci 184:1–95
208. van Haveren J, Oostveen EA, Micciche F, Noordover BAJ, Koning CE, van Benthem RATM, Frissen AE, Weijnen JGJ (2007) Resins and additives for powder coatings and alkyd paints, based on renewable resources. J Coat Technol Res 4:177–186
209. Siracusa V, Lotti N, Munari A, Rosa MD (2015) Poly(butylene succinate) and poly(butylene succinate-co-adipate) for food packaging applications: gas barrier properties after stressed treatments. Polym Degrad Stab 119:35–45
210. Luo S, Li F, Yu J, Cao A (2010) Synthesis of poly(butylene succinate-co-butylene terephthalate) (PBST) copolyesters with high molecular weights via direct esterification and polycondensation. J Appl Polym Sci 115:2203–2211

211. Wu L, Mincheva R, Xu Y, Raquez J-M, Dubois P (2012) High molecular weight poly (butylene succinate-co-butylene furandicarboxylate) copolyesters: from catalyzed polycondensation reaction to thermomechanical properties. Biomacromolecules 13:2973–2981
212. Rosenboom JG, Hohl DK, Fleckenstein P, Storti G, Morbidelli M (2018) Bottle-grade polyethylene furanoate from ring-opening polymerization of cyclic oligomers. Nat Commun 9:2701
213. Kanetaka Y, Yamazaki S, Kimura K (2016) Preparation of poly(ether ketone)s derived from 2,5-furandicarboxylic acid via nucleophilic aromatic substitution polymerization. J Polym Sci Part A Polym Chem 54:3094–3101
214. Kaneko T, Matsusaki M, Hang TT, Akashi M (2004) Thermotropic liquid-crystalline polymer derived from natural cinnamoyl biomonomers. Macromol Rapid Commun 25:673–677
215. Kaneko T, Thi TH, Shi DJ, Akashi M (2006) Environmentally degradable, high-performance thermoplastics from phenolic phytomonomers. Nat Mater 5:966–970
216. Tateyama S, Masuo S, Suvannasara P, Oka Y, Miyazato A, Yasaki K, Teerawatananond T, Muangsin N, Zhou SM, Kawasaki Y, Zhou LB, Zhou ZM, Takaya N, Kaneko T (2016) Ultrastrong, transparent polytruxillamides derived from microbial photodimers. Macromolecules 49:3336–3342
217. Puanglek S, Kimura S, Enomoto-Rogers Y, Kabe T, Yoshida M, Wada M, Iwata T (2016) In vitro synthesis of linear α-1,3-glucan and chemical modification to ester derivatives exhibiting outstanding thermal properties. Sci Rep 6:30479
218. Puanglek S, Kimura S, Iwata T (2017) Thermal and mechanical properties of tailor-made unbranched α-1,3-glucan esters with various carboxylic acid chain length. Carbohydr Polym 169:245–254

Adv Polym Sci (2019) 283: 37–86
https://doi.org/10.1007/12_2019_46

Published online: 18 June 2019

Quiescent Crystallization of Poly(Lactic Acid) and Its Copolymers-Based Materials

Hideto Tsuji

Contents

1 Introduction 38
2 Molecular Structures of Lactic Acid or Lactide-Based Homopolymers and Copolymers 39
3 Parameters Affecting Crystallization 39
4 Bulk Crystallization 43
4.1 Effects of Molecular Weight 43
4.2 Effects of Terminal Group 45
4.3 Effects of Copolymerization 49
4.4 Effects of Branching 63
4.5 Effects of Nucleating or Crystallization-Accelerating Agents 66
4.6 Effects of Incorporated Polymers 73
5 Solution Crystallization 77
6 Thermal Properties 78
7 Conclusions 81
References 81

Abstract Quiescent homo-crystallization and formed higher-ordered structures of poly(lactic acid) and its copolymers-based materials are affected by numerous parameters such as polymer architectures, additives, crystallization methods, and conditions and influence their physical and biochemical properties and biodegradation behavior. The present chapter overviews the effects of various parameters on the quiescent homo-crystallization in bulk from the melt and in solution, formed higher-ordered structures, and thermal properties of poly(lactic acid) and its copolymers-based materials, in terms of crystallization rate and mechanism, crystalline species

H. Tsuji (✉)
Department of Applied Chemistry and Life Science, Graduate School of Engineering, Toyohashi University of Technology, Toyohashi, Aichi, Japan
e-mail: tsuji@chem.tut.ac.jp

(α- and δ-forms) and morphology, and the incorporation of comonomer units in the crystalline regions or the exclusion of comonomer units from the crystalline regions.

Keywords Branching · Copolymerization · Copolymers · Crystallization · Molecular structures · Molecular weight · Nucleating agent · Poly(lactic acid) · Poly (lactide) · Spherulites · Star-shaped · Stereocomplex · Terminal group · Thermal properties

1 Introduction

Poly(lactide) or poly(lactic acid) (PLA) and its copolymers are biodegradable polyesters derived from plant-based renewable raw materials such as corn and sugar cane and now widely used in various applications including commodity, biomedical, pharmaceutical, and environmental applications [1]. Crystallization of PLA and its copolymers-based materials is a matter of concern because it can improve their mechanical properties and thermal stability required for specific applications [1]. Furthermore, crystallization behavior and the formation of higher-ordered structures can affect physical properties and biodegradation behavior of PLA and its copolymers-based materials and their biochemical response from the living body [1]. In the present chapter, the effects of molecular architecture of PLA and additives on the quiescent homo-crystallization in bulk from the melt or in solution, formed higher-ordered structures, and physical properties of PLA and its copolymers-based materials are stated, focusing on crystallization rate [especially radial growth rate of spherulites (G)] and mechanism, crystalline species (α- and δ-forms) and morphology, and the incorporation of comonomer units in the crystalline regions or the exclusion of comonomer units from the crystalline regions. Controlling the crystallization behavior and the formation of higher-ordered structures of PLA and its copolymers-based materials are crucial because their physical and biochemical properties and biodegradation behavior are determined by the crystallization behavior and formed higher-ordered structures.

Previous basic information regarding the crystallization of PLA and its copolymers-based materials is summarized in the author's book chapters for PLA [2, 3]. Also, stereocomplex (SC) crystallization between enantiomeric PLAs, i.e., poly(L-lactide) or poly(L-lactic acid) (PLLA) and poly(D-lactide) or poly(D-lactic acid) (PDLA), is summarized in previous numerous articles [4–11], and therefore, information regarding SC crystallization is included in the section of stereo block copolymerization in the section of stereo copolymerization (Sect. 4.3.1) only as additional information to that of homo-crystallization and in the section of stereocomplexes of unsubstituted and substituted poly(lactic acid)s (Sect. 4.5.1) in the section of nucleating or crystallization-accelerating agents (Sect. 4.5). Moreover, if required, it is suggested that readers refer to some excellent review articles and book chapters dealing with the crystallization of PLA-based materials [7, 12–15].

2 Molecular Structures of Lactic Acid or Lactide-Based Homopolymers and Copolymers

Figure 1 shows the molecular structures of lactic acid (LA) or lactide-based homopolymers and copolymers with 2-hydroxyalkanoic acids and alanine. PLA includes L-form homopolymer, i.e., PLLA; D-form homopolymer, i.e., PDLA; syndiotactic PLA or alternating copolymer of L- and D-lactic acids, i.e., poly(L-lactic acid-*alt*-D-lactic acid); alternating copolymers of L- and D-lactides (or L- and D-lactic acid cyclic dimers), i.e., heterotactic PLA; random copolymers of L- and D-lactic acids or L- and D-lactides, i.e., poly(L-lactic acid-*co*-D-lactic acid) or poly(L-lactide-*co*-D-lactide); and stereo block PLA copolymers, i.e., poly(L-lactic acid)-*b*-poly(D-lactic acid) and poly(L-lactide)-*b*-poly(D-lactide). It should be noted that the expression of the stereo block copolymers can be used to show the molecular structures of random copolymers. The representative L-lactic acid (LLA) or L-lactide-based random copolymers with other 2-hydroxyalkanoic acids which are frequently used in biomedical and pharmaceutical applications are those with a comonomer glycolic acid or glycolide (i.e., cyclic dimer of glycolic acid). Other LLA or L-lactide-based random copolymers dealt in the present manuscript are those with comonomers L- or D-2-hydroxybutanoic acid and L-alanine. Alanine has a chemical structure that is very similar to that of LLA. A wide variety of branched or multiarmed PLA and copolymers were synthesized. Figure 1 shows the molecular structures of two- and four-armed PLLA and two-armed and four-armed stereo diblock copolymers of PLLA and PDLA, which are discussed in the present chapter.

3 Parameters Affecting Crystallization

As in other polymers, crystal modification, crystallization rate, mechanism, and morphology of PLA and its copolymers-based materials depend on the parameters summarized in Table 1, which include polymer architectures, additives, and other parameters such as crystallization temperature and time (T_c and t_c, respectively). Overall crystallization rate or G is mainly determined by T_c and becomes maximum at a certain T_c. In the case of bulk crystallization, in addition to crucial parameters such as T_c and t_c, melting conditions such as the temperature and time for melting and the type and pressure of surrounding gas, which vary the degrees of memory effect and thermal degradation, affect the crystallization behavior and formed higher-ordered structures. If surrounding gas contains oxygen and water, correspondingly oxidation and hydrolytic degradation of PLA and its copolymers occur at elevated temperature during melting or crystallization, resulting in changes in molecular structures and decreased molecular weight and thereby affecting the crystallization behavior and formed higher-ordered structures. Also, the thermal process or program before crystallization such as melt-quenching process (Fig. 2) [16] or the presence of additive causes nucleation, resulting in rapid overall

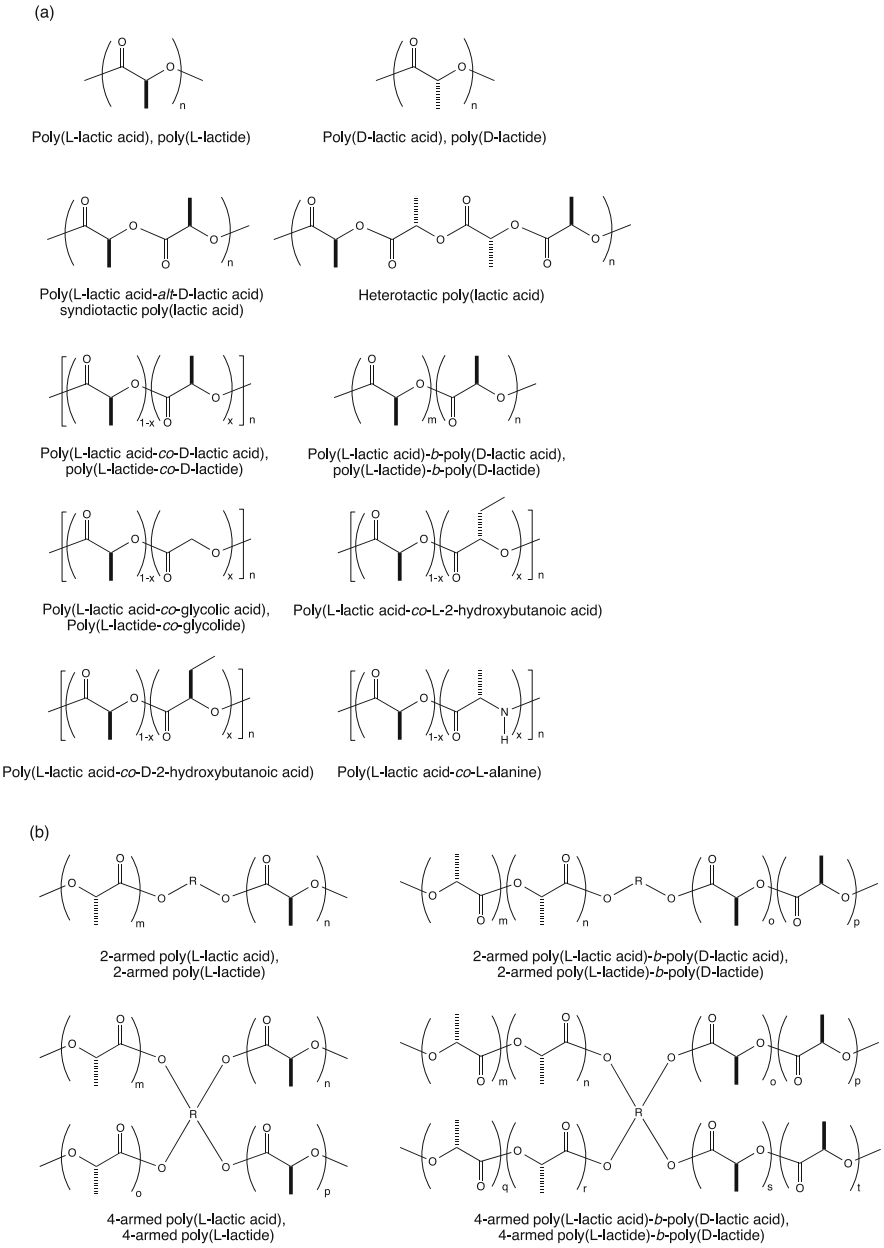

Fig. 1 Molecular structures of lactic acid (LA) or lactide-based homopolymers and copolymers with 2-hydroxyalkanoic acids, and alanine: (**a**) linear one-armed and (**b**) branched multiarmed homopolymers and copolymers

Table 1 Crystallization parameters in bulk and solution crystallization

Condition	Bulk crystallization	Solution crystallization
Quiescent	1. Polymer architecture 2. Type and concentration of additive 3. Temperature and time for melting 4. Crystallization temperature and time (T_c and t_c, respectively) 5. Incorporation of melt-quenching or low temperature ($<T_g$) annealing before isothermal crystallization 6. Type and pressure of surrounding gas 7. Material shape and dimensions 8. Other outer conditions	1. Polymer architecture and concentration 2. Type of solvent 3. Type and concentration of additive 4. Dissolution temperature and time 5. T_c and t_c 6. Other outer conditions
Dynamic	1. Polymer architecture 2. Type and concentration of additive 3. Temperature and time for melting 4. Dynamic factors and parameters such as cooling rate from the melt or heating rate after melt-quenching (temperature programing) 5. Type and pressure of surrounding gas 6. Material shape and dimensions 7. Other outer conditions	1. Polymer architecture and concentration 2. Type of solvent 3. Type and concentration of additive 4. Dissolution temperature and time 5. Dynamic parameters such as cooling rate 6. Other outer conditions

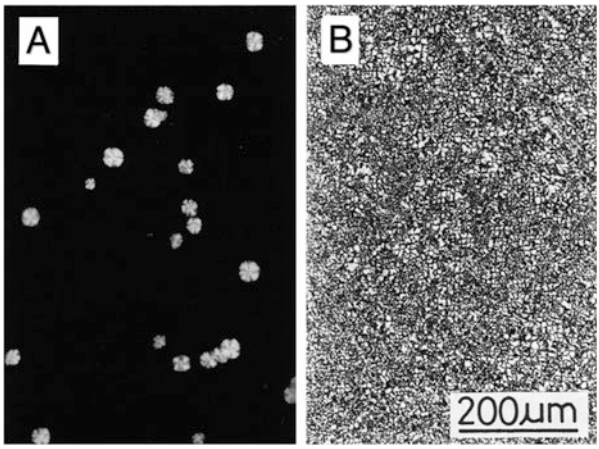

Fig. 2 Polarized optical photomicrographs of PLLA crystallized at crystallization temperature (T_c) = 140°C for crystallization time (t_c) = 10 min from the melt without quenching (**a**) and with quenching (**b**) before crystallization [16] (with permission from Elsevier B.V.)

crystallization in the following isothermal and non-isothermal crystallization. Furthermore, annealing of PLLA below glass transition temperature (T_g) is known to cause enthalpy relaxation toward a metastable state, which then results in accelerated crystallization at a higher temperature after annealing [17–23]. Androsch and Di Lorenzo reported that the time of nuclei formation of PLLA increases exponentially with decreasing temperature, so that aging at 50°C (323 K) requires a minimum time of 10^4 s and the extrapolated time for generation of nuclei at 22°C (295 K) is about

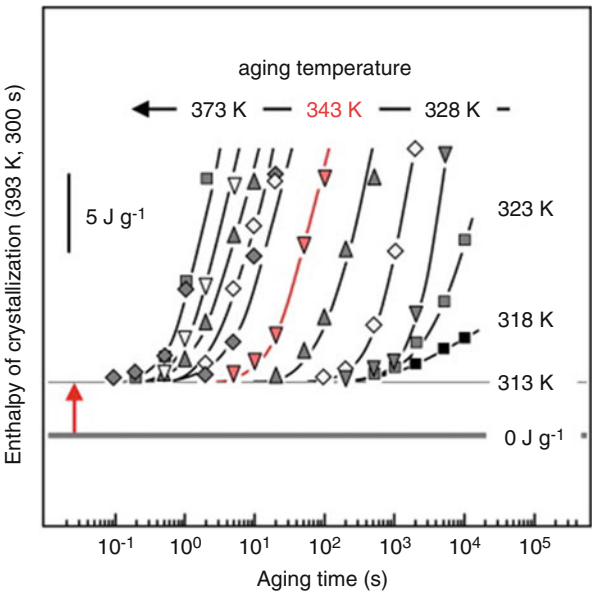

Fig. 3 Enthalpy of crystallization of PLLA at 120°C (393 K) for 300 s as a function of aging time at different temperatures between 40 and 100°C (313 and 373 K) [22] (with permission from Elsevier B.V.)

10^8 s [21]. Figure 3 shows the effects of aging temperature and time on crystallization enthalpy at 120°C (393 K) for 300 s [22].

The crystal polymorphism and morphology of PLA formed under different conditions are summarized in an excellent book chapter written by Lotz [15]. In the case of solution crystallization, polymer concentration, solvent type, and dissolution temperature and time affect the crystallization behavior and formed higher-ordered structures, in addition to polymer architecture, additives, T_c, and t_c. In the case of dynamic crystallization, in addition to the parameters stated for quiescent crystallization, other dynamic parameters as summarized in Table 1 affect the crystallization behavior and formed higher-ordered structures.

It should be noted that although the given conditions for melt or solution crystallization may be quiescent, actual conditions are not. For example, upon crystallization, polymers or segments with higher crystallizability crystallize first (i.e., a sort of fractionation crystallization), leaving polymers or segments with lower crystallizability. Such fractionation crystallization readily occurs in solution rather than in bulk due to the higher chain or segmental mobility in the presence of solvent molecules and may affect the crystallization behavior at the late stage and formed higher-ordered structures. Therefore, the term "quiescent" in the present chapter means that the applied conditions (not actual conditions) for crystallization are static.

4 Bulk Crystallization

4.1 Effects of Molecular Weight

Linear one-armed PLLA homopolymers are synthesized by polycondensation of lactic acid (LA) or ring-opening polymerization of cyclic dimer of LA (i.e., lactide). When linear one-armed PLLA homopolymers are synthesized by the latter method, a coinitiator moiety is attached to the terminal of PLLA molecules. If the coinitiator molecule is sufficiently large or has strong interaction, it affects the crystallization behavior and formed higher-ordered structures (see Sect. 4.2).

Of the architectural parameters affecting crystallization, the effects of the molecular weight of linear one-armed PLLA homopolymers have been frequently investigated [1, 24–27]. Figure 4 shows the polarized optical photomicrographs of linear one-armed low and high molecular weight linear one-armed PLLA homopolymers crystallized from the melt [24]. In sample codes, L means linear one-armed PLLA homopolymer and figures immediately following the polymer code L are number-average molecular weights monitored by gel permeation chromatography (GPC) $[M_n(\mathrm{GPC})]/10^3$. This type of polymer code is used in the following section. As seen in both samples, the spherulites had a Maltese cross, indicating that the lamellae of PLLA homopolymers were aligned in a radial direction. The lower numbers of spherulites per unit area of the low molecular weight PLLA (L31) compared to the high molecular weight PLLA (L104) are attributable to the lower degrees of supercooling ($\Delta T = T_m{}^0 - T_c$, when $T_m{}^0$ is equilibrium melting temperature) of

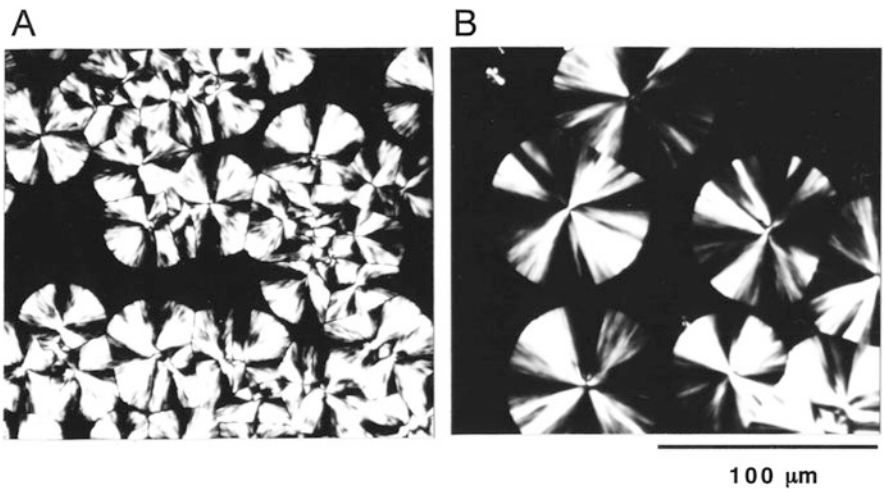

Fig. 4 Polarized optical photomicrographs of poly(L-lactide) (PLLA) homopolymers and copolymers crystallized at crystallization temperature (T_c) = 120°C from the melt: (**a**) L104, crystallization time (t_c) = 5 min; (**b**) L31, t_c = 3 min [24] (with permission from Elsevier B.V.). In sample codes, L means linear one-armed PLLA and figures after L are number-average molecular weights monitored by gel permeation chromatography $[M_n(\mathrm{GPC})]/10^3$

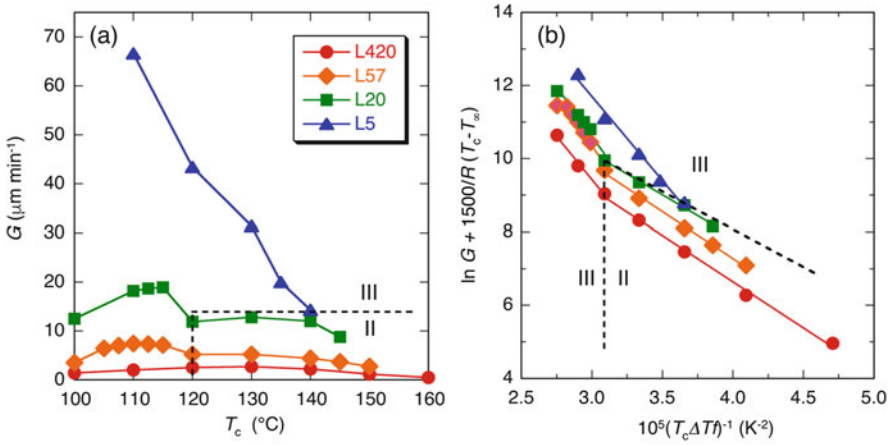

Fig. 5 Radial growth rate of spherulites (G) (**a**) and ln G + 1,500/$R(T_c - T_\infty)$ (**b**) of PLLAs with different molecular weights as functions of crystallization temperature (T_c) and $1/(T_c\Delta Tf)$, respectively [25] (with permission from American Chemical Society)

the former, due to a lower melting temperature (T_m) of low molecular weight L31 compared to that of high molecular weight L104. Figure 5a shows the G of linear one-armed PLLA homopolymers with different molecular weights [24]. The first detailed study on the effect of molecular weight on G was performed by Vasanthakumari and Pennings using the relatively high molecular weight linear one-armed PLLA homopolymers [viscosity-average molecular weight (M_v) = 1.5–6.9 g mol^{-1}] [26]. As seen in Fig. 5a, G values decrease monotonically with an increase in M_n(GPC), in agreement with the result reported by Vasanthakumari and Pennings [26] and Miyata and Masuko [27].

The nucleation constant (K_g) and the front constant (G_0) of the samples were estimated using the nucleation theory established by Hoffman et al. (Hoffman-Lauritzen analysis) [28, 29], in which G can be expressed by the following equation:

$$G = G_0 \exp\left[-U^*/R(T_c - T_\infty)\right] \exp\left[-K_g/(T_c\Delta Tf)\right], \quad (1)$$

where f is the factor expressed by $2T_c/(T_m^0 + T_c)$ which accounts for the change in the heat of fusion as the temperature is decreased below T_m^0, U^* is the activation energy for the transportation of segments to the crystallization site, R is the gas constant, and T_∞ is the hypothetical temperature where all motion associated with viscous flow ceases [28, 29]. The ln G + 1,500/$R(T_c$–$T_\infty)$ of linear one-armed PLLA homopolymers are plotted in Fig. 5b as a function of $1/(T_c\Delta Tf)$, using $T_m^0 = 212$°C of homo-crystallites for linear one-armed PLLA homopolymers [16], $U^* = 1{,}500$ cal mol^{-1}, and $T_\infty = T_g - 30$ K. Excluding lowest molecular weight PLLA (L5), all PLLA homopolymers had the two regimes (regimes III and II) with transition T_c [T_c(III–II)] = 120°C [24, 25]. Similarly, T_c(III–II) was observed at 120 and 128°C for PLLA with $M_w = 1.01 \times 10^5$ g mol^{-1} by Di Lorenzo [30, 31],

whereas Vasanthakumari and Pennings first observed the transition from regime II to regime I at T_c [T_c(II–I)] = 163°C for PLLA with the lowest $M_v = 1.5 \times 10^5$ g mol^{-1} [26]. On the other hand, Abe et al. observed three regimes III, II, and I with T_c(III–II) and T_c(II–I) at 120 and 147°C, respectively, for linear one-armed PLLA thin films with a thickness of 100 nm when the growth rate was monitored along the *b* axis direction [32]. The transition of crystal growth kinetics at T_c around 120°C can be ascribed to well-known crystal growth mechanism change or crystal form transition from δ-form to α-form at T_c = 120°C [33–36]. However, there is a probability that both crystal growth mechanism change and crystal form transition occur at the same or similar T_c. Pan et al. reported that the δ- and α-form crystals are formed at low and high T_c values, respectively, regardless of the molecular weight of linear one-armed PLLA [33]. Androsch et al. found that in the investigated weight-average molecular weight (M_w) range of 6.0×10^4–5.8×10^5 g mol^{-1}, the kinetics of PLLA crystal nucleation is independent on the chain length below T_g, whereas at 100°C, which is far higher than T_g and the temperature of maximum nucleation rate, time required for the formation of stable crystal nuclei decreased distinctly and systematically with decreasing M_w [37].

4.2 *Effects of Terminal Group*

The crystallization rate and mechanism vary depending on terminal group. Linear one-armed PLLA homopolymers having a terminal *n*-alkyl group with a wide variety of lengths (C0–C22) were synthesized by ring-opening polymerization of L-lactide in the presence of coinitiators of L-lactic acid (LLA) (C0), 1-hexanol (C6), 1-dodecanol (C12), and 1-docosanol (C22) (Fig. 6) and their isothermal crystallization behavior was investigated [38–40]. Here, the codes C0, C6, C12, and C22 stand

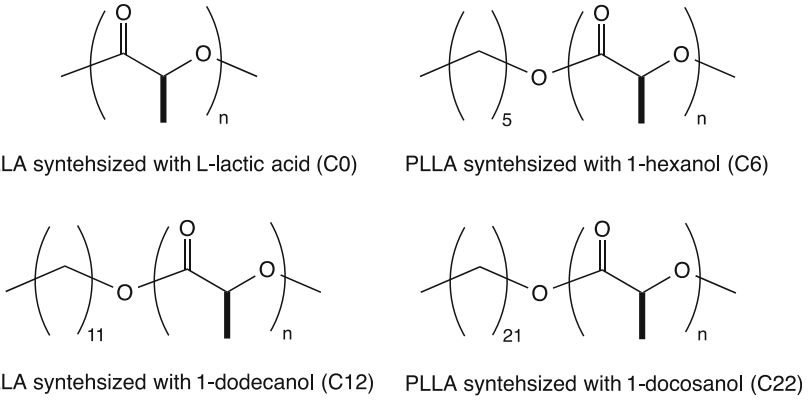

Fig. 6 Molecular structures of PLLAs synthesized with L-lactic acid (C0), 1-hexanol (C6), dodecanol (C12), and 1-docosanol (C22)

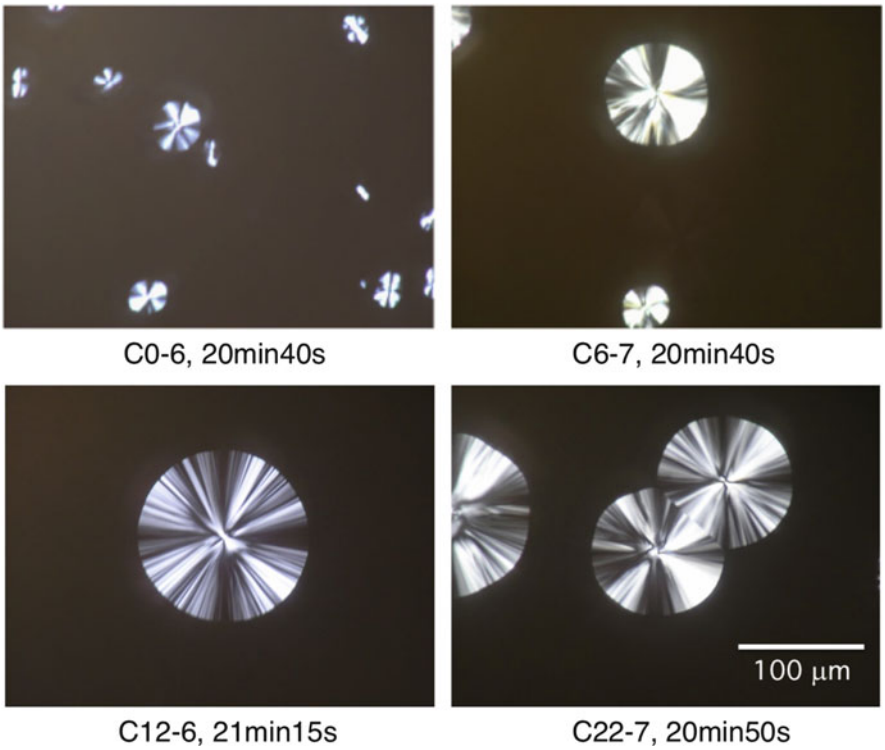

Fig. 7 Polarized optical photomicrographs of spherulites of relatively low molecular weight PLLAs (C0-6, C6-7, C12-6, and C22-7) crystallized at crystallization temperature (T_c) = 110°C for shown crystallization times [40] (with permission from Elsevier B.V.)

for the linear one-armed PLLA homopolymers synthesized using LLA, 1-hexanol, 1-dodecanol, and 1-docosanol, respectively, and the numbers immediately following the polymer codes are the number-average molecular weights [M_n(GPC)]/10^3 g mol^{-1} [40]. Figure 7 shows the polarized photomicrographs of spherulites of the linear one-armed PLLA homopolymers with relatively low molecular weights (C0-6, C6-7, C12-6, and C22-7) melt-crystallized at T_c = 110°C for shown crystallization times [40]. Since the effect of the length of terminal *n*-alkyl groups on spherulitic morphology is expected to be higher for relatively low molecular weight PLLA homopolymers than for relatively high molecular weight PLLA homopolymers, the polarized photomicrographs of only the former are shown. Normal spherulites with Maltese crosses were observed for all types of PLLA homopolymers, indicating that the length of terminal *n*-alkyl group does not affect the spherulitic morphology [40].

Figure 8 shows the G of the relatively low molecular weight linear one-armed PLLA homopolymers (C0-6, C6-7, C12-6, and C22-7) and of the relatively high molecular weight linear one-armed PLLA homopolymers (C0-23, C6-22, C12-20, and C22-20) as a function of T_c [40]. The G values of relatively low molecular

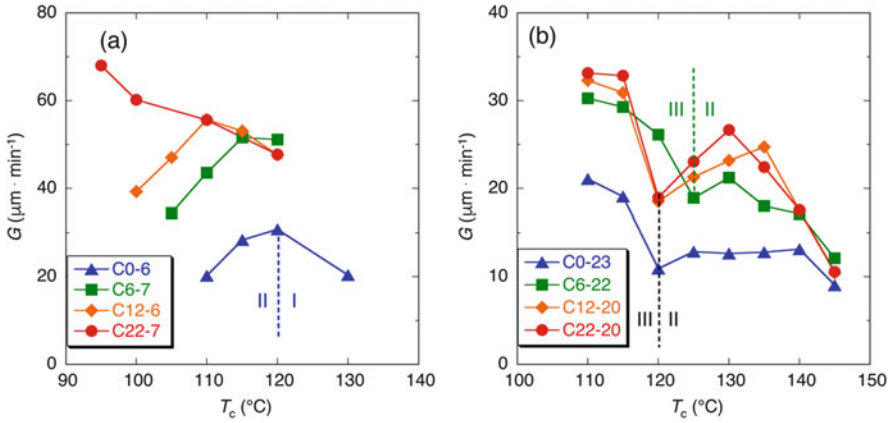

Fig. 8 Radial growth rate of spherulites (G) of relatively low molecular weight PLLAs (C0-6, C6-7, C12-6, and C22-7) (**a**) and of relatively high molecular weight PLLAs (C0-23, C6-22, C12-20, and C22-20) (**b**) as a function of crystallization temperature (T_c) [40] (with permission from Elsevier B.V.)

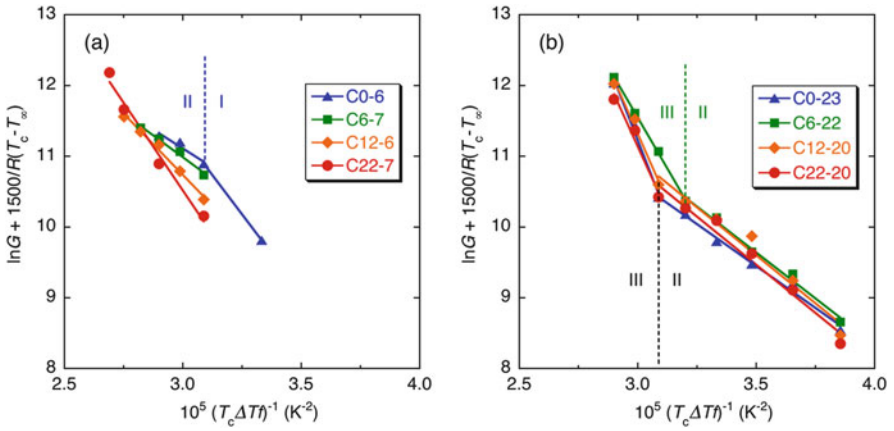

Fig. 9 ln G − 1,500/R(T_c − T_∞) of relatively low molecular weight PLLAs (C0-6, C6-7, C12-6, and C22-7) (**a**) and of relatively high molecular weight PLLAs (C0-23, C6-22, C12-20, and C22-20) (**b**) as a function of $1/(T_c\Delta Tf)$ [40] (with permission from Elsevier B.V.). The notations of regimes and broken lines were added to the original figures

weight PLLA homopolymers increased with increasing the length of terminal n-alkyl group, whereas the G values of PLLA homopolymers having the terminal n-alkyl groups were higher than those of C0-23 with no terminal n-alkyl group [40]. Figure 9 shows ln G + 1,500/R(T_c–T_∞) of the linear one-armed PLLA homopolymers with the terminal n-alkyl group having different carbon numbers as a function of $1/(T_c\Delta Tf)$ [40]. The relatively low molecular weight C0-6 had two regimes (regimes II and I), whereas all the relatively high molecular weight PLLAs

had two regimes (regimes III and II) [40]. The T_c(II–I) for the relatively low molecular weight PLLA homopolymer and the T_c(III–II) for the relatively high molecular weight PLLA homopolymers were 120°C and 120 or 125°C, respectively. The latter indicates that the length of terminal *n*-alkyl group did not largely affect the T_c(III–II) of relatively high molecular weight PLLA homopolymers. As stated above, these transitions are attributable to the crystalline form transition from δ- to α-form. Although the following sections do not include the same statement, T_c(III–II) or T_c(II–I) (i.e., regime transition from III to II or regime transition from II to I) may be caused by the growth of two different crystal polymorphs at different T_c values (i.e., δ- and α-forms).

Figure 10 shows the wide-angle X-ray diffraction (WAXD) profiles of the relatively low molecular weight linear one-armed PLLA homopolymers (C0-6,

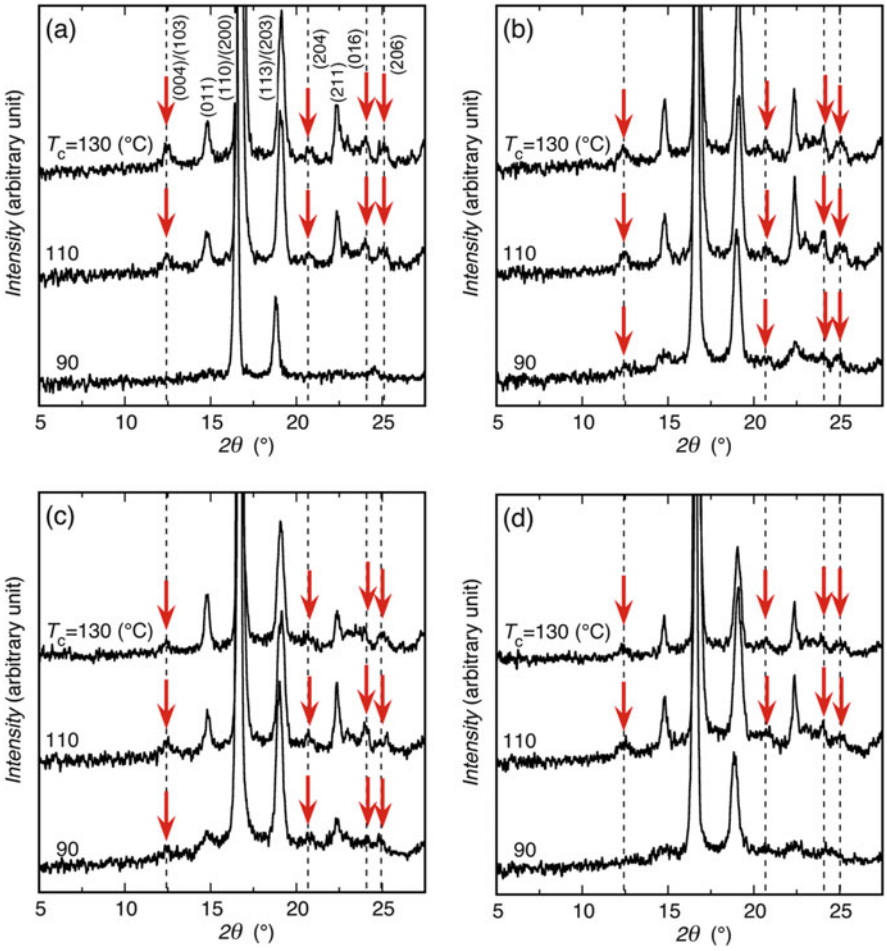

Fig. 10 WAXD profiles of relatively low molecular weight PLLAs [C0-6 (**a**), C6-7 (**b**), C12-6 (**c**), and C22-7 (**d**)] crystallized at different T_c values. Red arrows indicate crystalline diffractions observed only for α-form [40] (with permission from Elsevier B.V.)

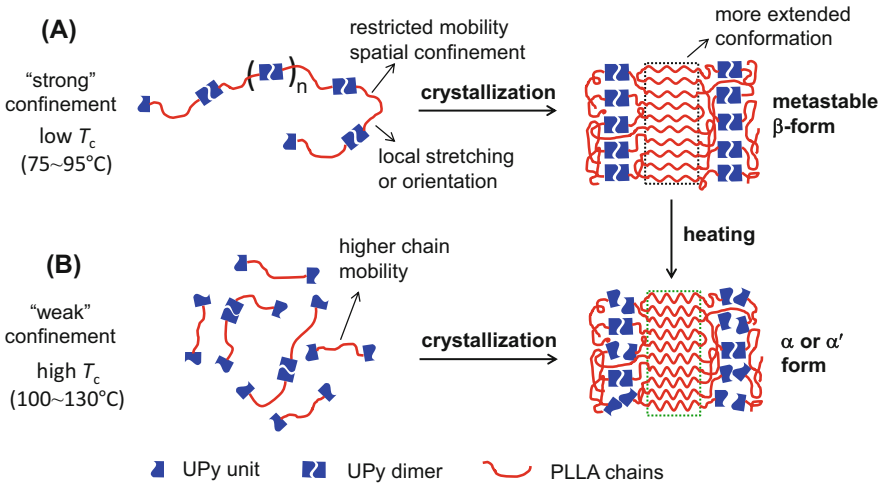

Fig. 11 Schematic presentation of formation of β- and α-forms of two-armed PLLA terminated with UPy at low and high T_c [strong (a) and weak (b) confinement], respectively [42] (Courtesy of Prof. Pengju Pan) (with permission from American Chemical Society)

C6-7, C12-6, and C22-7) crystallized at different T_c values. Red arrows indicate crystalline diffractions observed only for α-form [40]. The transition T_c from δ-form to α-form [$T_c(\delta\text{-}\alpha)$] can be estimated by the use of these inherent peaks. For C0-6 and C22-7, T_c(δ-α) was in the range of 90–110°C, whereas for C6-7 and C12-6, T_c(δ-α) was below 90°C. In contrast, the T_c(δ-α) for all relatively high molecular weight PLLA homopolymers were the identical T_c(δ-α) of 110–130°C [40]. The results are indicative of the fact that for the relatively low molecular weight PLLA homopolymers, the presence of terminal *n*-alkyl group with carbon numbers of 6 and 12 decreases T_c(δ-α), whereas for the relatively high molecular weight PLLA homopolymers, the effect of terminal groups on T_c(δ-α) was insignificant.

On the other hand, 2-ureido-4[1*H*]-pyrimidinone (UPy)-terminated PLAs, which can be connected with each other via multiple hydrogen bonds of UPy terminals, were synthesized [41–43]. Bao et al. found that UPy terminals of two-armed PLLA induce the formation of β-form crystal at low T_c below 100°C due to strong confinements of UPy terminals and UPy-UPy interactions, which exert stretching and orientation effects during crystallization (Fig. 11) [42].

4.3 Effects of Copolymerization

Copolymerization includes random, alternating, heterotactic, block, and graft copolymerization and can be subdivided into stereo and other types. Although numerous papers have been published regarding the copolymerization of LA or lactide with other monomers [1], discussion is limited to the linear one-armed LA or lactide-

based copolymers and the effects of stereo copolymerization and copolymerization with other 2-hydroxyalkanoic acids (α-hydroxyalkanoic acids) or 2-amino acids (α-amino acids). The representative chemical structures of the copolymers are summarized in Fig. 1.

4.3.1 Stereo Copolymerization

Stereo Random Copolymerization

The distribution and randomness of monomer units depend on the combination of monomers and polymerization conditions. As stated above, PLA can be synthesized from LA and its cyclic dimer lactide. Equimolar stereo random copolymers synthesized from LLA and D-lactic acid (DLA) or L- and D-lactides are random based on monomer unit and dimer units, respectively. The randomness of monomer units is intermediate between these two types of stereo copolymers, when the meso-type lactide, which is composed of an LLA and a DLA, is used for copolymerization. Figure 12 shows the polarized photomicrographs of L-lactide-rich poly(L-lactide-*co*-D-lactide) copolymers with different percentage LLA unit contents (X_L) crystallized at different T_c values for 1,000 min from the melt [44]. As seen, the L-lactide-rich poly(L-lactide-*co*-D-lactide) sample with the highest X_L value (99%) shows well-defined Maltese crosses, reflecting the lamella orientation, whereas the L-lactide-rich poly(L-lactide-*co*-D-lactide) sample with lower X_L values (95 and 92%) had rather disordered Maltese crosses. Too small a size or high density of spherulites disturbed the morphology observation at $T_c = 100°C$, whereas in addition to Maltese cross morphology, periodical extinction was observed at $X_L = 92\%$ and $T_c = 120°C$, indicating that the periodical rotation of lamellae was facilitated by the incorporated D-lactide units.

Figure 13 shows the G and $\ln G + 1{,}500/R(T_c - T_\infty)$ of L-lactide-rich poly(L-lactide-*co*-D-lactide) copolymers with different X_L values [24]. In this figure, "LD" means poly(L-lactide-*co*-D-lactide), and the numbers immediately following the polymer code "LD" are the number-average molecular weights $[M_n(\mathrm{GPC})]/10^3$ g mol^{-1}. As expected, G values decreased with decreasing X_L or optical purity, which is consistent with the results reported by Huang et al. for poly(L-lactide-*co*-meso-lactide) [45], Baratian et al. for poly(L-lactide-*co*-D-lactide) and poly(L-lactide-*co*-meso-lactide) [46], and Di Lorenzo et al. for poly(L-lactide-*co*-D-lactide) [47]. Baratian et al. reported that the crystallinity, lamellar thickness, and G values are higher for poly(L-lactide-*co*-D-lactide) than for poly(L-lactide-*co*-meso-lactide) when compared at similar X_L and ΔT [46]. This finding strongly suggests that the disturbance effect of DLA units on the crystallization of LLA units was weaker for D-lactide units which cause concentrated incorporation of DLA *dimer* units in the polymer chains than for meso-lactide units which induce separate incorporation of DLA *monomer* units in the polymer chains. Kolstad found the incorporation of meso-lactide in the copolymers increases the crystallization half time of poly(L-lactide-*co*-meso-lactide) [48]. Similar to the result of G values, Androsch et al. reported that overall crystallization rate of poly(L-lactide-*co*-D-lactide) decreases

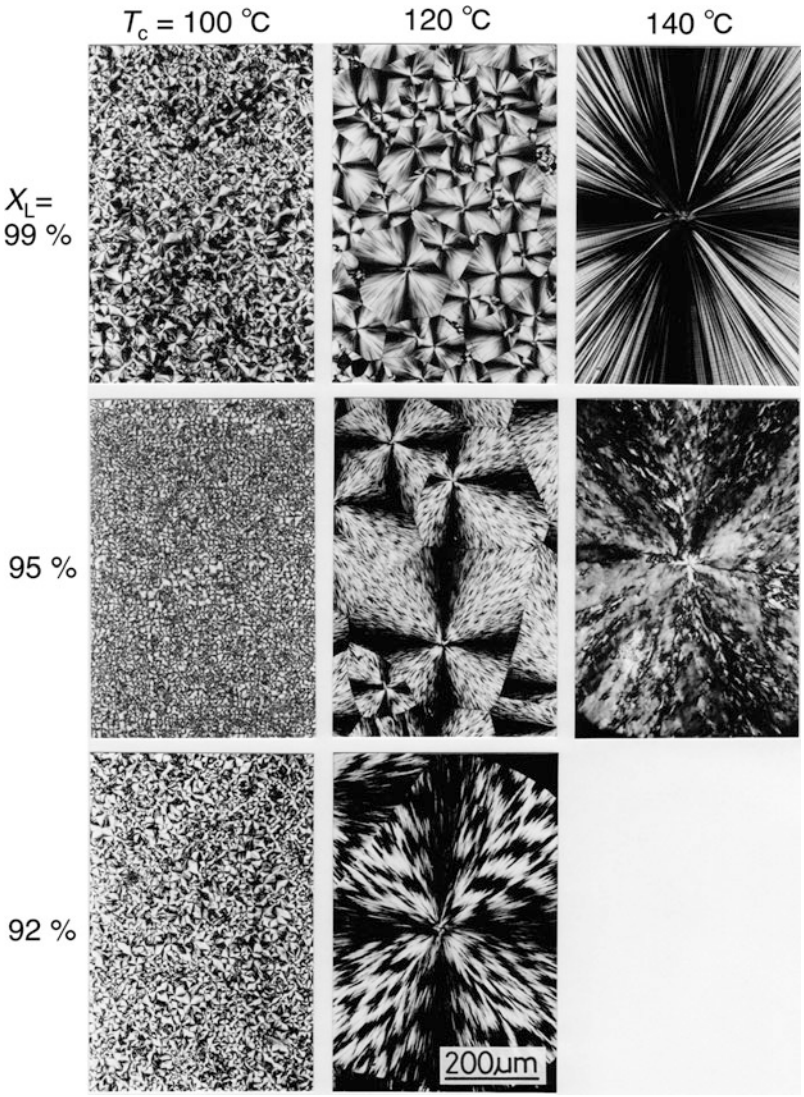

Fig. 12 Polarized optical photomicrographs of L-lactide-rich poly(L-lactide-*co*-D-lactide) copolymers with different percentage LLA unit content (X_L) crystallized at different crystallization temperature (T_c) values for 1,000 min [44] (with permission from Wiley-VCH Verlag GmbH & Co.)

with decreasing X_L (Fig. 14) [49]. The data of gray-filled triangles were obtained for a one-armed PLLA homopolymer with similar molecular weight in a previous study [50].

The Hoffman-Lauritzen analysis indicates that L-lactide-rich poly(L-lactide-*co*-D-lactide) copolymers with high X_L values (100 and 97%) had two regimes (regimes III

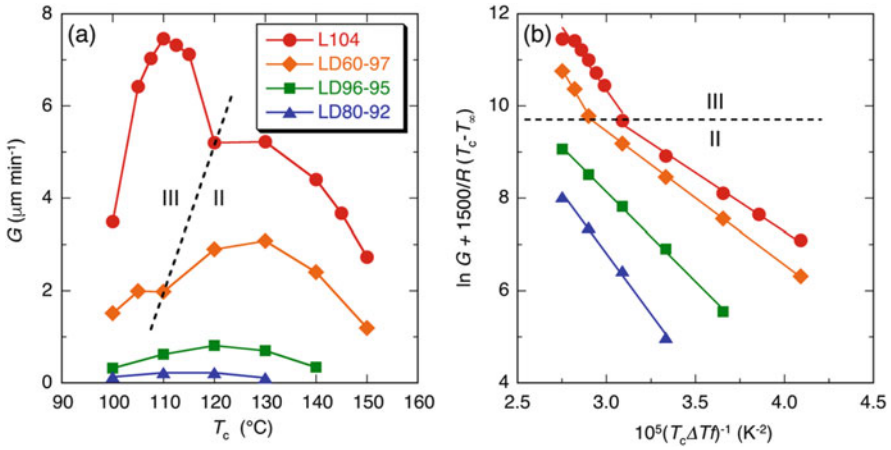

Fig. 13 Radial growth rate of spherulites (G) (**a**) and ln G + 1,500/R($T_c - T_\infty$) (**b**) of L-lactide-rich poly(L-lactide-*co*-D-lactide) copolymers with different percentage LLA unit contents as functions of crystallization temperature (T_c) and 1/($T_c\Delta Tf$), respectively [24] (with permission from Elsevier B.V.)

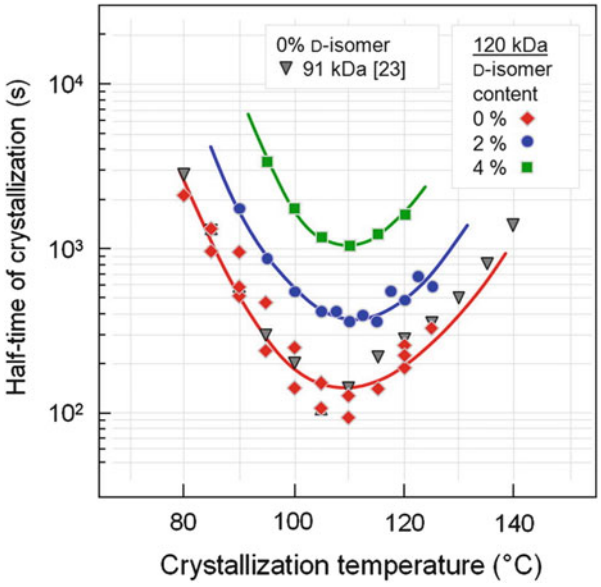

Fig. 14 Half-time of melt-crystallization of PLLA ($M_w = 1.20 \times 10^5$ g mol^{-1}) containing 0% (red diamonds), 2% (blue circles), and 4% D-isomer co-units (green squares) as a function of the crystallization temperature [49] (with permission from Elsevier B.V.). The data of gray-filled triangles were obtained for an one-armed PLLA homopolymer (0% D-isomer content) with the similar molecular weight of 91 kDa in a former study [50]

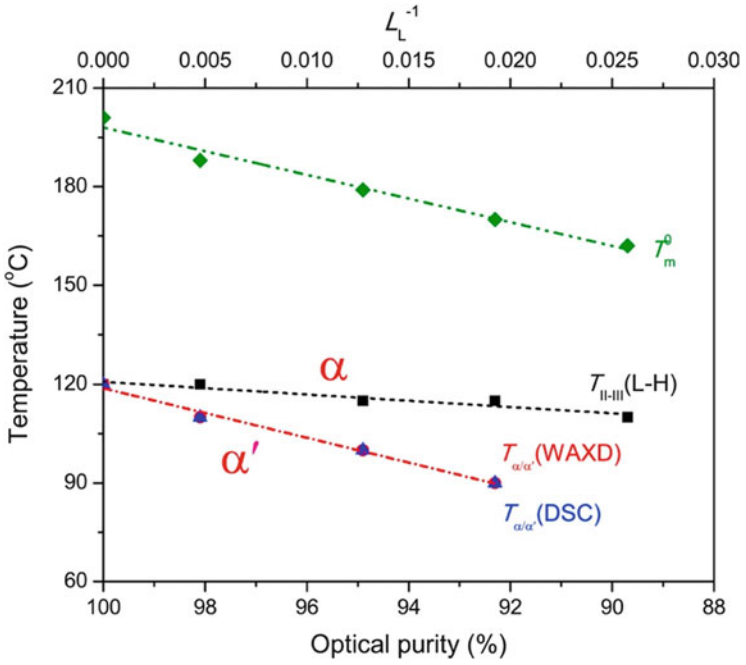

Fig. 15 Relationships between optical purity/sequence length and temperature-dependent crystal polymorphism of PLAs [52] (with permission from Elsevier B.V.)

and II), whereas L-lactide-rich poly(L-lactide-*co*-D-lactide) copolymers with high X_L values (95 and 92%) had only one regime (regime II) due to a narrow crystallizable T_c range limited by their lower T_m values (153 and 107°C) compared to the former (177 and 167°C). Di Lorenzo reported that PLLA and L-lactide-rich poly(L-lactide-*co*-D-lactide) copolymers with 2 and 4% D-lactide units crystallized in δ-form (α′-form) when crystallized at 90°C from the melt [51]. Also, Song et al. found that the T_c(δ-α) of L-lactide-rich poly(L-lactide-*co*-D-lactide) copolymers decreased slowly with decreasing LLA unit content or optical purity and T_c(III–II) increased more slowly with decreasing LLA unit content or optical purity (Fig. 15) [52]. Baratian et al. reported that D-lactic acid (DLA) units of L-lactide-rich poly(L-lactide-*co*-D-lactide) copolymers are incorporated in the crystalline regions of LLA units under certain crystallization conditions [46], in agreement with the result reported by Zell et al. that LLA units of D-lactide-rich poly(L-lactide-*co*-D-lactide) copolymers were incorporated in the crystalline regions of DLA units [53]. Interestingly in the case of L-lactide-rich poly(L-lactide-*co*-meso-lactide) copolymers, DLA units are excluded from the crystalline regions of LLA units [45]. Also, Androsch and Schick reported for L-lactide-rich PLA that the relaxation of the glass toward the structure/enthalpy of the supercooled liquid state is independent of the presence of D-lactide units in the chain and that the slower formation of homogeneous crystal nuclei in L-lactide-rich PLA compared to the PLLA homopolymer is not caused by different chain segment

mobility in the glassy state but by the segregation of chain defects in this early stage of the crystallization process [54].

Stereo Alternating Copolymerization

Alternating copolymerization of LLA and DLA yields poly(L-lactic acid-*alt*- D-lactic acid) or syndiotactic PLA (s-PLA), whereas alternating copolymerization of L-lactide and D-lactide gives heterotactic PLA [55–57]. The molecular structures of s-PLA and heterotactic PLA are shown in Fig. 1. Although no detailed crystallization behavior was reported for s-PLA, we recently reported the synthetic method of s-PLA based on the procedure reported by Stayshich and Meyer [58, 59] and the detailed crystallization behavior and physical properties of neat s-PLA and its blend with one of isotactic PLA (i-PLA) homopolymers, PLLA, as well as those of neat PLLA [60]. In this article, i-PLA (PLLA) was synthesized by the same procedure as that of s-PLA. Figure 16 shows the WAXD profiles of the neat i-PLA, s-PLA, and their blends [60]. For preparation of isothermally crystallized samples, each sample was melted at 170°C for 3 min, crystallized at a T_c for 3 h. The neat s-PLA samples had the highest, second highest, and third highest crystalline peaks at around 14.4°, 22.5°, and 19.9°, whose diffraction patterns are completely different from those of the neat i-PLA samples, indicating that the crystal modification of s-PLA is different from those of i-PLA [60]. Also, the WAXD profiles revealed that in marked contrast with isotactic and syndiotactic poly(methyl methacrylate) blends, in the i-PLA/s-PLA blends, i-PLA and s-PLA crystallized separately or only i-PLA crystallized, without SC formation or their cocrystallization [60].

The G and the induction period for spherulite growth (t_i) of the neat i-PLA and s-PLA samples are plotted in Fig. 17 as a function of T_c [60]. The G values of the neat i-PLA sample showed a typical bell-shaped curve with a maximum G value of 18 μm min^{-1} at $T_c = 120$°C [60]. The t_i values of the neat i-PLA sample increased

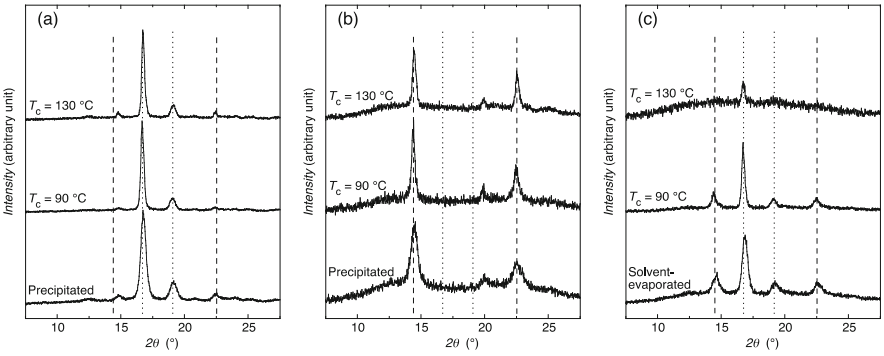

Fig. 16 WAXD profiles of neat i-PLA (**a**), s-PLA (**b**), and their blends (**c**). Dashed and broken lines are main crystalline diffraction angles of neat i-PLA and s-PLA, respectively [60] (with permission from The Royal Society of Chemistry)

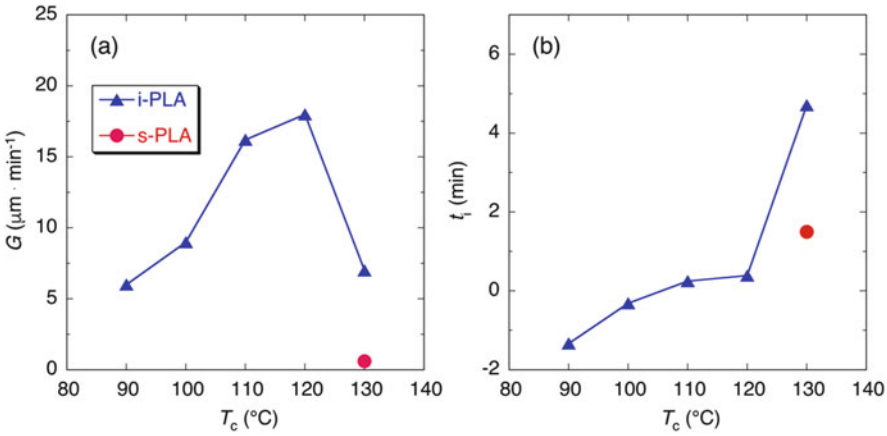

Fig. 17 Radial growth rate of spherulites (G) (**a**) and induction period for spherulite growth (t_i) (**b**) neat i- and s-PLAs as a function of T_c [60] (with permission from The Royal Society of Chemistry)

monotonically with increasing T_c or approaching T_m from −1.3 min at $T_c = 90°C$ to 4.7 min at $T_c = 130°C$ [60]. The negative t_i values of the neat i-PLA sample at T_c below 100°C indicates that the spherulite growth started during cooling before reaching these T_c values [60]. The G and t_i values of the neat s-PLA sample could be measured only for $T_c = 130°C$ (0.6 μm min^{-1} and 1.5 min), which were lower than those of the neat i-PLA sample at the same T_c (7.0 μm min^{-1} and 4.7 min) [60]. Such low G and short t_i values of the neat s-PLA sample are attributed to fully extended chains with planar zigzag conformation and low chain flexibility even in the amorphous state [60], which should have disturbed the spherulite growth but accelerated the formation of nuclei. In the case of the i-PLA/s-PLA blend sample, no spherulite or crystalline assemblies were traced even when the observation was continued for 1 h, although WAXD could monitor its crystallization after 3 h (Fig. 16) [60].

Stereo Block Copolymerization

In the case of linear one-armed stereo diblock poly(L-lactic acid)-*b*-poly(D-lactic acid) copolymers (1-LD polymers), crystalline species changes depending on the total molecular weight and mol fraction of LLA units. Figure 18b shows the crystalline species reported for 1-LDs with LLA unit contents of 50–100% crystallized at different T_c values from the melt, together with those of branched four-armed stereo diblock poly(L-lactic acid)-*b*-poly(D-lactic acid) copolymers (4-LDs) and low molecular weight linear one-armed PLLA/linear one-armed PDLA (1-L/1-D) blends [61–63]. In the case of 1-L/1-D blends (Fig. 18c), crystalline species changed from only homo-crystallites to SC and homo-crystallites, and then to only SC crystallites, with altering LLA unit content from 100 to 50% [62]. In contrast, in the case of 1-LD

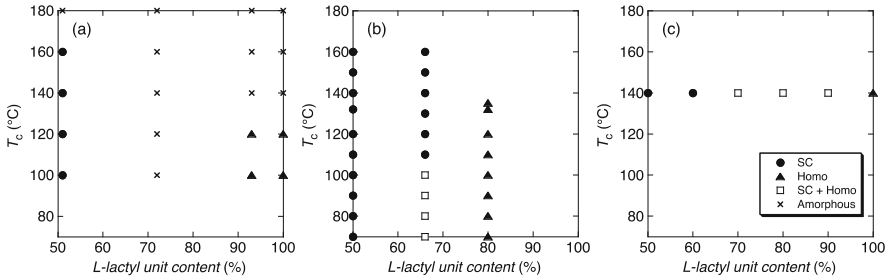

Fig. 18 Crystalline species in 4-LD polymers (**a**), 1-armed PLLA-*b*-PDLA (1-LD) polymers (**b**), and low molecular weight 1-armed PLLA/1-armed PDLA (1-L/1-D) blends (**c**) having different LLA unit contents crystallized at different T_c values from the melt [61] (with permission from American Chemical Society)

copolymers (Fig. 18b), for the relatively low T_c range below 100°C, crystalline species changed from only homo-crystallites to SC and homo-crystallites, and then to only SC crystallites, with altering LLA unit content from 100 to 50%, whereas for the relatively high T_c range above 110°C, crystalline species changed directly from only homo-crystallites to only SC crystallites without formation of both SC and homo-crystallites at medium LLA unit contents [63]. In the case of 4-LD copolymers (Fig. 18a), crystalline species changed from only homo-crystallites to amorphous, and then to only SC crystallites, with altering LLA unit content from 100 to 50%, reflecting that both crystalline species were not formed in 4-LD copolymers at intermediate LLA unit contents [61]. Han et al. investigated crystallization behavior of one-, three-, and six-armed stereo diblock PLAs and found that crystallization temperature during cooling, T_m, crystallinity, G, crystalline size, and long period decreased with increasing arm number or decreasing PLLA and PDLA block lengths [64].

The long period (L) and crystalline and amorphous layer thicknesses (l_c and l_a, respectively) of 1-LD(50/50) increased monotonically with an increase in T_c (Fig. 19a) [63]. As the lamellar models are shown in Fig. 19b, the number of lamellar folding decreased with increasing T_c. The models were constructed considering the length of the extended chain (31 nm). There is no detailed report on *isothermal* crystallization of 1-LD copolymers with unbalanced PLLA and PDLA block lengths and a wide range of molecular weight, although *non-isothermal* crystallization of 1-LD copolymers with unbalanced PLLA and PDLA block lengths and a wide range of molecular weight from the melt is reported [65, 66], wherein the temperature for melting samples largely affects the crystallization behavior.

4.3.2 Random Copolymerization with 2-Hydroxyalkanoic Acid

Most studied random copolymers of LA with 2-hydroxyalkanoic acid is poly(lactic acid-*co*-glycolic acid) [P(LA-*co*-GA)], which has been used for the biomedical applications of biodegradable suture, scaffold, and matrices of drug release [67–70].

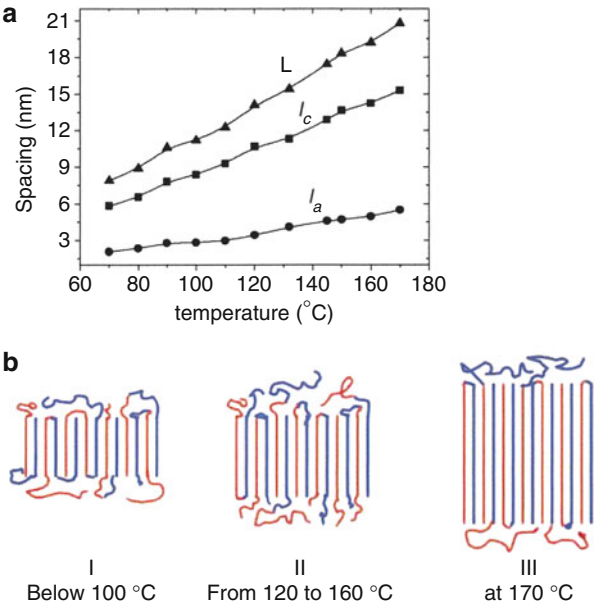

Fig. 19 Morphological parameters of 1-LD(50/50) isothermally crystallized at different crystallization temperatures (**a**). Schematic picture of the lamellar crystals (**b**) [63] (with permission from American Chemical Society)

LA is a chiral 2-hydroxypropanoic acid, while glycolic acid is an achiral 2-hydroxyethanoic acid or 2-hydroxyacetic acid. P(LA-*co*-GA) copolymers can be synthesized by copolymerization of LA and glycolic acid or of lactide and glycolide. For P(LA-*co*-GA) with LLA units, i.e., poly(L-lactic acid-*co*-glycolic acid) or poly(L-lactide-*co*-glycolide) [P(LLA-*co*-GA)] (Fig. 1) crystallizes in the monomer content ratio ranges of 100/0–80/20 and 20/80–0/100 [71–74]. Figure 20 shows the WAXD profiles of precipitate and melt-crystallized P(LLA-*co*-GA) copolymers with different LLA unit contents [74]. Black dashed and dotted lines are the main diffraction angle values of neat PLLA and poly(glycolide) or poly(glycolic acid) (PGA), respectively. In this figure, P(LLA-*co*-GA) copolymers are abbreviated as LLA*X*, where *X* indicates the mol% of LLA units in the copolymer [74]. The shifts of diffraction peak angles and the change in the peak shape with altering LLA unit content around 0 and 100 mol% reflect the incorporation of minor monomer units in the crystalline regions of major monomer units. With the incorporation of minor monomer units, interplanar distance (*d*) and crystallographic parameters (*a* and *b*) of P(LLA-*co*-GA) copolymers changed depending on the content of minor monomer units, as shown in Fig. 21 [74].

The random copolymers of *optically active* L-lactic acid (LLA) and D-2-hydroxybutanoic acid (D-2HB) [P(LLA-*co*-D-2HB)s] with the *opposite configurations* and 2-hydroxybutanoic acid (2HB) unit content range of 0–100 mol% were synthesized by polycondensation, and their crystallization behavior was compared with that reported for the random copolymers composed of *optically active* L-lactic acid and L-2-hydroxybutanoic acid (L-2HB) [P(LLA-*co*-L-2HB)s] with the *identical configurations* [75, 76]. Surprisingly, as shown in Fig. 22, poly(L-lactic acid-*co*-L-2-hydroxybutaoinc acid) [P(LLA-*co*-L-2HB)] is crystallizable for LLA unit content of

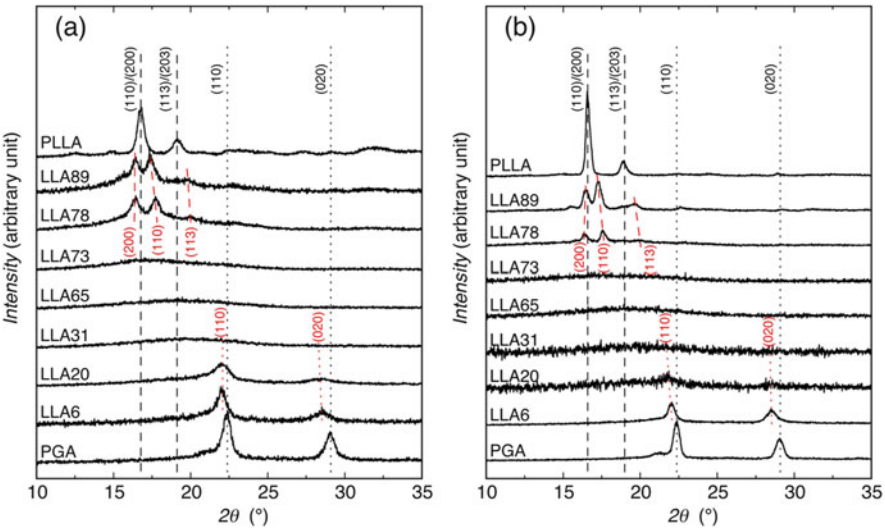

Fig. 20 WAXD profiles of precipitated (**a**) and melt-crystallized (**b**) PLLA, P(LLA-*co*-GA) copolymers, and PGA. Black dashed and dotted lines are the main diffraction angle values of neat PLLA and PGA [74] (with permission from Springer Nature)

0–100 mol%, when samples were crystallized by precipitation or isothermal crystallization (T_c = 70°C) from the melt [75, 76]. In contrast, P(LLA-*co*-D-2HB) copolymers were crystallizable at 2HB unit contents only around 0 and 100 mol% (i.e., 0–11 and 95–100 mol%) [76]. In this figure P(LLA-*co*-L-2HB) and P(LLA-*co*-D-2HB) are abbreviated as HB*X* where *X* indicates 2-hydroxybutaoinc acid (2HB) unit fraction (mol%) in the copolymer. The finding here indicates that the disturbance effect of minor monomer units with the configuration *opposite* to that of the major monomer units on the crystallization of the random copolymers is much stronger than that of the minor monomer units with the configuration *identical* to that of the major monomer units [76].

The shifts of crystalline diffraction peak angles (Fig. 22) and *d* values (Fig. 23) of the highest and second highest peaks of P(LLA-*co*-L-2HB) copolymers depending on L-2HB unit content and the insignificant change of crystalline diffraction peak angles and *d* values of P(LLA-*co*-D-2HB) reveal that the minor monomer units are incorporated in the crystalline regions of the major monomer units when two types of monomers have the *identical configurations*, although the minor monomer units are excluded from the crystalline regions of the major monomer units when two types of monomers have the *opposite configurations* [75, 76]. The cocrystallization of monomer units of random copolyesters is well-summarized in the review article by Pérez-Camargo et al. [77]. Although the X_c values of P(LLA-*co*-L-2HB) copolymers were lower than those of PLLA and P(L-2HB) homopolymers, they remained positive for all L-2HB unit contents (Fig. 23) [75, 76]. Interestingly, as reported in the supporting information of the paper [75], P(LLA-*co*-L-2HB) copolymers with

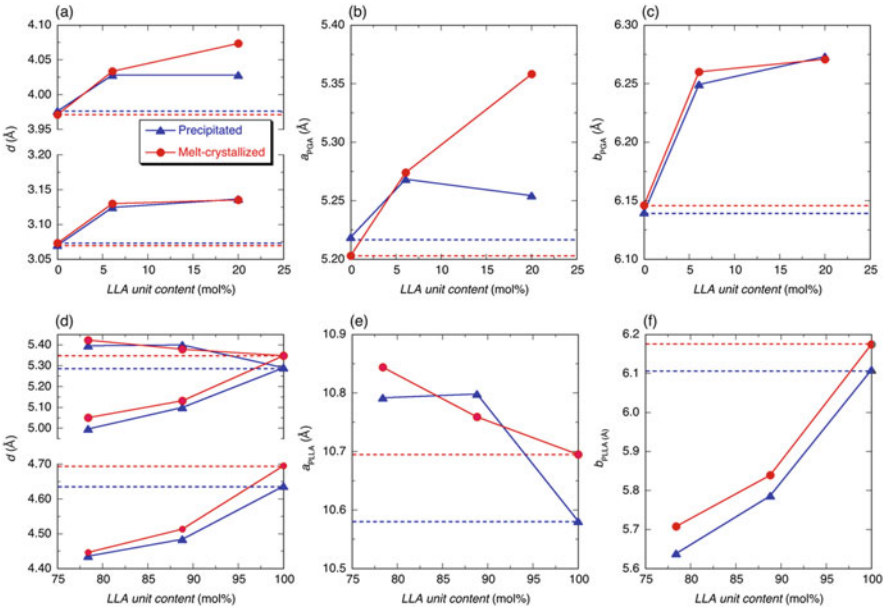

Fig. 21 Interplanar distance (d) values for the (110) and (020) planes of PGA ($d_{110,PGA}$ and $d_{020,PGA}$) (**a**), lattice parameters a and b of PGA (a_{PGA} and b_{PGA}, respectively) (**b**, **c**), d values for the (200), (110), and (113) planes of PLLA ($d_{200,PLLA}$, $d_{110,PLLA}$, and $d_{113,PLLA}$) (**d**), and lattice parameters a and b of PLLA (a_{PLLA} and b_{PLLA}, respectively) (**e**, **f**) for precipitated and melt-crystallized PLLA, P(LLA-GA) copolymers, and PGA, as a function of the LLA unit content in the polymers. Dashed lines show the d, a, and b values for PGA (0 mol% LLA unit content) or PLLA (100 mol% LLA unit content) [74] (with permission from Springer Nature). The solid lines are to guide the viewer

L-2HB unit content of 27–74 mol% were not crystallizable during solvent evaporation or differential scanning calorimetry (DSC) heating of melt-quenched samples at 10°C min^{-1} after melt-quenching. The aforementioned P(LLA-*co*-L-2HB) random copolymers were chemically synthesized, but biosynthesized enantiomeric poly(D-lactic acid-*co*-D-2-hydroxybutaoinc acid) random copolymers showed the cocrystallization behavior similar to that of P(LLA-*co*-L-2HB) random copolymers [78].

Figure 24 shows the polarized optical photomicrographs of the P(L-2HB), P(LLA-*co*-L-2HB) copolymers, and PLLA samples crystallized at $T_c = 70°C$ for 5 h from the melt, together with that of the PLLA sample immediately after the sample reached 70°C (0 h) from the melt [75]. The P(L-2HB) homopolymer sample had large-sized spherulites with a Maltese cross and a radius larger than 100 μm, whereas the PLLA homopolymer sample showed a rather complicated morphology composed of relatively large spherulites (radius of 10–40 μm) with a Maltese cross and relatively small spherulites (radius < 10 μm) [75]. As evident from the photo of the PLLA homopolymer sample at 0 h, the formation of relatively large spherulites should have taken place during cooling from the melt before reaching $T_c = 70°C$,

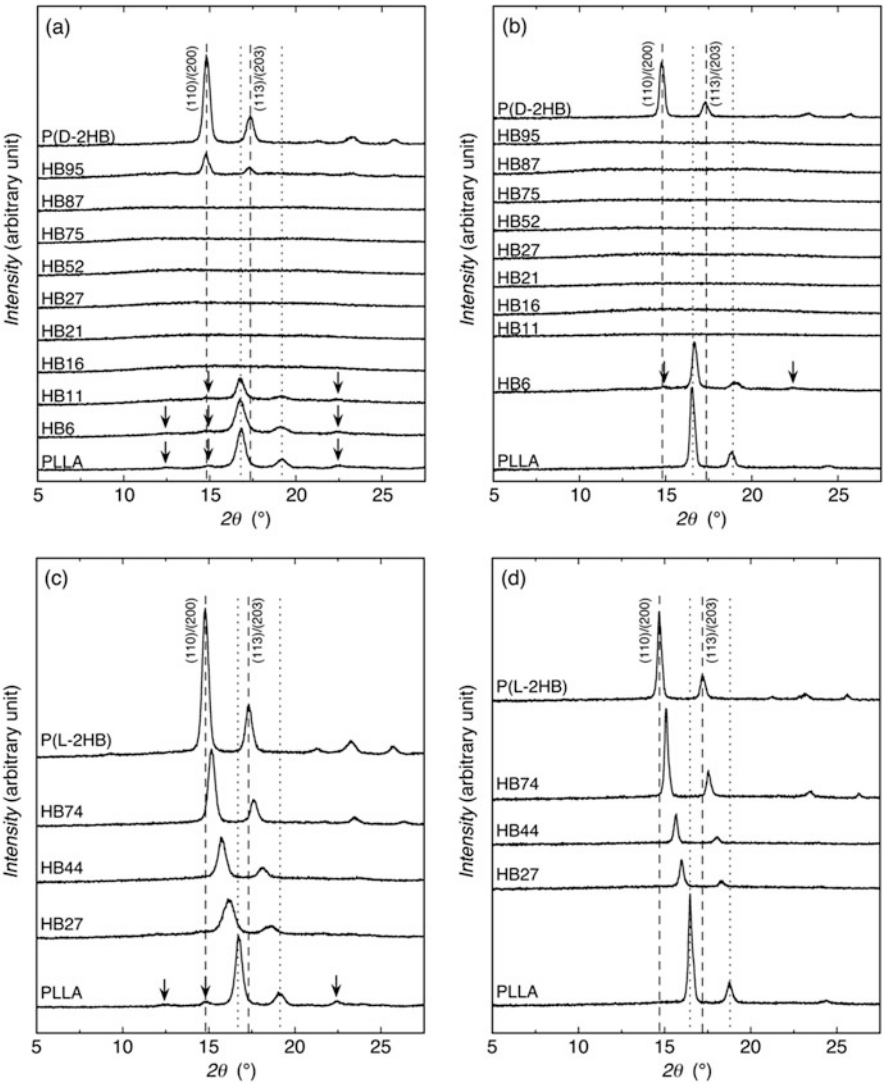

Fig. 22 WAXD profiles of purified (**a**) and melt-quenched-crystallized (**b**) P(LLA-*co*-D-2HB) samples, purified (**c**) and melt-crystallized (**d**) P(LLA-*co*-L-2HB) samples. The dashed and dotted lines are the crystalline diffraction angles of P(D-2HB) or P(L-2HB) and PLLA, respectively. The arrows indicate the crystalline diffractions specific only to α-form [75, 76] (with permission from Elsevier B.V. and American Chemical Society)

and, therefore, the relatively small spherulites are attributed to those formed at 70°C [75]. The HB74 copolymer sample had the spherulites with morphology similar to those of the P(L-2HB) homopolymer sample, although the spherulitic sizes were smaller than those of the P(L-2HB) homopolymer sample [75]. The HB44 and HB27

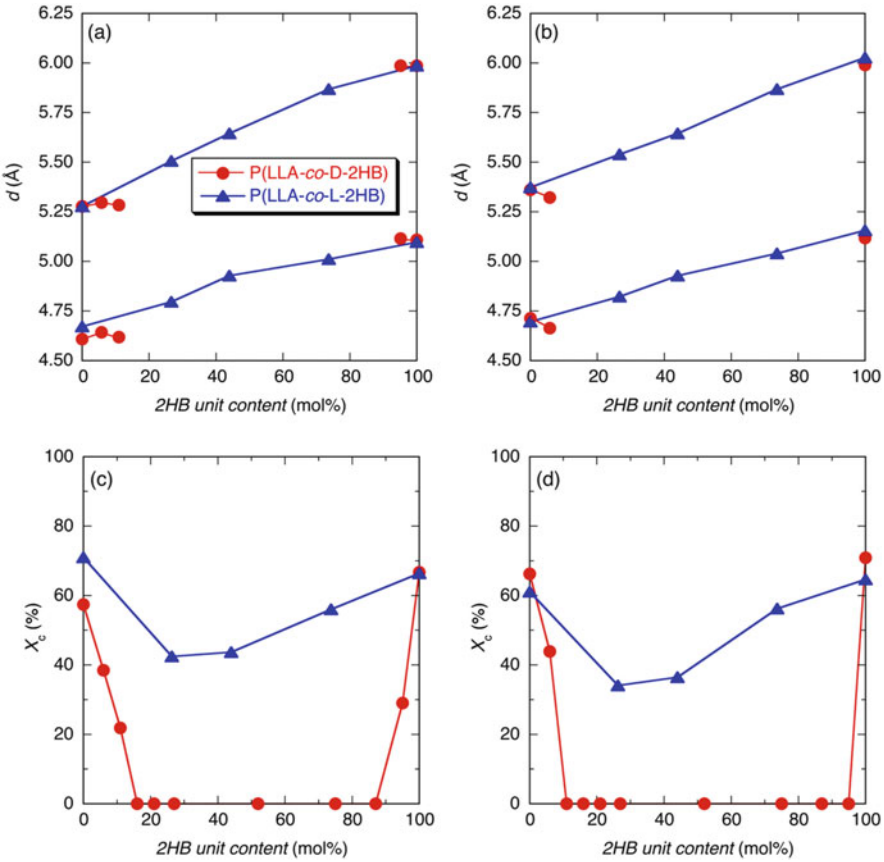

Fig. 23 Interplanar distance (d) of purified P(LLA-*co*-D-2HB) and P(LLA-*co*-L-2HB) samples (**a**), and melt-quenched-crystallized P(LLA-*co*-D-2HB) samples and melt-crystallized P(LLA-*co*-L-2HB) samples (**b**) crystallinity (X_c) of purified P(LLA-*co*-D-2HB) and P(LLA-*co*-L-2HB) samples (**c**), and melt-quenched-crystallized P(LLA-*co*-D-2HB) samples and melt-crystallized P(LLA-*co*-L-2HB) samples (**d**), as a function of 2HB unit content [75, 76] (with permission from Elsevier B.V. and American Chemical Society)

copolymer samples consisted of a large number of small spherulites, morphology of which is similar to those of the smaller spherulites formed in the PLLA sample at 70°C [not during cooling from the melt (Fig. 24, PLLA, 0 h)] [75].

The incorporation of chiral and achiral 2-hydroxyalkanoic acids other than LLA in the crystalline regions of LLA units and their exclusion from the crystalline regions of LLA units have been investigated by Marubayashi et al. [79]. They found that small-sized comonomer units such as *achiral* glycolic acid, *achiral* 2-hydroxyisobutyric acid (2-hydroxy-2-methylpropanoic acid), and *chiral* L-2-hydroxy-3-methylbutanoic acid units are incorporated in crystalline regions of LLA units, whereas large-sized monomer units like *chiral* L-2-hydroxy-4-methylpentanoic acid units are excluded from the crystalline regions [79].

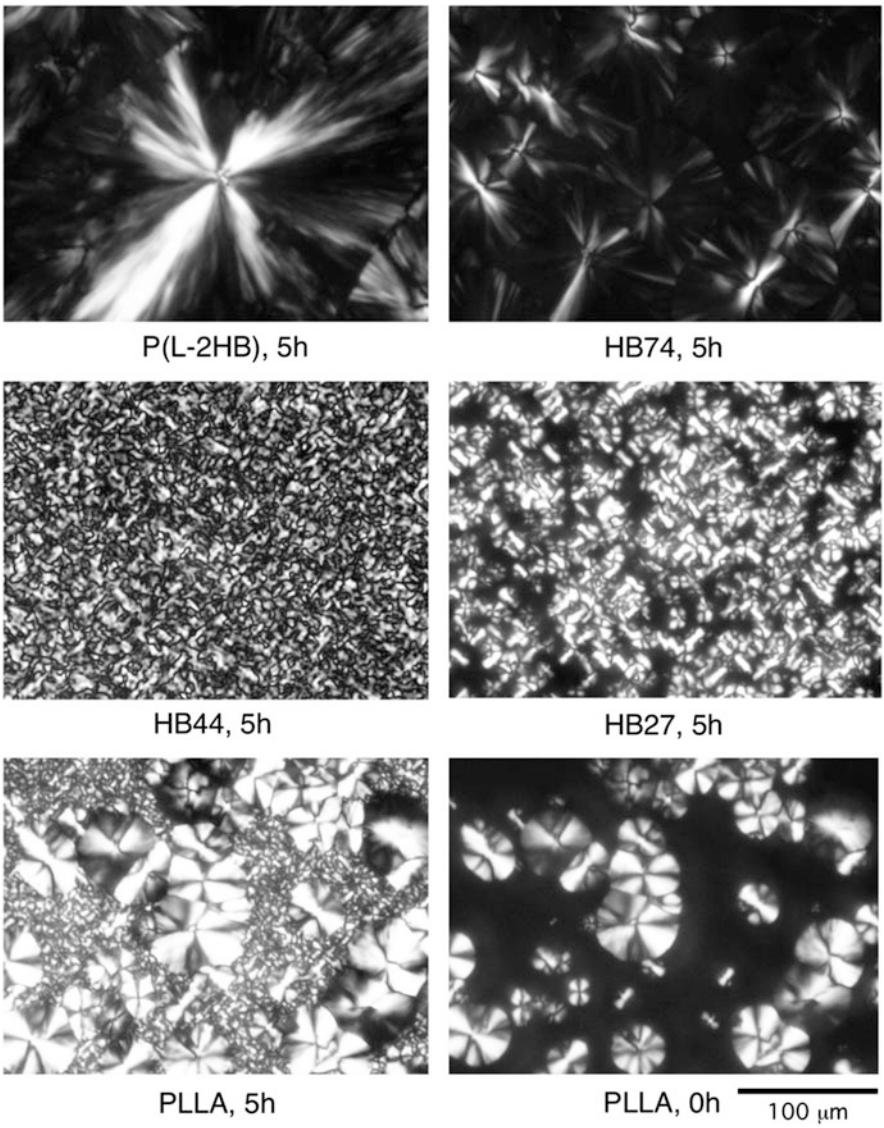

Fig. 24 Polarized optical photomicrographs of P(L-2HB), P(LLA-*co*-L-2HB), and PLLA crystallized at $T_c = 70°C$ for shown crystallization times from the melt. Crystallization time = 0 h for PLLA means the photo was taken immediately after the sample reached 70°C from the melt [75] (with permission from Elsevier B.V.)

4.3.3 Random Copolymerization with α-Amino Acid

Excluding the block copolymers with other types of polymer chains such as those with poly(ethylene oxide) block(s), only ester linkage is included in LA or lactide-based random copolymers. Very recently, the random copolymers of

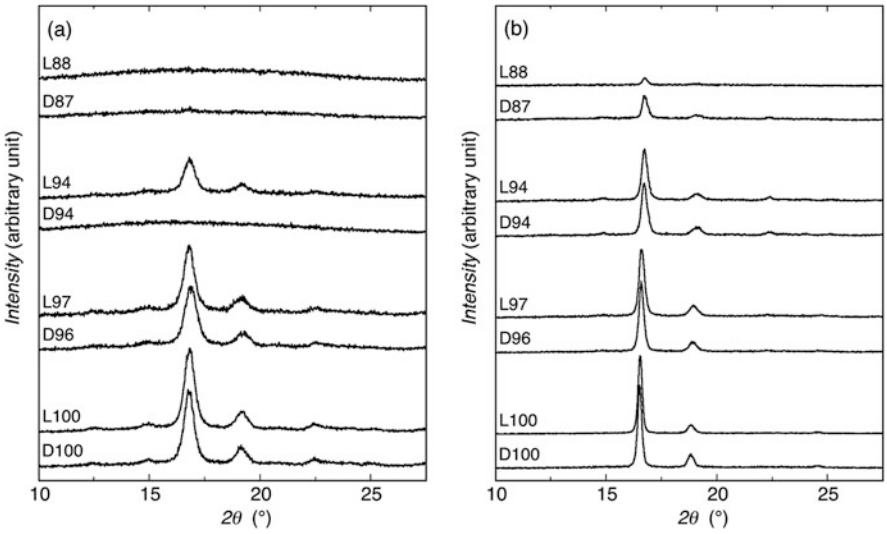

Fig. 25 WAXD profiles of solution-crystallized (**a**) and melt-crystallized (**b**) P(LLA-LAL) and P(DLA-DAL) samples [80] (with permission from The Royal Society of Chemistry)

poly(L-lactic acid-*co*-L-alanine) [P(LLA-LAL)] and poly(D-lactic acid-*co*-D-alanine) [P(DLA-DAL)] with both *ester* and *amide* linkages were synthesized, and their homo-crystallization and SC crystallization were investigated [80]. Figure 25 shows the WAXD profiles of solution-crystallized and melt-crystallized ($T_c = 100°C$) nonblended P(LLA-LAL) and P(DLA-DAL) samples [80]. In this figure, P(LLA-LAL) and P(DLA-DAL) are abbreviated as L*X* and D*X*, respectively, where *X* indicates LA fraction (mol%) in the copolymer. The *d* values of solution- and melt-crystallized P(LLA-LAL) and P(DLA-DAL) samples are shown in Fig. 26 [80]. The *d* values of solution-crystallized samples (Fig. 26a) did not show the clear dependence of *d* values on alanine unit content, whereas those of melt-crystallized samples (Fig. 26b) monotonically decreased with an increase in alanine unit content [80]. The latter finding strongly suggests for the melt-crystallized nonblended samples that the alanine units were incorporated in the crystalline regions of LA units and the incorporated alanine units decreased the crystalline lattice sizes of LA units [80]. In addition to the results of *d* values, Fourier transform infrared spectroscopy (FTIR) measurements revealed that depending on crystallization procedures of solvent evaporation and melt crystallization, alanine units are correspondingly excluded from and included in the crystalline regions of LA units.

4.4 Effects of Branching

The crystallization of branched PLLA polymers should be affected by at least four factors: (1) presence of a branching point which also can be regarded as a point of

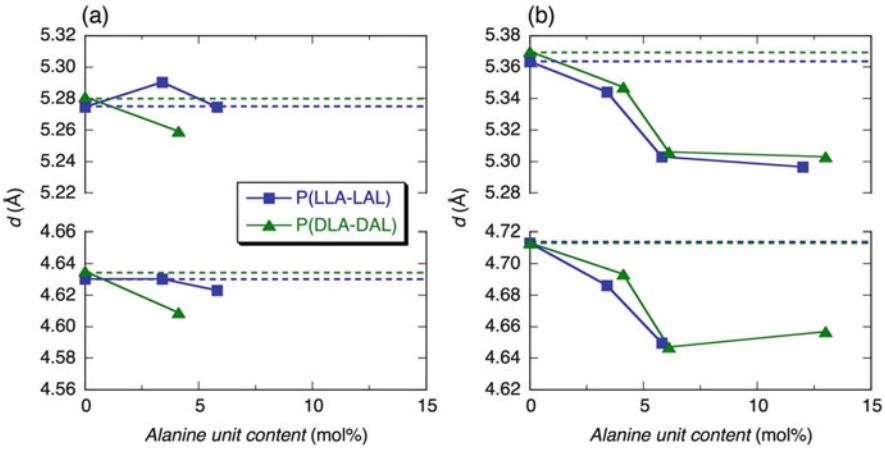

Fig. 26 Interplanar distance (d) of solution-crystallized (**a**) and melt-crystallized (**b**) non-blended (**a**, **b**) P(LLA-LAL) and P(DLA-DAL) samples. Dashed lines indicate the d values at nil alanine unit content [80] (with permission from The Royal Society of Chemistry)

intersegmental connection, (2) incorporation of coinitiator moiety for branching in the middle of chain especially when it is bulky, (3) presence of many hydrophilic hydroxyl groups at chain terminals caused by a polyol coinitiator, which enhance the formation of hydrogen bonding, and (4) chain directional change at a branching point. All these factors are expected to disturb the segmental mobility for the nuclei formation and/or the growth of crystallites.

Figure 27 shows the typical polarized photomicrographs of the spherulites of low molecular weight linear two-armed and branched four-armed PLLA homopolymers (2L and 4L, respectively) crystallized isothermally in the α-form (and regime II) at ΔT in the range of 32–35°C [81]. In these figures, the numbers immediately following the polymer codes "2L" and "4L" are the number-average molecular weights estimated by ^{1}H nuclear magnetic resonance (NMR) [M_n(NMR)]/10^3 g mol^{-1}. Normal spherulites were formed in all 2L homopolymers and 4L homopolymers having M_n exceeding 1.0×10^4 g mol^{-1}, whereas rather disordered spherulites were seen in 4L9 ($M_n < 1.0 \times 10^4$ g mol^{-1}). The latter disorder strongly suggests that the branching in the 4L homopolymer with the lowest molecular weight (4L9) caused the macroscopic structural defects in the spherulites, due to increased number per unit mass of branching points [81].

Figure 28 shows the G values of the 2L and 4L homopolymers [81]. Evidently, the 4L homopolymers have lower G values compared to those of the 2L homopolymers. In contrast with linear one-armed PLLA (1L) homopolymers, wherein the G values of linear two-armed 2L and branched four-armed 4L homopolymers increased with decreasing molecular weight and became maximum at M_n [M_n(max)] = 1.1×10^4 and 1.8×10^4 g mol^{-1} for the 2L and 4L homopolymers, respectively, and further decrease of molecular weight induced the decrease of G values. With decreasing molecular weight, the chain mobility increases and thereby the crystallization rate is elevated, whereas the density of coinitiator moiety

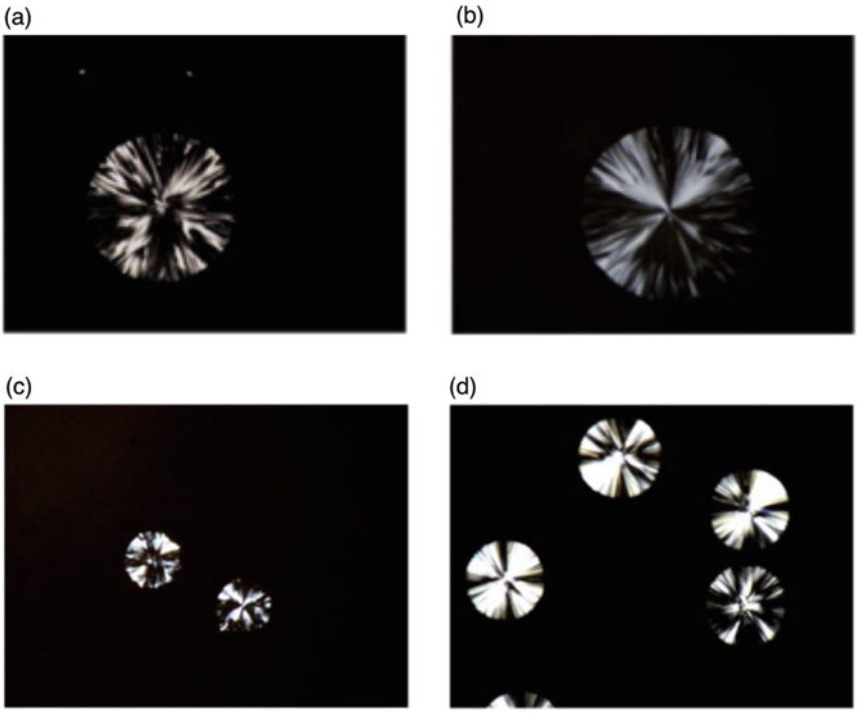

Fig. 27 Polarized photomicrographs of spherulites of 2-L an 4-L crystallized at the shown temperatures and times (crystallized in α-form and regime II) [81]. (**a**) 2L5 (T_c = 110°C, ΔT = 32.2°C, 5.0 min). (**b**) 2L11 (T_c = 125°C, ΔT = 32.8°C, 5.0 min). (**c**). 4L9 (T_c = 105°C, ΔT = 33.5°C, 10 min). (**d**) 4L18 (T_c = 120°C, ΔT = 32.4°C, 5.5 min) (with permission from Elsevier B.V.)

which disturbs crystallization increases and thereby the crystallization rate decreases. With decreasing the molecular weight down to the M_n(max) values, the former effect is stronger than the latter effect, whereas with further decrease of M_n below the M_n(max) values, the latter effect prevails the former effect.

The ln G + 1,500/R(T_c–T_∞) of the 2L and 4L homopolymers are plotted in Fig. 29 as a function of 1/($T_c\Delta Tf$) [81]. The lowest molecular weight 2L5 and the second lowest molecular weight 2L11 had three regimes (regimes III, II, and I) depending on T_c, whereas the highest molecular weight 2L38 and the second highest molecular weight 2L20 showed only two regimes (regimes III and II) [81]. The medium molecular weight 4L30 and 4L18 had three regimes (regimes III, II, and I), whereas the highest molecular weight 4L57 and the lowest molecular weight 4L9 showed only two regimes (regimes III and II and regimes II and I, respectively) [81]. The regime transition temperatures of the 2L and 4L homopolymers are higher for a sample with a higher molecular weight. Figure 30 shows the T_c(δ-α) of the 2L and 4L homopolymers [81]. As seen, the T_c(δ-α) values depend on M_n per one arm [M_n(arm)] rather than M_n [81]. If T_c(δ-α) was plotted only as a function of M_n, the conclusion would be that T_c(δ-α) decreases with an increase in arm number.

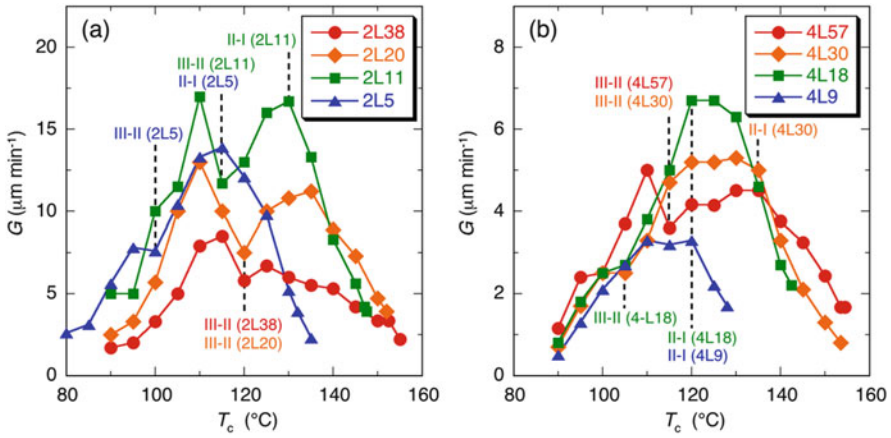

Fig. 28 Radial growth rate of spherulites (G) of two-armed (**a**) and four-armed (**b**) PLLAs (2-L and 4-L, respectively) as a function of crystallization temperature (T_c) [81] (with permission from Elsevier B.V.)

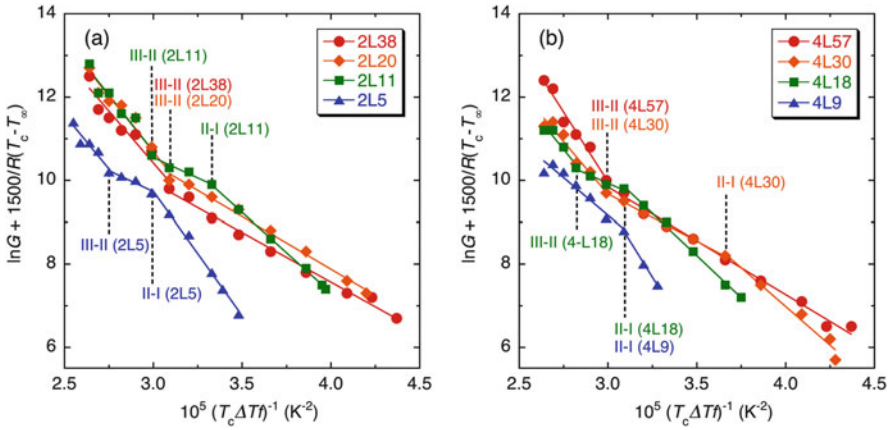

Fig. 29 ln G − 1,500/R(T_c − T_∞) of two-armed (**a**) and four-armed (**b**) PLLAs (2-L and 4-L, respectively) as a function of $1/(T_c\Delta Tf)$ [81] (with permission from Elsevier B.V.)

4.5 *Effects of Nucleating or Crystallization-Accelerating Agents*

4.5.1 Stereocomplexes of Unsubstituted and Substituted Poly(Lactic Acid)s

Nucleating agents are effective to reduce the processing time and production cost. Numerous nucleating agents are reported for linear one-armed PLLA homocrystallization [3]. Here, a representative nucleating agent, SC of linear one-armed

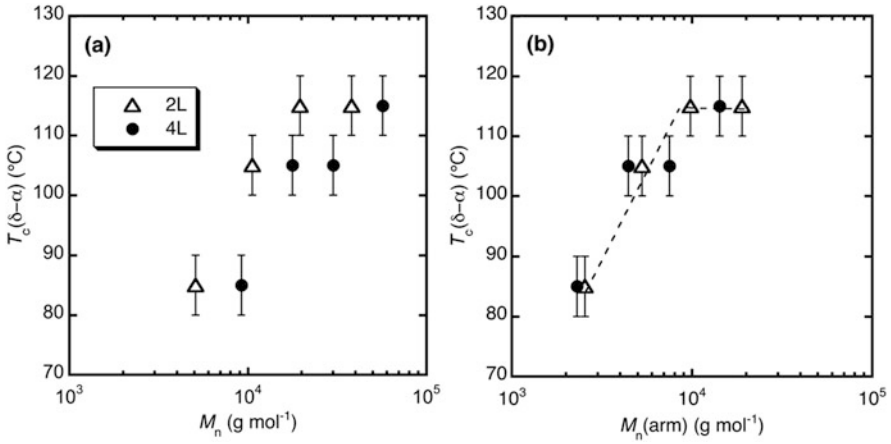

Fig. 30 T_c values at which the transition from δ-form to α-form took place [T_c(δ-α)] of 2-L and 4-L as functions of M_n (**a**) and M_n per one arm [M_n(arm)] (**b**) [81] (with permission from Elsevier B.V.)

PLLA and its enantiomer linear one-armed PDLA, which T_m (220–230°C) is higher than that of PLLA or PDLA (170–180°C), is mainly discussed [82–87]. SC is a very effective nucleating agent, which is formed upon blending PLLA with PDLA and readily dispersed in PLLA materials. Therefore, it had no issue of phase separation or leaching out from PLLA materials. Figure 31 shows the polarized optical photomicrographs of linear one-armed PLLA films having different contents of linear one-armed PDLA taken at 135°C after the saturation of spherulite growth [84]. In this study, PLLA and PDLA with different molecular weights (1.2×10^5 g mol^{-1} and 5.4×10^4 g mol^{-1}, respectively) were used [84]. In Fig. 32, the PLLA spherulite density (number per unit area) estimated from the polarized optical photomicrographs is plotted as a function of T_c [84]. The number per unit area of PLLA spherulites tends to increase with PDLA content, reflecting the fact that the SC crystallites formed in the films by the addition of PDLA acted effectively as a nucleating agent for PLLA spherulites or crystallites [84]. Figure 33a shows the G values of PLLA films with different contents of PDLA [84]. The G values were not altered by the incorporation of PDLA [84]. If PDLA were present in the amorphous state, the low molecular weight PDLA should have enhanced the chain mobility of PLLA and thereby increased the G values. However, since PDLA should have been present in the SC crystalline state at the T_c range of PLLA below the T_m of SC crystallites as evidenced by WAXD [84], the difference in molecular weight of PDLA compared with that of PLLA should have not affected the mobility of PLLA chains and did not alter the G values of blends (Fig. 33a) [84]. However, the G values may be increased by the addition of very low molecular weight PDLA such as 10^3 g mol^{-1}, if a significant number of molecules remain un-stereocomplexed. Due to no significant change of G values by addition of PDLA, the plots of ln G + 1,500/$R(T_c-T_\infty)$ were similar, irrespective of PDLA content (Fig. 33b) [84].

Narita et al. reported that SC crystallites melted just above the endset temperature of SC melting (228–238°C) and recrystallized during cooling were found to act as

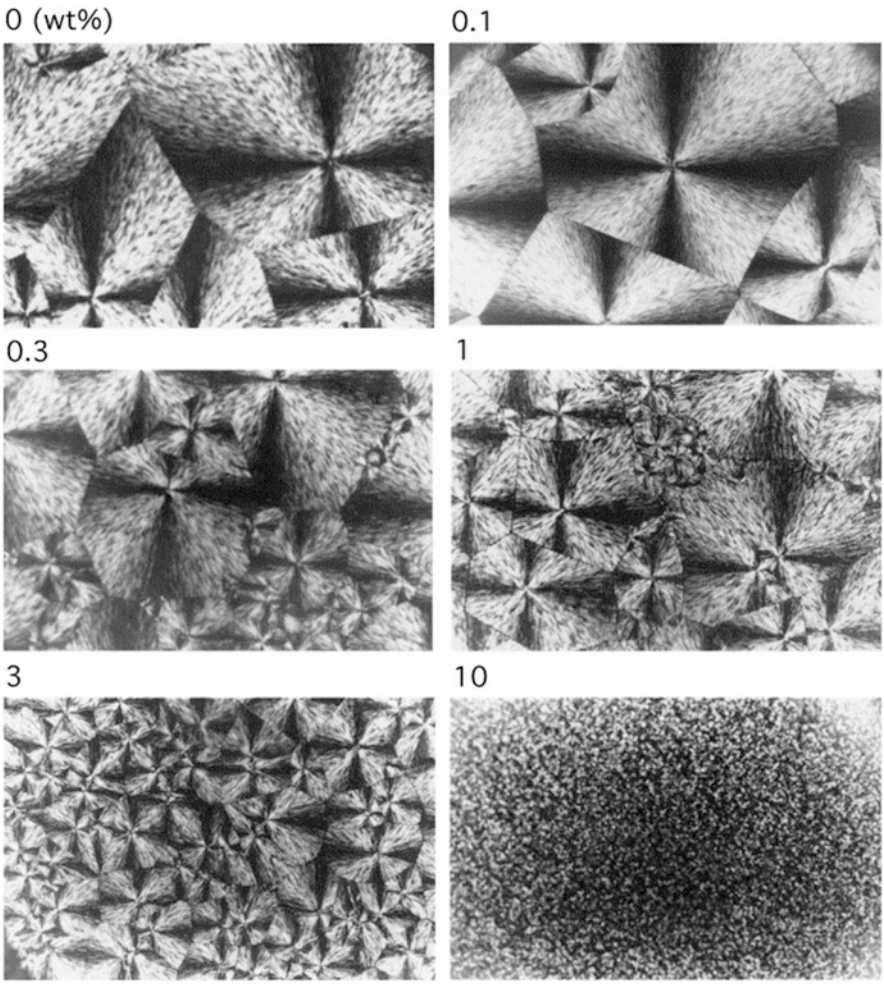

Fig. 31 Polarized optical photomicrographs of PLLA films containing different contents of PDLA crystallized at 135°C after saturation of spherulite formation [84] (with permission from Elsevier B.V.)

the most effective nucleating agent for enhancing the crystallization of linear one-armed PLLA compared to the partially melted SC crystallites (211–227°C) or those melted far above the endset temperature of SC melting (240 and 250°C) and recrystallized during cooling [86, 87]. Although non-melted and non-recrystallized SC crystallites processed at 180–200°C had the nucleating effect on the linear one-armed PLLA crystallization as high as those processed at 228–238°C, the former processing temperature cannot be used because too high viscosity of PLLA near its melting temperature will cause the issues of flow marks or jetting with an injection molding process [86, 87].

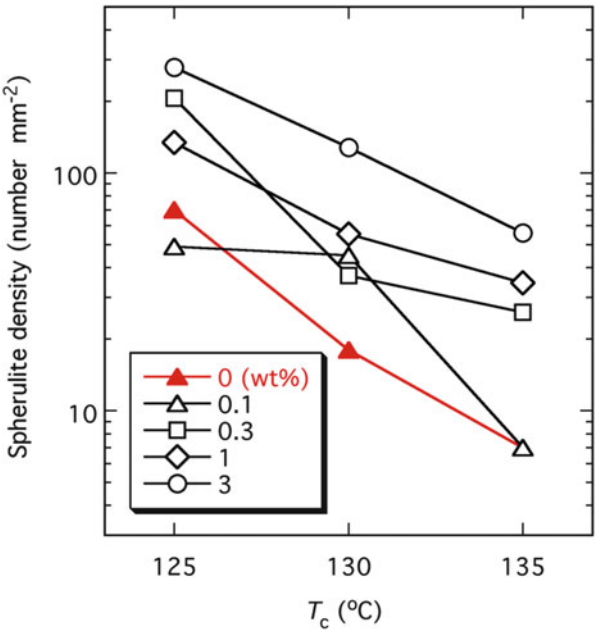

Fig. 32 Spherulite density (number per unit area) of PLLA films with different contents of PDLA as a function of T_c [84] (with permission from Elsevier B.V.)

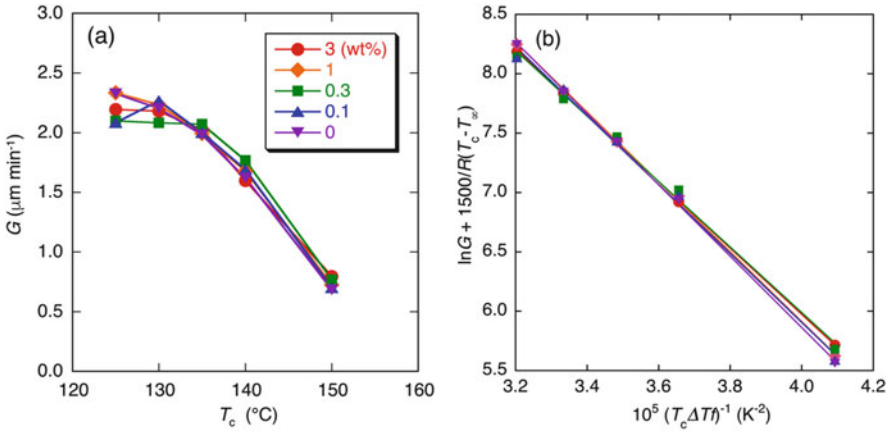

Fig. 33 Radial growth rate of spherulites (G) (**a**) and ln G + 1,500/$R(T_c - T_\infty)$ (**b**) of PLLA films with different contents of incorporated PDLA as functions of crystallization temperature (T_c) and $1/(T_c\Delta Tf)$, respectively [84] (with permission from Elsevier B.V.)

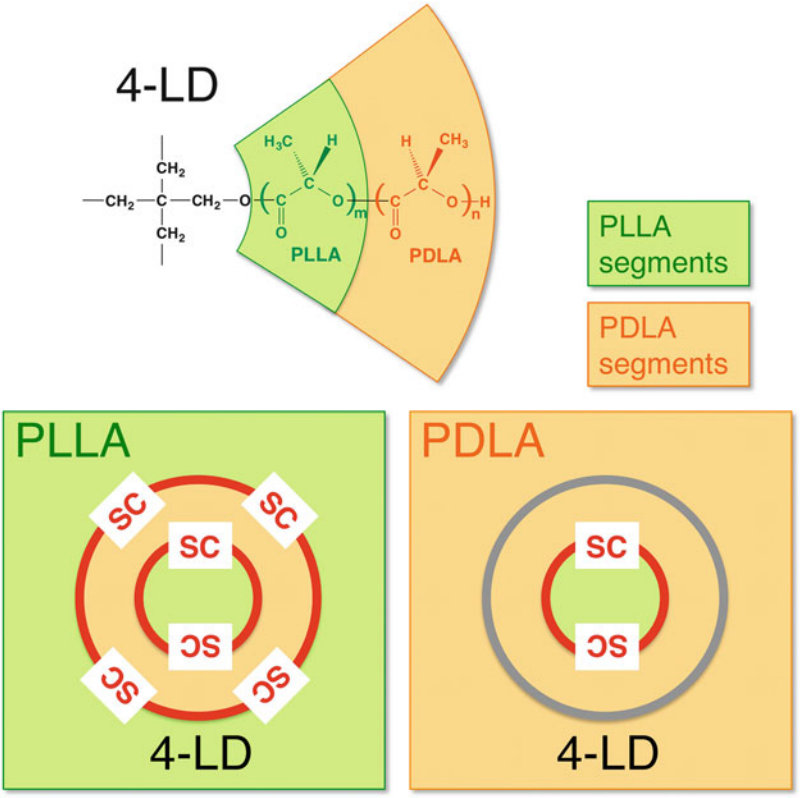

Fig. 34 Molecular structure of 4-LD and material models of PLLA or PDLA with 4-LD [88] (with permission from Springer Nature). The light yellow green and light orange color parts are composed of PLLA and PDLA segments, respectively. 4-LD is four-armed stereo diblock PLA with equimolar L- and D-lactide units and is shown with the concentric circles

Branched four-armed stereo diblock PLLA-*b*-PDLA copolymers, i.e., 4-LD, with PLLA core and PDLA shell, and high molecular weight linear one-armed PLLA and PDLA were synthesized, and the crystallization-accelerating effect of 4-LD on linear one-armed PLLA or PDLA was investigated (Fig. 34) [88]. Interestingly, the accelerating effect was higher for PLLA/4-LD with the opposite configurations of linear one-armed PLLA and the PDLA shell of 4-LD than for PDLA/4-LD with the identical configurations of linear one-armed PDLA and the PDLA shell of 4-LD [88]. In the former case, SC crystallites are formed at the interface between the linear one-armed PLLA and PDLA shell of 4-LD, which should effectively act as the nucleating agent and accelerate the homo-crystallization of the linear one-armed PLLA. However, in the latter case, since SC crystallites are formed inside 4-LD not the interface between PDLA and 4-LD, 4-LD should have a very low nucleating effect on the homo-crystallization of linear one-armed PDLA. Although the experiments were performed during heating or cooling, similar results are expected to be obtained for isothermal crystallization.

In addition to SC crystallites of unsubstituted PLLA and PDLA, homo-crystallization of linear one-armed PLLA is also accelerated by the presence of one of linear one-armed substituted PLLA homopolymers, i.e., linear one-armed poly(L-2-hydroxybutanoic acid) [P(L-2HB)]; one of linear one-armed substituted PDLA, i.e., linear one-armed poly(D-2-hydroxybutanoicacid) [P(D-2HB)]; and their mixture [P(L-2HB)/P(D-2HB)] [89]. At T_c range of PLLA above 100°C, P(L-2HB) remains amorphous in PLLA, whereas PLLA/P(D-2HB) hetero-stereocomplex and P(L-2HB)/P(D-2HB) homo-stereocomplex or PLLA/P(L-2HB)/P(D-2HB) ternary SC should be formed and acted as biodegradable nucleating agents of PLLA [89] (Ternary stereocomplex was first reported in 2012 [90] and therefore in [89], only the formation of P(L-2HB)/P(D-2HB) homo-stereocomplex not P(L-2HB)/P(D-2HB)/PLLA ternary stereocomplex is discussed). The accelerating effect of incorporated polymers decreased in the following order: P(L-2HB)/P(D-2HB) > P(D-2HB) > P(L-2HB) > none, for T_c = 130 and 135°C [89]. Moreover, free low molecular weight P(L-2HB) and P(D-2HB) have a plasticizing effect and accelerate the homo-crystallization of PLLA [89].

4.5.2 Other Nucleating or Crystallization-Accelerating Agents

Some melt-recrystallizable nucleating agents induce various assembled structures of linear one-armed PLLA [91–93]. The morphology of *N,N′,N″*-tricyclohexyl-1,3,5-benzenetricarboxylamide (TMC-328) assemblies formed by hydrogen bonding in the PLLA melt varies depending on its concentration, inducing the characteristic crystal morphologies, i.e., the cone-like (PLLA-0.2), shish kebab-like (PLLA-0.3), and needle-like (PLLA-0.5) structures, respectively (Fig. 35) [91]. Here, PLLA-*X* indicates the weight percentage of TMC-328. The schematic representation of the evolution of crystal morphologies during crystallization of PLLA nucleated with different loading levels of TMC-328 is shown in Fig. 36 [91]. Shish kebab-like structure contained bundled lamellae as kebab, which is different from conventional shish kebab structure wherein lamellar single crystals are periodically located on the shish core and packing density of lamellae around shish is much higher than that in Fig. 36 [91]. Similarly, depending on the annealing temperature and tetramethylene-dicarboxylic di-(2-hydroxybenzohydrazide) (TMBH) concentration, TMBH may remain crystalline, or partially/completely dissolve into a PLLA melt, which greatly affected the crystallization kinetics and crystalline morphology of PLLA [92]. Also, the oxalamide compounds triggered the shish kebab morphology of PLLA crystals [93]. Although the nucleating agents enhance the crystallization of α-form PLLA, the change of the crystalline modification has not been reported [93].

On the other hand, a series of biodegradable polyesters, poly[(*R*)-3-hydroxybutyrate] (PHB), poly(ε-caprolactone) (PCL), and PGA, were found to be effective crystallization-accelerating agents for PLLA, although the crystallization was performed non-isothermally during heating or cooling from the melt [94, 95]. Such accelerating effects were ascribed to a nucleation-assisting effect of PCL and PGA and a spherulite growth-accelerating effect of PHB, although the

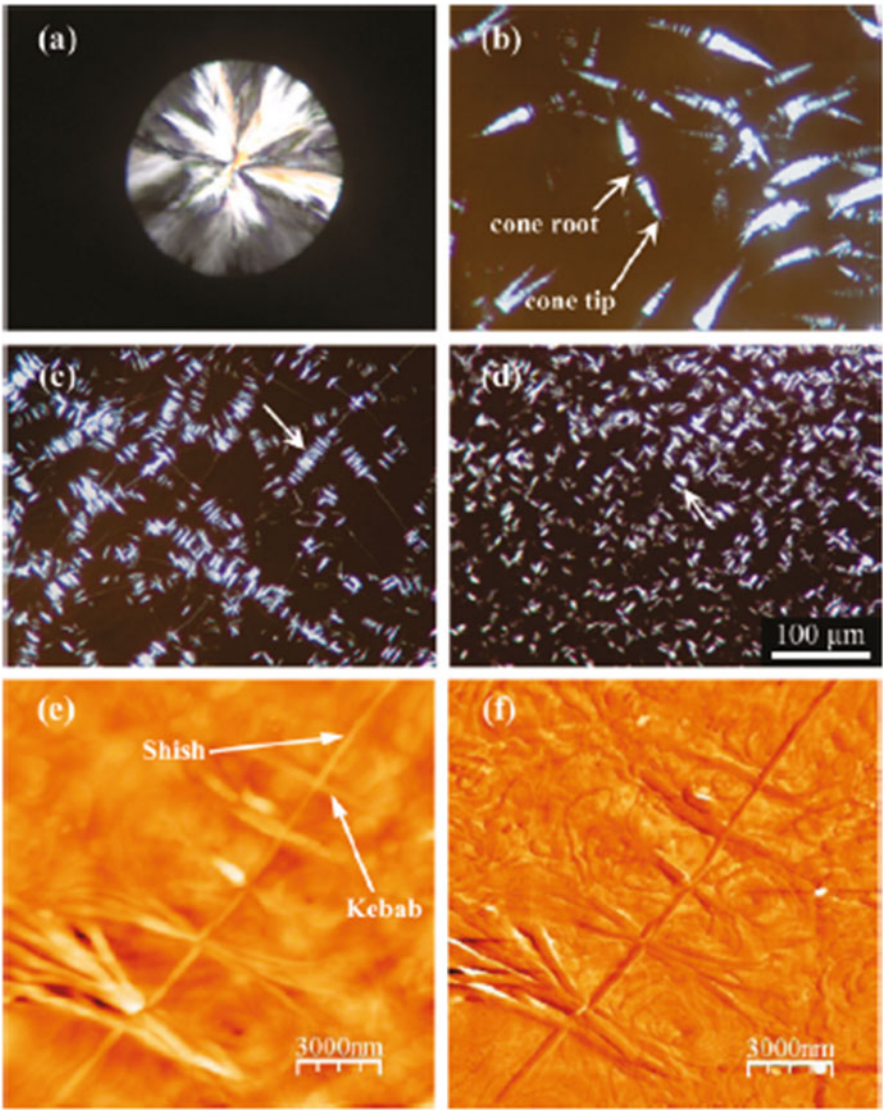

Fig. 35 POM micrographs of crystal morphology for PLLA with different loading levels of TMC-328: PLLA-0 (**a**), PLLA-0.2 (**b**), PLLA-0.3 (**c**), and PLLA-0.5 (**d**) prepared by isothermal crystallization at 130°C for 55, 7, 10, and 10 min, respectively, and AFM image height (**e**) and phase (**f**) of PLLA-0.2 [91] (with permission from American Chemical Society)

incorporated PHB lowered the spherulite number of PLLA per unit area [94]. The spherulite growth-accelerating effect of PHB was probably attributed to the relatively high miscibility of PLLA with PHB and the lower glass transition temperature of PHB compared to that of PLLA [94].

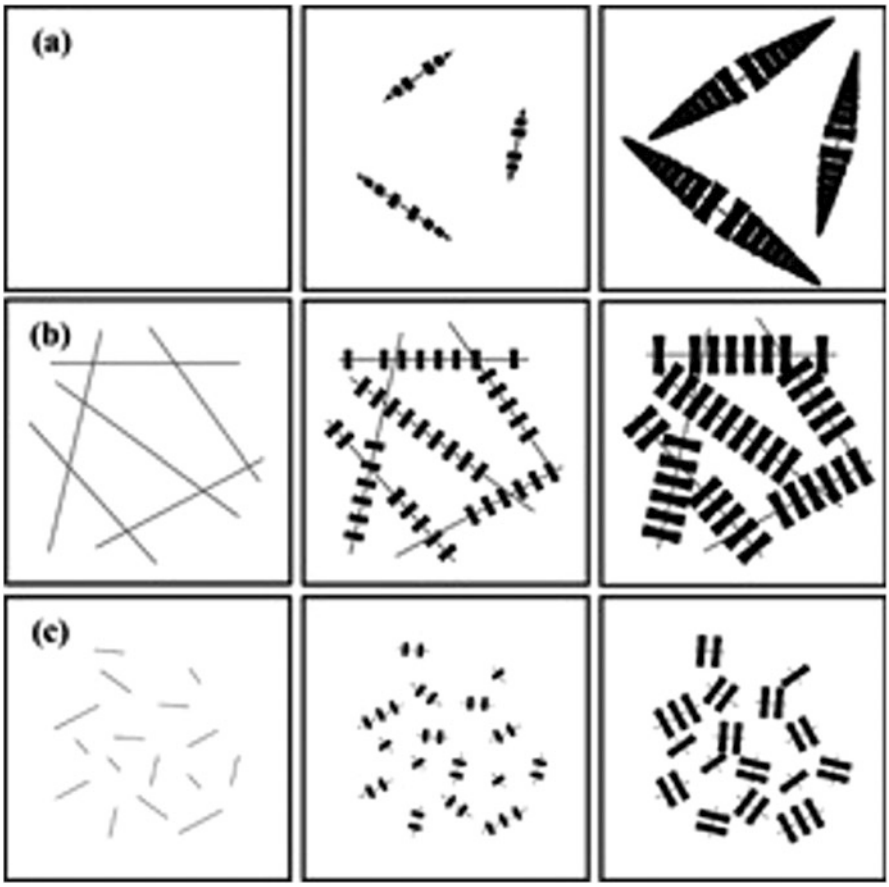

Fig. 36 Schematic representation of the evolution of crystal morphologies during crystallization nucleated PLLA with different loading levels of TMC-328: (**a**) PLLA-0.2, (**b**) PLLA-0.3, and (**c**) PLLA-0.5 [91] (with permission from American Chemical Society)

4.6 Effects of Incorporated Polymers

Finally, the effects of incorporated polymers are discussed based on the miscibility and cocrystallizability. In the miscible polymer blends, crystallization rate and induction period for PLLA crystallization will be affected by the content of a second polymer, whereas in the completely phase-separated polymer blends of PLLA, the crystallization rate and induction period of PLLA should not be affected, except for an interfacial nucleating effect which can reduce the induction period for crystallization and increase overall crystallization rate. Even when PLLA and a second polymer are phase-separated in their blends, a very small amount of the second polymer incorporated in PLLA-rich domains can affect the crystallization behavior and formed higher-ordered structures.

4.6.1 Effects of Incorporated Amorphous Polymers

In linear one-armed PLLA/linear one-armed *amorphous* poly(DL-lactide) or poly(DL-lactic acid) (PDLLA) blends, two polymer components are reported to be phase-separated during crystallization from the melt [36]. PLLA is crystallizable in PLLA/PDLLA blends even when PLLA content [X_{PLLA} = PLLA/(PLLA + PDLLA)] is decreased to 0.3 or 0.2 but is not crystallizable at $X_{PLLA} \leq 0.1$ [36, 96]. Figure 37 shows the polarized optical photomicrographs of the neat PLLA and PLLA/PDLLA blend films with different X_{PLLA} values isothermally crystallized at T_c of 130°C for 10 h [36]. For X_{PLLA} above 0.7, the normal spherulites were observed, whereas for X_{PLLA} = 0.3–0.5, rather disordered spherulites or crystalline assemblies were noticed [96]. With decreasing X_{PLLA}, the number of spherulites per unit area decreased and the spherulite size increased [36, 96]. Despite the fact that PLLA and PDLLA in their blends are reported to be phase-separated during crystallization, G decreased with increasing PDLLA content (Fig. 38a) [36] but increased with decreasing the molecular weight of PDLLA [97]. However, as seen in Figs. 38b and 39, three regimes (regimes III, II, and I) were observed for all the samples, and T_c(III–II) and T_c(II–I) values were not altered by PDLLA content, whereas T_c(δ-α) values (110–120°C) were not altered by PDLLA content [36]. However, Pan et al. reported that T_c(δ-α) decreased with decreasing from 110°C at X_{PLLA} = 1 to 80°C at X_{PLLA} = 0.5 [98].

4.6.2 Effects of Incorporated Crystallizable Polymers

LLA- or L-lactide-based copolymers with high LLA unit contents can cocrystallize with PLLA homopolymer. Figure 40 shows the polarized photomicrographs of blends of linear one-armed PLLA with linear one-armed *crystallizable* P(LLA-GA) (78/22) and poly(L-lactide-*co*-D-lactide) (77/23) [99]. PLLA and P(LLA-GA) (78/22) cocrystallized in their *miscible* blends, whereas PLLA and poly(L-lactide-*co*-D-lactide) (77/23) crystallized separately in each *phase-separated* domain [99]. As a result, as seen in Fig. 40, PLLA/P(LLA-GA) (78/22) blend with PLLA content of 40 wt% formed normal spherulites, whereas PLLA/poly(L-lactide-*co*-D-lactide) (77/23) blend with PLLA content of 40 wt% showed complicated morphology, although spherulitic structures were observed [99].

Figure 41 shows the G of neat PLLA/P(LLA-GA) (78/22) and PLLA/poly(L-lactide-*co*-D-lactide) (77/23) blend films as a function of T_c. T_c(δ-α) and T_c(II-I) in this figure are those reported for neat PLLA in [100]. The PLLA/P(LLA-GA) (78/22) blend films with X_{PLLA} = 0.4–1 gave the two maximum G [G(max)]values at different two T_c values of 110 and 125°C [abbreviated as T_c(max) values] [99]. The formation of these two maxima can be attributed to the existence of two different crystalline forms [α- or δ-(α′-)form] or the transition from regime III to II [99]. On the other hand, the PLLA/poly(L-lactide-*co*-D-lactide) (77/23) blend films with X_{PLLA} = 0.1–0.8 gave only one G(max) value at T_c around 130°C, in contrast with the result for the PLLA/P(LLA-GA) (78/22) blend films. The G(max) values of

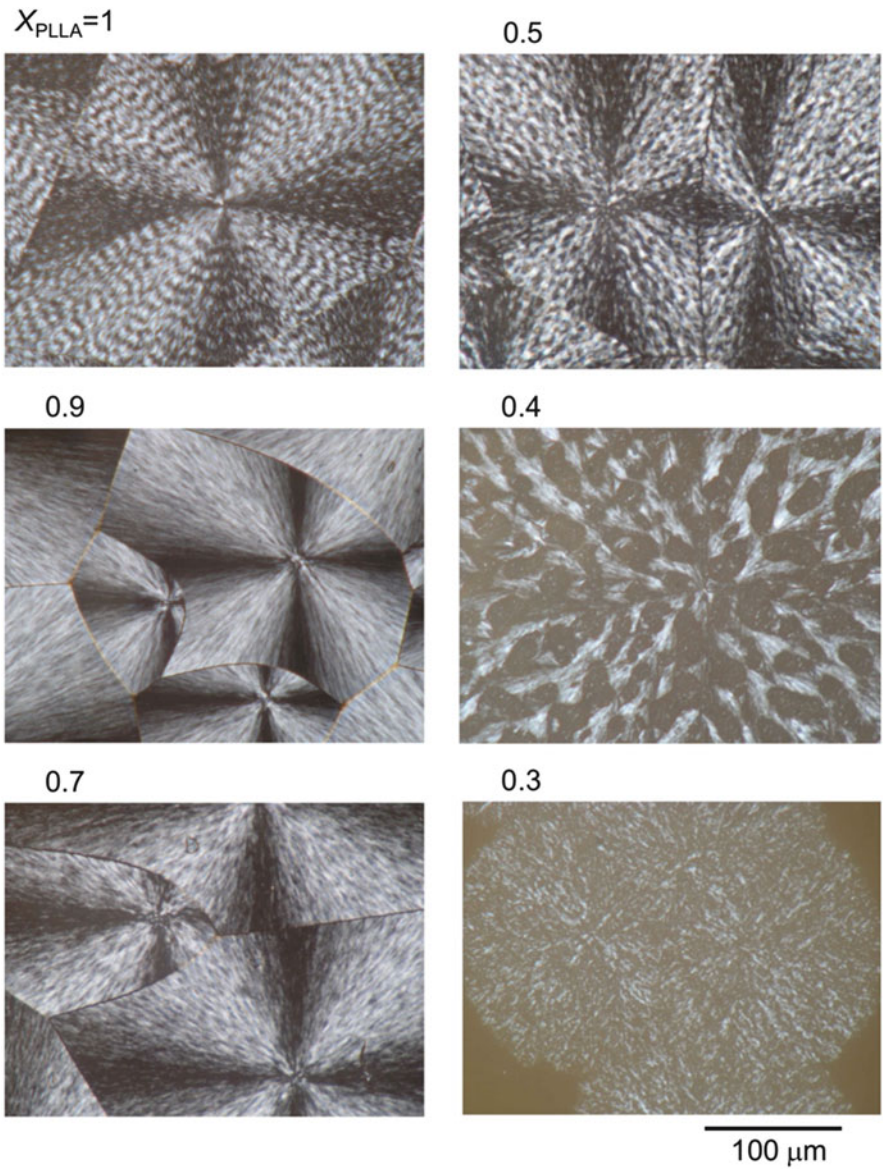

Fig. 37 Polarized photomicrographs of pure PLLA and PLLA/PDLLA blend films with different X_{PLLA} = PLLA/(PLLA + PDLLA) values crystallized isothermally at T_c = 130°C for 10 h from the melt [36] (with permission from Elsevier B.V.)

the PLLA/P(LLA-GA) (78/22) and PLLA/poly(L-lactide-*co*-D-lactide) (77/23) blend films decreased slowly and rapidly with decreasing X_{PLLA} [99]. Thus, the miscibility of PLLA with the crystallizable second polymer determines the dependence of G on X_{PLLA}.

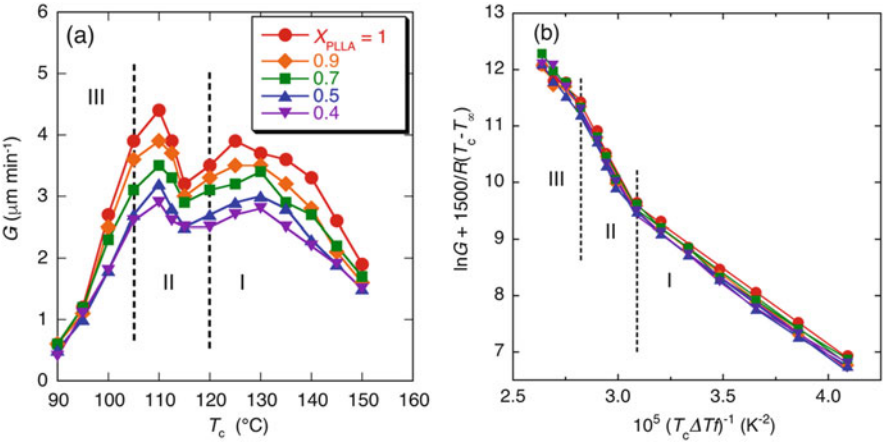

Fig. 38 Radial growth rate of spherulites (G) (**a**) and ln G + 1,500/R(T_c − T_∞) (**b**) of PLLA/PDLLA films with different contents of incorporated PDLLA as functions of crystallization temperature (T_c) and 1/($T_c\Delta Tf$), respectively [36] (with permission from Elsevier B.V.)

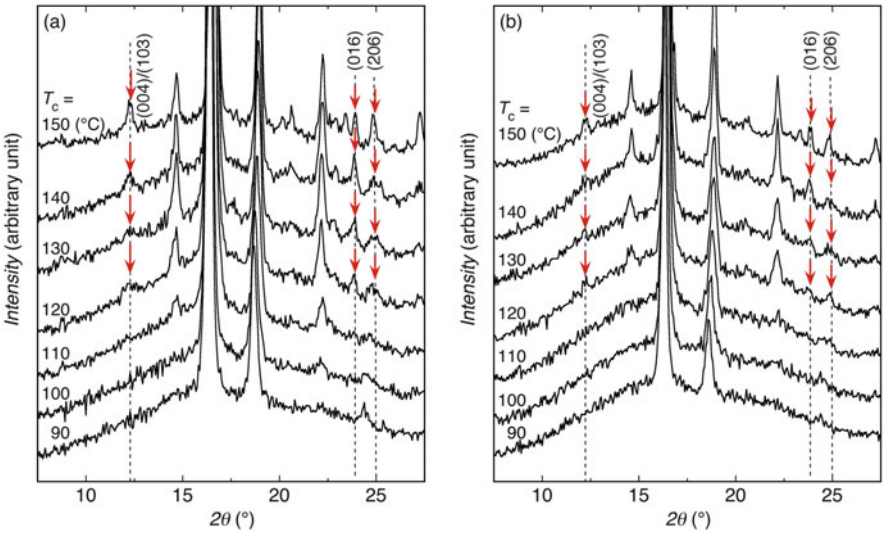

Fig. 39 WAXD profiles of neat PLLA ($X_{PLLA} = 1$) (**a**) and PLLA/PDLLA blend ($X_{PLLA} = 0.5$) (**b**) crystallized at different T_c values [36] (with permission from Elsevier B.V.). Red arrows indicate crystalline diffractions observed only for α-form

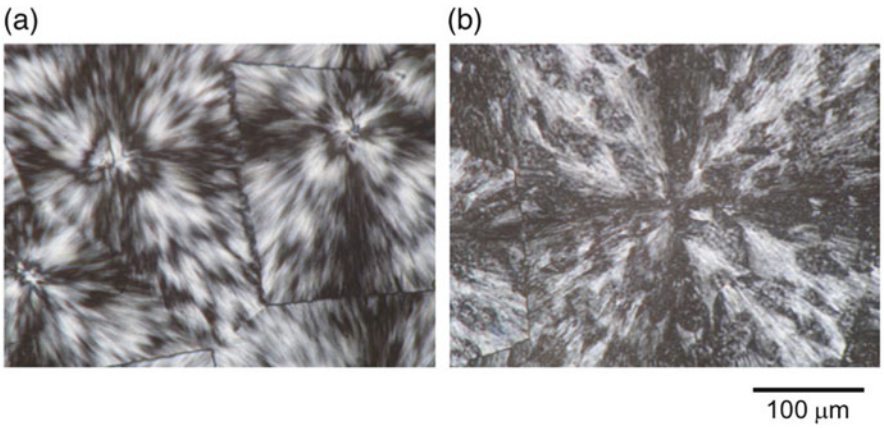

Fig. 40 Polarized photomicrographs of blends of PLLA with crystallizable P(LLA-GA) (78/22) and poly(L-lactide-*co*-D-lactide) (77/23) ($X_{PLLA} = 0.4$) crystallized isothermally at $T_c = 130°C$ for 10 h from the melt [99] (with permission from Wiley-VCH Verlag GmbH & Co.)

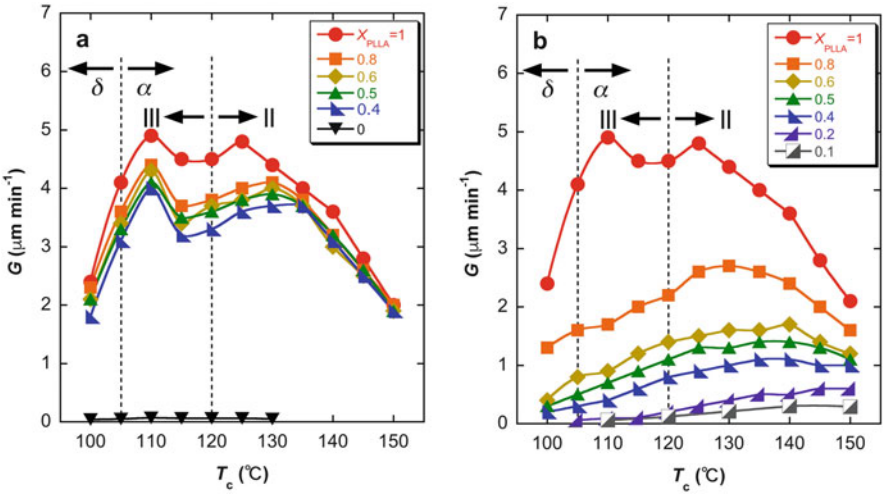

Fig. 41 Radial growth rate of spherulite (G) of neat PLLA, P(LLA-GA), and their blend films (**a**) and neat PLLA, P(LLA-DLA), and their blend films (**b**) as a function of crystallization temperature (T_c) [99] (with permission from Wiley-VCH Verlag GmbH & Co.). Transition temperatures from the α′-(δ-) to the α-form and from regime III to II are those reported for neat PLLA in [100]

5 Solution Crystallization

As shown in Table 1, type of solvent, polymer architecture and concentration, and crystallization temperature and time are main parameters to affect the crystallization behavior and formed higher-ordered structure of PLA. Fischer et al. investigated in

detail the formation of single crystals of PLLA and L-lactide-rich poly(L-lactide-*co*-D-lactide) in 0.1% dilute solutions in xylene at different T_c values from 49 to 102°C or degree of super cooling ΔT ($= T_m - T_c$) from 48 to 6°C [101]. It was found that L-lactide-rich poly(L-lactide-*co*-D-lactide) with the D-lactide unit contents of 0–13% could crystallize in the dilute solutions and DLA units were excluded from the crystalline regions of LLA units, i.e., the crystalline regions had lower D-lactide unit contents compared to those in the amorphous regions [101]. The degree of exclusion of D-lactide units became higher with increasing ΔT [101]. Such exclusion is different from the result for bulk crystallization, wherein the incorporation of DLA units (LLA units) in the crystalline regions of LLA units (DLA units) was observed [46, 51] (see section "Stereo Random Copolymerization"). The long period and crystalline thickness increased with increasing T_c, whereas with increasing D-lactide unit content, long period increased but crystalline thickness remained unchanged compared at the same T_c but long period remained unchanged but crystalline thickness decreased when compared at the same ΔT [101].

Kalb and Pennings observed lozenge-shaped and hexagonal single crystals with thicknesses of 10 and 12 nm when PLLA was crystallized at 0.08 wt% in toluene (55°C) and *p*-xylene (90°C) [102]. Also, Iwata and Doi prepared lozenge- and hexagonal-shaped α-form PLLA single crystals with reciprocal parameters of $a^* = 9.35$ Å, $b^* = 16.26$ Å, $\gamma = 90°$ in *p*-xylene (Fig. 42) [103, 104]. The latter single crystals have a pseudo-orthorhombic unit cell with cell parameters of $a = 10.34$ Å, $b = 5.97$ Å, and $\alpha = \beta = \gamma = 90°$.

Acetonitrile is frequently used for solution crystallization of PLA [105, 106], because especially crystalline PLLA or L-rich PLA were insoluble at an ambient temperature but soluble at around boiling temperature of acetonitrile (82°C). Miyata and Masuko reported that PLLA isothermally crystallized in α-form (orthorhombic, $a = 0.78$ Å, $b = 6.04$ Å, $c = 28.7$ Å, $\alpha = \beta = \gamma = 90°$) well-defined lozenge-shaped crystals (ca. 6 μm in the short direction and 13 μm in the long direction and thickness of 10–11 nm) with developed spiral dislocation growths at 25°C in dilute acetonitrile solutions (0.01 or 0.08 wt%) [106]. The crystal sizes in the short and long directions of PLLA crystals increased with increasing crystallization time [106].

6 Thermal Properties

T_g and melting temperature (T_m) are affected by molecular and higher-ordered structures and processing history including thermal history. Amorphous region includes mobile (free) amorphous and rigid (restrained or restricted) amorphous region. The difference in their hydrolyzability depends on the hydrolysis medium and conditions [107, 108]. To remove the effect of thermal history, the T_g values of LLA-based random copolymers estimated for melt-quenched samples are shown in Fig. 43a indicates that T_g values of two- and four-armed PLLAs are determined by total M_n (not M_n per each arm) and not affected by branching architecture. The T_g value (51.9°C) of high molecular weight one-armed random copolymer of D- and

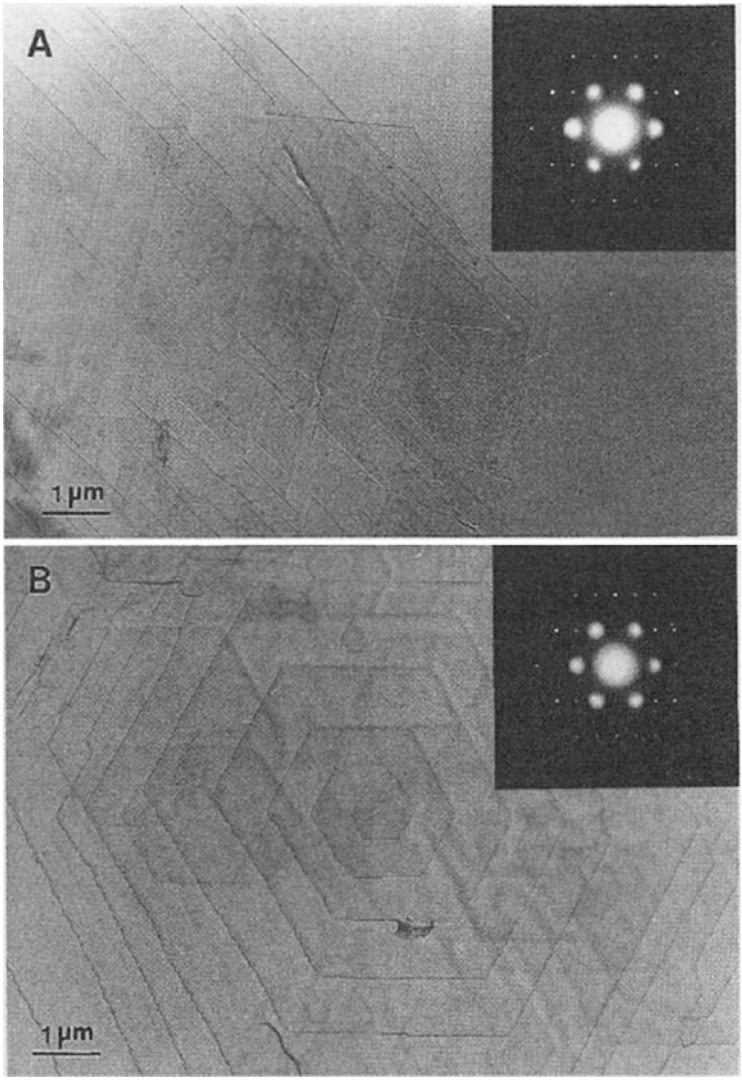

Fig. 42 Electron micrographs after shadowing with a Pt-Pd alloy of PLLA lamellar single crystals with screw dislocations grown from solution in *p*-xylene, and typical electron diffraction diagrams: lozenge-shaped (**a**) and hexagonal-shaped (**b**) single crystals [103] (with permission from American Chemical Society)

L-lactides (50/50), i.e., PDLLA ($M_n = 3.1 \times 10^5$ g mol^{-1}), was reported to be lower than that (57.9°C) of high molecular weight one-armed isotactic PLLA ($M_n = 2.9 \times 10^5$ g mol^{-1}) when samples were made amorphous by melt-quenching [36]. This result indicates that the disordered chain structure of PDLLA reduces the intersegmental interaction and increases the segmental mobility, resulting in a lower

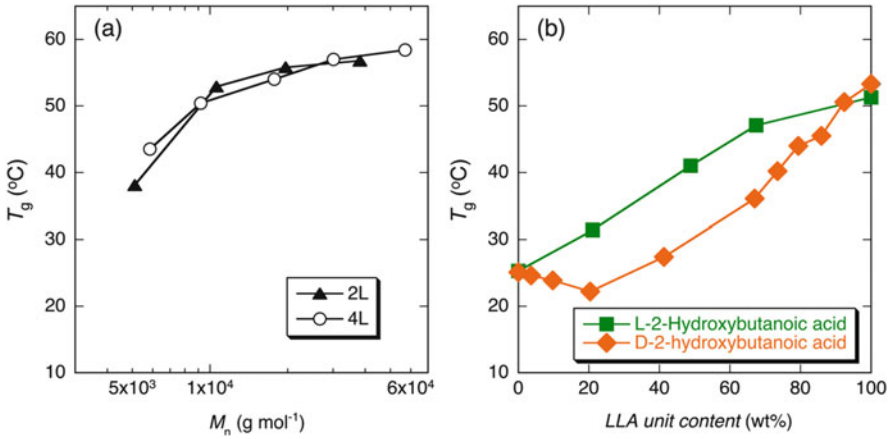

Fig. 43 T_g of melt-quenched two-armed and four-armed PLLAs (2-L and 4-L) (**a**) and L-lactic acid (LLA)-based copolymers (**b**) as a function of number-average molecular weight (M_n) and LLA unit content, respectively. The number-average molecular weight (M_n) values of LLA-based random copolymer are as follows: M_n = 1.3–1.4 × 10^4 g mol^{-1} (L-2-hydroxybutanoic acid) and M_n = 0.9–1.4 × 10^4 g mol^{-1} (D-2-hydroxybutanoic acid). The T_g data for 2-L and 4-L were reproduced from [81] and those for LLA-based random copolymers were reproduced from [75] (L-2-hydroxybutanoic acid) and [76] (D-2-hydroxybutanoic acid) (with permission from Elsevier B.V. and American Chemical Society)

T_g compared to that of PLLA. As seen in Fig. 43b, LLA-based random copolymers with L- or D-2-hydroxybutanoic acid decreased monotonically with a decrease in LLA unit content. However, interestingly, the T_g values of random LLA copolymers with L-hydroxybutanoic acid having the identical configuration with that of LLA were higher than that those with D-hydroxybutanoic acid having the opposite configuration with that of LLA.

The T_m values of melt-quenched two-armed and four-armed PLLA are shown in Fig. 44a. This means that crystalline regions which T_m values were observed were formed during DSC heating scanning. It is interesting to note that T_m values were determined by M_n per each arm not total M_n. For high molecular weight (HMW) PLLA, T_m varies depending on processing and crystallization conditions. As shown in Fig. 44b, the T_m values of as-cast HMW PLLA samples were not largely altered by further crystallization at 100–160°C which is lower than T_m of PLLA (cast-crystallized samples), whereas T_m depends on crystallization temperature (T_c) when crystallization is performed after melting (melt-crystallized and melt-quenched-crystallized samples). The lower temperature T_m values observed in the range of 140–155°C for melt-crystallized and melt-quenched-crystallized samples crystallized at T_c = 100–110°C are ascribed to δ-(α′-)form crystallites, whereas higher temperature T_m values observed in the range of 175–195°C are attributed to α-form crystallites. As in many random copolymers, T_m values of LLA-based random copolymers decreased monotonically with decreasing LLA unit content, irrespective of the type of comonomer units (Fig. 44c).

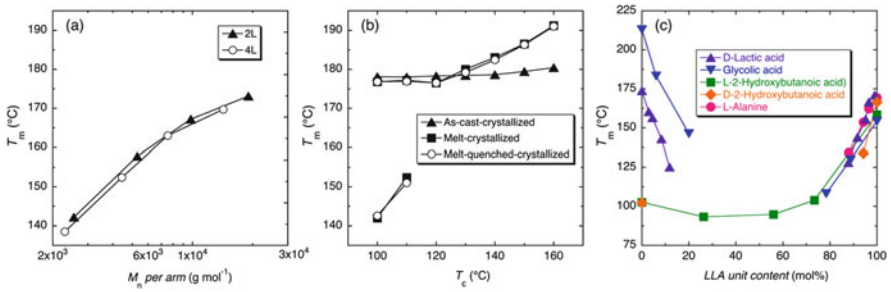

Fig. 44 T_m of melt-quenched 2-aremd and 4-aremd PLLAs (2-L and 4-L, respectively) (**a**), as-cast-crystallized, melt-crystallized, and melt-quenched-crystallized PLLA ($M_n = 6.1$ g mol^{-1}) (**b**), melt-(quenched-)crystallized L-lactic acid (LLA)-based random copolymers (**c**), as a function of M_n per arm or LLA unit content, T_c, and LLA unit content, respectively. The number-average molecular weight (M_n) and crystallization conditions of LLA-based random copolymer are as follows: $M_n = 0.5$–3.0×10^4, melted at 250°C for 1 min and crystallized at 100°C for 1,000 min (D-lactic acid), $M_n = 0.9$–6.4×10^3, melted at 230°C for 3 min and crystallized at 80°C for 24 h (glycolic acid), $M_n = 1.3$–1.4×10^4, melted at 200°C for 3 min and crystallized at 70°C for 5 h (L-2-hydroxybutanoic acid), $M_n = 0.9$–1.4×10^4, melted at 190°C for 3 min, quenched at 0°C for 5 min, and crystallized at 70°C for 24 h (D-2-hydroxybutanoic acid), and $M_n = 1.2$–1.7×10^4, 250°C for 100 s and crystallized at 100°C for 1 h (L-alanine). The T_m data for 2-L and 4-L were reproduced from [81] and those for high molecular weight PLLA were reproduced form [16], whereas T_m data for LLA-based copolymers were reproduced from [44] (D-lactic acid), [74] (glycolic acid), [75] (L-2-hydroxybutanoic acid), [76] (D-2-hydroxybutanoic acid), and [80] (L-alanine) (with permission from Wiley-VCH Verlag GmbH & Co., Springer Nature, Elsevier B.V., American Chemical Society, and The Royal Society of Chemistry)

7 Conclusions

The quiescent homo-crystallization and the formed higher-ordered structures of PLA and its copolymers-based materials, which affect their physical and biochemical properties and biodegradation behavior, depend on the polymer architecture and additives, crystallization methods, and conditions. Therefore, the physical and biochemical properties and biodegradation behavior of PLA and its copolymers-based materials required for each application can be controlled by these parameters.

References

1. Auras R, Lim L-T, Selke SEM, Tsuji H (eds) (2010) Poly(lactic acid): synthesis, structures, properties, processing, and applications. Wiley series on polymer engineering and technology. Wiley, Hoboken
2. Tsuji H (2002) Polylactides. In: Doi Y, Steinbuchel A (eds) Polyesters 3 (biopolymers), vol 4, chap 5. Wiley, Weinheim, pp 129–177
3. Tsuji H (2014) Poly(lactic acid). In: Kabasci S (ed) Bio-based plastics: materials and applications, chap 8. Wiley, Hoboken, pp 171–239

4. Slager J, Domb AJ (2003) Biopolymer stereocomplexes. Adv Drug Deliv Rev 55:549–583
5. Tsuji H (2005) Poly(lactide) stereocomplexes: formation, structure, properties, degradation, and applications. Macromol Biosci 5:569–597
6. Fukushima K, Kimura Y (2006) Stereocomplexed polylactides (Neo-PLA) as high-performance bio-based polymers: their formation, properties, and application. Polym Int 55:626–642
7. Pan P, Inoue Y (2009) Polymorphism and isomorphism in biodegradable polyesters. Prog Polym Sci 34:605–640
8. Saravanan M, Domb AJ (2013) A contemporary review on – polymer stereocomplexes and its biomedical application. Eur J Nanomed 5:81–86
9. Jing Y, Quan C, Jiang Q, Zhang C, Chao Z (2016) A mini-review on the study of functional biomaterials based on poly(lactic acid) stereocomplex. Polym Rev 56:262–286
10. Tsuji H (2016) Poly(lactic acid) stereocomplexes: a progress of decade. Adv Drug Deliv Rev 107:97–135
11. Tan BH, Muiruri JK, Li Z, He C (2016) Recent progress in using stereocomplexation for enhancement of thermal and mechanical property of polylactide. ACS Sustain Chem Eng 4:5370–5391
12. Fambri L, Migliaresi C (2010) Crystallization and thermal properties. In: Auras R, Lim L-T, Selke SEM, Tsuji H (eds) Poly(lactic acid): synthesis, structures, properties, processing, and applications. Wiley series on polymer engineering and technology, chap 9. Wiley, Hoboken, pp 113–124
13. Saeidlou S, Huneault MA, Li H, Park CB (2012) Poly(lactic acid) crystallization. Prog Polym Sci 37:1657–1677
14. Androsch R, Schick C, Di Lorenzo ML (2018) Kinetics of nucleation and growth of crystals of poly(L-lactic acid). In: Di Lorenzo ML, Androsch R (eds) Synthesis, structure and properties of poly(lactic acid). Advances in polymer science book series (Polymer, vol 279). Springer, New York, pp 235–272
15. Lotz B (2018) Crystal polymorphism and morphology of polylactides. In: Di Lorenzo ML, Androsch R (eds) Synthesis, structure and properties of poly(lactic acid). Advances in polymer science book series (Polymer, vol 279). Springer, New York, pp 273–302
16. Tsuji H, Ikada Y (1995) Properties and morphologies of poly(L-lactide): 1. Annealing condition effects on properties and morphologies of poly(L-lactide). Polymer 36:2709–2716
17. Cai H, Dave V, Gross RA, McCarthy SP (1996) Effects of physical aging, crystallinity, and orientation on the enzymatic degradation of poly(lactic acid). J Polym Sci B Polym Phys 34:2701–2708
18. Pan P, Zhu B, Inoue Y (2007) Enthalpy relaxation and embrittlement of poly(L-lactide) during physical aging. Macromolecules 40:9664–9671
19. Pan P, Liang Z, Zhu B, Dong T, Inoue Y (2008) Roles of physical aging on crystallization kinetics and induction period of poly(L-lactide). Macromolecules 41:8011–8019
20. Tsuji H, Sawada M (2010) Accelerated crystallization of poly(L-lactide) by physical aging. J Appl Polym Sci 116:1190–1196
21. Androsch R, Di Lorenzo ML (2013) Crystal nucleation in glassy poly(L-lactic acid). Macromolecules 46:6048–6056
22. Androsch R, Di Lorenzo ML (2013) Kinetics of crystal nucleation of poly(L-lactic acid). Polymer 54:6882–6885
23. Androsch R, Di Lorenzo ML, Schick C (2018) Optical microscopy to study crystal nucleation in polymers using a fast scanning chip calorimeter for precise control of the nucleation pathway. Macromol Chem Phys 219:1700479
24. Tsuji H, Tezuka Y, Saha SK, Suzuki M, Itsuno S (2005) Spherulite growth of L-lactide copolymers: effects of tacticity and comonomers. Polymer 46:4917–4927
25. Tsuji H, Miyase T, Tezuka Y, Saha SK (2005) Physical properties, crystallization, and spherulite growth of linear and 3-arm poly(L-lactide)s. Biomacromolecules 6:244–254

26. Vasanthakumari R, Pennings AJ (1983) Crystallization kinetics of poly(L-lactic acid). Polymer 24:175–178
27. Miyata T, Masuko T (1998) Crystallization behaviour of poly(L-lactide). Polymer 39:5515–5521
28. Hoffman JD, Davis GT, Lauritzen Jr JI (1976) The rate of crystallization of linear polymers with chain folding. In: Hannay NB (ed) Treatise on solid state chemistry. Crystalline and noncrystalline solids, vol 3, chap 7. Plenum Press, New York, pp 497–614
29. Hoffman JD, Frolen LJ, Ross GS, Lauritzen Jr JI (1975) On the growth rate of spherulites and axialites from the melt in polyethylene fractions: regime I and regime II crystallization. J Res Nat Bur Std A Phys Chem 79A:671–699
30. Di Lorenzo ML (2001) Determination of spherulite growth rates of poly(L-lactic acid) using combined isothermal and non-isothermal procedures. Polymer 42:9441–9446
31. Di Lorenzo ML (2005) Crystallization behavior of poly(L-lactic acid). Eur Polym J 41:569–575
32. Abe H, Kikkawa Y, Inoue Y, Doi Y (2001) Morphological and kinetic analyses of regime transition for poly[(s)-lactide] crystal growth. Biomacromolecules 2:1007–1014
33. Pan P, Kai W, Zhu B, Dong T, Inoue Y (2007) Polymorphous crystallization and multiple melting behavior of poly(L-lactide): molecular weight dependence. Macromolecules 40:6898–6905
34. Kawai T, Rahma N, Matsuba G, Nishida K, Kanaya T, Nakano M, Okamoto H, Kawada J, Usuki A, Honma N, Nakajima K, Matsuda M (2007) Crystallization and melting behavior of poly (L-lactic acid). Macromolecules 40:9463–9469
35. Pan P, Zhu B, Kai W, Dong T, Inoue Y (2008) Effect of crystallization temperature on crystal modifications and crystallization kinetics of poly(L-lactide). J Appl Polym Sci 107:54–62
36. Bouapao L, Tsuji H, Tashiro K, Zhang J, Hanesaka M (2009) Crystallization, spherulite growth, and structure of blends of crystalline and amorphous poly(lactide)s. Polymer 50:4007–4017
37. Androsch R, Di Lorenzo ML, Schick C (2017) Effect of molar mass on enthalpy relaxation and crystal nucleation of poly(L-lactic acid). Eur Polym J 96:361–369
38. Tsuji H, Sugiura Y, Sakamoto Y, Bouapao L, Itsuno S (2008) Crystallization behavior of linear 1-arm and 2-arm poly(L-lactide)s: effects of coinitiators. Polymer 49:1385–1397
39. Báez JE, Marcos-Fernández A, Galindo-Iranzo P (2011) Exploring the effect of alkyl end group on poly(L-lactide) oligo-esters. Synthesis and characterization. J Polym Res 18:1137–1146
40. Tsuji H, Sugimoto S (2014) Long terminal linear alkyl group as internal crystallization accelerating moiety of poly(L-lactide). Polymer 55:4786–4798
41. Brzeziński M, Biela T (2015) Supramolecular polylactides by the cooperative interaction of the end groups and stereocomplexation. Macromolecules 48:2994–3004
42. Bao J, Chang X, Xie Q, Yu C, Shan G, Bao Y, Pan P (2017) Preferential formation of β-form crystals and temperature-dependent polymorphic structure in supramolecular poly(l-lactic acid) bonded by multiple hydrogen bonds. Macromolecules 50:8619–8630
43. Bao J, Chang R, Shan G, Bao Y, Pan P (2016) Promoted stereocomplex crystallization in supramolecular stereoblock copolymers of enantiomeric poly(lactic acid)s. Cryst Growth Des 16:1502–1511
44. Tsuji H, Ikada Y (1996) Crystallization from the melt of poly(lactide)s with different optical purities and their blends. Macromol Chem Phys 197:3483–3499
45. Huang J, Lisowski MS, Runt J, Hall ES, Kean RT, Buehler N, Lin JS (1998) Crystallization and microstructure of poly(L-lactide-co-meso-lactide) copolymers. Macromolecules 31:2593–2599
46. Baratian S, Hall ES, Lin JS, Xu R, Runt J (2001) Crystallization and solid-state structure of random polylactide copolymers: poly(L-lactide-co-D-lactide)s. Macromolecules 34:4857–4864

47. Di Lorenzo ML, Rubino P, Luijkx R, Hélou M (2014) Influence of chain structure on crystal polymorphism of poly(lactic acid). Part 1: effect of optical purity of the monomer. Colloid Polym Sci 292:399–409
48. Kolstad JJ (1996) Crystallization kinetics of poly(L-lactide-co-meso-lactide). J Appl Polym Sci 62:1079–1091
49. Androsch R, Di Lorenzo ML, Schick C (2016) Crystal nucleation in random L/D-lactide copolymers. Eur Polym J 75:474–485
50. Yasuniwa M, Tsubakihara S, Iura K, Ono Y, Dan Y, Takahashi K (2006) Crystallization behavior of poly(L-lactic acid). Polymer 47:7554–7563
51. Di Lorenzo ML, Androsch R (2016) Stability and reorganization of α-crystals in random L/D-lactide copolymers. Macromol Chem Phys 217:1534–1538
52. Song P, Sang L, Jin C, Wei Z (2018) Temperature-dependent polymorphic crystallization of poly(L-lactide)s on the basis of optical purity and microstructure. Polymer 134:163–174
53. Zell MT, Padden BE, Paterick AJ, Hillmyer MA, Kean RT, Thakur KAM, Munson EJ (1998) Direct observation of stereodefect sites in semicrystalline poly(lactide) using ^{13}C solid-state NMR. J Am Chem Soc 120:12672–12673
54. Androsch R, Schick C (2016) Interplay between the relaxation of the glass of random L/D-lactide copolymers and homogeneous crystal nucleation: evidence for segregation of chain defects. J Phys Chem B 120:4522–4528
55. Ovitt TM, Coates GW (1999) Stereoselective ring-opening polymerization of meso-lactide: synthesis of syndiotactic poly(lactic acid). J Am Chem Soc 121:4072–4073
56. Ovitt TM, Coates GW (2002) Stereochemistry of lactide polymerization with chiral catalysts: new opportunities for stereocontrol using polymer exchange mechanisms. J Am Chem Soc 124:1316–1326
57. Kapelski A, Okuda J (2013) Ring-opening polymerization of rac- and meso-lactide initiated by indium bis(phenolate) isopropoxy complexes. J Polym Sci A Polym Chem 51:4983–4499
58. Stayshich RM, Meyer TY (2010) New insights into poly(lactic-co-glycolic acid) microstructure: using repeating sequence copolymers to decipher complex NMR and thermal behavior. Am Chem Soc 132:10920–10934
59. Stayshich RM, Meyer TY (2008) Preparation and microstructural analysis of poly(lactic-alt-glycolic acid). J Polym Sci A Polym Chem 46:4704–4711
60. Tsuji H, Arakawa Y (2018) Synthesis, properties, and crystallization of the alternating stereocopolymer poly(L-lactic acid-alt-D-lactic acid) [syndiotactic poly(lactic acid)] and its blend with isotactic poly(lactic acid). Polym Chem 9:2446–2457
61. Tsuji H, Matsumura N, Arakawa Y (2016) Stereocomplex crystallization and homocrystallization of star-shaped four-armed stereo diblock poly(lactide)s with different L-lactyl unit contents: isothermal crystallization from the melt. J Phys Chem B 120:1183–1193
62. Tsuji H, Hyon S-H, Ikada Y (1993) Stereocomplex formation between enantiomeric poly (lactic acids). 9. Stereocomplexation from the melt. Macromolecules 26:6918–6926
63. Li L, Zhong Z, De Jeu WH, Dijkstra PJ, Feijen J (2004) Crystal structure and morphology of poly(L-lactide-*b*-D-lactide) diblock copolymers. Macromolecules 37:8641–8646
64. Han L, Shan G, Bao Y, Pan P (2015) Exclusive stereocomplex crystallization of linear and multiarm star-shaped high-molecular-weight stereo diblock poly(lactic acid)s. J Phys Chem B 119:14270–14279
65. Tsuji H, Tajima T (2015) Non-isothermal crystallization behavior of stereo diblock polylactides with relatively short poly(D-lactide) segments from the melt. Polym Int 64:54–65
66. Tsuji H, Tajima T (2014) Crystallization behavior of stereo diblock poly(lactide)s with relatively short poly(D-lactide) segment from partially melted state. Macromol Mater Eng 299:1089–1105
67. Jain RA (2000) The manufacturing techniques of various drug loaded biodegradable poly (lactide-co-glycolide) (PLGA) devices. Biomaterials 21:2475–2490
68. Södergård A, Stolt M (2002) Properties of lactic acid based polymers and their correlation with composition. Prog Polym Sci 27:1123–1163

69. Panyam J, Labhasetwar V (2003) Biodegradable nanoparticles for drug and gene delivery to cells and tissue. Adv Drug Deliv Rev 55:329–347
70. Danhier F, Ansorena E, Silva JM, Coco R, Le Breton A, Préat V (2012) PLGA-based nanoparticles: an overview of biomedical applications. J Control Release 161:505–522
71. Gilding K, Reed AM (1979) Biodegradable polymers for use in surgery-polyglycolic/poly (lactic acid) homo- and copolymers: 1. Polymer 20:1459–1464
72. Tsuji H, Ikada Y (1994) Stereocomplex formation between enantiomeric poly(lactic acid)s. X. Binary blends from poly(D-lactide-co-glycolide) and poly(L-lactide-co-glycolide). J Appl Polym Sci 53:1061–1071
73. Wang Z-Y, Zhao Y-M, Wang F, Wang J (2006) Syntheses of poly(lactic acid-co-glycolic acid) serial biodegradable polymer materials via direct melt polycondensation and their characterization. J Appl Polym Sci 99:244–252
74. Tsuji H, Kikkawa K, Arakawa Y (2018) Cocrystallization of monomer units of biobased and biodegradable poly(L-lactic acid-co-glycolic acid) random copolymers. Polym J 50: 1079–1088. https://doi.org/10.1038/s41428-018-0093-z
75. Tsuji H, Sobue T (2015) Cocrystallization of monomer units in lactic acid-based biodegradable copolymers, poly(L-lactic acid-co-L-2-hydroxybutanoic acid)s. Polymer 72:202–211
76. Tsuji H, Noda S, Arakawa Y, Tadashi Sobue T (2018) Strong disturbance effect of comonomer units with opposite configuration on crystallization of optically active monomer-based random copolymers. Cryst Growth Des 18:6155–6164
77. Pérez-Camargo RA, Arandia I, Safari M, Cavallo D, Lotti N, Soccio M, Müller AJ (2018) Crystallization of isodimorphic aliphatic random copolyesters: pseudo-eutectic behavior and double-crystalline materials. Eur Polym J 101:233–247
78. Kabe T, Matsumoto K, Terai S, Hikima T, Takata M, Miyake M, Taguchi S, Iwata T (2016) Co-crystallization phenomena in biosynthesized isotactic poly[(R)-lactate-co-(R)-2-hydroxybutyrate]s with various lactate unit ratios. Polym Degrad Stab 132:137–144
79. Marubayashi H, Asai S, Hikima T, Takata M, Iwata T (2013) Biobased copolymers composed of L-lactic acid and side-chain-substituted lactic acids: synthesis, properties, and solid-state structure. Macromol Chem Phys 214:2546–2561
80. Tsuji H, Sato S, Masaki N, Arakawa Y, Kuzuya A, Ohya Y (2018) Synthesis, stereocomplex crystallization and homo-crystallization of enantiomeric poly(lactic acid-co-alanine)s with ester and amide linkages. Polym Chem 9:565–575
81. Sakamoto Y, Tsuji H (2015) Crystallization behavior and physical properties of linear 2-arm and branched 4-arm poly(L-lactide)s: effects of branching. Polymer 54:2422–2434
82. Schmidt SC, Hillmyer MA (2001) Polylactide stereocomplex crystallites as nucleating agents for isotactic polylactide. J Polym Sci B Polym Phys 39:300–313
83. Yamane H, Sasai K (2003) Effect of the addition of poly(D-lactic acid) on the thermal property of poly(L-lactic acid). Polymer 44:2569–2575
84. Tsuji H, Takai H, Saha SK (2006) Isothermal and non-isothermal crystallization behavior of poly(L-lactic acid): effects of stereocomplex as nucleating agent. Polymer 47:3826–3837
85. Rahman N, Kawai T, Matsuba G, Nishida K, Kanaya T, Watanabe H, Okamoto H, Kato M, Usuki A, Matsuda M, Nakajima K, Honma N (2009) Effect of polylactide stereocomplex on the crystallization behavior of poly(L-lactic acid). Macromolecules 42:4739–4745
86. Narita J, Katagiri M, Tsuji H (2011) Highly enhanced nucleating effect of melt-recrystallized stereocomplex crystallites on poly(L-lactic acid) crystallization. Macromol Mater Eng 296:887–893
87. Narita J, Katagiri M, Tsuji H (2013) Highly enhanced accelerating effect of melt-recrystallized stereocomplex crystallites on poly(L-lactic acid) crystallization, 2-effects of poly(D-lactic acid) concentration. Macromol Mater Eng 298:270–282
88. Tsuji H, Ozawa R, Matsumura N (2016) Effect of incorporated star-shaped four-armed stereo diblock poly(lactide) on the crystallization behavior of linear one-armed poly(L-lactide) or poly(D-lactide). Polym J 48:209–213

89. Tsuji H, Yamamoto S, Okumura A (2011) Homo- and hetero-stereocomplexes of substituted poly(lactide)s as promising biodegradable crystallization-accelerating agents of poly(L-lactide). J Appl Polym Sci 122:321–333
90. Tsuji H, Hosokawa M, Sakamoto Y (2012). ACS Macro Lett 1:687–691
91. Bai H, Zhang W, Deng H, Zhang Q, Zu Q (2011) Control of crystal morphology in poly(L-lactide) by adding nucleating agent. Macromolecules 44:1233–1237
92. Xing Q, Wang Z, Li R, Dong X, Wang D (2016) Effect of solubility of a hydrazide compound on the crystallization behavior of poly(L-lactide). RSC Adv 6:113377–113389
93. Ma P, Xu Y, Shen T, Dong W, Chen M, Lemstra PJ (2015) Tailoring the crystallization behavior of poly(L-lactide) with self-assembly-type oxalamide compounds as nucleators:1. Effect of terminal configuration of the nucleators. Eur Polym J 70:400–411
94. Tsuji H, Sawada M, Bouapao L (2009) Biodegradable polyesters as crystallization-accelerating agents of poly(L-lactide). ACS Appl Mater Interfaces 1:1719–1730
95. Tsuji H, Tashiro K, Bouapao NJ (2008) Polyglycolide as a biodegradable nucleating agent for poly(L-lactide). Macromol Mater Eng 293:947–951
96. Tsuji H, Ikada Y (1995) Blends of isotactic and atactic poly(lactide). I. Effects of mixing ratio of isomers on crystallization of blends from melt. J Appl Polym Sci 58:1793–1802
97. Tsuji H, Ikada Y (1996) Blends of isotactic and atactic poly(lactide)s: 2. Molecular-weight effects of atactic component on crystallization and morphology of equimolar blends from the melt. Polymer 37:595–602
98. Pan P, Liang Z, Zhu B, Dong T, Inoue Y (2009) Blending effects on polymorphic crystallization of poly(L-lactide). Macromolecules 42:3374–3380
99. Tsuji H, Tashiro K, Bouapao L, Hanesaka M (2012) Separate crystallization and cocrystallization of poly(L-lactide) in the presence of L-lactide-based copolymers with low crystallizability, poly(L-lactide-co-glycolide) and poly(L-lactide-co- D-lactide). Macromol Chem Phys 213:2099–2112
100. Tsuji H, Tashiro K, Bouapao L, Hanesaka M (2012) Synchronous and separate homocrystallization of enantiomeric poly(L-lactic acid)/poly(D-lactic acid) blends. Polymer 53:747–754
101. Fischer EW, Sterzel HJ, Wegner G (1973) Investigation of the structure of solution grown crystals of lactide copolymers by means of chemical reactions. Kolloid Z Z Polym 251:980–990
102. Kalb B, Pennings AJ (1980) General crystallization behaviour of poly(L-lactic acid). Polymer 21:607–612
103. Iwata T, Doi Y (1998) Morphology and enzymatic degradation of poly(L-lactic acid) single crystals. Macromolecules 31:2461–2467
104. Iwata T, Doi Y (1999) Crystal structure and biodegradation of aliphatic polyester crystals. Macromol Chem Phys 200:2429–2442
105. Tsuji H, Hyon S-H, Ikada Y (1992) Stereocomplex formation between enantiomeric poly (lactic acids). 5. Calorimetric and morphological studies on the stereocomplex formed in acetonitrile solution. Macromolecules 25:2940–2946
106. Miyata T, Masuko T (1997) Morphology of poly(L-lactide) solution-grown crystals. Polymer 38:4003–4009
107. Tsuji H, Miyauchi S (2001) Poly(L-lactide): 7. Enzymatic hydrolysis of free and restricted amorphous regions in poly(L-lactide) films with different crystallinities and a fixed crystalline thickness. Polymer 42:4463–4467
108. Tsuji H, Tezuka Y, Yamada K (2005) Alkaline and enzymatic degradation of L-lactide copolymers. II. Crystallized films of poly(L-lactide-co-D-lactide) and poly(L-lactide) with similar crystallinities. J Polym Sci B Polym Phys 43:1064–1075

Adv Polym Sci (2019) 283: 87–118
https://doi.org/10.1007/12_2019_49

Published online: 16 October 2019

Poly(Lactic Acid): Flow-Induced Crystallization

Alicyn Rhoades and Roberto Pantani

Contents

1 Introduction 88
2 Generalities on PLA Crystallization 89
2.1 Quiescent Growth Rate 90
2.2 Quiescent Nucleation 90
2.3 Stereocomplex Crystallization 91
3 Generalities on Flow-Induced Crystallization 93
4 Methods for Assessing 95
5 Flow-Induced Crystallization of PLA 95
6 Effect of FIC on Nucleation Rate 96
7 Non-isothermal FIC 99
7.1 Conditions to Create Shish-Kebab Microstructure 100
7.2 Crystallization Under Continuous Shear 101
8 Flow-Induced Crystallization of Stereocomplex PLA 101
9 Effects of Molecular Weight and Chain Branching 103
10 Effects of Fillers and Nucleating Agents 103
11 FIC in PLA Processing 105
11.1 Injection Molding and Related Processes 106
11.2 Foam Injection Molding 109
11.3 Extrusion Casting 109
11.4 Melt Spinning 110
11.5 Additive/Fused Filament Deposition Modeling 110
12 Conclusions 111
References 112

A. Rhoades (✉)
Department of Plastics Engineering Technology, Penn State Erie, The Behrend College, Erie, PA, USA
e-mail: alicyn@psu.edu

R. Pantani
Department of Industrial Engineering, University of Salerno, Fisciano, SA, Italy
e-mail: rpantani@unisa.it

Abstract Poly(lactic acid) is surely one of the most interesting commercially available biodegradable polymers. Being a slowly crystallizing material, it generally does not have the time to crystallize at the cooling rates involved in the common processing techniques. However, the properties induced by crystallinity are extremely interesting for tuning the characteristics of the obtained parts, and this leads the research to find the routes to an enhancement of PLA crystallization kinetics. During processing, polymer melts are subjected to very high deformation rates, and the stretch resulting from this orientation gives rise to shorter crystallization times and also to peculiar crystalline structures. The so-called flow-induced crystallization is therefore a phenomenon that for PLA can be considered strategic toward the realization of parts with enhanced properties. In this work, a state of the art on flow-induced crystallization of PLA is presented.

Keywords Cylindrites · Morphology · PLA · Processing · Shish-kebab

Nomenclature

E	Tensile modulus
ΔG_f	Energy barrier for flow-induced crystallization
ΔG_q	Quiescent nucleation energy barrier
ΔS_f	Degree of entropy reduction by shear
G	Growth rate
k_a	Avrami kinetic constant
N	Nucleation density
n_a	Avrami exponent
$t_{1/2}$	Half crystallization time
X	Absolute crystallinity degree
$\dot{\gamma}$	Shear rate
ε	Ultimate strain
ξ	Relative crystallinity degree
ρ	Density
σ	Tensile strength

1 Introduction

Poly(lactic acid) (PLA) is presently the most successful commercial bio-based thermoplastic, boasting applications that range from food packaging to medical implants. PLA is also the most commonly used polymer in fused filament modeling style of additive manufacturing. PLA is both *bio-renewable*, meaning the raw materials used to produce the polymer are from nonpetroleum (plant) sources, and

biodegradable, meaning the polymer will decompose relatively quickly into lactic acid when subject to heat, moisture, and basic conditions. The mechanical and degradation properties of PLA are direct functions of the polymer microstructure. Microstructure, in turn, is a function of the polymer backbone chemistry (isomer content and chain branching) as well as molecular weight and molecular weight distribution. However, polymer microstructure is also strongly influenced by the melt flow incurred during polymer processing. Developing ideal mechanical and degradation property profiles in a manufactured part therefore requires a comprehensive understanding of PLA chemistry and melt crystallization kinetics under flow, much of which is still under development in the research community. For example, the idealized PLA microstructure to optimize mechanical tensile strength (oriented crystal microstructure) is obviously different than that which would result in the toughest PLA sample (semicrystalline content with idealized free volume), but the current state of the art cannot yet dial in conditions to produce such microstructure with a high level of certainty. Neither are the processing methods broadly optimized to control microstructure due to the competing degradation and the slow crystallization processes of PLA. Nonetheless, rapid progress is being made on many fronts. This chapter aims to provide the reader with a summary of the current understanding of flow-induced crystallization (FIC) as it is observed and quantified for PLA and also review the polymer processing techniques that potentially induce FIC in PLA.

2 Generalities on PLA Crystallization

Lactic acid has an asymmetric carbon atom, which leads to two optically different active forms, L-lactic acid and D-lactic acid. The polymers coming from pure L- or pure D-forms are referred to as PLLA and PDLA, respectively. Commercially, the homopolymer in L-form or L-form-rich copolymers is the most important. The abbreviation PLLA is commonly adopted also for L-form-rich copolymers. This review focuses on PLLA, which is a crystallizable polymer with a maximum crystallinity of 60–70% in the case of the homopolymer [1]. The quiescent crystallization kinetics of PLLA is slow, with halftimes of the order of minutes [2]. PLLA is polymorphic: under quiescent conditions, when crystallized above 120°C, the material presents the *α-phase*, whereas the *α′-phase* develops at temperatures lower than about 100°C [3]. Both phases can develop between 100 and 120°C. The α′-crystals are less ordered, stable at the temperatures at which they form, but able to transform into the more stable α-crystals upon heating at about 150°C. Other crystalline phases are found in PLLA: the β-form, which develops when the α-phase is stretched at elevated temperatures [4], and the γ-form, which is generated by epitaxial crystallization [5]. PLLA and PDLA can co-crystallize together and form a stereocomplex which presents a melting point about 50°C higher than that of PLLA homocrystal.

PLLA is a slowly crystallizing polymer, with the fastest crystallization rate at about 110°C [1, 6, 7]. The crystallization halftime increases on increasing the

molecular weight and the D-lactide content. For the homopolymer, molecular weights of about 100 kDa allow a maximum crystallization halftime of the order of 1 min. Commercial PLLA grades, with D-lactide contents of about 2%, have crystallization times about one order of magnitude larger [8, 9]. This slow crystallization kinetics makes the material unable to crystallize at the cooling rates involved in normal processing conditions. However, significant crystal microstructure is sometimes found in injection-molded parts [10], thus suggesting that flow can significantly influence the phenomenon of crystallization, as better explained below in this chapter.

The overall crystallization kinetics of PLA is composed of two independent phenomena: crystal nucleation and subsequent crystal growth.

2.1 Quiescent Growth Rate

In quiescent, isothermal conditions, PLA crystalline structures grow spherically with a constant growth rate, G. This is confirmed when the evolution of crystallinity under quiescent conditions is analyzed by Avrami's model:

$$\xi(T,t) = 1 - \exp[-(k_a(T)\ t)^{n_a}] \tag{1}$$

in which ξ is the relative crystallinity degree, k_a is the Avrami constant, and n_a is the Avrami exponent; this latter takes a value close to 3 (describing predetermined, spherical growth) independently on the molecular weight and on the D-lactide content [2, 11].

The direct measurements of growth rate by polarized optical microscopy (POM) reveal that this phenomenon depends on the molecular weight and on the D-lactide content [1]. In particular, a higher content of D-lactide and a higher molar mass decrease the spherulitic growth rate [7].

The maximum growth rate for PLLA spherulites is reported as about 30 μm/min [12] at 110–120°C. In this range of temperatures, the maximum growth rate is normally found for most of PLLA grades. Commercial grades present a maximum growth rate of about 2.5 μm/min in the range 105–130°C [2, 6]. Just for comparison, in the same range of temperature, isotactic polypropylene presents a growth rate of about 1 μm/s, or about two orders of magnitude larger.

2.2 Quiescent Nucleation

If overall crystallization rate and growth rate are measured and reported in many literature works, the data concerning the nucleation rate of PLA are rare. It is generally assumed that the nucleation phenomenon in commercial PLA grades is athermal

(heterogeneous), so that a given number of nuclei are formed at each temperature instantaneously and the number does not change with time. Sporadic nucleation, with a number of nuclei increasing with time, has been found at temperatures below the glass transition [3].

In most of literature works, the number of nuclei per unit volume (nucleation density, N) in isothermal conditions is estimated by using the relationship between volume space filling and crystallization halftime, $t_{1/2}$:

$$t_{1/2} = \left(\frac{\ln(2)}{\frac{4}{3}\pi N G^3} \right)^{\frac{1}{3}} \tag{2}$$

which allows calculating the nucleation density N from the growth rate and the crystallization halftime assessed by means of calorimetric data:

$$N = \frac{3}{4\pi} \left(\frac{\ln(2)}{\left(t_{1/2} * G\right)^3} \right) \tag{3}$$

It has to be mentioned that the presence of a third power makes the calculation of N extremely sensitive to uncertainties in the measurements of G and $t_{1/2}$.

On the other hand, measuring N from POM is difficult because the nuclei can be counted on a surface, but the observed volume is not easily evaluated. This is the reason why many data of nucleation density are expressed in nuclei/mm^2 (viz., surface nucleation density) [6], which is useful for understanding a trend, but not for having data of volume nucleation.

Just a few literature works report the volume nucleation density. Some results are summarized in Fig. 1. It can be noticed that, apart from the huge scattering of data (notably also measurements made on the same PLA grade provide differences of about two orders of magnitude), the nucleation rate of PLA is comparable to that of iPP. This means that the enormous difference in overall crystallization rate between the two polymers can be ascribed mainly to the growth rate, which moreover appears in the equation for halftime of crystallization (Eq. 2) with a power 3.

2.3 Stereocomplex Crystallization

Typically, PLA is produced via the ring-opening polymerization of lactide, which is the cyclic dimer of the chiral lactic acid. As such, there are three diastereoisomers of lactide: L-lactide (composed of two L-units), D-lactide (composed of two D units), and meso-lactide (containing one of each D and L units). Depending on the ratio of these diastereoisomers in the monomer feed, polymerized PLA can be of several stereostructures, including poly(L-lactide) (PLLA), poly(D-lactide) (PDLA), poly (DL-lactide) (PDLLA), and other stereocopolymers. D- and L-isomers of PLA in

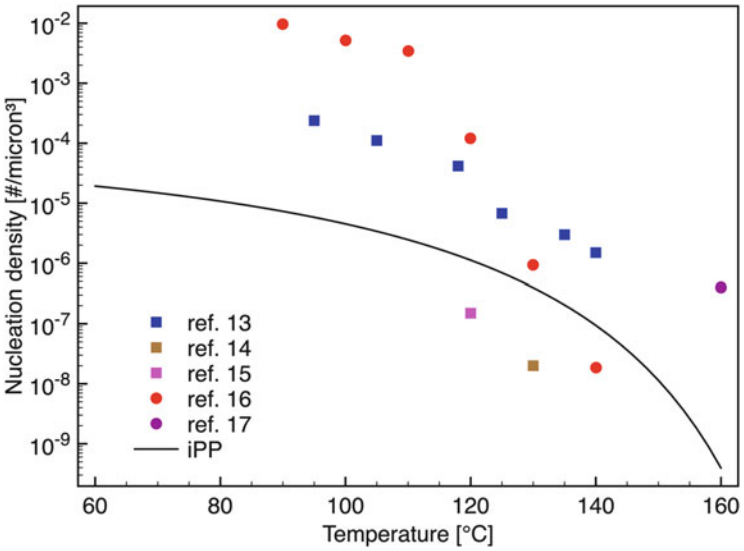

Fig. 1 Nucleation density of PLA grades from literature works. Squares refer to the same PLA grade (2002D from NatureWorks) [13–15]. Circle refers to a PLA with D-content of 1.1–1.7% [16, 17]. The line refers to the nucleation density measured on a iPP [18] and is given for comparison

helical conformations can interact side by side with each other to create a specific crystalline chain-packing state that is called "stereocomplex" (SC) [19]. SC content within PLA has a strong effect on crystallization from the melt. In particular, the overall crystallization rate of the stereocomplex is higher with respect to crystallization of PLLA homocrystal (HC). It is recognized that this increase of crystallization rate is primarily due to stereocomplex crystallites that act as nucleating agents for PLLA spherulites [20], but there is also a slight increase of growth rate (within 20%) observed only at low percentages of stereocomplex [21]. The nucleating effect is considerable: it is reported that a 30-fold reduction on the crystallization halftime can be reached by using 10% by weight of low molecular weight in PDLA, whereas the same amount of talc in the same material only allowed a reduction by a factor of about 2 [22].

The results reported in the literature make the SC extremely interesting for enhancing the crystallization rate [23].

While the lamellar PLLA crystallites exhibit a hexagonal form, the SC crystal displays a triangular morphology as observed with transmission electron microscopy or atomic force microscopy. Additionally, the wide-angle X-ray diffraction (WAXD) pattern of SC-PLA differs from the diffraction pattern of PLLA; the WAXD pattern comparison is shown in Fig. 2 [24, 25].

Perhaps as a result of the enhanced and different crystallizations, SC-PLA also boasts improved thermal resistance, hydrolytic stability, and mechanical properties relative to PLLA [26, 27] (Table 1).

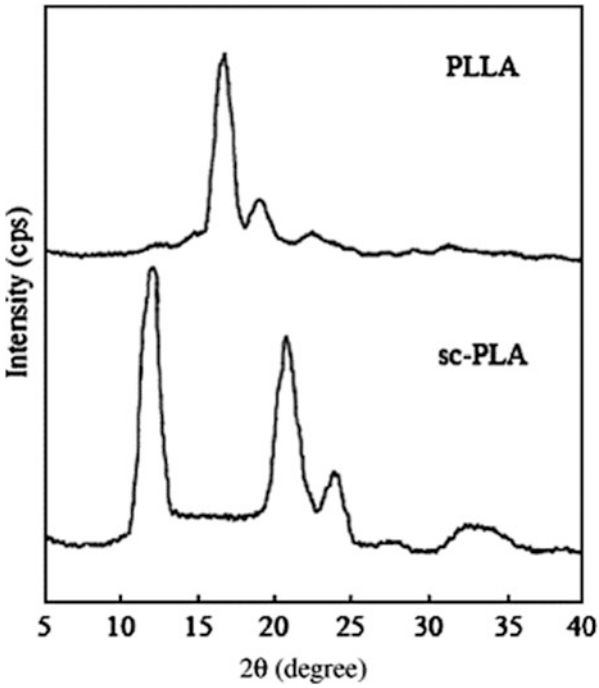

Fig. 2 Wide-angle X-ray diffraction pattern for PLLA and SC-PLA, indicative of different crystal structures formed upon cooling from the melt [24]. Copyright 2006, John Wiley and Sons

Table 1 Summary of physical and mechanical properties of PLA, PLLA, and PDLLA [27]

Properties		PLA	PLLA	PDLLA
Density (ρ)	g/cm^3	1.21–1.25	1.24–1.30	1.25–1.27
Tensile strength (σ)	MPa	21–60	15.5–150	27.6–50
Tensile modulus (E)	GPa	0.35–3.5	2.7–4.14	1–3.45
Ultimate strain (ε)	%	2.5–6	3.0–10.0	2.0–10.0
T_g	°C	45–60	55–65	50–60
T_m	°C	150–162	170–200	Amorphous

3 Generalities on Flow-Induced Crystallization

While the quiescent crystallization of PLA has been broadly studied, the achieved understanding is not directly transferred to the polymer engineering of PLA, because quiescent crystallization studies describe PLA behavior in the absence of melt flow and orientation. For practical engineering implementation, the flow-induced crystallization (FIC) of PLA must also be understood.

Flow-induced crystallization is a broad term that describes the crystallization of polymers during and after they have been subject to shear flow [28]. Historically, most experimental investigations of FIC have focused on olefin-based polymers, and models which describe FIC behavior are almost exclusively derived from these flexible polymers. Research specific to FIC in PLA provide important insight to the influence of the flexible backbone, intramolecular interactions, and SC aspects of PLA.

Relative to quiescent crystallization, FIC exhibits increased nucleation density, the crystallization kinetics are accelerated, and the resulting microstructure is oriented or anisotropic. To explain the thermodynamics which drive FIC phenomena, the entropy-reduction model (ERM), originally proposed by Flory, is perhaps the most widely accepted model [29–31]. During melt flow, some fraction of the longest chains become oriented and stretch in the melt. This orientation leads to an entropy reduction, which lowers the energy barrier for FIC according to Eq. (4). The energy barrier for FIC is expressed in terms of the quiescent nucleation energy barrier (ΔG_q) and the degree of entropy reduction by shear (ΔS_f) [32]:

$$\Delta G_f = \Delta G_q + T_s \Delta S_f \ (\Delta S_f < 0) \tag{4}$$

Both the reptation time and the Rouse time of the polymer are important characteristics that dictate the amount of flow required to induce FIC [33]. Three resulting microstructure regimes have been identified that stem from the competition of shear flow and polymer relaxation in the FIC process. The first regime occurs if the shear rate does not exceed the reciprocal of the relaxation time; no noticeable FIC effects will be observed. The second regime requires increasing the strength of the shear flow such that the shear rate exceeds the reciprocal of the relaxation time but does not exceed the reciprocal of the polymer Rouse time. This regime will yield enhanced point-like nuclei and accelerated crystallization kinetics, but the morphology will remain isotropic. The third regime, which results from increasing shear work, will result in oriented or "row" nuclei. If the shear rate exceeds the reciprocal of the polymer Rouse time, then these long chains extend during flow and ultimately form the anisotropic shish-kebab structures indicative of the fourth regime [34]. While many outstanding questions remain with regard to the exact mechanism of nucleation in FIC, most studies indicate that the extended chains act as precursors to nucleate crystallization.

As the reader will observe, to date no published studies have shown all *four* regimes for PLA in a single study that quantifies the shear work required to induce enhanced nucleation (second regime), oriented nuclei (third regime), and shish-kebab structures (fourth regime). However, taking a comprehensive look at the literature, one can hypothesize that PLA behaves according to the three-regime model when comparing the results of different researchers in light of their experimental protocol. For example, pooling the data from Zhong and coworkers [35] with that of Xu and coworkers as shown in Table 2 [36], the following data indicate that increasing shear work in PLLA (NatureWorks 4032D) prior to crystallization at 135°C can yield each of the four regimes. In other words, increasingly intense shearing conditions must be introduced to cause the PLA melt to crystallize in increasingly nucleated and oriented microstructure. These two studies will be discussed in more detail later in the text.

Table 2 Summary conditions used to produce FIC effects per regime I (no effect), regime II (enhanced nucleation), regime III (oriented nuclei), and regime IV (shish-kebab) in PLLA (NatureWorks 4032D) [35, 36]

	T_m (°C)	T_c (°C)	Sample thickness (μm)	Shear time (s)	$\dot{\gamma}$ (s^{-1}) I → II	$\dot{\gamma}$ (s^{-1}) II → III	$\dot{\gamma}$ (s^{-1}) III → IV
Zhong	190	135	10	Variable	0.0076	0.45	
Xu	200	135	20	1			100

4 Methods for Assessing

The characterization techniques used to assess the extent of FIC that a polymer undergoes after shear flow are much the same as those used to characterize quiescent crystallization [37]. POM is used to identify both enhanced nucleation density and anisotropy of the final microstructure. Accelerated crystallization kinetics can be observed using hot-stage microscopy, where the appearance of crystal growth occurs faster than the quiescent equivalent upon cooling or isothermal crystallization. Rotational rheology is commonly used to first impose a controlled shear field on the melt and then subsequently observe crystallization through a very small oscillatory motion at constant temperature or during cooling [34, 38, 39]. Calorimetry will reveal higher crystallization temperatures upon cooling of sheared samples, and the stable flow-induced nuclei are known to nucleate crystallization at high supercooling via fast scanning calorimetric measurements [40–42]. In addition, both small- and wide-angle X-ray diffraction techniques are used to quantify the crystalline fraction content, orientation, and phase characteristics.

5 Flow-Induced Crystallization of PLA

Both renewable sourcing and controlled biodegradation make PLA a top candidate for emerging engineering applications of the future. However, to optimize mechanical properties and degradation profiles, the crystallization of PLA must be manipulated by engineers in order to control PLA microstructure during polymer product manufacturing. Most manufacturing processes used to transform PLA into the melt such as molding, casting, and extrusion subject molten PLA to a shear flow. Consequently, the flow-induced crystallization of PLA emerges as a critical phase transformation that is generating much interest from industrial and academic researchers alike [43]. Like other high polymers, PLA is known to form spherulitic morphology after zero or low shear deformation, to experience enhanced nucleation and isotropic growth at after experiencing moderate flow and to exhibit cylindrites and shish-kebab structures after strong shearing in the melt. Examples of PLA spherulites and shish-kebabs are shown in Fig. 3. The specific relationships between molecular architecture, molecular weight, shearing temperature, shear rate, and

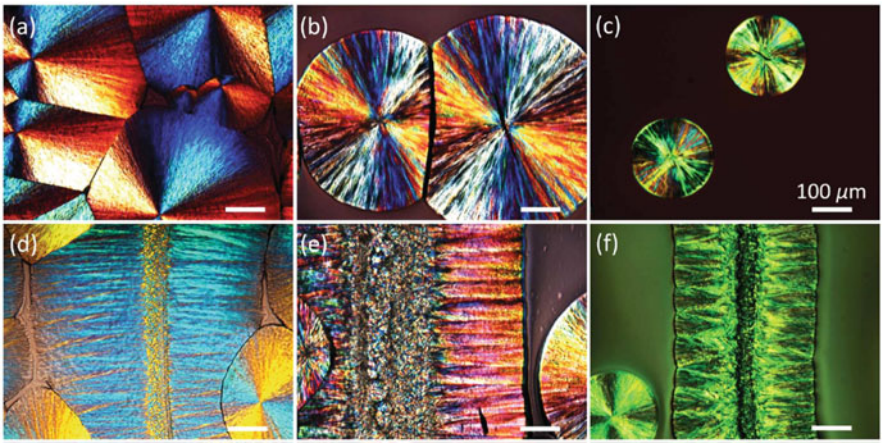

Fig. 3 POM imaging reveals PLA spherulites (**a**–**c**) and cylindrites or shish-kebabs (**d**–**f**) formed at 150°C (**a**, **d**), 165°C (**b**, **e**), and 180°C (**c**, **f**). From [44]. Copyright 2016, John Wiley and Sons

crystallization temperature that ultimately drive the resulting morphology are not thoroughly understood at present. However, much progress toward quantifying the FIC behavior of PLA has taken place in recent years, forming the foundation of current active research in PLA flow-induced crystallization.

The first forays into the FIC behavior of PLA were broached by those interested in the solidification of PLA fibers [45–48]. The extreme deformation experienced by the polymer during fiber formation results in both typical FIC where the polymer is first oriented and then allowed to crystallize, in addition to the deformation that occurs when the original crystal structure is disrupted by solid-state drawing [49]. The PLA fibers studied by Cicero and coworkers displayed increased melting temperature and greatly improved mechanical properties relative to the quiescently crystallized PLA. Similarly, Mahendrasingam found that shish-kebab morphology developed in PLA after rapid tensile deformation [50].

6 Effect of FIC on Nucleation Rate

With respect to FIC forming upon melt cooling, Fitz and coworkers were the first to explore the influence of shear flow on the isothermal crystallization kinetics of PLLA [51]. After a controlled shear step at crystallization temperatures between 80°C and 150°C (shear rate 1 s^{-1}, duration 1 s, sample thickness 300 μm, and diameter 30 mm), they observed increase in nucleation density and an increase in the rate of conversion, relative to the quiescent equivalent. Polarized light microscopy is commonly used to observe the increased nucleation density that results from a previous shear step. Such images were developed by Zhong and coworkers as they

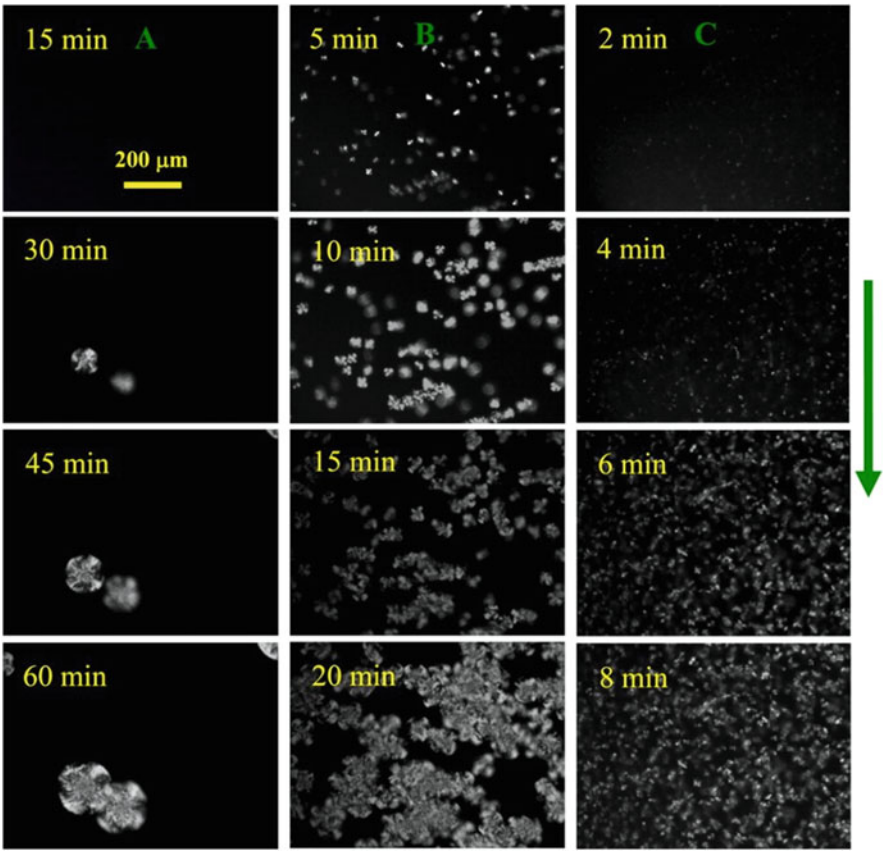

Fig. 4 Selected POM micrographs for PLA during isothermal crystallization at T_c of 135°C after being sheared at a shear rate of 10 s^{-1} for different times of (**a**) 0 s, (**b**) 4 s, and (**c**) 40 s. The yellow-colored scale bar in the top left micrograph represents 200 μm and is applied to all other micrographs. Crystallization times are indicated in the micrographs. The green-colored arrow on the right side of the figure indicates the shear flow direction. From [35], Copyright 2013, American Chemical Society

determined the critical shear rates to increase the nucleation rate of PLA and are shown in Fig. 4.

In this study, to determine the shear rate and time requirements necessary to enhance the nucleation of PLA (2% D-content, 160 kg/mol), a rotational rheometer was used. The critical shear rates for the orientation and stretch of the longest chains at 135°C were determined to be 0.0076 and 0.45 s^{-1}, respectively. The samples detailed in Fig. 4 were subject to a shear rate of 10 s^{-1} for the indicated duration, clearly exceeding the threshold of 0.45 s^{-1}. After shear for the indicated time, the nucleation rate of the PLA increased with increasing shear time. Using similar rheological techniques, Fang and coworkers observed the onset of crystallization of PLA (4% D-content, 87 kg/mol) after the polymer was held in the melt at 250°C

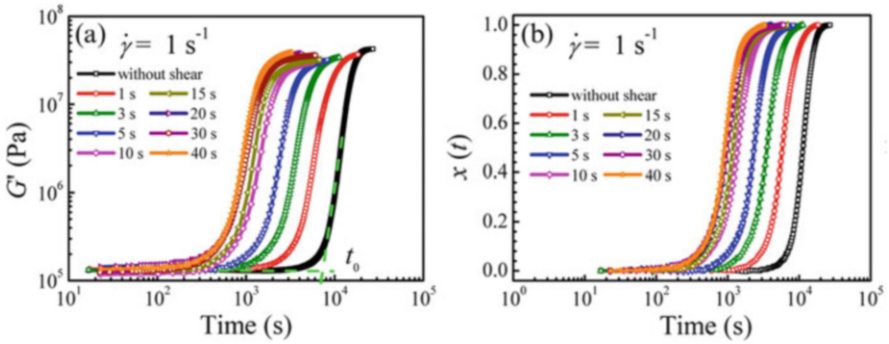

Fig. 5 Changes of (**a**) storage modulus, $G0$, and (**b**) percent crystallinity, $x(t)$, with time during crystallization at T_c of 120°C at the shear rate of $\dot{\gamma}$ 1 s^{-1} with different shear times for linear PLA (4% D-content, 87 kg/mol) [15]. Copyright 2013, American Chemical Society

before being cooled to the target shearing temperature of 120°C where a steady shear pulse was applied for the indicated time. After shearing, an oscillatory time sweep was used to monitor the increase of storage modulus (G') with time. The storage modulus increases as crystallization occurs in the melt and is directly related to the relative crystallinity by applying a logarithmic normalization of the G' data as was developed by Pogodina and coworkers [52]. Without shear, the onset of increasing storage modulus due to the onset of crystallization, t_0, is approximately 7,300 s. Considering the sheared samples, it can be easily seen that the onset of crystallization detailed in Fig. 5 decreases with increasing shearing time.

The halftimes of crystallization for the sheared and quiescent PLLA samples are shown in Fig. 6. Notice that the accelerating influence of FIC is most dramatic at high crystallization temperatures. At these high temperatures, crystallization is controlled by heterogeneous nucleation, and the order introduced to the melt during flow yields precursors that act to nucleate the surrounding melt [53].

Using shear rates less than or equal to 5 s^{-1}, Fitz et al. did not observe anisotropic or fibrillary morphology in PLLA (M_n and PDI were 50,000 g/mol and 2.34, respectively). However, to reach anisotropic morphologies, a stronger dose of deformation must be applied to the melt. Stronger shear fields were subsequently explored, revealing the relationship between shear flow, crystallization kinetics, and resulting morphology. Huang and coworkers used an optical shear cell to first induce flow in PLLA (M_n and PDI were 34,100 g/mol and 1.39, respectively) and then directly observed the isothermal crystallization at several temperatures after shearing. They determined that applying a shear rate of 20 s^{-1} for 5 s was required to induce a complete conversion to α-crystal content morphology after isothermal crystallization at 115°C. However, all shear rates studied caused an increase in α-crystal content relative to unsheared samples for a given crystallization temperature [54]. Additionally, in sheared PLLA the α-crystal was able to form at lower temperatures than in the quiescent samples. For example, after crystallization at 96.5°C, the α-crystal is typically a minor component among the majority α′-crystal

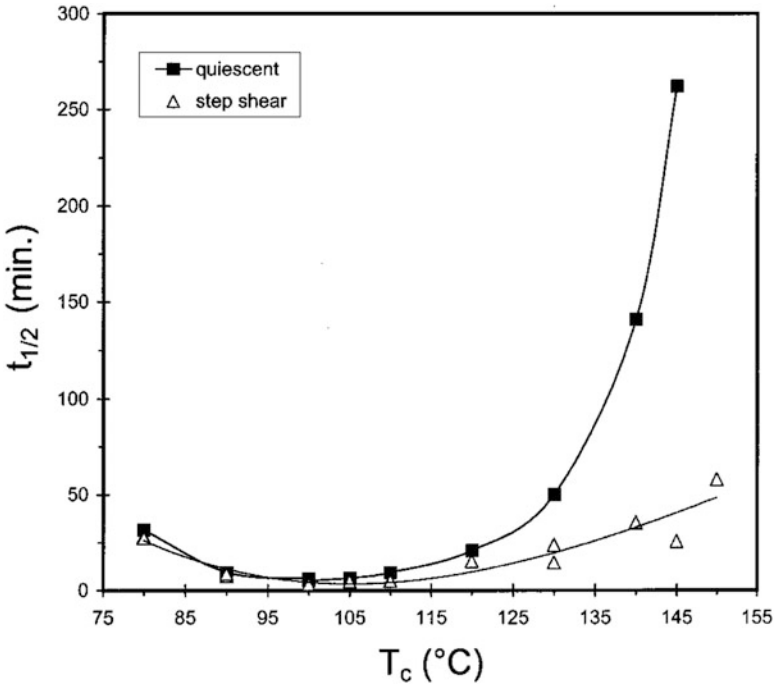

Fig. 6 Crystallization halftime as a function of crystallization temperature for quiescent and sheared PLLA samples [51]. Copyright 2002, American Chemical Society

mesophase. As shown in Fig. 7, with increasing shear, the WAXD reflections (0 1 0) (2 1 0) and other reflections at higher 2θ become stronger with increasing shear rate, indicating more ordered α-crystal content.

7 Non-isothermal FIC

Li and coworkers used a similar experimental procedure but observed PLLA crystallization upon cooling. They determined that PLLA required a shear rate greater than 5 s^{-1} to form cylindrites, and this rate was successfully employed by others to form "shish-like" crystals [55, 56]. This study also revealed that the cooling rate employed *while* the melt was experiencing shear, during non-isothermal crystallization, strongly influenced the resulting nucleation density, microstructure, and ultimate percentage crystallinity. After experiencing a shear rate of 5 s^{-1}, the PLLA did not crystallize if cooled at a rate of 5 K/min but was able to crystallize to about 15% if cooled at 3 K/min and 42.36% when cooled at 1 K/min. Without shear, PLLA required a cooling rate less than 3 K/min to crystallize any measureable amount.

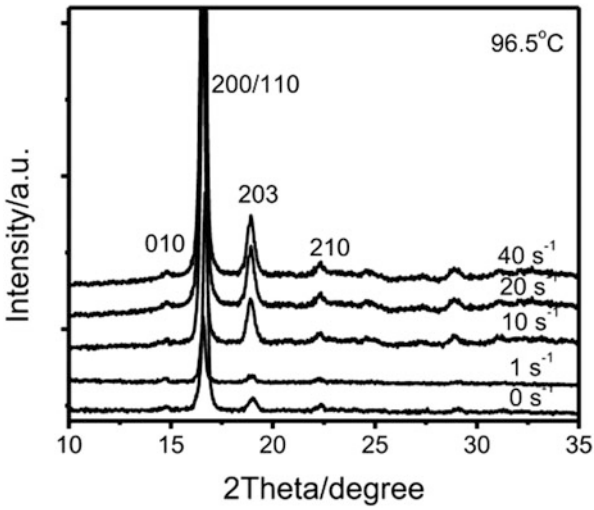

Fig. 7 WAXD patterns of PLLA crystallized at 96.5°C after being subjected to different shear rates [41]. Copyright 2001, American Chemical Society

The size and number of cylindrite-like crystals decreased with cooling rate, likely due to the relaxation of chain orientation in the melt.

In an effort to apply existing FIC theory to PLA melt flow and crystallization, Zhong and coworkers first established the rheological properties of the industrially relevant NatureWorks 4032D grade PLA, which contains 0.7 mol% L-isomeric content [35]. The longest reptation time and the Rouse time were estimated from the relaxation spectra, and this data was used to calculate the target shear rate and conditions required to initiate FIC. Using rotational rheology, the group monitored the onset of crystallization after shearing and confirmed that the critical shear rate to stretch the longest chains of this grade of PLA at 135°C was 0.45 s^{-1}. Above this rate, the crystallization process was greatly enhanced compared to the quiescent conditions, and the crystallization kinetics increased with increasing shear rate due to an increase in nucleation density. For a singular shear rate, there was a critical shearing time required, and additional shearing time did not lead to faster crystallization kinetics under either isothermal or non-isothermal conditions.

7.1 Conditions to Create Shish-Kebab Microstructure

Acknowledging the property enhancements that result from developing shish-kebab microstructure in PLA melt-manufactured product, Xu and coworkers developed two methods – one requiring a long shear step and a second requiring instead a quick shear pulse – to form this microstructure in PLLA. The first required an ultrasonic force to maintain energy input to an injection-molded part until gate freeze, and as a result of the long exposure time to shear, several shish-kebabs were identified in the

final-molded samples [57]. However, under extensive shear, PLA will undergo a degradation mechanism that results in a loss of molecular weight [58]. To circumvent this degradation, a short pulse of strong shear, such as 100 s^{-1} for 1 s, may also be used to induce shish-kebab structure. The shish created under such circumstances has been shown to be comprised of a higher conformational order than the surrounding kebabs or independently nucleated spherulites [36].

7.2 Crystallization Under Continuous Shear

While most FIC investigations first subject the PLA melt to a shear flow and then observe the crystallization behavior and resulting morphology after the cessation of flow, PLA will also crystallize under a continuous shear flow. Yang and coworkers used an optical shear cell to first melt PLA to 200°C before cooling to 110°C, where the melt was then subject to a shear rate of 0.16 s^{-1} for 1,500 s or until crystallization was complete [59]. This continuous shearing study was monitored by wide-angle WAXD and POM. Results showed that both shish-kebabs and cylindrically stacked lamellae could form, survive, and grow under flow provided the shear rate exceeded a critical rate. Weak continuous shear flow yielded more crystallinity, while high shear rates reduced ultimate crystallinity.

8 Flow-Induced Crystallization of Stereocomplex PLA

As described in section "Stereocomplex Crystallization," the SC of the L-isomer and D-isomer poly(lactic acid) co-crystallizing yields a SC crystalline structure that melts about 50 K higher than that of the PLLA homocrystal. The higher melting point of the SC crystal is of interest for commercial PLA formulations, because the ratio and microstructure of SC can be tailored to result in bulk properties competitive to traditional engineering thermoplastics. Because most engineering thermoplastics undergo some type of melt processing prior in the manufacture of industrial and consumer parts, the FIC of stereocomplex PLA has gained interest in recent years [60].

Pan and coworkers determined that in the absence of shear, the kinetics of HC formation, either L/L or D/D homocrystallization, are more favorable than the formation of the SC crystal phase. However, several researchers have confirmed that shear flow increases the amount of SC crystal that forms in a PDLA/PLLA mixture [17]. In order to form SC crystals from the melt, D- and L-chains must at least partially mix, and segments of D- and L-chains must align prior to crystallization, and a shearing promotes this phase mixing [61]. Bojda established that, for identical shearing conditions, PLA with 2.8% PDLA content crystallizes at a higher crystallization temperature upon cooling than does PLA with only 1.5% PDLA content, but during slow cooling both blends result in the same crystalline content [62]. Bai and coworkers determined the

role of SC in the PLA melt by preparing a series of blends with increasing D-content. They discovered that, in low-frequency melt behaviors of the blends, the slope of the storage modulus curve decreases with increasing D-content, indicating a slower relaxation of the melt with increasing D-content because the SC phase restrains the long-range motion of the PLLA chains in the melt [17].

To promote crystallization in the mixed phase, both increasing shear and decreasing the shearing temperature act to reduce chain mobility. Importantly, the molecular weights of both the PLLA and PDLA components drive the miscibility of the polymer blend in the melt, with blends displaying multiple melting peaks when molecular weights ranged from 23 to 50 kg/mol but single melting behaviors if the PLLA and PLDA were of lower molecular weights. This is likely due to short chains in the melt having sufficient mobility to form SC, while longer chains are hampered by entanglement [63]. Song and coworkers studied equimolar blends of PDLA and PLLA to also determine that increasing shear rate prior to crystallization led to an increase in SC content [23]. As SC content increases, the α-crystal content formed by PLLA decreases accordingly. As confirmed by several researchers, the increased rate of crystallization is largely due to an increased number of SC nuclei that form under flow conditions. The increase in nucleation can be easily observed in the crystallized samples formed after flow, which contain many more and smaller spherulites relative to their quiescently crystallized counterparts [60]. Increasing the pressure of a crystallizing PLA blend, however, promotes HC formation while suppressing SC formation, due to the reduced free volume of the melt [64].

Ultimately, the microstructure that results from flow-induced crystallization of PLA is a function of the material properties, shearing conditions, and crystallization temperature. One must exercise attention to detail when comparing results from the numerous studies in the literature, because a wide variety of conditions are reported for experimental setup. For example, both Bai and Xie studied the microstructure formed after flow-induced crystallization of similar PLLA/PDLA blends [17, 44]. Though both examined the microstructure after crystallization in the range of 160°C, one study sheared the PLA at 100 s^{-1} for 1 s, while the second study sheared the PLA at 1 s^{-1} for 10 s. The sample experiencing the higher shear rate (but shorter duration) formed shish-kebab, anisotropic microstructure, while the material experiencing the lower shear rate for a longer time interval formed many small spherulites. In order to fully promote the formation of the SC phase, Xu and coworkers pulled a glass fiber through the melt above the melting temperature of the HC, but below the melting temperature of the SC [65]. This technique enables the selective FIC of the stereocomplex under conditions which eliminate the possibility of HC forming. Physical testing after solidification revealed that the pullout strength of the glass fiber embedded into the SC-PLA was more than three times higher than a similar fiber embedded in an HC-rich, quiescently crystallized sample of the same PLA.

9 Effects of Molecular Weight and Chain Branching

Although, as mentioned above, under quiescent condition, the molecular weight has a significant effect on the crystallization kinetics of PLA; the studies concerning this property on the flow-induced crystallization are rare.

Jalali et al. [8] investigated the effect of shear rate and shear strain on the crystallization kinetics of PLA. Using a controlled hydrolytic degradation technique, they obtained two materials having the same D-L content but lower MW than the starting polymer.

They found that the crystallization induction time decreased upon increasing the MW in the presence of the shear flow. This was ascribed to a longer relaxation time. They also found that shear flow promoted the formation of the α-phase at elevated temperature, 130°C, for all different molecular weights. Furthermore, it was found that shear promoted the formation of the α-phase below 100°C, namely, at temperatures where the samples crystallized in quiescent conditions only showed the formation of the α′-phase. Finally, it was observed that shear induced the formation of cylindrite morphology only in high molecular weight PLA, whereas spherulitic morphology was developed for the low and medium molecular weight PLA in the same conditions.

Apart from the average molecular weight, the importance of the high molecular mass tails in polymer melt on the formation of oriented, anisotropic structures was pointed out by several researchers. For linear PLA a fast relaxation after shear takes place, which reduces the efficiency of shear flow in altering the nucleation ability and crystalline morphology. High molecular weight tails increase the relaxation time and thus drastically enhance the crystallization kinetics and the formation of the shish-kebab structure. Fang et al. [15] analyzed the effects of long-chain branching, LCB, on the nucleation density enhancements and crystalline morphological evolution for shear-induced crystallization of PLA under isothermal conditions. They showed that LCB-PLA crystallized much faster than linear PLA under the same shear conditions. In situ POM observations demonstrated the LCB-PLA not only presented a larger nucleation density for the same shear time but also formed shish-kebab structures after being sheared for the sufficiently longer time.

10 Effects of Fillers and Nucleating Agents

In many processes, deformation rates are applied on a PLLA melt containing nucleating agents. Many studies conducted on several polymers concluded that the contribution of nucleating agents and flow to nucleation density is often additive but can be synergistic.

Among nucleating agents for PLLA, the most common is talc [58]. Refaa et al. [66] investigated the effect of shear flow on pure PLA and on PLA with 5 wt% of talc, evidencing a synergistic effect.

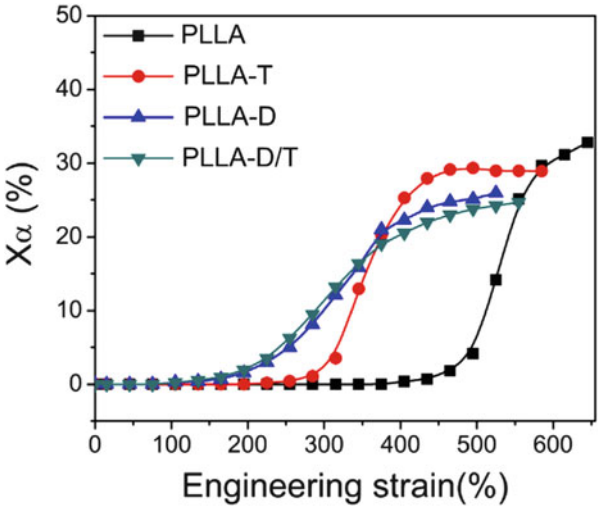

Fig. 8 Development of a crystal in neat and nucleated PLLA as a function of engineering strain during uniaxial stretching at 75°C. The stretching speed was 0.0125/s [68]. Copyright 2015, Elsevier

Though FIC of stereocomplex PLA phase has been discussed, the SC phase should also be highlighted as a true nucleating moiety for PLA crystallization. Wei et al. [67] investigated the crystallization behavior of a PLLA/PDLA blend (99/1 wt/wt) under shear to explore the combined effect of shear and stereocomplex crystallites on the crystallization rate of PLLA. As mentioned above, stereocomplex is probably the most efficient nucleating agent for PLA. Also in this case, the results showed that the crystallization rate of PLLA was synergistically accelerated by SC crystallites and shear. The authors ascribed this effect to a much slower relaxation behavior of PLLA/PDLA blend with respect to neat PLLA, possibly due to the cross-linking effect of SC crystallites.

Yin et al. [68] investigated the orientation and crystallization of PLLA combining the effect of nucleating agents and mechanical stretching. They combined both talc and stereocomplex. In particular, they used talc (1 wt%), PDLA (5 wt%), and also a combination of the two (1% of talc + 5% of PDLA). During continuous uniaxial stretching at 75°C with a low stretching speed, nucleating agents remarkably enhance the crystallization of PLLA. It was found that the effect of the nucleating agents is dependent on the mechanically applied strain. At small strain, the crystallization of PLLA is remarkably enhanced by the nucleating agents. While at higher strain, the effect of the nucleating agents is obscured by the dominant effect of the strain-induced orientation on the crystallization of PLLA. The results are summarized in Figs. 8 and 9.

Tang et al. [69] considered the simultaneous effect of shear flow and carbon nanotubes (CNTs), another quite effective nucleating agent for PLA [70]. The results show more than an additive effect of CNTs and shear flow on enhancing crystallization of PLA in non-isothermal conditions.

The synergic effect was attributed to the extra nucleating sites produced by the interplay of shear flow and CNTs. The authors ascribed the origin of these extra sites

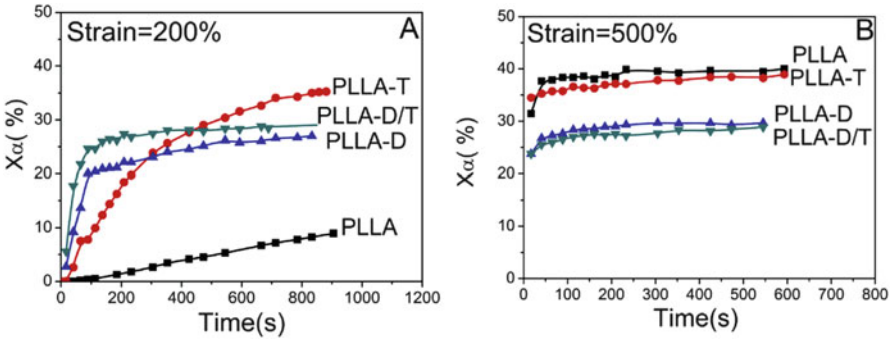

Fig. 9 Variation of a crystal in neat and nucleated PLLA as a function of time during isothermal process at 75°C after step stretching to 200% (**a**) and 500% (**b**), respectively [68]. Copyright 2015, Elsevier

to the anchoring effect of CNTs on shear-induced crystallization of PLA and suppressing effect of CNTs on the relaxation of shear-induced nuclei. By using oscillatory shear injection molding technique on samples loaded with 0.1 wt% of CNTs, the authors obtained samples with a crystallinity degree of more than 20% in the whole thickness, whereas the samples made of pure PLA presented a percentage of about 15% at the skin and were essentially amorphous in the core (Fig. 10).

Different results are reported by Xie et al. [71], who studied the crystallinity distribution in molded PLLA samples containing 0.05% of CNT and in molded PLLA samples containing 5% of SC, and noticed that the promoting effect on crystallization of PLLA by intense shear flow was so significant that the nucleation effect of nucleating agents CNT and SC could be neglected. On the contrary, the addition of nucleating agent resulted in a decreased crystallinity of PLLA at high mold temperature (higher than T_g). This result was ascribed to the spatial restriction of the chain segment folding into the lattice and formation of less perfect crystals.

A synergistic effect of CNT and deformation was assessed in extensional flow by Li et al. [72]. By applying intense extensional flow on PLA melt containing 0.3 wt% of CNT, they obtained two types of special aligned crystalline microstructures (shish): homogeneous crystalline fibrils only consisting of PLA extended chains and hybrid crystalline fibrils characterized by CNTs coated with PLA extended chain as depicted in Fig. 11.

11 FIC in PLA Processing

PLLA can be processed by most of the conventional techniques for thermoplastics [73, 74]. The change imparted to PLLA during melt processing is more than simply creating the net shape of a PLLA part. Changes imparted by melt flow, including chain orientation, crystallization, and degradation, may result in substantial changes

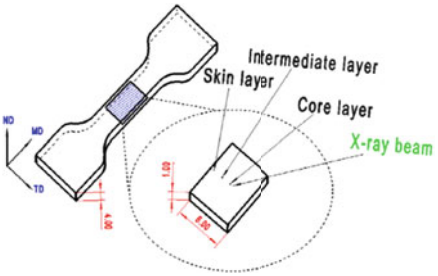

Sample	*Skin*	*Intermed.*	*Core*
CIM PLA	15%	0	0
CIM PLA/CNT	19%	9%	0
OSIM PLA	16%	1%	0
OSIM PLA/CNT	20%	28%	21%

Fig. 10 Crystallinity in different positions (as indicated in the left figure – measures in mm) for samples made by conventional injection molding (CIM) and oscillatory shear injection molding (OSIM) with and without CNT [69]. Copyright 2012, American Chemical Society

to mechanical properties. In 2010, Carrasco and coworkers detailed both the chain degradation and the improvement in mechanical properties that were attributed to injection molding and annealing a PLA with 4.25% D-content [75]. Simply injection molding the PLA did not induce crystallization because of the fast cooling time, but it did allow for PLA chains to orient and then crystallize in a subsequent annealing step. The impressive property improvements induced by crystallization during annealing are shown in Table 3.

Like most studies reported in the literature, Carrasco and coworkers did not directly discuss or quantify FIC as a driving force for crystalline development in the samples described above. However, the high flow rate and resulting polymer orientation inherent in the injection molding process provide optimal conditions for FIC to occur, and the mechanical property results indicate that the annealing process was very efficient after melt flow, orientation, and solidification. Therefore, in the following we review the studies reporting processing techniques that show evidence of flow-induced crystallization.

11.1 Injection Molding and Related Processes

Considering the fast cooling rates involved in injection molding, PLLA should not crystallize at all if just the quiescent crystallization kinetics are considered. Despite this, several literature works report non-negligible crystallinity degrees in injection-molded PLLA parts. Gosh et al. [76], for instance, obtained injection-molded samples of a PLLA homopolymer in several different molding conditions (according to a design of experiments array) and found a non-negligible overall crystallinity degree (up to about 6%) in the 2-mm-thick samples. They observed that this crystallinity content increased the maximum shear stress, clearly evidenced a phenomenon of flow-induced crystallization. This observation is consistent with the results reported in the paper by Tang et al. [69] mentioned above that in injection-molded parts, the skin region is more crystalline than the core, which can be justified

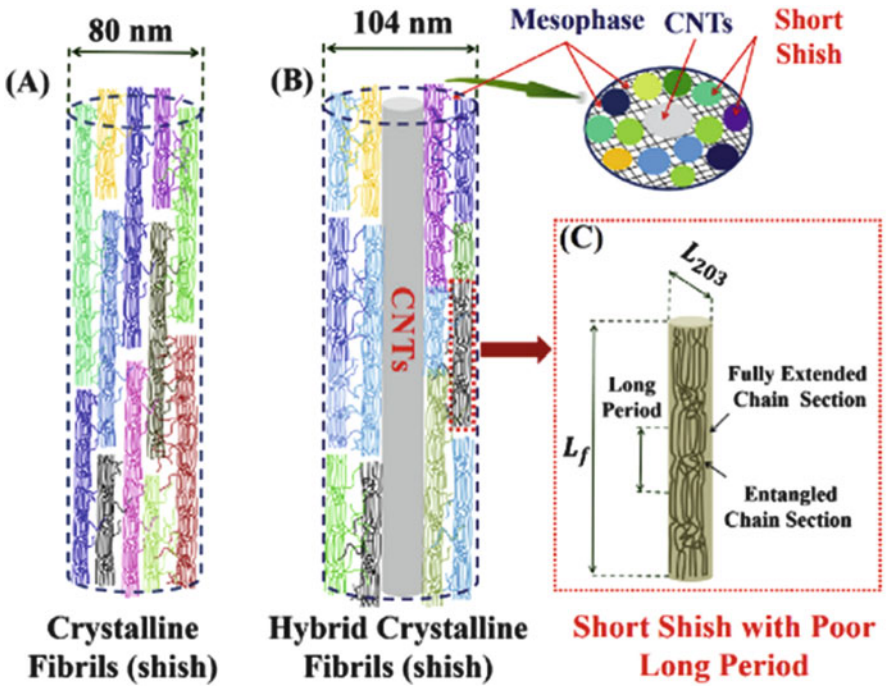

Fig. 11 (**a**, **b**) Schematic drawing showing the multiple short-length shish in neat PLA and CNT/PLA nanocomposite, respectively. (**c**) Schematic illustration of molecular arrangement in the short-length shish. The extensional flow direction is vertical [62]. Copyright 2016, Elsevier

Table 3 Mechanical properties of injection-molded tensile bars produced from PLA containing 4.25% D-content, as molded and after annealing [75]

	As injection molded	Post-annealing
% Crystallinity	<1%	33%
Young's modulus (E) (GPa)	3.7	4.1
Yield strength (σ_y) (MPa)	65.6	75.4
Elongation at break (%)	4.0	2.5

only by an effect of flow-induced crystallization since the cooling rates are higher at the skin and lower at the core.

It is important to note that for PLLA grades with significant amount of D-lactide, injection-molded parts are reported to be amorphous [77], and only special molding protocols can provide crystalline samples [78, 79]. This suggests that the enhancement effect on crystallization due to flow could be not enough to compensate the high cooling rates.

In order to obtain molded samples with a higher degree of crystallization, some variants of the conventional injection molding (CIM) were applied to PLA. The shear-controlled orientation injection molding (SCORIM) technique is based on a

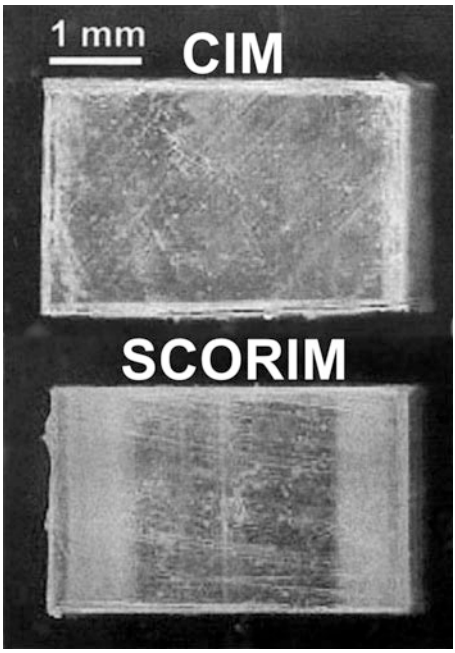

Fig. 12 Optical images of samples obtained by conventional injection molding (CIM) and SCORIM (adapted from [80]). Copyright 2004, Springer Nature

device that is attached to the injection nozzle and is composed of a hot runner circuit that divides the melt stream into two channels where two hydraulically actuated pistons are operated during the holding pressure stage. Compared to CIM, where the molten material solidifies under the influence of an almost static pressure, in SCORIM the polymer melt is continuously displaced inside the mold cavity by the action of the hydraulic pistons. This causes, as the solidification takes place progressively from the skin to core regions, a continuous shear imposed to the melt, with a considerable enhancement of flow-induced crystallization effects.

Altpeter et al. [80] compared the results obtained in terms of crystallinity in PLLA samples molded with CIM and SCORIM. They found that the degree of crystallinity was higher than 20% for the SCORIM and about 5% for the conventional sample. They also found that the crystalline structure of SCORIM processed moldings were highly oriented.

The authors also report optical images of the molded samples (reproduced in Fig. 12), from which it is clear that samples obtained by CIM are transparent, whereas samples obtained by SCORIM present an opaque skin layer due to a significant crystalline degree.

Ghosh et al. [81] analyzed the effect of several processing conditions on SCORIM and compared the results with CIM. Concerning the morphology, the authors noticed that the samples obtained by SCORIM presented a core-free morphology, in contrast to the skin-core morphology of CIM. The extent of core fibrillation increased with shearing time. The authors noticed that all the SCORIM

processed PLLA exhibited higher toughness and higher maximum stress compared with CIM processed PLLA.

Another technique based on SCORIM is the so-called oscillatory shear injection molding (OSIM). Similar to SCORIM, in OSIM there are two hydraulically actuated pistons to generate a shear stress field during the cooling solidification of melt in the cavity. Contrasting to SCORIM where the multi-piston oscillating packing unit is an independent device, in OPIM a hot runner system is adopted, combined to a double live-feed device to injection molding machine. This greatly improves the SCORIM device.

Xie et al. [71] measured the crystallinity profile inside PLLA (D-lactide content 0.4 wt%) samples obtained by CIM and OSIM. They observed that, with a mold temperature of 40°C, in CIM, the samples were completely amorphous, whereas in OSIM the crystallinity degree was as high as 40% up to about 500 μm from the skin (the core was amorphous). The authors found an increase of the Vicat softening temperature in the OSIM processed samples. Similar results are also reported by Sang et al. [82], who also noticed an improvement of Young's modulus and tensile strength in OSIM processed samples with respect to CIM processed samples.

11.2 Foam Injection Molding

Foam injection molding is a process to make parts having better dimensional stability with less material and a faster production cycle with respect to the conventional injection molding process. A physical blowing agent mixed with the polymer melt allows the reduction of the processing temperatures due to its plasticization effect that reduces the melt viscosity. This is a great advantage for the processing of PLA, well-known for its thermal sensibility and narrow processing window.

The dissolution of both CO_2 [83, 84] and N_2 [85] in PLA enhances the crystallization kinetics in quiescent conditions. It is reported in the literature [86, 87] that the presence of CO_2 and biaxial stretching during foaming can both significantly increase the PLA crystallization rate, so that detectable crystallization content (approximately 10%) is found in foam injection-molded parts [10], despite the fast cooling rates experienced by the material during processing.

11.3 Extrusion Casting

A study of the effect of flow rate during extrusion was conducted by Tabatabei and Park [84]. They found that the PLA crystallization during extrusion could be promoted by flow at a temperature higher than the melting point.

Biaxially stretching extruded films were proved to be an effective method to develop the final crystallinity of PLA. Yu et al. [88] reported that stretching of a melt drawn PLA film induces crystallization. Ching-Chun Tsai et al. [89] also report a

study on the effect of stress-induced nucleation on the crystallization behavior of films of PLA.

Houichi et al. [90] carried out a study on the crystallization kinetics and spherulitic morphology of poly(lactic acid) induced by casting process. They found that that the rate of cold crystallization was sharply increased with draw ratio.

11.4 Melt Spinning

The deformation rates during melt spinning are very high, and thus it is expected that flow-induced crystallization plays a significant role during this process. Several studies about the PLA melt-spinning process showed that the crystallinity considerably increased on increasing the melt-draw ratio (MDR) [91]. Cicero et al. [45] and Fambri et al. [92] found an increase of crystallinity (from 0 to 51%) either on increasing the draw ratio or on decreasing the draw temperature.

Shim et al. [93] analyzed the effects of a spinning speed in the range 1,000–4,000 m/min on a PLLA with 2 wt% D-content. They found a linear increase of crystallinity with the speed, until a value of 25% at 4,000 m/min. Similar results were found by Schmack et al. [91] adopting a PLA with a lower content of L-lactide (92 wt%).

Hossain et al. [94] related the crystallinity of the spun fiber to the diameter of the fiber. They found a significant increase of crystallinity, and of the crystal size of the fiber, on decreasing the fiber diameter and on increasing the orientation.

11.5 Additive/Fused Filament Deposition Modeling

At present, PLA represents one of the most common materials used for the fused filament deposition modeling type of additive manufacturing. In this technique, a solid filament of PLA is fed through a small heated extruder head, which laterally traverses a solid surface, while the molten polymer is "pushed" out of the extruder nozzle and deposited on the build surface. While the nozzle diameter is constant, several process parameters can be modified that logically influence the crystallization of PLA after printing. Specifically, melt temperature, printing speed, and the temperature of the build plate dictate the viscosity, cooling rate, and shear rate experienced by the PLA during printing. Therefore, it is logical that FIC may occur if the thermal and flow conditions of the printing process are properly manipulated.

Indications in these directions were recently found by applying in situ Raman spectroscopy to fused filament deposition experiments conducted with a polycaprolactone [95]. McIlroy and Graham [96] made an attempt to model polymer stretch and orientation during typical non-isothermal fused filament fabrication flow and to determine the conditions under which flow-enhanced nucleation can occur

due to residual stretch. To date, however, no results have been reported that calculate the development of specific work for PLA during the printing process, and therefore no direct evidence exists as such.

However, several studies have confirmed the relationship between PLA printing conditions and final printed part properties. Though several different grades of PLA were used for the various investigations, results consistently suggest that minimizing the printed layer height frequently results in the highest tensile properties of a printed part [97]. While the print pattern also drives stress propagation during tensile or torsional deformation, the importance of developing crystallinity in printed PLA is beginning to emerge. Layer height and build plate temperature have proven to be important variables that influence the development of PLA crystallinity. While not defined as "FIC" in the literature, the results of the work of Gardner and coworkers certainly fit the description of FIC [98]. When printing PLA, they discovered that, if all other variables are held constant and the build plate was held at high temperature (160°C), a 0.2 mm layer height contained *more*, *smaller spherulites* than the sample produced with a 0.4 mm layer height. This PLA printed in a 0.2 mm layer height would be, all else the same, subject to higher shear rate than the 0.4 mm counterpart, resulting in an increased nucleation density and ultimate higher percentage of crystalline content, both indicative of FIC. Similarly, Chacón and coworkers found that a thin printed layer thickness combined with a high feed rate is recommended for optimal strength and stiffness [99]. However, the development of good interfacial strength between the printed layers and the resulting interfacial mechanical property development may suffer with increasing PLA crystallization. In a subsequent study, Wang and Gardner [98] confirmed that, as a result of PLA densification due to crystallization at the interface, voids form that ultimately decrease interfacial strength. This serves as a good reminder that one must consider the future mechanical loading of a printed part and design the printing strategy accordingly, maximizing tensile strength in the direction of printing in the anticipation of tensile loading and maximizing interfacial strength if torsional loads are expected.

12 Conclusions

The enhancing effect of flow field on the crystallization kinetics of PLLA has been assessed by several literature works. This phenomenon is obviously extremely significant for engineering applications, which require the melt processing of PLA to produce final parts and demand increasingly custom property profiles, often with the goal of maximizing mechanical properties or controlling the degradation rate of the final thermoplastic product. The state of the art suggests that to achieve a high degree of control and precision, the influence of the PLA properties such as isomer content, molecular weight, and branching must be considered to design proper melt processing conditions that result in controlled flow-induced crystallization and, ultimately, predictable PLA microstructure. In spite of all these studies, all the effects remain phenomenological, and a comprehensive and systematic understanding is not

yet complete. Therefore, ongoing studies must continue to develop these complex relationships before engineering predictable PLA microstructure development becomes commonplace.

References

1. Roozemond PC, van Drongelen M, Peters GWM (2016) Modeling flow-induced crystallization. Springer, Berlin. https://doi.org/10.1007/12_2016_351
2. Pantani R, De Santis F, Sorrentino A, De Maio F, Titomanlio G (2010) Crystallization kinetics of virgin and processed poly(lactic acid). Polym Degrad Stab 95:1148–1159. https://doi.org/10.1016/j.polymdegradstab.2010.04.018
3. Androsch R, Schick C, Di Lorenzo ML (2017) Kinetics of nucleation and growth of crystals of poly(L-lactic acid). Adv Polym Sci 279:235–272. https://doi.org/10.1007/12_2016_13
4. Eling B, Gogolewski S, Pennings AJ (1982) Biodegradable materials of poly(L-lactic acid): 1. Melt-spun and solution-spun fibres. Polymer 23:1587–1593. https://doi.org/10.1016/0032-3861(82)90176-8
5. Cartier L, Okihara T, Ikada Y, Tsuji H, Puiggali J, Lotz B (2000) Epitaxial crystallization and crystalline polymorphism of polylactides. Polymer 41:8909–8919. https://doi.org/10.1016/S0032-3861(00)00234-2
6. Saeidlou S, Huneault MA, Li H, Park CB (2012) Poly(lactic acid) crystallization. Prog Polym Sci 37:1657–1677. https://doi.org/10.1016/j.progpolymsci.2012.07.005
7. Garlotta D (2001) A literature review of poly(lactic acid). J Polym Environ 9:63–84. https://doi.org/10.1023/A:1020200822435
8. Jalali A, Huneault MA, Elkoun S (2017) Effect of molecular weight on the nucleation efficiency of poly(lactic acid) crystalline phases. J Polym Res 24:182. https://doi.org/10.1007/s10965-017-1337-x
9. De Meo A, De Santis F, Pantani R (2018) Dynamic local temperature control in micro-injection molding: effects on poly(lactic acid) morphology. Polym Eng Sci 58:586–591. https://doi.org/10.1002/pen.24784
10. Volpe V, De Filitto M, Klofacova V, De Santis F, Pantani R (2018) Effect of mold opening on the properties of PLA samples obtained by foam injection molding. Polym Eng Sci 58:475–484. https://doi.org/10.1002/pen.24730
11. Zaldua N, Mugica A, Zubitur M, Iturrospe A, Arbe A, Lo RG, Raquez J-M, Dubois P, Müller AJ (2016) The role of PLLA-g-montmorillonite nanohybrids in the acceleration of the crystallization rate of a commercial PLA. CrstEngComm 18:9334–9344. https://doi.org/10.1039/C6CE02005D
12. Tsuji H, Sugiura Y, Sakamoto Y, Bouapao L, Polymer I-S (2008) Crystallization behavior of linear 1-arm and 2-arm poly (L-lactide) s: effects of coinitiators. Polymer 49:1385–1397. https://doi.org/10.1016/j.polymer.2008.01.029
13. Aziz AA, Hay JN, Jenkins MJ (2018) The melting of poly (L-lactic acid). Eur Polym J 100:253–257. https://doi.org/10.1016/j.eurpolymj.2018.01.041
14. Wang J, Bai J, Zhang Y, Fang H, Wang Z (2016) Shear-induced enhancements of crystallization kinetics and morphological transformation for long chain branched polylactides with different branching degrees. Sci Rep 6:26560. https://doi.org/10.1038/srep26560
15. Fang H, Zhang Y, Bai J, Wang Z (2013) Shear-induced nucleation and morphological evolution for bimodal long chain branched polylactide. Macromolecules 46:6555–6565. https://doi.org/10.1021/ma4012126
16. Nam J, Ray S, Okamoto M (2003) Crystallization behavior and morphology of biodegradable {polylactide/layered} silicate nanocomposite. Macromolecules 36:7126–7131. https://doi.org/10.1021/ma034623j

17. Bai J, Wang J, Wang W, Fang H, Xu Z, Chen X, Wang Z (2016) Stereocomplex crystallite-assisted shear-induced crystallization kinetics at a high temperature for asymmetric biodegradable PLLA/PDLA blends. ACS Sustain Chem Eng 4:273–283. https://doi.org/10.1021/acssuschemeng.5b01110
18. De Santis F, Pantani R, Santis F (2013) Nucleation density and growth rate of polypropylene measured by calorimetric experiments. J Therm Anal Calorim 112:1–10. https://doi.org/10.1007/s10973-012-2732-5
19. Li S, Hu Y (2015) Polylactide stereo-complex: from principles to applications. In: Jiménez A, Peltzer M, Ruseckaite R (eds) Poly(lactic acid) science and technology: processing, properties, additives and applications. Royal Society of Chemistry, Cambridge, pp 37–65
20. Rahman N, Kawai T, Matsuba G, Nishida K, Kanaya T, Watanabe H, Okamoto H, Kato M, Usuki A, Matsuda M, Nakajima K, Honma N (2009) Effect of polylactide stereocomplex on the crystallization behavior of poly(L-lactic acid). Macromolecules 42:4739–4745. https://doi.org/10.1021/ma900004d
21. Zou G, Qu X, Zhao C, He Y, Li J (2018) Self-nucleation efficiency of PDLA in PLAs: crystallization behavior and morphology. Polym Sci Ser A 60:206–214. https://doi.org/10.1134/S0965545X18020165
22. Schmidt SC, Hillmyer MA (2001) Polylactide stereocomplex crystallites as nucleating agents for isotactic polylactide. J Polym Sci Part B Polym Phys 39:300–313. https://doi.org/10.1002/1099-0488(20010201)39:3<300::AID-POLB1002>3.0.CO;2-M
23. Song Y, Zhang X, Yin Y, de Vos S, Wang R, Joziasse CAP, Liu G, Wang D (2015) Enhancement of stereocomplex formation in poly(L-lactide)/poly(D-lactide) mixture by shear. Polymer 72:185–192. https://doi.org/10.1016/j.polymer.2015.07.023
24. Fukushima K, Kimura Y (2006) Stereocomplexed polylactides (Neo-PLA) as high-performance bio-based polymers: their formation, properties, and application. Polym Int 55:626–642. https://doi.org/10.1002/pi.2010
25. Ikada Y, Jamshidi K, Tsuji H, Hyon S (1987) Stereocomplex formation between enantiomeric poly(lactides). Macromolecules 20:904–906. https://doi.org/10.1021/ma00170a034
26. Farah S, Anderson DG, Langer R (2016) Physical and mechanical properties of PLA, and their functions in widespread applications – a comprehensive review. Adv Drug Deliv Rev 107:367–392. https://doi.org/10.1016/j.addr.2016.06.012
27. Van De Velde K, Kiekens P (2002) Biopolymers: overview of several properties and consequences on their applications. Polym Test 21:433–442. https://doi.org/10.1016/S0142-9418(01)00107-6
28. Ma Z, Balzano L, Portale G, Peters GWM (2014) Flow induced crystallization in isotactic polypropylene during and after flow. Polymer 55(23):6140–6151. https://doi.org/10.1016/j.polymer.2014.09.039
29. Flory PJ (1949) Thermodynamics of crystallization in high polymers. IV. A theory of crystalline states and fusion in polymers, copolymers, and their mixtures with diluents. J Chem Phys 17:223–240. https://doi.org/10.1063/1.1747230
30. Flory PJ (1947) Thermodynamics of crystallization in high polymers II. Simplified derivation of melting-point relationships. J Chem Phys 15:684. https://doi.org/10.1063/1.1746627
31. Flory PJ (1947) Thermodynamics of crystallization in high polymers. I. Crystallization induced by stretching. J Chem Phys 15:397–408. https://doi.org/10.1063/1.1746537
32. Wang Z, Ma Z, Li L (2016) Flow-induced crystallization of polymers: molecular and thermodynamic considerations. Macromolecules 49:1505–1517. https://doi.org/10.1021/acs.macromol.5b02688
33. van Meerveld J, Peters GWM, Hütter M (2004) Towards a rheological classification of flow induced crystallization experiments of polymer melts. Rheol Acta 44:119–134. https://doi.org/10.1007/s00397-004-0382-7
34. Housmans RJA, Roozemond PC, Peters GWM, Meijer HEH (2009) Saturation of pointlike nuclei and the transition to oriented structures in flow-induced crystallization of isotactic polypropylene. Macromolecules 42:5728–5740. https://doi.org/10.1021/ma802479c

35. Zhong Y, Fang H, Zhang Y, Wang Z, Yang J, Wang Z (2013) Rheologically determined critical shear rates for shear-induced nucleation rate enhancements of poly(lactic acid). ACS Sustain Chem Eng 1:663–672. https://doi.org/10.1021/sc400040b
36. Xu H, Xie L, Hakkarainen M (2015) Beyond a model of polymer processing-triggered shear: reconciling shish-kebab formation and control of chain degradation in sheared poly(L-lactic acid). ACS Sustain Chem Eng 3:1443–1452. https://doi.org/10.1021/acssuschemeng.5b00320
37. Cui K, Ma Z, Tian N, Su F, Liu D, Li L (2018) Multiscale and multistep ordering of flow-induced nucleation of polymers. Chem Rev 118:1840–1886. https://doi.org/10.1021/acs.chemrev.7b00500
38. Seo J, Takahashi H, Nazari B, Rhoades AM, Schaake RP, Colby RH (2018) Isothermal flow-induced crystallization of polyamide 66 melts. Macromolecules 51:4269–4279. https://doi.org/10.1021/acs.macromol.8b00082
39. Mykhaylyk OO, Chambon P, Graham RS, Fairclough JPA, Olmsted PD, Ryan AJ (2008) The specific work of flow as a criterion for orientation in polymer crystallization. Macromolecules 41:1901–1904. https://doi.org/10.1021/ma702603v
40. Rhoades AM, Gohn AM, Seo J, Androsch R, Colby RH (2018) Sensitivity of polymer crystallization to shear at low and high supercooling of the melt. Macromolecules 51:2785–2795. https://doi.org/10.1021/acs.macromol.8b00195
41. Somani RH, Hsiao BS, Nogales A, Fruitwala H, Srinivas S, Tsou AH (2001) Structure development during shear flow induced crystallization of i-PP: in situ wide-angle X-ray diffraction study. Macromolecules 34:5902–5909. https://doi.org/10.1021/ma0106191
42. Somani Hsiao BS, Nogales A, Srinivas S, Tsou AH, Sics I, Balta-Calleja FJ, Ezquerra TARH (2000) Structure development during shear flow-induced crystallization of i-PP: in-situ small-angle X-ray scattering study. Macromolecules 33:9385–9394. https://doi.org/10.1021/ma001124z
43. Liu G, Zhang X, Wang D (2014) Tailoring crystallization: high-performance poly(lactic acid). Adv Mater 26:6905–6911. https://doi.org/10.1002/adma.201305413
44. Xie L, Xu H, Li Z-M, Hakkarainen M (2016) Structural hierarchy and polymorphic transformation in shear-induced shish-kebab of stereocomplex poly(lactic acid). Macromol Rapid Commun 37:745–751. https://doi.org/10.1002/marc.201500736
45. Cicero JA, Dorgan JR, Janzen J, Garrett J, Runt J, Lin JS (2002) Supramolecular morphology of two-step, melt-spun poly(lactic acid) fibers. J Appl Polym Sci 86:2828–2838. https://doi.org/10.1002/app.11267
46. Cicero JA, Dorgan JR, Garrett J, Runt J, Lin JS (2002) Effects of molecular architecture on two-step, melt-spun poly(lactic acid) fibers. J Appl Polym Sci 86:2839–2846. https://doi.org/10.1002/app.11268
47. Gupta B, Revagade N, Hilborn J (2007) Poly(lactic acid) fiber: an overview. Prog Polym Sci 32:455–482. https://doi.org/10.1016/j.progpolymsci.2007.01.005
48. Solarski S, Ferreira M, Devaux E (2005) Characterization of the thermal properties of PLA fibers by modulated differential scanning calorimetry. Polymer 46:11187–11192. https://doi.org/10.1016/j.polymer.2005.10.027
49. Barham P, Keller A (1975) A criterion for distinguishing between polymer fibers of fundamentally different origin. J Polym Sci Polym Lett Ed 13:197–202. https://doi.org/10.1002/pol.1975.130130402
50. Mahendrasingam A, Blundell DJ, Parton M, Wright AK, Rasburn J, Narayanan T, Fuller W (2005) Time resolved study of oriented crystallisation of poly(lactic acid) during rapid tensile deformation. Polymer 46:6009–6015. https://doi.org/10.1016/j.polymer.2005.05.081
51. Fitz BD, Jamiolkowski DD, Andjeli S (2002) Tg depression in poly (L (−)-lactide) crystallized under partially constrained conditions. Macromolecules 35:5869–5872
52. Pogodina NV, Winter HH, Srinivas S (1999) Strain effects on physical gelation of crystallizing isotactic polypropylene. J Polym Sci Part B Polym Phys 37:3512–3519. https://doi.org/10.1002/(SICI)1099-0488(19991215)37:24<3512::AID-POLB12>3.0.CO;2-#

53. Li X, Li Z, Zhong G-J, Li L-B (2008) Steady–shear-induced isothermal crystallization of poly (L-lactide) (PLLA). J Macromol Sci Part B 47:511–522. https://doi.org/10.1080/00222340801955313
54. Huang S, Li H, Jiang S, Chen X, Polymer A-L (2011) Crystal structure and morphology influenced by shear effect of poly (L-lactide) and its melting behavior revealed by WAXD, DSC and in-situ POM. Polymer 15:3487. https://doi.org/10.1016/j.polymer.2011.05.044
55. Li X, Zhong G, Li Z (2010) Non-isothermal crystallization of poly(L-lactide) (PLLA) under quiescent and steady shear conditions. Chinese J Polym Sci 28:357–366. https://doi.org/10.1007/s10118-010-9015-z
56. Yamazaki S, Itoh M, Oka T, Journal K-K (2010) Formation and morphology of "shish-like" fibril crystals of aliphatic polyesters from the sheared melt. Eur Polym J 46:58–68. https://doi.org/10.1016/j.eurpolymj.2009.09.003
57. Xu H, Zhong G-J, Fu Q, Lei J, Jiang W, Hsiao BS, Li Z-M (2012) Formation of Shish-Kebabs in injection-molded poly(L-lactic acid) by application of an intense flow field. ACS Appl Mater Interfaces 4:6774–6784. https://doi.org/10.1021/am3019756
58. De Santis F, Pantani R (2015) Melt compounding of poly (lactic acid) and talc: assessment of material behavior during processing and resulting crystallization. J Polym Res 22:242. https://doi.org/10.1007/s10965-015-0885-1
59. Yang I-K, Wu C-H (2014) Real-time SAXS measurements and rheological behavior of poly (lactic acid) crystallization under continuous shear flow. J Polym Res 21:609. https://doi.org/10.1007/s10965-014-0609-y
60. Bai H, Deng S, Bai D, Zhang Q, Fu Q (2017) Recent advances in processing of stereocomplex-type polylactide. Macromol Rapid Commun 38:1700454. https://doi.org/10.1002/marc.201700454
61. Hemmi K, Matsuba G, Tsuji H, Kawai T, Kanaya T, Toyohara K, Oda A, Endou K (2014) Precursors in stereo-complex crystals of poly(L-lactic acid)/poly(D-lactic acid) blends under shear flow. J Appl Cryst 47:14–21. https://doi.org/10.1107/S1600576713031907
62. Bojda J, Piorkowska E (2016) Shear-induced nonisothermal crystallization of two grades of PLA. Polym Test 50:172–181. https://doi.org/10.1016/j.polymertesting.2016.01.006
63. Shao J, Xiang S, Bian X, Sun J, Li G, Chen X (2015) Remarkable melting behavior of PLA stereocomplex in linear PLLA/PDLA blends. Ind Eng Chem Res 54:2246–2253. https://doi.org/10.1021/ie504484b
64. Song Y, Zhao Q, Yang S, Ru J, Lin J, Xu J, Lei J, Li Z (2018) Flow-induced crystallization of polylactide stereocomplex under pressure. J Appl Polym Sci 135:46378. https://doi.org/10.1002/app.46378
65. Xu J-Z, Li Y, Li Y-K, Chen Y-W, Wang R, Liu G, Liu S-M, Ni H-W, Li Z-M (2018) Shear-induced stereocomplex cylindrites in polylactic acid racemic blends: morphology control and interfacial performance. Polymer 140:179–187. https://doi.org/10.1016/j.polymer.2018.02.048
66. Refaa Z, Boutaous M, Xin S, Fulchiron R (2017) Synergistic effects of shear flow and nucleating agents on the crystallization mechanisms of poly (lactic acid). J Polym Res 24:18. https://doi.org/10.1007/s10965-016-1179-y
67. Wei X-F, Bao R-Y, Gu L, Wang Y, Ke K, Yang W, Xie B-H, Yang M-B, Zhou T, Zhang A-M (2014) Synergistic effect of stereocomplex crystals and shear flow on the crystallization rate of poly(L-lactic acid): a rheological study. RSC Adv 4:2733–2742. https://doi.org/10.1039/C3RA45402A
68. Yin Y, Zhang X, Song Y, de Vos S, Wang R, Joziasse CAP, Liu G, Wang D (2015) Effect of nucleating agents on the strain-induced crystallization of poly(L-lactide). Polymer 65:223–232. https://doi.org/10.1016/j.polymer.2015.03.061
69. Tang H, Chen J-B, Wang Y, Xu J-Z, Hsiao BS, Zhong G-J, Li Z-M (2012) Shear flow and carbon nanotubes synergistically induced nonisothermal crystallization of poly(lactic acid) and its application in injection molding. Biomacromolecules 13:3858–3867. https://doi.org/10.1021/bm3013617

70. Xu J, Chen T, Yang C, Li Z, Mao Y, Zeng B, Hsiao B (2010) Isothermal crystallization of poly (L-lactide) induced by graphene nanosheets and carbon nanotubes: a comparative study. Macromolecules 43:5000–5008. https://doi.org/10.1021/ma100304n
71. Xie X-L, Sang Z-H, Xu J-Z, Zhong G-J, Li Z-M, Ji X, Wang R, Xu L (2017) Layer structure by shear-induced crystallization and thermal mechanical properties of injection-molded poly (L-lactide) with nucleating agents. Polymer 110:196–210. https://doi.org/10.1016/j.polymer.2017.01.004
72. Li C, Guo J, Jiang T, Zhang X, Xia L, Wu H, Guo S, Zhang X (2018) Extensional flow-induced hybrid crystalline fibrils (shish) in CNT/PLA nanocomposite. Carbon 129:720–729. https://doi.org/10.1016/j.carbon.2017.12.063
73. Avolio R, Castaldo R, Avella M, Cocca M, Gentile G, Fiori S, Errico ME (2018) PLA-based plasticized nanocomposites: effect of polymer/plasticizer/filler interactions on the time evolution of properties. Compos Part B Eng 152:267–274. https://doi.org/10.1016/j.compositesb.2018.07.011
74. Kühnert I, Spörer Y, Brünig H, Tran NHA, Rudolph N (2017) Processing of poly(lactic acid). In: Di Lorenzo M, Androsch R (eds) Industrial applications of poly(lactic acid). Springer, Cham, pp 1–33
75. Carrasco F, Pagès P, Gámez-Pérez J, Santana OO, Maspoch ML (2010) Processing of poly (lactic acid): characterization of chemical structure, thermal stability and mechanical properties. Polym Degrad Stab 95:116–125. https://doi.org/10.1016/j.polymdegradstab.2009.11.045
76. Ghosh S, Viana JC, Reis RL, Mano JF (2007) Effect of processing conditions on morphology and mechanical properties of injection-molded poly(L-lactic acid). Polym Eng Sci 47:1141–1147. https://doi.org/10.1002/pen.20799
77. Pantani R, Sorrentino A (2013) Influence of crystallinity on the biodegradation rate of injection-moulded poly(lactic acid) samples in controlled composting conditions. Polym Degrad Stab 98:1089–1096. https://doi.org/10.1016/j.polymdegradstab.2013.01.005
78. De Santis F, Volpe V, Pantani R (2017) Effect of molding conditions on crystallization kinetics and mechanical properties of poly(lactic acid). Polym Eng Sci 57:306–311. https://doi.org/10.1002/pen.24414
79. Harris AM, Lee EC (2007) Improving mechanical performance of injection molded PLA by controlling crystallinity. J Appl Polym Sci 107(4):2246–2255. https://doi.org/10.1002/app.27261
80. Altpeter H, Bevis MJ, Grijpma DW, Feijen J (2004) Non-conventional injection molding of poly(lactide) and poly(epsilon-caprolactone) intended for orthopedic applications. J Mater Sci Mater Med 15:175–184. https://doi.org/10.1023/B:JMSM.0000011820.64572.a5
81. Ghosh S, Viana JC, Reis RL, Mano JF (2008) Oriented morphology and enhanced mechanical properties of poly(L-lactic acid) from shear controlled orientation in injection molding. Mater Sci Eng A 490:81–89. https://doi.org/10.1016/j.msea.2008.01.003
82. Sang Z-H, Chen Y, Li Y, Xu L, Lei J, Yan Z, Zhong G-J, Li Z-M (2018) Simultaneously improving stiffness, toughness, and heat deflection resistance of polylactide using the strategy of orientation crystallization amplified by interfacial interactions. Polym Cryst 1:e10004. https://doi.org/10.1002/pcr2.10004
83. Sankarpandi S, Park CB, Ghosh AK (2017) CO_2-induced crystal engineering of polylactide and the development of a polymeric nacreous microstructure. Polym Int 66:1587–1597. https://doi.org/10.1002/pi.5417
84. Tabatabaei A, Park CB (2017) In-situ visualization of PLA crystallization and crystal effects on foaming in extrusion. Eur Polym J 96:505–519. https://doi.org/10.1016/j.eurpolymj.2017.09.026
85. Ameli A, Nofar M, Jahani D, Rizvi G, Park CB (2015) Development of high void fraction polylactide composite foams using injection molding: crystallization and foaming behaviors. Chem Eng J 262:78–87. https://doi.org/10.1016/j.cej.2014.09.087

86. Mihai M, Huneault MA, Favis BD (2009) Crystallinity development in cellular poly(lactic acid) in the presence of supercritical carbon dioxide. J Appl Polym Sci 113:2920–2932. https://doi.org/10.1002/app.30338
87. Zhai W, Ko Y, Zhu W, Wong A, Park C (2009) A study of the crystallization, melting, and foaming behaviors of polylactic acid in compressed CO2. Int J Mol Sci 10:5381–5397. https://doi.org/10.3390/ijms10125381
88. Yu L, Liu H, Xie F, Chen L, Li X (2008) Effect of annealing and orientation on microstructures and mechanical properties of polylactic acid. Polym Eng Sci 48:634–641. https://doi.org/10.1002/pen.20970
89. Tsai CC, Wu RJ, Cheng HY, Li SC, Siao YY et al (2010) Crystallinity and dimensional stability of biaxial oriented poly (lactic acid) films. Polym Degrad Stab 95(8):1292–1298. https://doi.org/10.1016/j.polymdegradstab.2010.02.032
90. Houichi H, Maazouz A, Elleuch B (2015) Crystallization behavior and spherulitic morphology of poly(lactic acid) films induced by casting process. Polym Eng Sci 55:1881–1888. https://doi.org/10.1002/pen.24028
91. Schmack G, Jehnichen D, Vogel R, Tändler B, Beyreuther R, Jacobsen S, Fritz H-G (2001) Biodegradable fibres spun from poly (lactide) generated by reactive extrusion. J Biotechnol 86:151–160. https://doi.org/10.1016/S0168-1656(00)00410-7
92. Fambri L, Pegoretti A, Fenner R, Incardona SD, Migliaresi C (1997) Biodegradable fibres of poly (L-lactic acid) produced by melt spinning. Polymer 38:79–85. https://doi.org/10.1016/S0032-3861(96)00486-7
93. Shim E, Pourdeyhimi B, Shiffler D (2016) Process-structure-property relationship of melt spun poly(lactic acid) fibers produced in the spunbond process. J Appl Polym Sci 133:47. https://doi.org/10.1002/app.44225
94. Hossain KM, Parsons AJ, Rudd CD, Ahmed I, Thielemans W (2014) Mechanical, crystallisation and moisture absorption properties of melt drawn polylactic acid fibres. Eur Polym J 53:270–281. https://doi.org/10.1016/j.eurpolymj.2014.02.001
95. Northcutt LA, Orski SV, Migler KB, Kotula AP (2018) Effect of processing conditions on crystallization kinetics during materials extrusion additive manufacturing. Polymer 154:182–187. https://doi.org/10.1016/j.polymer.2018.09.018
96. McIlroy C, Graham RS (2018) Modelling flow-enhanced crystallisation during fused filament fabrication of semi-crystalline polymer melts. Addit Manuf 24:323–340. https://doi.org/10.1016/j.addma.2018.10.018
97. Tymrak BM, Kreiger M, Pearce JM (2014) Mechanical properties of components fabricated with open-source 3-D printers under realistic environmental conditions. Mater Des 58:242–246. https://doi.org/10.1016/j.matdes.2014.02.038
98. Wang L, Gramlich WM, Gardner DJ (2017) Improving the impact strength of poly(lactic acid) (PLA) in fused layer modeling (FLM). Polymer 114:242–248. https://doi.org/10.1016/j.polymer.2017.03.011
99. Chacón JM, Caminero MA, García-Plaza E, Núñez PJ (2017) Additive manufacturing of PLA structures using fused deposition modelling: effect of process parameters on mechanical properties and their optimal selection. Mater Des 124:143–157. https://doi.org/10.1016/j.matdes.2017.03.065

Adv Polym Sci (2019) 283: 119–142
https://doi.org/10.1007/12_2019_50

Published online: 21 August 2019

Crystallization of Poly[(R)-3-hydroxybutyrate]

Maria Laura Di Lorenzo and René Androsch

Contents

1 Introduction 120
2 Crystal Structure and Morphology of PHB Crystals 122
3 Crystallization Kinetics of PHB 126
4 The Rigid Amorphous Fraction 129
5 Melting of PHB Crystals 133
6 Conclusions 136
References 136

Abstract Poly[(R)-3-hydroxybutyrate] (PHB) is the first produced and most studied polyhydroxyalkanoate (PHA), a class of polymers that can be synthesized by a variety of bacteria through fermentation. PHB, and with it most PHAs, is produced in vivo, contrarily to all other types of bio-based and biodegradable polymers that are attained by chemical reactions, like polycondensation or ring-opening polymerization. The in vivo polymerization leads to a number of special features, like the absence of catalyst residues and other impurities typically present in synthetic polymers, which can promote crystal nucleation. Moreover, PHB has a perfectly isotactic structure with all chiral carbon atoms in (R)-configuration. These peculiarities make PHB a model compound for the study of polymer crystallization; hence its crystallization behavior has received considerable attention over the years. The main properties of the polymer are presented and discussed, together with literature data

M. L. Di Lorenzo (✉)
Institute of Polymers, Composites and Biomaterials (CNR), Pozzuoli, NA, Italy
e-mail: dilorenzo@ipcb.cnr.it

R. Androsch
Interdisciplinary Center for Transfer-oriented Research in Natural Sciences (IWE TFN), Martin Luther University Halle-Wittenberg, Halle (Saale), Germany
e-mail: rene.androsch@iw.uni-halle.de

on crystal structure and morphology of PHB. This is followed by in-depth analysis of the crystallization kinetics, including both the primary crystal nucleation and crystal growth. Secondary crystallization is also discussed, as it largely affects time-dependent properties of molded PHB products, which progressively becomes brittle upon storage: the glass transition of PHB is around 0°C; hence at room temperature PHB amorphous chains have sufficient mobility to continue to crystallize, which in turn implies also vitrification of part of the amorphous chains coupled with the crystals, the rigid amorphous fraction (RAF). The influence of the RAF on crystallization of PHB is also discussed, since its vitrification during crystallization can hinder or even stop further crystal growth. The analysis of the crystallization behavior of PHB is completed by a thorough discussion of melting of PHB crystals, which also presents a number of notable features.

Keywords Crystal melting · Crystal morphology · Crystallization kinetics · Poly[(R)-3-hydroxybutyrate] · Polyhydroxyalkanoate · Rigid amorphous fraction

1 Introduction

Global dependence on petroleum-derived plastics has increased considerably over the years and with that the apprehension about the environmental effects of synthetically produced materials. This prompted much interest in bio-based polymers, particularly of the biodegradable class. Nowadays, biodegradable polymers produced from natural resources are gaining increasing interest, not only in small-volume fields like biomedical applications but also in packaging and consumer products [1–3]. These biopolymers are mainly polyesters or polyamides, most commonly synthesized by polycondensation or ring-opening polymerization, using metal catalysts. Among these types of polymers, only polyhydroxyalkanoates (PHAs) are produced in vivo, all others are polymerized by chemical reactions [4].

PHAs are linear polyesters synthesized by a variety of bacteria through fermentation of sugars, lipids, alkanes, alkenes, and alkanoic acids [5]. They are produced as discrete cytoplasmic inclusions in bacterial cells and, when extracted from the cells, can exhibit thermoplastic or elastomeric properties, depending on monomer type and chain length/structure. PHAs are not only bio-based but are also recyclable and easily degradable under either aerobic or anaerobic conditions. Compared to other biodegradable polymers, PHAs do not require special environmental conditions to be degraded to carbon dioxide and water; hence they are excellent replacements for petroleum-derived plastics in terms of physical characteristics and biodegradability. PHAs are also biocompatible, a feature exploited for a variety applications in the biomedical field, including screws and plates for cartilage and bone, membranes for periodontal treatment, or filaments for surgical sutures. They are also used for drug delivery, either as bulk material, or in the form of microspheres and microcapsules [6].

The oldest and the most studied PHA is poly[(R)-3-hydroxybutyrate] (PHB) [7–11]. PHB was first synthesized in the 1920s, via extraction from gram-positive bacteria using chloroform [5], but it was only in 1959 that industrial production of PHB started, by W.R. Grace and company. Unfortunately, the low synthesis efficiency and problems encountered with polymer purification forced to close the company [7]. Larger-scale production of PHB started in the 1980s, but still the market is small, compared to other bio-based and biodegradable polymers [7]. However, PHB producers still see potential in this biopolymer, with an estimated demand expected to grow tenfold by 2020 [8].

Major problems that limit a wider use of PHB arise from its poor thermal stability and rather weak mechanical properties [9]. The former complicates industrial processing of the polymer, as thermal degradation occurs at temperatures close to the melting point, with a decrease in molar mass due to chain scission according to a β-hydrogen elimination mechanism [10]. Regarding the mechanical properties, PHB undergoes progressive embrittlement upon storage. Soon after molding, PHB exhibits ductile behavior, but when the molded product is stored at room temperature, the material becomes very brittle [11, 12]. During molding, crystallization usually is incomplete within the processing cycle, due to the low crystallization rate. The glass transition temperature of PHB is around 0°C [13], and during storage at room temperature, the PHB chains exhibit sufficient mobility to further order, leading simultaneously to a gradual increase of the crystallinity and a reduced mobility of molecule segments in the amorphous regions, which causes progressive embrittlement of the material [14–19].

To overcome these drawbacks, (R)-3-hydroxybutyrate is often copolymerized with other hydroxyalcanoates (HA), with about 150 different PHAs known to date [20], or blended with other bio-based or biodegradable polymers [13]. The monomer units constituting the different types of PHAs vary in the lengths of their side chains, rather than in the length of the main chain; most common types include lactate, 4-hydroxybutyrate, 4-hydroxyvalerate, 5-hydroxyvalerate, and 6-hydroxyhexanoate [21]. Properties of PHAs, including the crystallization behavior, largely vary with the chain structure, as it is typical for copolymers. In this review, the focus is instead given to the oldest and most abundant PHA, poly[(R)-3-hydroxybutyrate], with a detailed description of the thermal properties, especially the crystallization and melting behaviors.

A full understanding of crystallization and melting behavior of PHB homopolymer, which can then be tailored by copolymerization or blending, is critical to control material properties and the processing required to obtain products with desired semicrystalline morphologies [22–29]. Interest in the study of crystallization of PHB originates also from the perfect isotactic structure of the polymer chains, with all chiral carbon atoms in (R)-configuration, and to the absence of catalyst residues and other impurities in the bacteria-produced polymer [30] that are often present in synthetic polymers and largely influence the crystallization kinetics. For these reasons, PHB is often used as a model compound for quantitative analysis of time-dependent effects in polymer crystallization and melting [13].

2 Crystal Structure and Morphology of PHB Crystals

Similar to other polyesters, PHB can crystallize into different crystal modifications. Upon crystallization from the quiescent supercooled melt, as well as on solution crystallization, PHB crystallizes into the so-called α-modification. The structure of α-crystals has been determined by X-ray diffraction (XRD) and by energy calculation of the molecular chains. The α-form has two antiparallel chains in the left-handed helix conformation, packed in an orthorhombic unit cell with $a = 0.576$ nm, $b = 1.320$ nm, and c (fiber axis) $= 0.596$ nm, with the space group $P2_12_12_1$ [31–34].

A different crystal modification, named β-form, is recognized as a strain-induced para-crystalline structure with highly extended chains [30] adopting a twisted planar zigzag conformation. The unit cell is also orthorhombic with lattice parameters of $a = 0.528$ nm, $b = 0.920$ nm, and c (fiber axis) $= 0.470$ nm [35, 36]. The XRD patterns of the α- and β-modifications of PHB are illustrated in Fig. 1, together with the respective chain conformations [37].

The metastable β-polymorph was first observed in hot-drawn PHB thin films [32] and later in melt- or electro-spun fibers of PHB [38–43]. The β-form is known to not

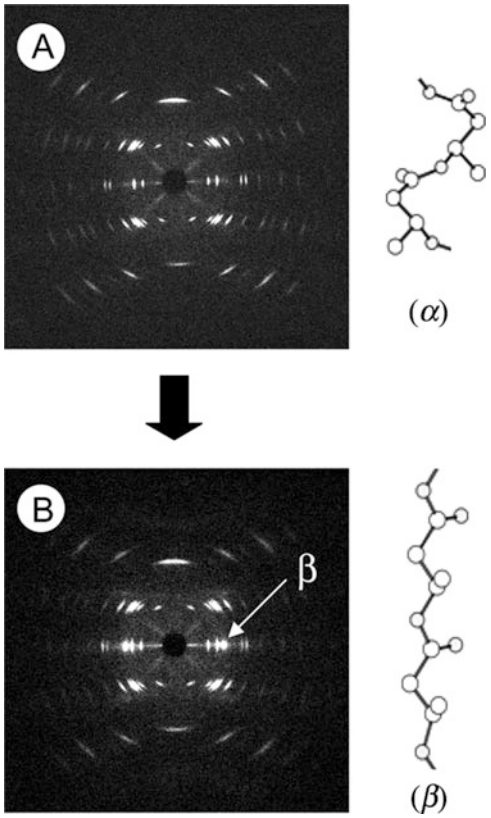

Fig. 1 XRD fiber patterns of stretched films of PHB and the corresponding structure/conformation of molecules. (**a**) Hot-drawn film in which exclusively the α-form crystal with a 2/1 helix conformation is present; (**b**) two-step drawn and annealed film in which both the α- and β-forms are present. In the latter modification, molecules adopt a planar zigzag conformation. Reprinted from Ref. [37]. Copyright (2005) American Chemical Society

undergo secondary crystallization and remains relatively unchanged for months at room temperature [40, 44]. Conversely, in the presence of α-crystals, an increase of crystallinity is observed upon storage at room temperature [11, 12, 14–19], as mentioned above. The β-structure has long been accepted to originate from orientation of the free chains in the amorphous phase between the α-form lamellar crystals [37, 40, 41, 45]. When experiencing high stretching forces, the tie molecules between the lamellar crystals orient along the stretching direction, to adopt a planar zigzag conformation. The formation of β-crystals has a deep impact on material properties, including mechanical response [37–40, 44, 46], biodegradability [41, 47], and piezoelectricity [48].

As typical for semicrystalline polymers, when crystallized in absence of solvents or mechanical solicitation, PHB forms aggregates of lamellae, most commonly of a spherical shape, named spherulites. PHB is usually produced from biological sources and does not contain foreign particles that may act as heterogeneous nucleation sites. This results in a low nucleation density compared to most polymers, with development of extremely large spherulites, whose size can be of the order of few mm, or even cm, under favoring crystallization conditions [13, 49].

PHB forms banded spherulites upon crystallization from the melt, with bands arising from the twisting of lamellar crystals. The periodicity and regularity of the banding texture depend on the crystallization temperature and on the molar mass. Examples of polarized-light optical microscopy (POM) images of banded PHB spherulites are shown in Fig. 2, together with the dependence of the band spacing on the crystallization temperature T_c [50]. The band spacing is non-monotonous with T_c, with a minimum around 60°C. Also, the optical micrographs of Fig. 2 were selected to show the morphology of PHB spherulites grown at the temperature where the minimum band spacing is observed as well as at temperatures above and below that temperature. A lower-molar-mass polymer gives a similar morphology to that obtained at higher crystallization temperatures, when using a higher-molar-mass grade [51]. Microfocus XRD using a synchrotron source was used for a point-to-point radial scan of the X-ray structure of a banded spherulite, with X-ray patterns collected inside each band [49]. This allowed confirming that the crystals smoothly rotate around the *a*-axis with increasing distance from the spherulite center, providing structural evidence that the extinction bands originate from a regular twisting of the lamellar crystals during their growth.

When PHB spherulites are cooled to room temperature, they often display radial cracks departing from the spherulite centers, as well as cracks running circumferentially around spherulites [52–55], as exampled in Fig. 3. It has been initially suggested that the cracks are caused by thermal stresses that develop during cooling from the crystallization temperatures to room temperature [55] or by volume shrinkage occurring upon cooling [52]. More recent analyses evidenced that the cracks seen in POM analyses originate at the contact surfaces between the squeezed polymer and the glass slides and are due to the differences in thermal expansion between the PHB film and the constraining glass slides; only the circumferential cracks are surface features that are caused by volume reduction during crystallization but still originate from constraints imposed by the substrate [54].

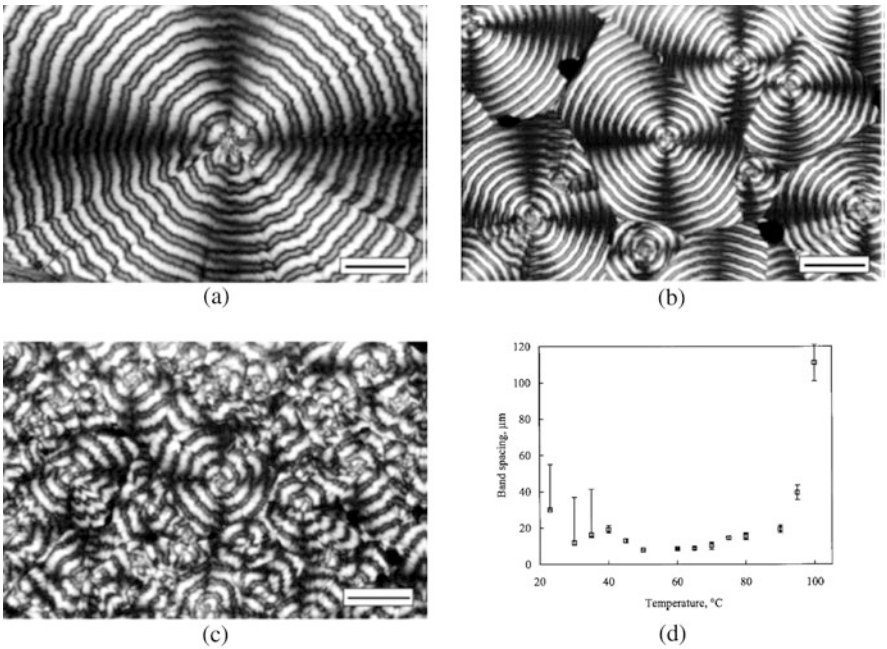

Fig. 2 POM micrographs of PHB spherulites, isothermally crystallized at (**a**) 80°C, (**b**) 50°C, and (**c**) 40°C. The scale bars represent a distance of 100 μm. (**d**) Band spacing in PHB spherulites as function of the crystallization temperature, measured for a PHB grade with weight- and number-average molar masses of 866 and 316 kg/mol, respectively. Adapted from Ref. [50], with permission from Wiley

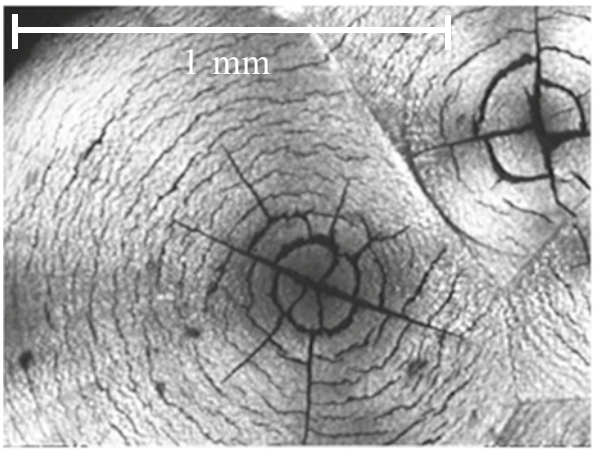

Fig. 3 POM micrograph of a PHB film, crystallized during cooling at 5 K/min, after prior melting at 200°C for 3 min. Reprinted by permission from Ref. [55], Copyright Springer Nature (2006)

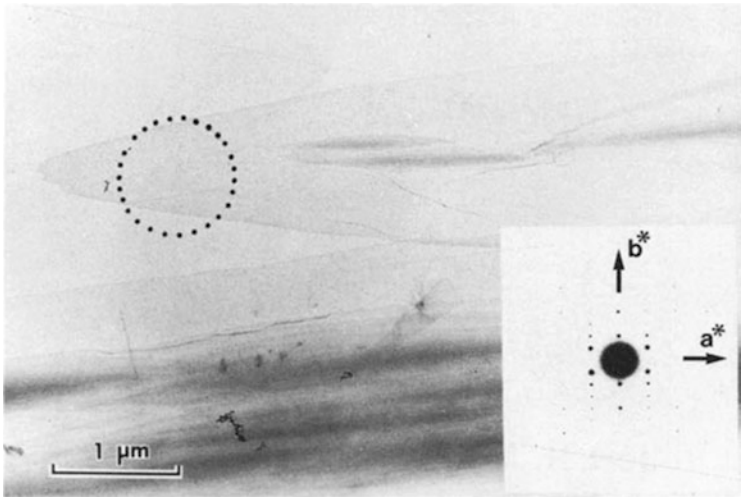

Fig. 4 TEM micrograph and its corresponding electron diffraction pattern of a single crystal of PHB. The circle shows the area from which the electron diffraction pattern was obtained. The crystal image is properly oriented with respect to the inset diffraction pattern. In the original negative, the diffraction spots extended to 0.1 nm resolution. Reprinted from Ref. [56], Copyright (1989), with permission from Elsevier

PHB can also develop single crystals upon precipitation from dilute solutions. Single crystals of PHB have been prepared using a variety of solvents, including poly(ethylene glycol)/methanol, chloroform/ethanol, and propylene carbonate, to name a few [56–69]. Typically, PHB forms lath-shape crystals with dimensions of around 0.3 ± 2 and 5 ± 10 μm for the short and long axes, respectively, as exampled in Fig. 4 that shows a transmission electron microscopy (TEM) image of PHB single crystals prepared from a propylene carbonate solution, at various crystallization temperatures.

All crystals have an elongated arrow-like shape, although the edges seem rough, particularly at low growth temperatures. In some cases, the crystals appear to have a three-dimensional tentlike structure. Selected-area diffraction from part of a crystal indicates that the crystallographic *a*-axis runs along the long direction of each crystal. An increase in temperature leads to formation of smaller crystals with oblong shape and inclined short sides [59]. Electron diffraction of PHB single crystals revealed that the polymer chains are oriented/aligned perpendicular to the base of the crystals and that the long axis of the single crystals is the crystallographic *a*-axis [69]. When PHB single crystals are stretched along the *a*-axis, periodic cracks develop along the long axis, whereas stretching perpendicular to the *a*-axis leads to destruction of the single crystals into small fragments along the long axis [51].

A notable feature of PHB crystals is the unusually low lamellar thickness. At low crystallization temperatures of around 30°C, the thickness of lamellae is only 5–6 nm when formed from the melt, while it is close to 4 nm when grown from solution. The latter only allows for 6 or 7 repeat units per fold stem [51].

3 Crystallization Kinetics of PHB

Polymer crystallization, like many other phase transitions, occurs through a process of nucleation and growth [70, 71]. Nucleation consists in the grouping of a few aligned polymer chain segments, forming a crystalline nucleus. This is followed by attachment of successive layers of polymer chains that leads to crystal growth. Crystallization usually does not stop with growth of the crystals until space filling (impingement), but a process called secondary crystallization occurs, which results in an increase of crystallinity and thickness of the already formed lamellar crystals. Crystallization is often accompanied by vitrification of part of the amorphous chains that are at the interface between crystal and amorphous structure, named rigid amorphous fraction (RAF) [72, 73]. Vitrification of the RAF was shown to interfere with crystal growth and hinders further crystallization for a number of polymers, including PHB [74, 75]; therefore this is treated in a separate paragraph. In this paragraph, main literature results on the kinetics of crystal nucleation and growth of PHB crystals as well as of the overall crystallization kinetics are discussed.

One key difficulty in the analysis of crystallization kinetics of PHB is its high sensitivity to exposure at high temperatures [10, 76, 77]. Heating the polymer to temperatures close to or above its melting point results in a decrease of the molar mass, which, in turn, leads to a faster crystallization [76, 77]. This was quantified for a PHB of molar mass of 435 kg/mol, by measuring the decrease of molar mass with temperature and time of melting [77]. An increase of both melt temperature and residence time leads to a higher extent of degradation, with a corresponding decrease of molar mass. At the same time, if the melting temperature is not high enough, incomplete melting leads to faster crystallization, mostly due to nucleation occurring via self-seeding. Quantitative analysis of the nucleation density of PHB after melting at various temperatures revealed that the temperature of melting needs to be at least 192–193°C to cancel memory of previous crystal order [77].

Due to its bacterial synthesis, PHB does not contain catalyst residues or other impurities that may act as nucleation sites. Therefore crystallization of the polymer often starts from homogeneous nuclei. The homogeneous nucleation kinetics of PHB is displayed in Fig. 5 [78, 79]. Data were measured in a wide temperature range, from 20 to 100°C, for a grade with a mass-average molar mass of 410 kg/mol, and reveal a maximum nucleation rate at 60–80°C. The growth rate of PHB spherulites (G) was quantified by several authors in a wide temperature range, from 30 to 160°C [51, 80–82]. The effect of molar mass was analyzed by Alfonso et al. [80], who reported G-data for PHB samples with molar masses ranging from 7 to 1,000 kg/mol, as shown in Fig. 5 (left). As expected [83], G increases with decreasing chain length. The temperature at which G reaches its maximum value depends on the molar mass and increases from 75 to 90°C when M_w is increased from 7 to 20 kg/mol, without further changes for higher-molar-mass polymers [80]. Analysis of the spherulite growth rates using the Lauritzen-Hoffman theory

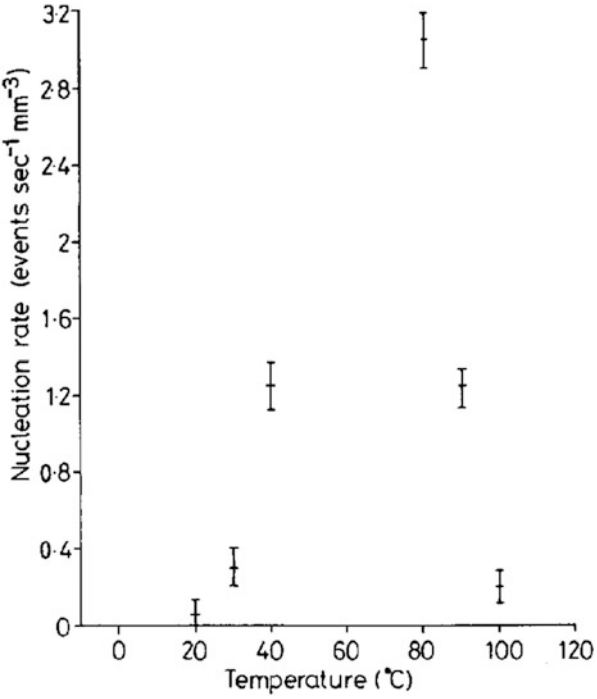

Fig. 5 Nucleation rate as function of temperature, for PHB cooled from the melt. Reprinted by permission from Ref. [78], Copyright Springer Nature (1984)

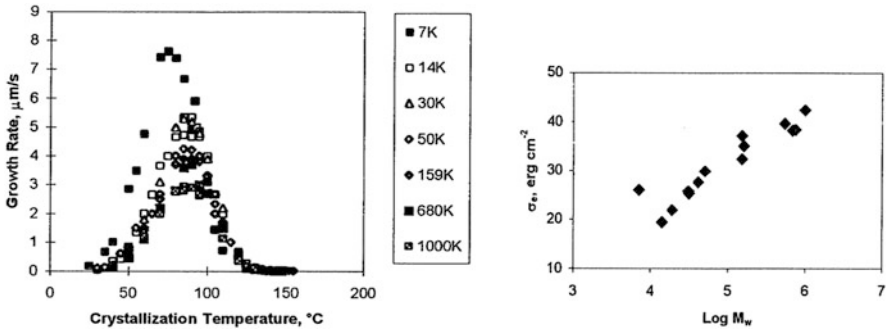

Fig. 6 Spherulite growth rates of PHB of different molar mass as function of crystallization temperature (left). Free energy of surface folding (σ_e) of PHB as function of molar mass (right). Reprinted from Ref. [80]

[83] showed a regime II→III transition at 130–140°C [51, 81]. From this analysis, the free energy of surface folding σ_e was determined as a function of the molar mass, as illustrated in the right part of Fig. 6 [80]; similar values were reported by other authors [81].

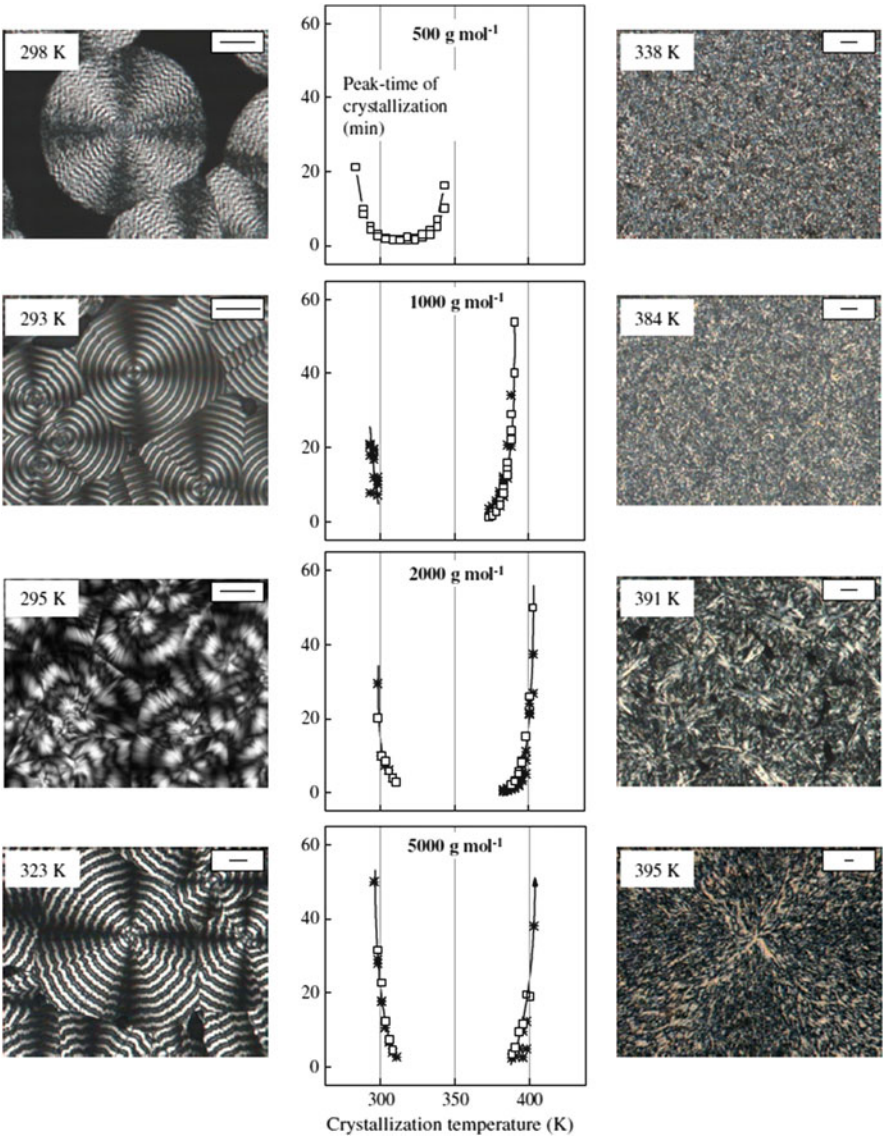

Fig. 7 Peak time of isothermal crystallization as a function of temperature of PHB of a different molecular weight (center graphs) and POM images of samples isothermally crystallized at the indicated temperatures. The scale bars are 20 μm. The different symbols in the graphs of the center column represent data obtained on different DSC instruments, respectively. Reprinted from Ref. [84], Copyright (2007), with permission from Elsevier

Further analysis of the effect of the chain length of PHB on the crystallization kinetics and morphology was conducted on samples with molar masses between 500 and 5,000 g/mol [84]. Figure 7 shows in the center column DSC peak times of

isothermal crystallization as a function of the crystallization temperature. The minimum in each data set corresponds to the temperature where the crystallization rate is maximum. In other words, the larger is the peak time of crystallization, the slower is the crystallization. In the case of PHB with a molar mass of only 500 g/mol, it was possible to collect data at all preselected crystallization temperatures, in contrast to the samples of higher molar mass. Comparison of the crystallization kinetics of the various samples studied reveals that the crystallization temperature range decreases toward lower temperature with decreasing molar mass, which likely is caused by the decrease of the equilibrium melting temperature [85] and of the glass transition temperature [84, 86].

The left and right column images in Fig. 7 show the POM structure after crystallization at high and low supercooling of the melt, respectively. The micrographs reveal spherulitic crystallization, regardless of the molar mass, however, with a distinct effect of the crystallization temperature on the perfection and size of spherulites. For samples with molar masses of 2 and 5 kg/mol, it seems that spherulites formed at low supercooling of the melt are less perfect, e.g., regarding banding or orientation of lamellae, than those formed at high melt supercooling. This observation parallels studies performed on high-molar-mass PHB [51] and on oligohydroxybutyrates of different end-group chemistry [87]. In case of the samples with molar masses of 1,000 and 500 g/mol, the different semicrystalline morphologies obtained after crystallization at high and low temperature are clearly caused by the different nucleation density/rate, as discussed above.

4 The Rigid Amorphous Fraction

Similar to other semicrystalline polymers, PHB has amorphous fractions of different mobility. The mobile amorphous fraction (MAF) is composed of chain segments that devitrify on heating at the glass transition temperature (T_g) of the bulk polymer. The rigid amorphous fraction (RAF) is made of amorphous chain segments coupled with the crystals and devitrifies at higher temperatures than the MAF, due to restraints created by the ordered phase [72, 73].

Vitrification of the RAF is directly linked to growth of the crystal phase and can even stop further crystal growth, as probed specifically for PHB. When the polymer is crystallized upon cooling or heating, ordering of macromolecules drastically slows down as soon as the vitrified RAF hinders the diffusion of chain segments toward the growing crystals [75]. It was found that cold crystallization on heating amorphous PHB proceeds via a two-stage process [75, 88, 89]. First, there is formation and simultaneous vitrification of the RAF, ultimately stopping further crystallization by the creation of an immobilized amorphous layer that surrounds the crystals. Second, upon further increase of the temperature, the RAF mobilizes, allowing the continuation of cold crystallization. Once the amorphous layer coupled with the crystals gained sufficient mobility, crystallization can proceed further [75]. This is illustrated in Fig. 8, which highlights the sequence of thermal events occurring upon cold

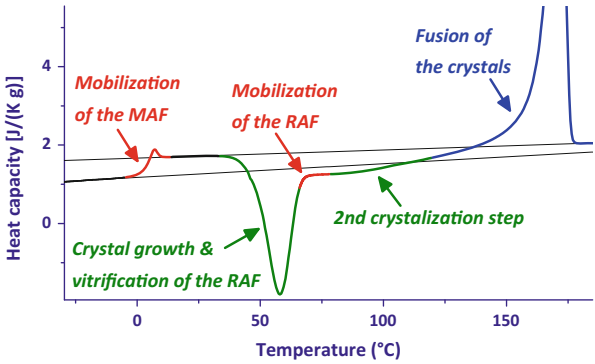

Fig. 8 Apparent heat capacity of initially amorphous PHB, measured upon heating at 20 K/min. The lower and upper solid gray lines represent solid and liquid heat capacities of PHB, respectively, as taken from Ref. [90]. Adapted with permission from Ref. [75]. Copyright (2012) American Chemical Society

crystallization of PHB. Mobilization of the MAF at T_g is followed by a sharp cold crystallization exotherm coupled with RAF formation and vitrification, and only after devitrification of the RAF, cold crystallization can be completed.

Understanding the kinetics of vitrification and devitrification of the RAF is therefore of importance for a full description of crystallization of this polymer. Schick and coworkers probed simultaneous development of the RAF with the crystal fraction at temperatures close to T_g of the MAF [91]. Crystallization at 23°C was measured by quasi-isothermal temperature-modulated DSC (TMDSC), to monitor the decay of the reversing heat capacity ($c_{p,\text{rev}}$) during the crystallization process, shown in the upper part of Fig. 9, and to determine the evolution of latent heat by integration of the average heat flow (HF) rate signal, shown in the lower part of Fig. 9. The crystallinity is obtained from integration of the heat flow rate curve and amounts to 64%. The reversing heat capacity $c_{p,\text{rev}}$ was found frequency-independent, which indicates that it varies only with the crystallinity. It decreases with time together with the progress of crystallization, to reach a value that corresponds to the solid fraction, that is, the crystal fraction and vitrified amorphous phase fraction, being 88%. The $c_{p,\text{rev}}$ vs. time plot determined from the experimental TMDSC data overlaps with the c_p-plot calculated under the assumption of vitrification of the RAF simultaneously to crystal growth, which proves that the RAF forms in parallel to the crystallinity [91].

Vitrification of the RAF in PHB depends on the temperature at which crystallization occurs. The RAF grows in parallel with the crystal phase during quasi-isothermal crystallization at 30°C or lower, as illustrated in Fig. 10, which reports the combined evolution of RAF, MAF, and crystallinity at 30°C. Conversely, during non-isothermal crystallization at higher temperatures, the RAF starts to develop at 70°C, in the final stage of the crystallization process [92]. This was measured for cooling the melt at 2 K/min, and it was found that upon heating at the same rate, the RAF mobilizes at the same temperature at which it had previously formed during cooling, with mobilization of the RAF completed at 70°C [92].

The influence of crystallization conditions on the development of the RAF was also studied. Figure 11 reports the RAF of PHB as function of crystal fraction, measured after cooling the melt at various rates followed by annealing at 25°C

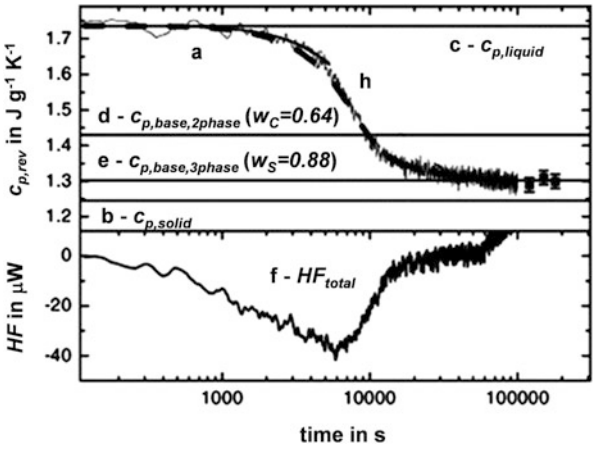

Fig. 9 Time evolution of the reversing heat capacity $c_{p,\mathrm{rev}}$ during quasi-isothermal crystallization of PHB at 23°C (curve *a*). Curves *b* and *c* represent the solid and liquid specific heat capacities, $c_{p,\mathrm{solid}}$ and $c_{p,\mathrm{liquid}}$, respectively. Curves *d* and *e* represent the expected heat capacity assuming a two-phase model (PHB composed of a crystalline fraction and a single amorphous fraction) and a three-phase model (PHB composed of a crystalline fraction, MAF, and RAF). Curve *f* shows the exothermal heat flow rate peak and the thick dashed line *h* the expected heat capacity evolution calculated taking into account RAF formation during crystallization. Adapted from Ref. [91], Copyright (2003), with permission from Elsevier

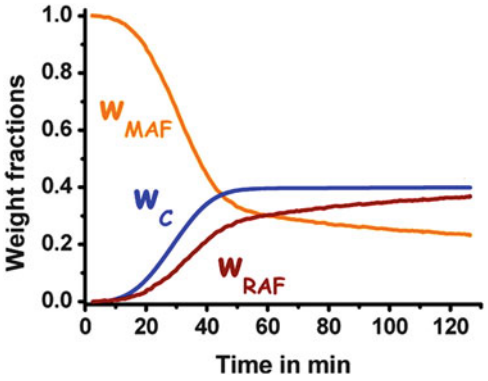

Fig. 10 Time evolution of the crystalline (w_C), mobile amorphous (w_{MAF}), and rigid amorphous (w_{RAF}) fractions of PHB during quasi-isothermal crystallization at $T_c = 30$°C. Adapted from Ref. [92]. Copyright (2013) American Chemical Society

[18]. Rapid cooling of the melt (200 K/min) allows obtaining fully amorphous PHB, with crystallinity only developing during subsequent annealing at room temperature. The early stage of crystal growth at room temperature of initially amorphous PHB is accompanied by vitrification of the amorphous chain portions, which are covalently

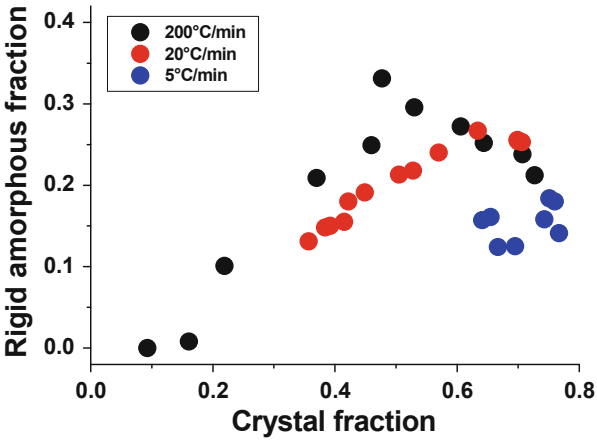

Fig. 11 RAF of PHB after cooling the melt at the indicated rates and annealing at 25°C, plotted as a function of the crystal fraction. Adapted from Ref. [19], Copyright (2013), with permission from Elsevier

coupled with the crystals. The low crystallization temperature limits rearrangements of the polymer chains, with the result that a large RAF develops. After long crystallization at 25°C, when the crystallization rate slows down, any further increase of the crystallinity leads to a reduction of the RAF, as also reported for several other semicrystalline polymers [73]. The maximum in the specific RAF, that is, RAF normalized to the crystal content [93, 94], also matches the end of the fast increase in crystallinity, that is, of the primary crystallization process [18, 19].

Variation of the crystallization path affects also the RAF. When PHB is slowly cooled from the melt, it partially crystallizes upon cooling, and a lower RAF vitrifies. During slower cooling from the melt, PHB crystals start to grow at temperatures higher than 25°C, which facilitates the chain rearrangements toward energetically more favorable conformations and leads to a reduced coupling at the crystal–amorphous phase boundary. Overall, this results in a reduced development of additional crystallinity and RAF during storage at room temperature, as attested by the trend of the maximum attainable RAF, which reaches 33, 27, and 15% when the polymer is annealed at 25°C after cooling at 200, 20, and 5 K/min, respectively. A lower cooling rate implies slower and more complete crystallization occurring at higher temperatures [95]. Despite being largely affected by the initial crystallization conditions, in PHB the RAF/crystallinity ratio seems to tend toward a single value, independent of the initial crystallization conditions, as seen in Fig. 11. This indicates that at 25°C, the three-phase structure in PHB evolves toward a metastable state that involves not only a higher fraction of ordered chains but also a reduced strain within the amorphous regions. The often observed embrittlement of PHB upon storage at room temperature [11, 12] mentioned above is then caused by the increase of both crystal and rigid amorphous fractions.

The RAF in PHB is also affected by molar mass, as proven by comparison of two PHB grades with molar masses of 5 and 500 kg/mol. The lower-molar-mass polymer develops much less RAF at parity of crystallinity [89]. This is illustrated in Fig. 12, which compares the RAF of PHB at the temperature of the glass transition of the

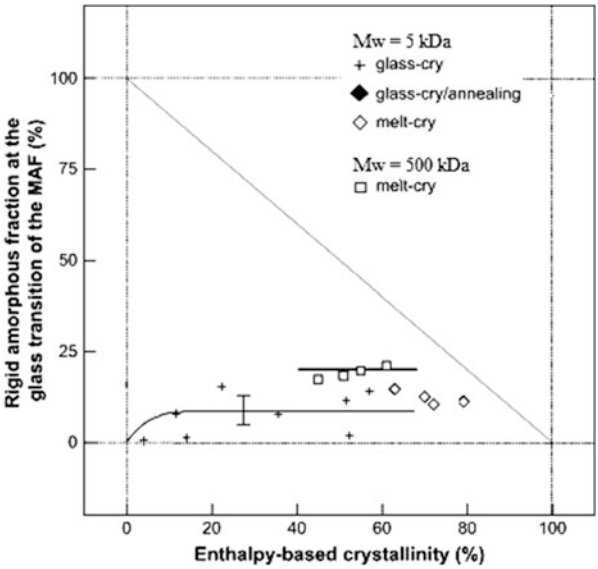

Fig. 12 Rigid amorphous fraction at the temperature of the glass transition of the MAF of PHB of molar mass of 5 and 500 kg/mol of different history of crystallization as a function of enthalpy-based crystallinity. The diagonal black solid line indicates the total amorphous fraction. Adapted from Ref. [89], Copyright (2008), with permission from Elsevier

MAF of the two polymers, after melt or cold crystallization followed by annealing, as a function of enthalpy-based crystallinity, with the diagonal line indicating the total amorphous fraction. It can clearly be recognized that the RAF of low-molar-mass PHB is consistently lower than the RAF in high-molar-mass PHB, which is rationalized taking into account the absence of wide loops/folds, long-chain cilia, and tie molecules in the low-molar-mass polymer [89].

5 Melting of PHB Crystals

Semicrystalline PHB heated at typical DSC rates (5–100 K/min) often displays multiple melting behaviors. The occurrence of multiple melting events may be caused by presence of more than one crystal modification, molecular-weight segregation that accompanies crystallization, different crystal morphologies/size, orientation effects, or reorganization processes that occur during heating [96]. In the case of PHB, it was shown that multiple melting arises from partial melting and recrystallization upon heating, with crystal perfection occurring not via chain sliding diffusion but by partial melting and subsequent melt recrystallization [12, 97–99].

Small- and wide-angle X-ray scattering (SAXS and WAXS) analyses of PHB single crystal showed that the lamellar thickness increases discontinuously upon heating [97, 99]. This is illustrated in Fig. 13, which shows a jump in lamellar thickness around 120–125°C, with the exact discontinuity temperature depending on molar mass as well as on the initial morphology. The lattice dimensions of the orthorhombic α-modification measured during heating at the same rate, presented in

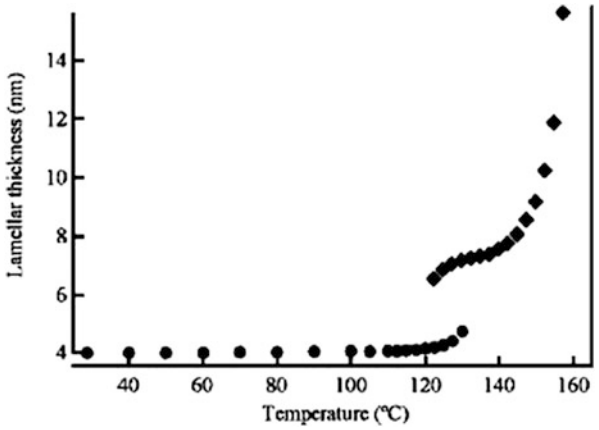

Fig. 13 Temperature dependence of the lamellar thickness of PHB single crystals mats isothermally grown in a 0.05 w/v% 1-octanol solution at 60°C for 24 h, upon heating at 10 K min^{-1}. Adapted from Ref. [97], with permission from Wiley

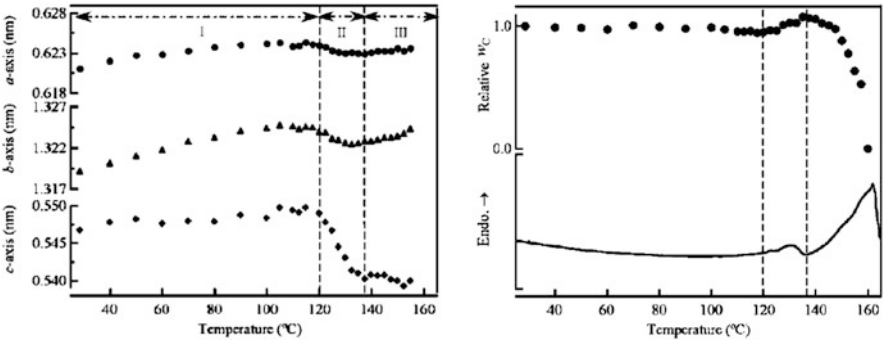

Fig. 14 PHB single crystals mats isothermally grown in a 0.05 w/v% 1-octanol solution at 60°C for 24 h, heated at 10 K min^{-1}: (**a**) lattice dimensions a function of temperature, calculated from the positions of the 200 (*a*-axis), 020 (*b*-axis), and 002 (*c*-axis) peaks; (**b**) crystallinity estimated from 2D-WAXS data as a function of temperature (top data) and DSC curve of the single crystal mats. Adapted from Ref. [97] with permission from Wiley

Fig. 14a, increase gradually up to about 120°C (region I), slightly reduce at temperatures between 120 and 135°C (region II), and finally increase or remain constant (region III) above 135°C. Region II parallels the transition region of lamellar thickening shown in Fig. 13. The crystal fraction, shown in Fig. 14b, starts to slightly decrease from 115–120°C, to reach a minimum around 125°C. Further heating leads to increase of the crystallinity up to 135°C, which finally drastically decreases due to crystal melting. The DSC heat flow rate plot is in line with the structural changes observed by SAXS and WAXS: the first decrease of the crystallinity from 115 to 125°C, which corresponds to the lower side of region II, occurs in

the range of the lower endotherm, indicating that the single crystals melt. The next increase (high-temperature side of region II) is associated with recrystallization, causing an exothermic peak at 136.5°C in the DSC curve. At this temperature, the crystal fraction recovers completely, suggesting that all original crystals completely transform to thicker ones in region II. The parallel evolution of heat flow rate and lattice dimensions in Fig. 14 indicates that the discontinuous increase in thickness of PHB single crystals upon heating is not caused by chain sliding diffusion but by partial melting and subsequent recrystallization [97, 98].

Since recrystallization requires prior melting [100–102], a major effect on the melting behavior is observed at low heating rates. The influence of crystallization temperature and heating rate on multiple melting of PHB was studied [82, 103, 104]. The melting/recrystallization process is more pronounced in samples crystallized at low temperatures, as expected due to the higher supercooling [96] and progressively reduce with increasing the crystallization temperature, since the original crystals, progressively more perfect, melt and recrystallize to a lower extent during a DSC scan. A minimum heating rate of 60 K/min was found to be needed to prevent recrystallization that occurs simultaneously with fusion when the polymer is crystallized at 130°C [104]. Quantitative analysis of the melting profile of PHB original non-reorganized crystals as a function of crystallization time revealed a double dependence on the crystallization time of the extrapolated onset (T_{ons}) and peak (T_p) temperatures of the main melting endotherm. The crystallization time at which T_{ons} and T_p change their trends was found to correspond to the spherulite impingement time, which revealed the link to primary and secondary crystallization, respectively [104].

Reversible melting and crystallization occurring at the lateral surface of crystals was investigated for PHB [89]. In semicrystalline polymers, reversible melting and crystallization refers to melting and crystallization without the need for nucleation. It occurs at the surface of crystals and involves only molecule segments that are in a state of lowered entropy when melted. In other words, it occurs at fold surfaces of crystals which are able for chain-sliding diffusion [105–107] or at the lateral growth faces [108–110]. The degree of reversible melting and crystallization, that is, the amount of material undergoing the phase transformation per temperature change [93, 94], is significantly affected by the crystal morphology [111–113]. Reversible crystal growth in the chain direction is not considered as the major mechanism in the case of PHB since it requires mobility of amorphous molecule segments near the crystal basal planes, in combination with capability of the polymer to perform chain-sliding diffusion through the crystal.

Molar mass largely affects reversible melting of PHB. As shown in Fig. 12 above, the rigid amorphous fraction of low-molar-mass PHB of 5 kg/mol is only 5–10% and at best half of that of high-molar-mass PHB of 500 kg/mol, despite identical crystallinity. This result is paralleled by observation of distinctly larger degree of reversible melting and crystallization in PHB of high molar mass [89]. The larger rigid amorphous fraction and higher degree of reversible melting and crystallization in PHB of high molar mass, consistently and independently, prove enhanced covalent coupling of crystals and amorphous structure, and/or de-coupling of segments of macromolecules which traverse between phases, respectively.

Largely scattered data appeared in the literature on the equilibrium melting temperature (T_m^o) of PHB. T_m^o is the melting temperature of a crystal with infinite size and without defects [96], a fundamental thermodynamic parameter needed to determine, for instance, the free energies of fold and lateral surfaces and the work required to fold a macromolecule [114]. The equilibrium melting temperature of PHB, obtained with Thomson-Gibbs equation, is around 200°C for PHB grades with molar masses between 130 and 400 kg/mol [51, 115, 116]. Lower T_m^o values were determined with the Hoffman-Weeks procedure, with T_m^o ranging from 186 to 198°C for samples with molar masses of 100–350 kg/mol [79, 85, 117–125]. Both the Hoffman-Weeks and the Thomson-Gibbs methods rely on a number of assumptions and approximations, and more reliable approaches, using nonlinear extrapolations, have been proposed [126, 127]. Using this approach, $T_m^o = 238$°C was determined for a PHB with molar mass $M_n = 260$ kg/mol [128].

6 Conclusions

In this review, a comprehensive summary of the present knowledge of the crystallization behavior of PHB is provided. It includes information about the kinetics of crystallization, the structure of crystals, as well as semicrystalline morphologies forming as a result of specific crystallization pathways. Specific features of crystallization of PHB arise from its production by bacteria fermentation, which leads to generation of a polymer that does not contain catalyst residues or other particles that may act as heterogeneous nuclei and which typically accelerate crystallization. The low nuclei density, together with the rather low crystal growth rate, often causes large superstructures and tendency for low-temperature secondary crystallization/aging. Both have detrimental effects on, e.g., mechanical properties, which, however, can be compensated by blending or copolymerization. The rather poor mechanical behavior of the PHB homopolymer is contrasted by excellent degradability which, together with its environment-friendly synthesis/production, may be considered as a major argument for continuation of research about the rather complicated relationship between melt-processing, structure, and properties. Biodegradability and production of the plastics from short-term renewable resources, as true for PHB, is highly demanded by the human society to protect our environment and may predict further development for this polymer, so far underestimated.

References

1. Bastioli C (2005) Handbook of biodegradable polymers. Rapra Technology, Shawbury
2. Zini E, Scandola M (2011) Green composites: an overview. Polym Compos 32:1905–1915

3. Reddy MM, Vivekanandhan S, Misra M, Bhatia SK, Mohanty AK (2013) Biobased plastics and bionanocomposites: current status and future opportunities. Prog Polym Sci 38:1653–1689
4. Chen GQ (2010) Plastics from bacteria. Microbiology monographs. Springer, Berlin
5. Philip S, Keshavarz T, Roy I (2007) Polyhydroxyalkanoates: biodegradable polymers with a range of applications. J Chem Technol Biotechnol 82:233–247
6. Roohi KB, Zaheer MR, Kuddus M (2018) PHB: (poly-β-hydroxybutyrate) and its enzymatic degradation. Polym Adv Technol 29:30–40
7. Możejko-Ciesielska J, Kiewisz R (2016) Bacterial polyhydroxyalkanoates: still fabulous? Microbiol Res 192:271–282
8. Aeschelmann F, Carus M et al (2015) Bio-based building blocks and polymers in the world – capacities, production and applications: status quo and trends toward. http://www.bio-based.eu/market_study/media/files/15-05-13_Bio-based_Polymers_and_Building_Blocks_in_the_World-nova_Booklet.pdf. Accessed 31 May 2018
9. Doi Y (1990) Microbial polyesters. VCH Publishers, New York
10. Kunioka M, Doi Y (1990) Thermal degradation of microbial copolyesters: poly(3-hydroxybutyrate-co-3-hydroxyvalerate) and poly (3-hydroxybutyrate-co-4-hydroxybutyrate). Macromolecules 23:1933–1936
11. de Koning GJM, Lemstra PJ (1993) Crystallization phenomena in bacterial poly[(R)-3-hydroxybutyrate]: 2 embrittlement and rejuvenation. Polymer 34:4089–4094
12. de Koning GJM, Scheeren AHC, Lemstra PJ, Peeters M, Reynaers H (1994) Crystallization phenomena in bacterial poly[(R)-3-hydroxybutyrate]: 3 toughening via texture changes. Polymer 35:4598–4605
13. Di Lorenzo ML, Raimo M, Cascone E, Martuscelli E (2001) Poly(3-hydroxybutyrate)-based copolymers and blends: influence of a second component on crystallization and thermal behavior. J Macromol Sci B 40:639–667
14. Biddlestone F, Harris A, Hay JN, Hammond T (1996) The physical ageing of amorphous poly(hydroxybutyrate). Polym Int 39:221–229
15. Hurrell BL, Cameron RE (1998) A wide-angle X-ray scattering study of the ageing of poly (hydroxybutyrate). J Mater Sci 33:1709–1713
16. Alata H, Aoyama T, Inoue Y (2007) Effect of aging on the mechanical properties of poly(3-hydroxybutyrate-co-3-hydroxyhexanoate). Macromolecules 40:4546–4551
17. Bergmann A, Owen A (2004) Dielectric relaxation spectroscopy of poly[(R)-3-hydroxybutyrate] (PHB) during crystallization. Polym Int 53:863–868
18. Di Lorenzo ML, Righetti MC (2013) Evolution of crystal and amorphous fractions of poly[(R)-3-hydroxybutyrate] upon storage. J Therm Anal Calorim 112:1439–1446
19. Di Lorenzo ML, Righetti MC (2013) Effect of thermal history on the evolution of crystal and amorphous fractions of poly[(R)-3-hydroxybutyrate] upon storage at ambient temperature. Eur Polym J 49:510–517
20. Raza ZA, Abid S, Banat IM (2018) Polyhydroxyalkanoates: characteristics, production, recent developments and applications. Int Biodet Biodegr 126:45–56
21. Gogolewski S, Jovanovic M, Perren SM, Dillon JG, Hughes MK (1993) The effect of melt-processing on the degradation of selected polyhydroxyacids: polylactides, polyhydroxybutyrate, and polyhydroxybutyrate-co-valerates. Polym Degrad Stab 40:313–322
22. Chuah JA, Yamada M, Taguchi S, Sudesh K, Doi Y, Numata K (2013). Polym Degrad Stab 98:331–338
23. Gunaratne LMWK, Shanks RA (2005) Multiple melting behaviour of poly(3-hydroxybutyrate-co-hydroxyvalerate) using step-scan DSC. Eur Polym J 41:2980–2988
24. Reddy CS, Ghai R, Rashmi, Kalia VC (2003) Polyhydroxyalkanoates: an overview. Bioresour Technol 87:137–146
25. Renstad R, Karlsson S, Albertsson AC, Werner PE, Westdahl M (1997) Influence of processing parameters on the mass crystallinity of poly(3-hydroxybutyrate-co-3-hydroxyvalerate). Polym Int 43:201–209

26. Yoshie N, Fujiwara M, Ohmori M, Inoue Y (2001) Temperature dependence of cocrystallization and phase segregation in blends of poly(3-hydroxybutyrate) and poly(3-hydroxybutyrate-co-3-hydroxyvalerate). Polymer 42:8557–8563
27. Ziaee Z, Supaphol P (2006) Non-isothermal melt- and cold-crystallization kinetics of poly(3-hydroxybutyrate). Polym Test 25:807–818
28. Abdelwahab MA, Flynn A, Chiou B, Imam S, Orts W, Chiellini E (2012) Thermal, mechanical and morphological characterization of plasticized PLA–PHB blends. Polym Degrad Stab 97:1822–1828
29. Canetti M, Urso M, Sadocco P (1999) Influence of the morphology and of the supermolecular structure on the enzymatic degradation of bacterial poly(3-hydroxybutyrate). Polymer 40:2587–2594
30. Laycock B, Halley P, Pratt S, Werker A, Lant P (2014) The chemomechanical properties of microbial polyhydroxyalkanoates. Prog Polym Sci 39:397–442
31. Okamura K, Marchessault RH (1967) X-ray structure of poly-b-hydroxybutyrate. In: Ramachandran GM (ed) Conformation of biopolymers, vol 2. Academic Press, New York, pp 709–720
32. Yokouchi M, Chatani Y, Tadokoro H, Teranishi K, Tani H (1973) Structural studies of polyesters: 5. Molecular and crystal structures of optically active racemic poly(β-hydroxybutyrate). Polymer 14:267–272
33. Cornibert J, Marchessault RH (1972) Physical properties of poly-β-hydroxybutyrate IV. Conformational analysis and crystalline structure. J Mol Biol 71:735–756
34. Brückner S, Meille SV, Malpezzi L, Cesaro A, Navarini L, Tombolini R (1988) The structure of poly(D-(2)-β-hydroxybutyrate). A refinement based on the Rietveld method. Macromolecules 21:967–972
35. Iwata T, Tanaka T (2010) Manufacturing of PHA as fibers. In: Chen GGQ (ed) Plastics from bacteria: natural functions and applications. Springer, Berlin, pp 257–282
36. Murakami R, Sato H, Dybal J, Iwata T, Ozaki Y (2007) Formation and stability of β-structure in biodegradable ultra-high-molecular-weight poly(3-hydroxybutyrate) by infrared, Raman, and quantum chemical calculation studies. Polymer 48:2672–2680
37. Iwata T, Fujita M, Aoyagi Y, Doi Y, Fujisawa T (2005) Time-resolved X-ray diffraction study on poly[(R)-3-hydroxybutyrate] films during two-step-drawing: generation mechanism of planar zigzag structure. Biomacromolecules 6:1803–1809
38. Iwata T, Aoyagi Y, Fujita M, Yamane H, Doi Y, Suzuki Y, Takeuchi A, Uesugi K (2004) Processing of a strong biodegradable poly[(R)-3-hydroxybutyrate] fiber and a new fiber structure revealed by micro-beam X-ray diffraction with synchrotron radiation. Macromol Rapid Commun 25:1100–1104
39. Furuhashi Y, Imamura Y, Jikihara Y, Yamane H (2004) Higher order structures and mechanical properties of bacterial homo poly(3-hydroxybutyrate) fibers prepared by cold-drawing and annealing processes. Polymer 45:5703–5712
40. Antipov EM, Dubinsky VA, Rebrov AV, Nekrasov YP, Gordeev SA, Ungar G (2006) Strain-induced mesophase and hard-elastic behaviour of biodegradable polyhydroxyalkanoates fibers. Polymer 47:5678–5690
41. Iwata T, Aoyagi Y, Tanaka T, Fujita M, Takeuchi A, Suzuki Y, Uesugi K (2006) Microbeam X-ray diffraction and enzymatic degradation of poly[(R)-3-hydroxybutyrate] fibers with two kinds of molecular conformations. Macromolecules 39:5789–5795
42. Tanaka T, Yabe T, Teramachi S, Iwata T (2007) Mechanical properties and enzymatic degradation of poly[(R)-3-hydroxybutyrate] fibers stretched after isothermal crystallization near Tg. Polym Degrad Stab 92:1016–1024
43. Gong L, Chase DB, Noda I, Liu J, Martin DC, Ni C, Rabolt JF (2015) Discovery of β-form crystal structure in electrospun poly[R-3-hydroxybutyrate-co-R-3-hydroxyhexanoate] (PHBHx) nanofibers: from fiber mats to single fibers. Macromolecules 48:6197–6205
44. Aoyagi Y, Doi Y, Iwata T (2003) Mechanical properties and highly ordered structure of ultra-high-molecular-weight poly[(R)-3-hydroxybutyrate] films: effects of annealing and two-step drawing. Polym Degrad Stab 79:209–216

45. Tanaka F, Doi Y, Iwata T (2004) The deformation of the chain molecules and crystallites in poly([R]-3-hydroxybutyrate) and poly(4-hydroxybutyrate) under tensile stress. Polym Degrad Stab 85:893–901
46. Tanaka T, Fujita M, Takeuchi A, Suzuki Y, Uesugi K, Ito K, Fujisawa T, Doi Y, Iwata T (2006) Formation of highly ordered structure in poly[(R)-3-hydroxybutyrate-co-(R)-3-hydroxyvalerate] high-strength fibers. Macromolecules 39:2940–2946
47. Ishii D, Lee WK, Kasuya KI, Iwata T (2007) Fine structure and enzymatic degradation of poly[(R)-3-hydroxybutyrate] and stereocomplexed poly(lactide) nanofibers. J Biotechnol 132:318–324
48. Fukada E, Ando Y (1986) Piezoelectric properties of poly-β-hydroxybutyrate and copolymers of β-hydroxybutyrate and β-hydroxyvalerate. Int J Biol Macromol 8:361–366
49. Gazzano M, Focarete M, Riekel C, Ripamonti A, Scandola M (2001) Structural investigation of poly(3-hydroxybutyrate) spherulites by microfocus X-ray diffraction. Macromol Chem Phys 202:1405–1409
50. Hobbs JK, Binger DR, Keller A, Barham PJ (2000) Spiralling optical morphologies in spherulites of poly(hydroxybutyrate). J Polym Sci B Polym Phys 38:1575–1583
51. Barham PJ, Keller A, Otun EL, Holmes PJ (1984) Crystallization and morphology of a bacterial thermoplastic: poly-3-hydroxybutyrate. J Mater Sci 19:2781–2794
52. Barham PJ, Keller A (1986) The relationship between microstructure and mode of fracture in polyhydroxybutyrate. J Polym Sci Polym Phys 24:69–77
53. Martinez-Salazar J, Sanchez-Cuesta M, Barham PJ, Keller A (1989) Thermal expansion and spherulite cracking in 3-hydroxybutyrate/3-hydroxyvalerate copolymers. J Mater Sci Lett 8:490–492
54. Hobbs JK, McMaster TJ, Miles MJ, Barham PJ (1996) Cracking in spherulites of poly (hydroxybutyrate). Polymer 37:3241–3246
55. Di Lorenzo ML, Sajkiewicz P, La Pietra P, Gradys A (2006) Irregularly shaped DSC exotherms in the analysis of polymer crystallization. Polym Bull 57:713–721
56. Revol JF, Chanzy HD, Deslandes Y, Marchessault RH (1989) High resolution electron microscopy of poly(β-hydroxybutyrate). Polymer 30:1973–1976
57. Lundgren DG, Alper R, Schnaitman C, Marchessault RH (1965) Characterization of poly-β-hydroxybutyrate extracted from different bacteria. J Bacteriol 89:245–251
58. Marchessault RH, Coulombe S, Morikawa H, Okamura K, Revol JF (1981) Solid-state properties of poly-β-hydroxybutyrate and its oligomers. Can J Chem 59:38–44
59. Mitomo H, Barham PJ, Keller A (1987) Crystallization and morphology of poly(β-hydroxybutyrate) and its copolymer. Polym J 19:1241–1253
60. Sudesh K, Abe H, Doi Y (2000) Synthesis, structure and properties of polyhydroxyalkanoates: biological polyesters. Prog Polym Sci 25:1503–1555
61. Marchessault RH, Bluhm TL, Deslandes Y, Hamer GK, Orts WJ, Sundararejan PR, Taylor MG, Bloembergen S, Holden DA (1988) Poly(β-hydroxyalkanoates): biorefinery polymers in search of applications. Macromol Symp 19:235–254
62. Welland EL, Stejny J, Hatler A, Keller A (1989) Selective degradation of chain-folded single crystals of poly(β-hydroxybutyrate). Polym Commun 30:302–304
63. Seebach D, Bürger HM, Müller HM, Lengweiler UD, Beck A, Sykes KE, Barker PA, Barham PJ (1994) Synthesis of linear oligomers of (R)-3-hydroxybutyrate and solid-state structural investigations by electron microscopy and X-ray scattering. Helv Chim Acta 77:1099–1123
64. Sykes KE, McMaster TJ, Miles MJ, Barker PA, Barham PJ, Seebach D, Müller HM, Lengweiler UD (1995) Direct imaging of the surfaces of poly(β)hydroxybutyrate and hydroxybutyrate oligomers by atomic force microscopy. J Mater Sci 30:623–627
65. Birley C, Briddon J, Sykes KE, Barker PA, Organ SJ, Barham PJ (1995) Morphology of single crystals of poly(hydroxybutyrate) and copolymers of hydroxybutyrate and hydroxyvalerate. J Mater Sci 30:633–638
66. Iwata T, Doi Y, Kasuya K, Inoue Y (1997) Visualization of enzymatic degradation of poly[(R)-3-hydroxybutyrate] single crystals by an extracellular PHB depolymerase. Macromolecules 30:833–839

67. Iwata T, Doi Y, Tanaka T, Akehata T, Shiromo M, Teramachi S (1997) Enzymic degradation and adsorption on poly[(R)-3-hydroxybutyrate] single crystals with two types of extracellular PHB depolymerase. Macromolecules 30:5290–5296
68. Iwata T, Doi Y (1999) Crystal structure and biodegradation of aliphatic polyester crystals. Macromol Chem Phys 200:2429–2442
69. Sudesh K, Abe H (2010) Practical guide to microbial polyhydroxyalkanoates1st edn. Smithers Rapra, Shawbury, p 26
70. Wunderlich B (1976) Macromolecular physics. Nucleation, crystallization, annealing, vol 2. Academic Press, New York
71. Mandelkern L (2004) Crystallization of polymers: volume 2, kinetics and mechanisms. Cambridge University Press, Cambridge
72. Wunderlich B (2003) Reversible crystallization and the rigid–amorphous phase in semicrystalline macromolecules. Prog Polym Sci 28:383–450
73. Di Lorenzo ML, Righetti MC (2018) Crystallization-induced formation of rigid amorphous fraction. Polym Cryst 2018:e10023
74. Wunderlich B (2012) Termination of crystallization or ordering of flexible, linear macromolecules. J Therm Anal Calorim 109:1117–1132
75. Di Lorenzo ML, Gazzano M, Righetti MC (2012) The role of the rigid amorphous fraction on cold crystallization of poly(3-hydroxybutyrate). Macromolecules 45:5684–5691
76. El-Hadi A, Schnabel R, Straube E, Müller G, Riemschneider M (2002) Effect of melt processing on crystallization behavior and rheology of poly(3-hydroxybutyrate) (PHB) and its blends. Macromol Mater Eng 287:363–372
77. Di Lorenzo ML, Sajkiewicz P, Gradys A, La Pietra P (2009) Optimization of melting conditions for the analysis of crystallization kinetics of poly(3-hydroxybutyrate). e-Polymers 9(1):1–12
78. Barham PJ (1984) Nucleation behaviour of poly-3-hydroxy-butyrate. J Mater Sci 19:3826–3834
79. Organ SJ, Barham PJ (1991) Nucleation, growth and morphology of poly(hydroxybutyrate) and its copolymers. J Mater Sci 26:1368–1374
80. Alfonso, GC, Castellano M, Casarino P, Bertoli L (1997) Effetto della massa molecolare nella cristallizzazione del PHB. In: Atti del XIII Convegno Italiano di Scienza e Tecnologia delle Macromolecole, Genova, 21–25 Sept 1997, p 237
81. Pearce R, Brown GR, Marchessault RH (1994) Crystallization kinetics in blends of isotactic and atactic poly(β-hydroxybutyrate). Polymer 35:3984–3989
82. Cimmino S, Iodice P, Martuscelli E, Silvestre C (1998) Poly(3-D(−)hydroxybutyrate)/atactic poly(methylmethacrylate) blends: morphology, miscibility and crystallization relationships. Thermochim Acta 321:89–98
83. Hoffman JD, Davis GT, Lauritzen JI (1976) Treatise on solid state chemistry, vol 3. Plenum Press, New York. Chap. 7
84. Androsch R, Radusch H-J, Funari SS (2007) Crystallization, glass transition and morphology of (R)-3-hydroxybutyrate oligomers. Eur Polym J 43:4961–4974
85. Organ SJ, Barham PJ (1993) On the equilibrium melting temperature of polyhydroxybutyrate. Polymer 34:2169–2174
86. Fox TG, Flory PJ (1950) Second-order transition temperatures and related properties of polystyrene. I. Influence of molecular weight. J Appl Phys 21:581–591
87. Organ SJ, Li J, Terry AE, Barham PJ (2006) Morphology and growth of a hydroxybutyrate oligomer with 24 repeat units. Polymer 47:5513–5522
88. Scandola M, Pizzoli M, Ceccorulli G, Cesaro A, Paoletti S, Navarini L (1988) Viscoelastic and thermal properties of bacterial poly(D-(−)-β-hydroxybutyrate). Int J Biol Macromol 10:373–377
89. Androsch R (2008) Surface structure of folded-chain crystals of poly(R-3-hydroxybutyrate) of different chain length. Polymer 49:4673–4679
90. Schick C, Wurm A, Mohamed A (2002) Dynamics of reversible melting revealed from frequency dependent heat capacity. Thermochim Acta 392−393:303–313

91. Schick C, Wurm A, Mohammed A (2003) Formation and disappearance of the rigid amorphous fraction in semicrystalline polymers revealed from frequency dependent heat capacity. Thermochim Acta 396:119–132
92. Righetti MC, Tombari E, Di Lorenzo ML (2013) The role of the crystallization temperature on the nanophase structure evolution of poly[(R)-3-hydroxybutyrate]. J Phys Chem B 117:12303–12311
93. Androsch R, Wunderlich B (2003) Specific reversible melting of polymers. J Polym Sci Polym Phys 41:2039–2051
94. Androsch R, Wunderlich B (2003) Specific reversible melting of polyethylene. J Polym Sci Polym Phys 41:2157–2173
95. Di Lorenzo ML, Silvestre C (1999) Non-isothermal crystallization of polymers. Prog Polym Sci 24:917–950
96. Wunderlich B (1980) Macromolecular physics. Crystal melting, vol 3. Academic Press, New York
97. Fujita M, Sawayanagi T, Tanaka T, Iwata T, Abe H, Doi Y, Ito K, Fujisawa T (2005) Synchrotron SAXS and WAXS studies on changes in structural and thermal properties of poly[(R)-3-hydroxybutyrate] single crystals during heating. Macromol Rapid Commun 26:678–683
98. Heo K, Yoon J, Jin KS, Jin S, Sato H, Ozaki Y, Satkowski MM, Noda I, Ree M (2008) Structural evolution in microbial polyesters. J Phys Chem B 112:4571–4582
99. Mitomo H, Doi Y (1999) Lamellar thickening and cocrystallization of poly(hydroxyalkanoate)s on annealing. Int J Biol Macromol 25:201–205
100. Furushima Y, Schick C, Toda A (2018) Crystallization, recrystallization, and melting of polymer crystals on heating and cooling examined with fast scanning calorimetry. Polym Cryst 1:e10005
101. Androsch R, Zhuravlev E, Schick C (2014) Solid-state reorganization, melting and melt-recrystallization of conformationally disordered crystals (α'-phase) of poly(L-lactic acid). Polymer 55:4932–4941
102. Jariyavidyanont K, Androsch R, Schick C (2017) Crystal reorganization of poly (butylene terephthalate). Polymer 124:274–283
103. Pearce R, Marchessault RH (1994) Multiple melting in blends of isotactic and atactic poly(β-hydroxybutyrate). Polymer 35:3990–3997
104. Righetti MC, Di Lorenzo ML (2011) Melting temperature evolution of non-reorganized crystals. Poly(3-hydroxybutyrate). Thermochim Acta 512:59–66
105. Strobl G, Schneider M, Voigt-Martin I (1980) Model of partial crystallization and melting derived from small-angle X-ray scattering and electron microscopic studies on low-density polyethylene. J Polym Sci Polym Phys 18:1361–1381
106. Hu W, Albrecht T, Strobl G (1999) Reversible surface melting of PE and PEO crystallites indicated by TMDSC. Macromolecules 32:7548–7554
107. Okazaki I, Wunderlich B (1997) Reversible melting in polymer crystals detected by temperature-modulated differential scanning calorimetry. Macromolecules 30:1758–1764
108. Ishikiriyama K, Wunderlich B (1997) Melting of poly(oxyethylene) analyzed by temperature-modulated calorimetry. Macromolecules 30:4126–4131
109. Androsch R, Wunderlich B (2001) Reversible crystallization and melting at the lateral surface of isotactic polypropylene crystals. Macromolecules 34:5950–5960
110. Pak J, Wunderlich B (2001) Melting and crystallization of polyethylene of different molar mass by calorimetry. Macromolecules 34:4492–4503
111. Pak J, Wunderlich B (2002) Reversible melting of polyethylene extended-chain crystals detected by temperature-modulated calorimetry. J Polym Sci Polym Phys 40:2219–2227
112. Androsch R, Wunderlich B, Radusch H-J (2005) Analysis of reversible melting in polytetrafluoroethylene. J Therm Anal Calorim 79:615–622
113. Androsch R, Wunderlich B (2000) Analysis of the degree of reversibility of crystallization and melting in poly(ethylene-co-1-octene). Macromolecules 33:9076–9089

114. Gohil RM, Patel KC, Patel RD (1974) Crystallization kinetics of polyacrylonitrile: single crystal growth rate and thermodynamic considerations. Polymer 15:402–406
115. Orts WJ, Marchessault RH, Bluhm TL (1991) Thermodynamics of the melting point depression in poly(β-hydroxybutyrate-co-β-hydroxyvalerate) copolymers. Macromolecules 24:6435–6438
116. Abe H, Doi Y, Aoki H, Akehata T (1998) Solid-state structures and enzymatic degradabilities for melt-crystallized films of copolymers of (R)-3-hydroxybutyric acid with different hydroxyalkanoic acids. Macromolecules 31:1791–1797
117. Avella M, Martuscelli E (1988) Poly-d-(−)(3-hydroxybutyrate)/poly(ethylene oxide) blends: phase diagram, thermal and crystallization behavior. Polymer 29:1731–1737
118. Dubini Paglia E, Beltrame PL, Canetti M, Seves A, Mercandalli B, Martuscelli E (1993) Crystallization and thermal behaviour of poly (d(−) 3-hydroxybutyrate)/poly(epichlorohydrin) blends. Polymer 34:996–1001
119. Biddlestone F, Harris A, Hammond T (1996) The physical ageing of amorphous poly (hydroxybutyrate). Polym Int 39:221–229
120. Xing P, Dong L, An Y, Feng Z, Avella M, Martuscelli E (1997) Miscibility and crystallization of poly(β-hydroxybutyrate) and poly(p-vinylphenol) blends. Macromolecules 30:2726–2733
121. Al-Salah HA (1998) Crystallization and morphology of poly(ethylene succinate) and poly (β-hydroxybutyrate) blends. Polym Bull 41:593–600
122. Yoon JS, Oh SH, Jim MN (1998) Compatibility of poly(3-hydroxybutyrate)/poly(ethylene-co-vinyl acetate) blends. Polymer 39:2479–2487
123. An Y, Dong L, Li G, Mo Z, Feng Z (2000) Miscibility, crystallization kinetics, and morphology of poly(β-hydroxybutyrate) and poly(methyl acrylate) blends. J Polym Sci Polym Phys 38:1860–1867
124. Chan CH, Kummerlöwe C, Kammer HW (2004) Crystallization and melting behavior of poly (3-hydroxybutyrate)-based blends. Macromol Chem Phys 205:664–675
125. Hsu SF, Wu TM, Liao CS (2006) Isothermal crystallization kinetics of poly(3-hydroxybutyrate)/layered double hydroxide nanocomposites. J Polym Sci Polym Phys 44:3337–3347
126. Marand H, Xu J, Srinivas S (1998) Determination of the equilibrium melting temperature of polymer crystals: linear and nonlinear Hoffman−weeks extrapolations. Macromolecules 31:8219–8229
127. Xu J, Srinivas S, Marand H, Agarwal P (1998) Equilibrium melting temperature and undercooling dependence of the spherulitic growth rate of isotactic polypropylene. Macromolecules 31:8230–8242
128. Righetti MC, Di Lorenzo ML (2012) Nonlinear determination of the equilibrium melting temperature from initial nonreorganized crystals of poly(3-hydroxybutyrate). Polym Eng Sci 52:2383–2390

Adv Polym Sci (2019) 283: 143–188
https://doi.org/10.1007/12_2019_47

Published online: 18 June 2019

Thermal Properties of Biobased Polyamide 11

Katalee Jariyavidyanont, Walter Focke, and René Androsch

Contents

1 Introduction 144
1.1 History 144
1.2 Synthesis 145
1.3 Structure, Properties, and Applications 146
1.4 Specific Features of PA 11 in Comparison to Other Polyamides 146
2 Thermodynamic Functions and Heat Capacity 149
3 Supermolecular Structure 154
3.1 Thermal-Pathway-Controlled Crystal Polymorphism 154
3.2 Nucleation-Controlled Semicrystalline Morphologies 157
4 Shear-Induced Crystallization 162
5 Thermomechanical Behavior 164
5.1 Temperature Dependence of Young's Modulus of PA 11 of Different Semicrystalline Morphology 164
5.2 Thermomechanical Performance of PA 11-Based Nanocomposites 166
6 Thermal Stability and Flame Retardancy of PA 11 170
6.1 Thermal Stability 170
6.2 Thermal Decomposition 171
6.3 Thermo-oxidative Degradation 172
6.4 Flame Retardancy 173
7 Summary 176
References 177

K. Jariyavidyanont and R. Androsch (✉)
Interdisciplinary Center of Transfer-Oriented Research in Natural Sciences, Martin Luther University Halle-Wittenberg, Halle, Germany
e-mail: rene.androsch@iw.uni-halle.de

W. Focke
Institute of Sustainable Malaria Control and Institute of Applied Materials, Department of Chemical Engineering, University of Pretoria, Pretoria, South Africa

Abstract Polyamide 11 (PA 11) is a semicrystalline high-performance thermoplastic engineering polymer with increasing production volume due to its balanced property profile and since it is produced from short-term renewable natural resources. In this review comprehensive information about thermal properties are provided. After an introduction in which general information about synthesis, structure, properties, and applications are given, the thermodynamic functions of state of the melt and crystal phase are provided, needed to predict equilibrium structural states at a given temperature. This is followed by a detailed description of structure formation from the relaxed melt, among others, considering different crystal-nucleation routes as a tool to generate PA 11 of largely different semicrystalline morphology, as well as by providing information about shear-induced crystallization which is relevant for understanding structure formation in processing. Application-relevant thermal-mechanical behavior is discussed based on the temperature dependence of Young's modulus, which is controlled by the initial structure at ambient temperature and which can be further tailored by modifying the polymer with nanofillers. In the final chapter, the thermal stability and current efforts to increase the flame retardancy of this important polymer are summarized.

Keywords Crystal polymorphism · Mechanical properties · Phase structure · Polyamide 11 · Thermal properties

1 Introduction

1.1 History

Polyamide 11 (PA 11) is a biobased high-performance polymer produced from renewable castor oil, containing long sequences of ten methylene units between neighbored amide groups within the chains. The history of PA 11 began more than 80 years ago; however, its development is sustainably moving forward due to its outstanding properties and thus a wide range of applications [1]. Inspired by the work of Carothers, in 1938, Joseph Zeltner found that undecanoic acid, which can be produced from castor oil, may be used to possibly synthesize a polyamide resin. The first synthesis of PA 11, however, was delayed due to the World War II and the death of Zeltner and was then only successful in the early 1940s, by Marcel Kastner and Michel Genas who inherited Zeltner's attempt. PA 11 has been commercialized under the trade name Rilsan® in the late 1940s by the company Organico which was later taken over in 1980s by Atochem [1, 2]. Today, the main manufacturer of biobased PA 11 is Arkema in France, offering a wide range of more than 30 different PA 11 grades, to be used in a variety of applications [3]. The production plants are located in France (Serquigny), the USA (Birdsboro), and China (Zhangjiagang) [1]. Furthermore, Arkema intends to have a new plant located in Asia to increase the global PA 11 production capacity from at present about 21,000 t/a by 50% in late 2021 [4, 5].

1.2 Synthesis

PA 11 is synthesized from castor oil which is an important feedstock highly demanded in industry due to its short-term renewability by nature, and non-competition as a primary food source, at best as a food additive [6, 7]. It consists of about 90% of unsaturated 18 carbon fatty acid, called ricinoleic acid, which is used as a feedstock of the PA 11 production, and about 10% of other fatty acids also extracted from the castor plant as side products [8]. The synthesis of 11-ω-aminoundecanoic acid, needed for the polycondensation reaction to yield PA 11, is shown in Fig. 1 [4, 9]. Methyl ricinoleic acid is first extracted from castor oil by methanolysis, that is, by transesterification using methyl alcohol. After that, pyrolysis of the methyl ricinoleic acid is performed at a temperature of about 500°C to obtain methyl undecylenic acid and, as a side product, heptaldehyde which is used for fragrances and other applications. The methyl undecylenic acid is then hydrolyzed to give undecylenic acid which is later treated with hydrogen bromide in peroxide and then with ammonia to obtain 11-ω-aminoundecanoic acid. The 11-ω-aminoundecanoic acid is used as a raw material/monomer for subsequent polycondensation, to yield PA 11.

The monomer 11-ω-aminoundecanoic acid is a solid crystalline powder which melts at around 190°C. As such the polycondensation to PA 11 is performed slightly above 200°C in an inert nitrogen atmosphere, permitting the removal of water during the course of the condensation reaction. It is reported that formation of cyclic oligomers is negligible and that phosphoric and phosphorous acids are catalyzing the polycondensation reaction by blocking the amino ($–NH_2$) end group, yielding polymers of increased melt viscosity [9].

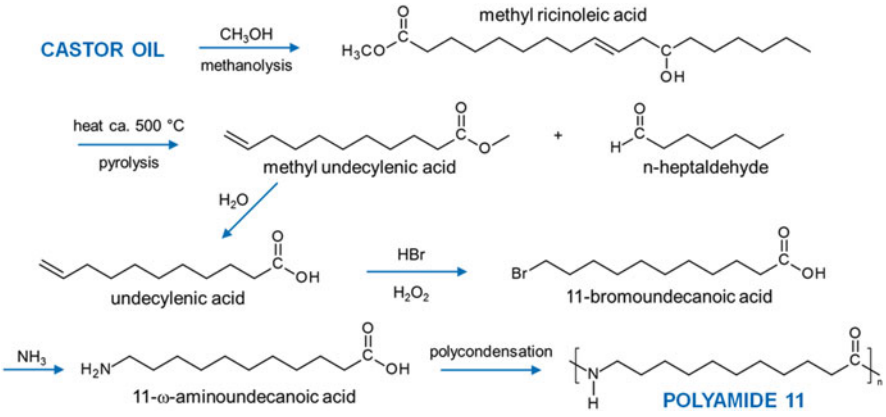

Fig. 1 Processing of castor oil to 11-ω-aminoundecanoic acid [4, 9]

1.3 Structure, Properties, and Applications

PA 11 is a crystallizable polymer and exhibits polymorphism, depending on crystallization conditions, with details provided below. Typically, after melt processing, the material is semicrystalline at ambient temperature, often containing lamellar crystals, grown to form a spherulitic superstructure. The maximum crystal fraction, similar as in the case of other linear polyamides, is well below 50%, however, contributing to its balanced property profile. PA 11 has good resistance to chemicals and solvents, including low permeability to oxygen and hydrocarbons which are optimal properties for using it for flexible pipes of oil and gas in offshore and onshore applications and for fluid transfer lines and air brake systems in automotive. PA 11 also shows excellent impact resistance specifically at low temperature down to about −40°C and good thermal stability up to temperatures of around 150°C. A further outstanding characteristic of PA 11 compared to other polyamides is its low moisture absorption, yielding a good dimensional stability. Therefore, it is utilized for electrical cable sheathing or as hydraulic and pneumatic hoses related to its high- and low-temperature performance and its applicability in a wide range of humidity environments. Owing to its rather low density, PA 11 is used in applications where high-specific strength is important such as for sporting goods like racket eyelets and bumpers, badminton shuttlecocks, or sport shoes [10]. Apart from these mainly extrusion- and injection-molding-based applications, it is also converted using rotomolding [11], while 3D printing using selective laser sintering is an important emerging new application [12, 13]. It is also used in some electronic device applications since it exhibits piezoelectricity and ferroelectricity, due to the large dipole moment of the amide groups in the molecular backbone [14–17].

1.4 Specific Features of PA 11 in Comparison to Other Polyamides

Polyamides are well-known engineering thermoplastics showing rather high melting temperatures/thermal stability, excellent toughness and impact strength, good abrasion resistance, low gas, and vapor permeability, thus being used in a wide range of high-performance engineering applications. Their outstanding properties are also related to the presence of hydrogen bonds between neighbored chains/amide groups, with their density then affecting literally all properties including the melting temperature or moisture absorption [2, 18].

Figure 2 shows the melting point of various polyamides with different concentration of amide groups within the repeat unit of the chains [2, 19]. The increases of the melting temperature with increasing concentration of amide groups in even-even-, odd-, and even-numbered polyamides are indicated with the black, red, and blue data points/lines, respectively, revealing that it is not only the hydrogen-bond concentration affecting the melting temperature but also their perfection/strength

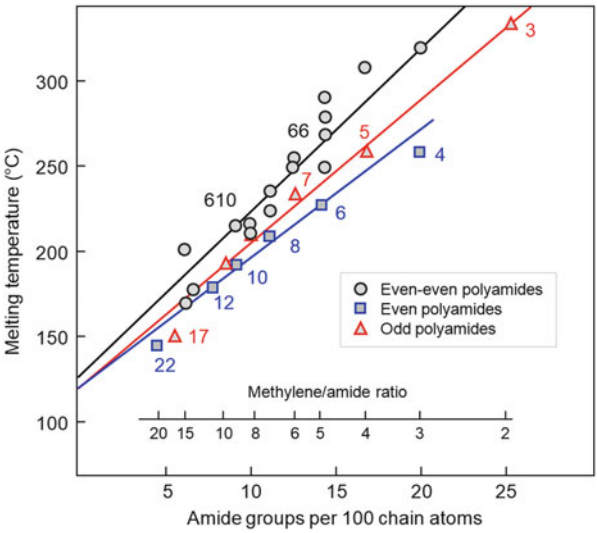

Fig. 2 Melting temperature of different aliphatic polyamides as a function of concentration of amide groups within the chain [2, 19]. Adapted/reproduced with kind permission from Hanser Publisher [2]

which is controlled by the packing characteristics of chain segments in the crystal. Within the odd-polyamide family, PA 11 shows a rather low melting temperature due to its long methylene sequence, or high methylene/amide group ratio, in its chain. Since the melting temperature is controlled also by the bulk enthalpy of melting, it was suggested that the latter quantity is also affected by the hydrogen-bond characteristics between neighbored amide groups [20]. Note that the specific heat of melting of polyethylene (PE) crystals (293 J/g [21]) is distinctly higher than that of polyamide crystals (e.g., 189–244 J/g in case of PA 11, discussed below in Sect. 2) despite a higher equilibrium melting temperature of the latter. This observation indicates that the melting temperature is not only controlled by the enthalpy of melting but also the entropy of melting.

Regarding the glass transition temperature T_g of the amorphous phase, a similar systematic effect of the length of the methylene sequence between the amide groups within the chains is observed. Figure 3 shows with the circles experimentally observed T_g values of selected polyamides clearly showing that T_g decreases with increasing methylene sequence length [22]. When treating the polyamides as copolymers consisting of a PA 6 unit and a PE unit with a specific number of methylene groups, then the data fit the Gordon-Taylor equation [23], as shown with the solid line in Fig. 3. Note that the T_g data were obtained by dynamic mechanical analysis (DMA) on heating in a controlled atmosphere; however, unfortunately, information about the moisture content of the samples as well as crystallinity, both affecting the glass transition, were not provided.

Regarding the effect of the molecular architecture of aliphatic polyamides on mechanical properties, the modulus of elasticity of isolated chains was modeled, considering their cross section as adapted within the crystal phase as well as the length of the repeat unit. The calculations revealed that the modulus is proportional to the repeat distance and inversely proportional to the cross-sectional area. As such,

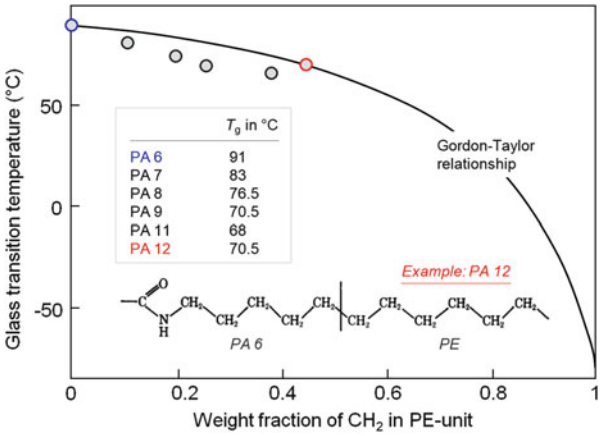

Fig. 3 Glass transition temperature of different aliphatic polyamides plotted as a function of concentration of methylene units in the chain. Data adapted/reproduced from [22] with kind permission from Wiley. The solid line represents the Gordon-Taylor relationship for predicting the glass transition temperature in copolymers [23]

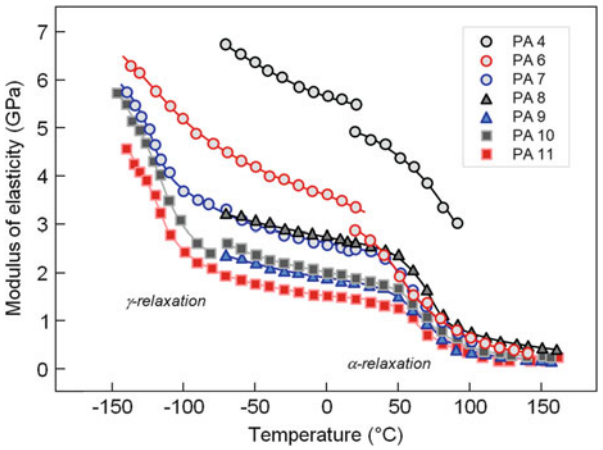

Fig. 4 Modulus of elasticity as a function of temperature for different ω-amino acid polymers, as indicated in the legend. Data were obtained by DMA using a frequency of 100 Hz. Data adapted/reproduced from [26] with kind permission from Wiley

the modulus of elasticity changes in the order PA 6 > PA 11 > PA 6.10 > PA 6.6 > PA 7, accounting for that in case of PA 6 and PA 11, chain cross-sectional area is lowest, compared to the other polyamides studied [24].

Comparison of the mechanical behavior of different polyamides in a semicrystalline state is difficult, since being affected by the specific morphology forming as a result of the crystallization pathway, including crystal fraction, crystal habit, and crystal superstructure. Nonetheless, in the literature, few attempts of comparing different polyamides regarding the mechanical characteristics are available [25, 26]. Among others, it was observed by DMA that the magnitude of the elastic modulus increases with the concentration of the amide groups in the chains. For illustration, in Fig. 4 is shown the modulus of elasticity of different polyamides as a function of temperature, clearly showing that the modulus of PA 4 with the highest amide-group concentration of the sample set investigated (top curve) is distinctly higher than in case of PA 11 (bottom curve) [26]. Moreover, in particular the loss-factor data

Table 1 Moisture absorption of different polyamides at 50 and 100% relative humidity (RH) [2, 18]

Polyamide	Water absorption at 23°C (m%)	
	50% RH	100% RH
46	3.8	15.0
66	2.5	8.5
6	2.8	9.5
69	1.8	4.5–5.0
610	1.4	3.3
612	1.2	3.0
11	1.0	1.9
12	0.8	1.6

(not shown) allowed identification of different dispersion regions [26]. Relaxation at about −120°C (γ-dispersion) was attributed to cooperative movement of methylene units between amide linkages, as the area of the corresponding loss-factor peak is linearly proportional to the number of methylene units between amide groups [26, 27]. Relaxation at around −50°C (β-dispersion, not seen in Fig. 4) is related to segmental motion involving non-hydrogen-bonded amide groups [26, 28], while the α-relaxation above 50°C groups represents the main glass transition.

The observation of a relatively low level of stiffness of semicrystalline PA 11 compared to the other polyamides investigated, despite the chain stiffness which is expected superior [24], may be attributed to the lower strength of hydrogen-bond-controlled intermolecular bonding and the rather low crystallinity. In contrast, PA 11 exhibits improved ductility and impact strength, e.g., compared to PA 6 [29].

PA 11 is less sensitive to moisture absorption than many other polyamides with a higher concentration on amide groups. Basically, molecular chains of polyamides exhibit polarity, featuring hydrophilic behavior which causes tendency of polyamide to absorb moisture. Since moisture absorption correlates with the number of amide groups/hydrogen bonds, and since PA 11 contains longer methylene sequences in its structure, there is relatively low moisture absorption. Table 1 is a listing of the percentage water absorption of polyamides at 23°C and at different relative humidity (RH) [2, 18]. As such, moisture absorption of PA 11 is 2.8 times lower than in case of PA 6 at 50% RH and even five times lower at 100% RH.

2 Thermodynamic Functions and Heat Capacity

The thermal properties of PA 11, like heat capacity, thermal expansion, or thermal conductivity, and the thermal behavior, that is, the material performance on changing the temperature, depend on the phase structure. As a function of the conditions of solidification of the melt, PA 11 may be fully amorphous at ambient temperature, or semicrystalline, containing one or more crystalline phases of different structure and stability. According to Gibbs' phase rule [30], for a one-component system, only a single phase is in equilibrium at given temperature T and pressure p, except at

specific conditions defined by coexistence lines or points in the T, p phase diagram. The thermodynamic stability of phases typically is judged by the free enthalpy G which is available as a function of temperature for the amorphous and crystalline phases of PA 11 together with the temperature dependence of the enthalpy H and entropy S [31]. These integral thermodynamic functions of state are derived from calculated or experimentally observed heat-capacity data according to Eqs. (1–3), as detailed in the literature [32, 33]:

$$G(T) = H(T) - T \times S(T) \tag{1}$$

$$H(T) = \int_{T_0}^{T} c_p \mathrm{d}T + H_0(T_0) + \Delta H_t \tag{2}$$

$$S(T) = \int_{T_0}^{T} c_p / T \mathrm{d}T + \Delta S_t \tag{3}$$

Integration of the heat capacity c_p from zero K (T_0) to the temperature of interest (T) yields the enthalpy $H(T)$ (Eq. 2), with H_0 being the unknown enthalpy of the crystal phase at T_0 and ΔH_t any latent heat contribution to the total enthalpy by first-order phase transformations in the temperature range from T_0 to T, like crystal-crystal phase transitions or melting. The temperature dependence of the entropy S (Eq. 3) is calculated in analogy to the enthalpy by integration of the term c_p/T, while the experimentally not-assessable entropy of first-order phase transitions ΔS_t at the equilibrium transition temperature $T_{t,0}$ equals $\Delta H_t/T_{t,0}$. With the availability of $H(T)$ and $S(T)$, Gibbs enthalpy can be derived according to Eq. (1) for each phase of interest.

Heat-capacity data for the amorphous and crystalline phases of PA 11 are reported in the literature and shown as a function of temperature with the gray squares and blue circles, respectively, in Fig. 5 [31, 34–36]. Below the glass transition temperature T_g at 316 K, the heat capacity of the glassy amorphous phase ($c_{p,\mathrm{glass}}$) is identical to that of the crystalline phase ($c_{p,\mathrm{cry}}$) since both are solid. The heat capacity of solids ($c_{p,\mathrm{solid}}$), that is, of the amorphous phase below T_g and of crystals, is attributed to skeletal and group vibrations, that is, torsion- and accordion-like motions of the backbone and motions of relatively isolated groupings of atoms along the backbone, respectively. Group vibrations of different kind, however, get increasingly excited at higher temperature, such that the heat capacity of crystals first approaches and then even exceeds the heat capacity of the liquid phase [37–40].

The heat capacity of the liquid phase ($c_{p,\mathrm{liquid}}$), that is, of the amorphous phase above T_g, is higher than that of the solid phase since the vibrations valid in the solid-phase motions now also include cooperative large-amplitude rotations, changes of conformations, and translations. The heat capacity on devitrification of the solid glass at T_g increases steplike by 69 J/(mol K) [= 183 g/mol × 0.38 J/(g K); 183 g/mol is the molar mass of the repeat unit] and increases with temperature related to the increase of the free volume. The heat-capacity step at T_g often is

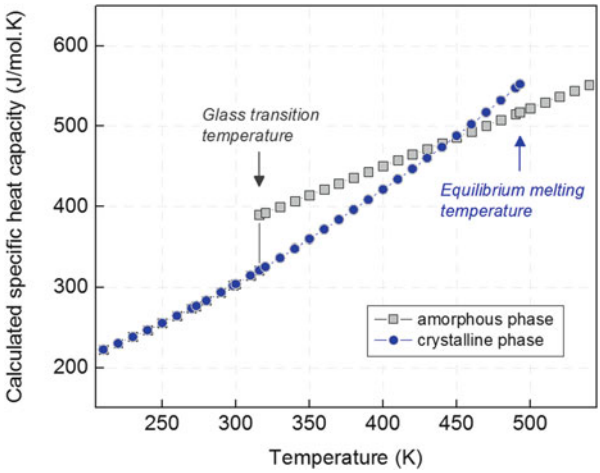

Fig. 5 Calculated specific heat capacities of the amorphous phase (gray squares) and crystalline phase (blue circles) of PA 11 as a function of temperature. The glass transition temperature of the amorphous phase and the equilibrium melting temperature of the crystalline phase are indicated with the arrows. Data were taken from [31]

approximated by the number of beads, that is, by the number of smallest molecular units gaining mobility at T_g [41]. For most polymers it was found that each unit contributes to the total heat-capacity step about 11 J/(mol K); however, in case of polyamides, in general, it seemed to reduce to 7.7 ± 1.3 J/(mol K) [36]. The temperature dependence of the heat capacity of the liquid phase of PA 11 then can be approximated by a linear function, as shown with Eq. (4) in which c_p and T are given in units of J/(mol K) and K, respectively:

$$c_{p,\text{liquid}} = 207.3514 + 0.6431 \times T \tag{4}$$

PA 11 typically is semicrystalline between the glass transition temperature of the amorphous phase and the melting temperature of the crystalline phase. The heat capacity in this temperature range is then given by the corresponding mass average of the contributions of the two coexisting phases according to Eq. (5):

$$c_{p,\text{semicry}} = m_{\text{liquid}}\, c_{p,\text{liquid}} + m_{\text{cry}}\, c_{p,\text{cry}} \tag{5}$$

Here, m_{cry} and m_{liquid} are the mass fractions of the crystalline and liquid phases, respectively. Such simple mixing rule, however, only holds with the assumption that the liquid phase, that is, the amorphous melt, is uniform/homogeneous and not consisting of different fractions caused by its covalent coupling to crystals. For many semicrystalline polymers, it has been shown that crystallization causes the formation of a rigid amorphous layer/fraction (RAF) of reduced entropy and mobility near the crystal surfaces [42–51]. Compared to the bulk, mobile amorphous phase, the RAF then devitrifies on heating only at a temperature higher than T_g, likely at the temperature of disappearance of crystals [52, 53], leading to a reduced heat-capacity increment as one would expect with the knowledge of the crystallinity (m_{cry}) and assuming a two-phase structure. For PA 11, formation of an RAF has been proven early [35], by analysis of the heat-capacity increment at T_g of samples crystallized at

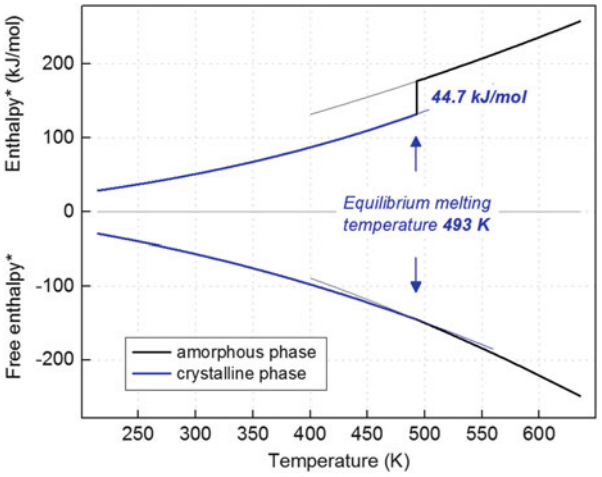

Fig. 6 Enthalpy* (H^*) [$= H - H_0$] (top) and free enthalpy* (G^*) [$= H^* - T.S$] (bottom) of the amorphous (black) and crystalline (blue) phases of PA 11 as a function of temperature. Data were taken from [31]

different conditions; quenching of PA 11 in liquid nitrogen led to formation of poor crystals causing complete disappearance of the c_p-step on heating, that is, formation of a distinct RAF. Though RAF formation in PA 11 has been confirmed later on, further systematic research is still lacking. Note that the RAF is expected to have rather large implications on the thermomechanical behavior of polymers as, for example, it reduces the decrease of Young's modulus on heating the material to above T_g since only a fraction of the amorphous phase converts from the glassy into the rubbery state or on barrier properties as its density is lower than that of the bulk amorphous structure [54–56].

Knowledge of the specific heat capacity of PA 11 at constant pressure yields important information about the thermodynamics of the different phases as it allows determination of their enthalpy H, entropy S, and free enthalpy G as function of temperature according to Eqs. (1–3), shown above. Note again, since the enthalpy of the crystalline phase at 0 K (H_0) is unknown and larger than zero, G and H are not available as absolute values, but only as offset by H_0, then named H^* and G^*. In Fig. 6, the temperature dependencies of these functions are shown for the amorphous (black) and crystalline (blue) phases of PA 11 in a rather narrow temperature range, which is important for application and processing [31]. The free-enthalpy* data of the amorphous and crystalline phase in the lower part of Fig. 6 reveal that the crystalline phase is thermodynamically stable with respect to the amorphous phase below the equilibrium melting temperature $T_{m,0}$ of 493 K. At $T_{m,0}$ both phases coexist in equilibrium, with their free enthalpies being identical. Only above 493 K, the amorphous melt is stable, since its free enthalpy is lower than that of the crystalline phase. In other words, to achieve/preserve equilibrium, the liquid melt must crystallize below $T_{m,0}$, and crystals must melt above $T_{m,0}$ since these transitions then are connected with a decrease of the free enthalpy. The corresponding change of the enthalpy of the system, hidden as latent heat, is indicated in the top part of the figure, amounting to 44.7 kJ/mol (244 J/g) if the phase transition would be complete and indeed occurring at $T_{m,0}$.

The entropy change on equilibrium melting at $T_{m,0}$ amounts to 0.09 kJ/(mol K) [= 44.7 kJ/mol/493 K]. However, the entropy production at $T_{m,0}$ is zero since the entropy increase on melting of crystals on one side and crystallization of the melt on the other side are fully compensated by the corresponding latent enthalpies of melting and crystallization that accompany these processes. In other words, the thermodynamically reversible equilibrium melting temperature is a so-called zero-entropy production melting temperature, as it is true for any melting process if metastable crystals transform into a melt of identical metastability. This is typically the case if crystals cannot undergo irreversible reorganization on heating nor are superheated. Both these effects (reorganization and superheating) then lead to melting with entropy production [57, 58].

Free-enthalpy data of the liquid and crystal phase of PA 11, as shown in Fig. 6, serve as a reference to judge the meta- or instability of non-equilibrium phases. Without going into detail, an irreversible phase transition, that is, a phase transition which is connected with a decrease of the free enthalpy and leading to a new stable or metastable structure, cannot occur at equilibrium conditions but at best close to them. The parent phase must exhibit a certain degree of instability which then provides the driving force/energy for the transformation into the daughter phase of lower free enthalpy, needed to overcome diverse energy barriers [59–65]. Irreversible crystallization, for example, requires supercooling of the melt, necessary for formation of crystal surfaces (crystal nucleation), often exceeding several ten K [62]; note that slow cooling of the melt of PA 11, as achieved in a typical differential scanning calorimetry (DSC) experiment, only causes crystallization well below 200°C (473 K), while $T_{m,0}$ = 493 K. Irreversible melting, in opposite, typically requires much less activation energy since melt nuclei in semicrystalline structures exist at all crystal surfaces; in other words, superheating of polymer crystals to above their zero-entropy production temperature is often negligible though never zero [58].

Figure 6 only comprises free-enthalpy data of the liquid phase of PA 11 and a single crystal phase. While adjustment of a global thermodynamic equilibrium state is possible for temperatures higher than $T_{m,0}$, being the relaxed melt, such equilibrium typically cannot be achieved at temperatures lower than $T_{m,0}$, where only the crystal phase is stable. As a general phenomenon in bulk crystallization of polymer melts, completion of the crystallization process is strongly hindered due to kinetic reasons, presence of entanglements, or the formation of RAF, leading at best to a semicrystalline structure in which crystals coexist with the amorphous liquid or glass [66]; in case of PA 11, the crystal fraction may not significantly exceed 30–40% [67]. Besides incompletion of the crystallization process, also the structure and morphology of the crystals are affected by the conditions of crystallization, that is, by the supercooling of the melt, often leading to formation of crystals with an increased free enthalpy. For numerous polymers it has been shown that slow crystallization at low supercooling of the melt allows formation of rather perfect crystals, while in crystallization at high melt-supercooling, close to T_g, only

poor crystals develop. In particular for polyamides, including PA 11, all intermediate stages of crystal perfection can be adjusted by the temperature of crystallization T_c, as in detail discussed below, leading to a wide spectrum of metastable states of structure.

3 Supermolecular Structure

3.1 Thermal-Pathway-Controlled Crystal Polymorphism

As a function of temperature, in thermodynamic equilibrium, PA 11 is liquid above $T_{m,0}$ and crystalline below this temperature. Due to topological constraints (entanglements), partial immobilization of the melt in the vicinity of crystals, as well as the inherent kinetics of the phase transformation of the liquid melt into the crystal phase, however, thermodynamic equilibrium often is not achieved. The crystallization process typically ends well before the entire liquid phase is exhausted, leading at best to a semicrystalline structure. In addition to this more general polymer-specific phenomenon, crystals of polyamide forming at different supercooling of the melt exhibit a different defect concentration, ultimately causing a specific α/δ′-crystal polymorphism, as is illustrated in Fig. 7 [68]. As in practice different supercooling of the melt can easily be realized by variation of the cooling rate, and in the left part of Fig. 7 is shown that fast cooling of the melt leads to the formation of a δ′-mesophase. The term mesophase is introduced here to account for the high concentration of conformational disorder and a smectic-like arrangement of molecular stems. The δ′-mesophase of PA 11 has first been discovered by ice-quenching experiments and parallels the behavior of other polyamides including PA 6, PA 6.6, or PA 6.10 [69–72]. For the mesophase of PA 6, detailed structural information are available which likely also hold for PA 11. It has been suggested that the chains are straight and nearly extended and having equal distance to all neighbors, that is, the basal plane of the unit cell exhibits hexagonal symmetry. Smectic periodicity along the chain axis has been proven with the detection of a

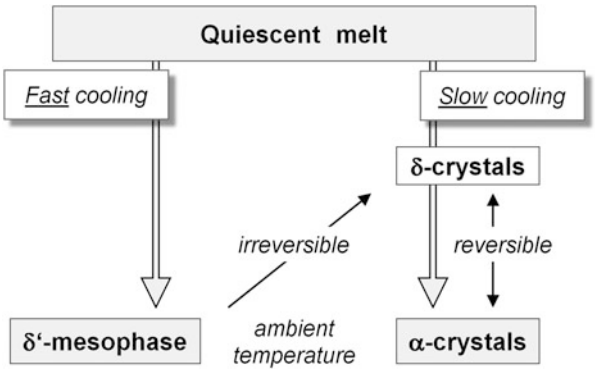

Fig. 7 Crystal polymorphs of PA 11 forming on fast (left path) and slow cooling (right path), which are equivalent to crystallization at high and low supercooling of the melt, respectively. Reproduced from [68], with kind permission from Wiley

meridional scattering peak in fiber pattern analysis [73]. However, the unit cell is not strictly hexagonal but only pseudohexagonal as the conformation of neighbored chain segments is not identical, therefore violating the requirement of long-range repeatability of structure for defining the δ′-phase as a true crystal. Conformational defects may be introduced by the formation of hydrogen bonds connecting the amide groups of neighbored chains which, however, are not strictly aligned but randomly oriented. As in the mesophase, there is also a random substitution of up and down chains, and conformational defects may compensate misorientation/mispositioning of amide groups, then still allowing almost-complete formation of hydrogen bonds, as confirmed by infrared spectroscopy [73–75]. Little is known about the thermodynamic stability of the δ′-mesophase of PA 11 as well as thermodynamic properties like specific enthalpy of melting or an equilibrium melting temperature; for PA 6, it was found that the bulk enthalpy of melting of the mesophase is distinctly lower than that of crystals [76]. Regarding the stability of the mesophase of PA 11, it only can be speculated that the zero-entropy production melting temperature is a few Kelvin higher than T_c, with the mesophase, however, reorganizing on rather slow heating. Specific reorganization experiments were not performed yet on PA 11; however, for PA 6, PA 6.6, and PA 6.10, it was found that at low reorganization temperatures, the pseudohexagonal symmetry may not change, while at sufficiently high temperature, the mesophase converts into the stable crystal form with a different crystal structure and hydrogen-bond arrangement [77–80]. In Fig. 7, it is indicated with the upward-directed arrow that the transition of the δ′-mesophase, which is metastable at low temperature, converts on heating into crystals. The transition is thermodynamically irreversible, that is, crystals will not transform back into the mesophase on cooling.

Slow cooling of the melt, or crystallization at high temperature, causes first formation of pseudohexagonal δ-crystals, with six equal-distance neighbors, similar as in the δ′-mesophase. To date, an unambiguous opinion about the hydrogen-bond network in the high-temperature δ-crystal modification, that is, whether there is a sheetlike alignment or a spatial network, does not yet exist [81, 82]. The δ-crystals then transform on cooling at the Brill transition temperature [83] into triclinic α-crystals. In the α-structure, the methylene sequence between the amide groups adopts a planar [84] or a distorted zigzag conformation [85], and neighbored molecular stems are aligned parallel, permitting layer-like but tilted arrangement of hydrogen bonds [84–86]; experimentally, on heating, the Brill transition most straightforward is detected by the merging of the two strong interchain diffraction peaks at 0.44 and 0.37 nm to an intermediate value of 0.42 nm. Note that the high-temperature form of the α-crystals also is often named α′-crystal phase since the α/α′-transition is reversible. The Brill transition has been detected in numerous different polyamides (see, e.g., [77–95]) and is still subject of research since its nature/origin is still debated; it is occasionally discussed as a gradual first-order phase transformation [93–95]: however, it may only be settled that the alkane segments undergo large-amplitude vibrational motion with the amide groups acting as pinning points [96–98].

Detailed information about the effect of the crystallization temperature on the formation of δ/α-crystals or of δ′-mesophase has only been gained recently, due to former difficulties in subjecting samples to a well-defined thermal history prior

to crystallization, in particular when attempting crystallization at high melt-supercooling. Such analysis requires fast cooling of the melt in order to suppress crystallization until the target crystallization temperature is reached. The use of traditional techniques like differential scanning calorimetry (DSC) only allows cooling at rates up to few hundred K/min [99–101] which only permits isothermal crystallization at rather low supercooling of the melt in case of PA 11 [102–104]. Analysis of crystallization of the supercooled melt of PA 11 in the entire temperature range down to T_g, only became possible with the introduction of fast scanning chip calorimetry (FSC), with the specific instrumentation explained elsewhere [105]. Since it is not possible to gain structural information by calorimetry only, the FSC technique has been combined with XRD [106–108]. In the experiment of Fig. 8, samples of PA 11 were rapidly cooled to different crystallization temperatures in an FSC, isothermally crystallized and subsequently analyzed regarding their X-ray structure [108]. In the top left part of Fig. 8 is shown a typical polymer sample with a thickness and lateral dimension of 10 and around 200 µm, respectively, which was exposed to an microfocus X-ray beam for obtaining the scattering curves. The data clearly reveal the formation of α-crystals at crystallization temperatures higher than 120°C, as in such cases different interchain distances are detected. However, with

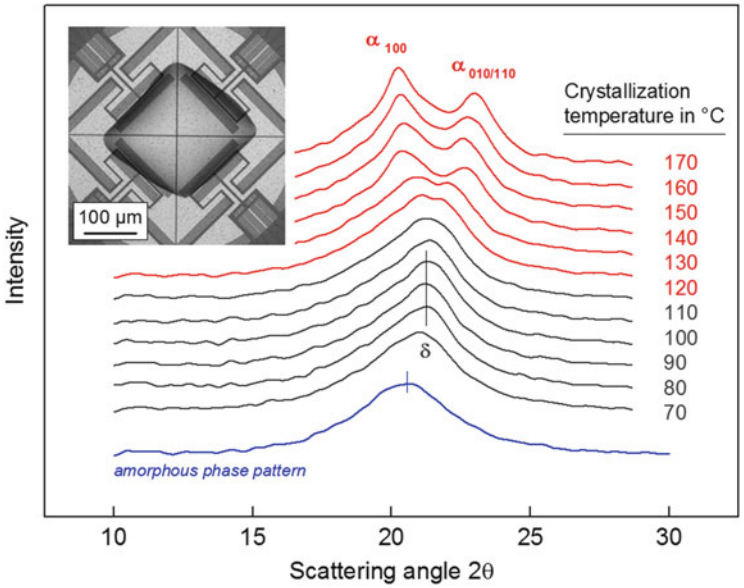

Fig. 8 XRD patterns of amorphous PA 11 (bottom curve, blue) and PA 11 isothermally crystallized at temperatures between 60 and 170°C, as is indicated at the right-hand side of the curves. Data were obtained on samples prepared in an FSC, which allows precise adjustment of crystallization conditions, in particular ensuring absence of crystallization occurring already on the approach of the crystallization temperature; a typically polymer sample on an FSC chip, used for XRD analysis, is shown in the top left inset. Data adapted from [108], Copyright (2016), with permission from Elsevier

decreasing crystallization temperature, the difference between the a- and b-unit cell constants of the triclinic lattice becomes smaller, to finally being equal if crystallization is performed at temperatures lower than 120°C; in such case only a single scattering peak is detected, revealing hexagonal symmetry and presence of the δ-phase. In other words, with decreasing crystallization temperature, there is a gradual decrease of the perfection of the α-crystal phase, being a phenomenon which is well-known for the family of aliphatic polyamides as it has been detected, for example, also for PA 6 [77–80, 109–113] or PA 66 [114, 115]. Note that the single-peak XRD patterns obtained on PA 11 crystallized at high supercooling of the melt, below 120°C, must not be confused with the amorphous-phase scattering as the maximum of the halo of the latter structure is located at a lower angle (see blue curve); to observe the scattering curve of fully amorphous PA 11, the sample was cooled at a rate of 1,000 K/s to below T_g.

Reports about the crystal density, the equilibrium melting temperature, and the bulk enthalpy of melting of the α-crystal phase of PA 11 are inconsistent; the crystal density at ambient temperature is between 1.12 and 1.19 g/cm^3 [9, 67, 84, 85], the equilibrium melting temperature is between 476 and 493 K [31, 67], and the bulk enthalpy of melting is between 189 and 244 J/g [2, 18, 67, 116]. Further polymorphs of PA 11 may develop upon solution crystallization from specific solvents [117, 118], while crystallization at elevated pressure seemed to have no effect on the crystal structure [86, 119, 120]. Regarding crystallization under pressure, it was found that crystals of different morphology (extended chain crystals) and therefore thermal stability can be produced.

3.2 Nucleation-Controlled Semicrystalline Morphologies

The density of crystal nuclei forming in a supercooled melt controls the final semicrystalline morphology. In simple words, if the nuclei density is rather low, then the nuclei may grow to large lamellar crystals, even leading to formation of μm-sized spherulites. In contrast, if the nuclei density is very high, then the growth of crystals is hindered, causing formation of only small crystals. Measurement of nucleation rates and densities most straightforward is possible by optical microscopy [121]; in situ analysis of the number of crystals/spherulites as a function of time provides information about the nucleation rate, while counting the spherulite number after completion of crystallization yields the nuclei number/density. Such analysis can be performed if the nuclei density is rather low, that is, at low supercooling of the melt when the distance between nuclei is of the order of magnitude of several micrometers. In case of a high nuclei density, the resolution of optical microscopes, however, may not be sufficient, and then at least the nucleation density may be evaluated using higher-resolution imaging techniques. For PA 11, however, we are not aware of dedicated and quantitative studies of the nucleation behavior using microscopy.

Alternatively, analysis of the temperature dependence of the gross crystallization rate also allows gaining information about nucleation mechanisms. For many polymers, it was observed that the crystallization rate shows a bimodal temperature dependence, with two separate crystallization-rate maxima located at largely different temperatures. Examples include iPP [122–124], PA 6 [125], PA 66 [126], or poly (butylene terephthalate) (PBT) [119, 127, 128], with a more general discussion of this phenomenon provided in recent reviews [120, 129–131]. A specific example of such a bimodal temperature dependence of the crystallization rate is presented with Fig. 9 for PA 11 [108, 132–134], with the crystallization rate quantified by a characteristic crystallization time (half- or peak time of crystallization). At low supercooling of the melt, at high crystallization temperatures, crystallization is governed by heterogeneous nucleation (red data points), that is, by the presence of heterogeneities of any kind including impurities or purposely added nucleation agent. The overall crystallization rate, however, levels or even passes a high-temperature maximum to then decrease caused by decreasing crystal-growth rate. However, due to the increase of the nucleation rate, that is, due to the increase of the number of homogeneous nuclei at temperatures lower than about 115°C (gray data points), the overall crystallization rate increases again to yield a low-temperature maximum close to T_g (see vertical dashed line). It is worth noting that the crossover temperature separating temperature ranges of heterogeneous and homogeneous nucleation depends on the specific formulation of the polymer, that is, on the type and content of heterogeneities. For example, for iPP [135–137], for poly (ε-caprolactone) (PCL) [138], as well as for PA 11 [139], it has been shown that the high-temperature branch is largely affected by nucleating agents or nanofillers.

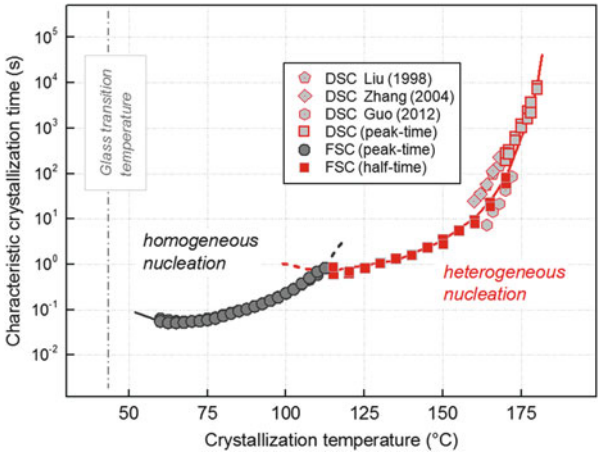

Fig. 9 Characteristic time of crystallization of PA 11 as a function of the crystallization temperature. Coloring of the symbols is used to emphasize temperature ranges of homogeneous and heterogeneous nucleation. The light-gray-filled symbols were obtained by DSC; otherwise data were collected using FSC. Halftimes of crystallization were extracted from conversion-time plots, while peak times were read directly from the crystallization isotherms as the time of maximum heat flow rate. Data adapted from [108], Copyright (2016), with permission from Elsevier

The interpretation of the bimodal temperature dependence of the crystallization rate in terms of different nucleation mechanism prevailing at low and high supercooling of the melt has been confirmed by analyses of the semicrystalline morphologies of iPP [140–144], PA 6 [145, 146], PA 66 [115], or PBT [119], crystallized at temperatures in which heterogeneous and homogeneous nucleation are dominating. These studies revealed that crystallization at low supercooling of the melt typically proceeds by spherulitic growth of lamellae with the spherulite centers, that is, sites of heterogeneous nucleation, separated by few micrometers. Crystallization at high supercooling of the melt, in contrast, showed that individually formed crystals grown from the homogeneous nuclei are separated only by few nanometers. For PBT, an estimation of the nucleation density suggested values of 10^6 and 10^{15} nuclei/mm^3 for crystallization at low and high supercooling of the melt, respectively [119]. Similar as in the case of the above polymers, also PA 11 was investigated regarding its semicrystalline morphology forming at different conditions of melt crystallization. In one of the early experiments, it was found that PA 11 forms "negative spherulites which exhibit zigzag extinction brushes" [147]. The ring spacing in the observed banded spherulites was decreasing as a function of the diameter since crystallization was performed on slow cooling; in other words, the band spacing decreases with decreasing crystallization temperature, being an observation valid for many polymers including polyethylene [148, 149] or polyhydroxybutyrate (PHB) [150]. More precise, crystallization of PA 11 at 165°C and 160°C yielded spherulites with band spacings of 3.5 and 1.8 μm, respectively, while at lower crystallization temperatures, rings were not resolvable anymore by optical microscopy. Lamellar crystals have been observed by solution crystallization [117], however were also detected in samples crystallized from the melt at well-defined conditions (Unpublished data; measurements were performed by T. Tighe, in analogy to a sister study on PA 66 [115], see experimental details therein). Representing bulk melt crystallization at low supercooling of the melt, Fig. 10 shows height-contrast scanning-probe-microscopy (SPM) images of PA 11 isothermally crystallized at 160°C in an FSC; the XRD pattern of the same sample has been shown in Fig. 8. The left image was taken at lower magnification and shows spherulites with a size of few μm, containing sheaflike grown lamellae [151, 152]. The image to the right shows the structure at a larger magnification revealing formation of lath-shaped lamellae which partially are viewed flat-on or at an intermediate angle. In an independent study, the thickness of lamellae of PA 11 melt-crystallized at 150°C was determined by small-angle X-ray scattering and is around 7 nm [67].

The DSC/FSC data allow straightforward interpretation of the microstructure of the PA 11 films shown in the right part of Fig. 11, obtained by polarized-light optical microscopy (POM) [153]. For easy assignment of thermal histories, the approximate cooling rate at the temperature of crystallization in the ballistic film cooling experiment is shown in the left graph by the boxed numbers. For PA 11 slowly cooled using rates of about 0.1 and 10 K/s (Fig. 11, images labeled 1 and 2, respectively), which crystallized at around 165 and 150°C, a space-filling spherulitic superstructure is observed. The spherulite size is around 10–20 μm,

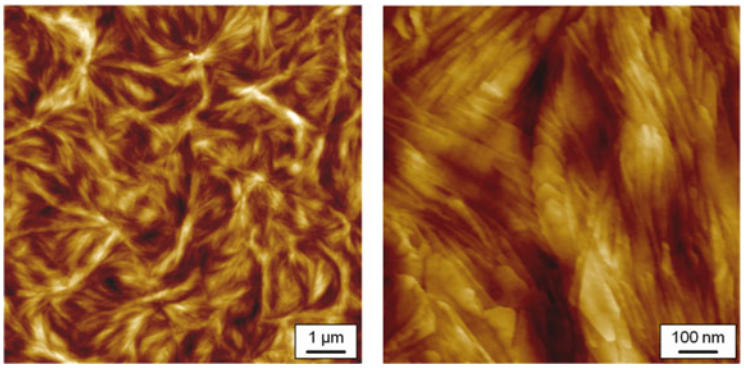

Fig. 10 Height-contrast scanning probe microscope images of PA 11 melt-crystallized at 160°C. The left, low-magnification image shows the spherulitic superstructure and sheaflike grown lamellae, while the higher-magnification image to the right shows flat-on viewed crystal lamellae within a spherulite (Unpublished data; measurements were performed by T. Tighe, in analogy to a sister study on PA 66 [115], see experimental details therein)

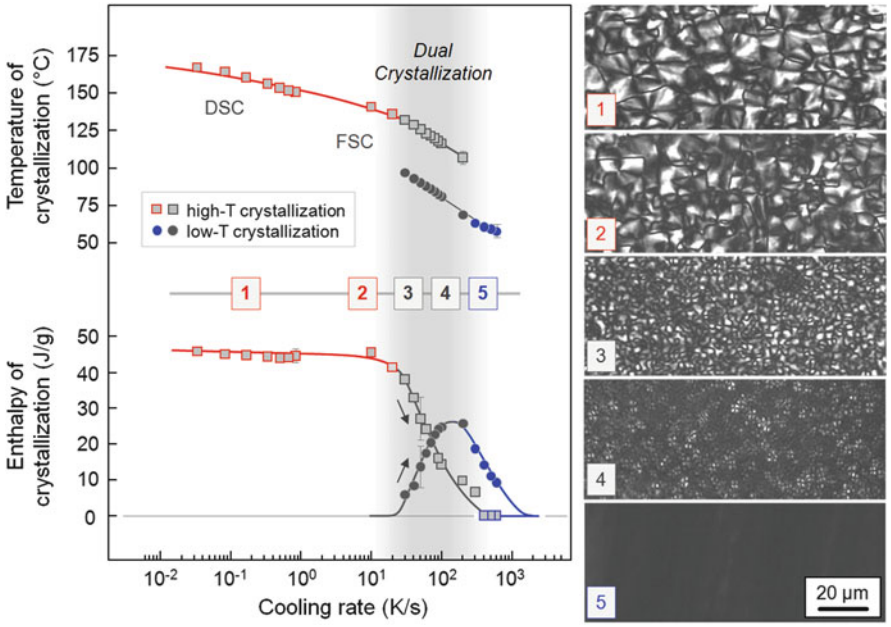

Fig. 11 Temperature (top) and enthalpy (bottom) of crystallization of PA 11 as a function of the cooling rate (left graph). Data were obtained by FSC ($\geq$10 K/s) and DSC cooling experiments ($\leq$0.833 K/s). Red, gray, and blue coloring of data serves for easy recognition of cooling-rate ranges, leading to high-temperature crystallization only, occurrence of two crystallization events, and low-temperature crystallization only, respectively. The POM images to the right were obtained on film samples which were ballistically cooled at different rate between about 0.1 K/s (top) and about 300 K/s (bottom). Data/images adapted from [153], with kind permission from Wiley

which agrees with the literature [147]. If the cooling rate is increased to 10–50 K/s (cooling history 3), then the size of spherulites is lower than 5 μm, being caused by the increased number of heterogeneous nuclei when decreasing the crystallization temperature to about 130°C. However, it seems that spherulitic crystallization is incomplete in some parts of the film, indicating deterioration of the high-temperature crystallization process and causing continuation of crystallization at lower temperature; in fact, monitoring the temperature profile during preparation of the film revealed exothermic heat flow at around 100°C, confirming the occurrence of the low-temperature crystallization process. Incomplete high-temperature crystallization is obvious on cooling at a rate of about 100 K/s (Fig. 11, image 4) since only isolated spherulites with a size of 2–4 μm surrounded by non-spherulitic structure are observed. As such, a dual semicrystalline morphology has been formed containing spherulitically grown lamellar crystals on one side, and crystals formed at low temperature from homogeneous nuclei. The latter, however, are invisible in POM, due to their smallness and non-concerted growth, thus not leading to a characteristic birefringence pattern. Cooling faster than 100 K/s (Fig. 11, image 5) finally leads to solidification of the entire melt at around 75°C. Note that it has been proven that the crystallinity of all films shown in Fig. 11 is similar, around 25%, being against the expectation by the FSC data shown in the left graph. However, in the FSC experiments, the cooling rate was constant, while in case of the ballistically cooled films, the cooling rate was lowering with decreasing temperature, allowing transformation of the entire crystallizable fraction of the melt before its vitrification at T_g.

The nanometer-scale structure of semicrystalline morphologies of various polyamides, formed at high supercooling of the melt, is shown in Fig. 12, resembling observations obtained on iPP [140–145] or PBT [119]. The images show numerous ordered, almost isometric domains with a size of the order of magnitude of 10 nm,

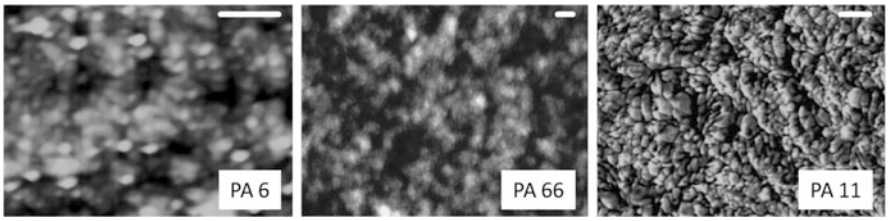

Fig. 12 SPM images of the nanometer-scale structure of PA 6 (left) [145], PA 66 (center) [115], and PA 11 (right) [154], formed by homogeneous nucleation at high supercooling of the melt. In case of PA 6 and PA 66, imaging was performed after cooling the melt in the FSC to the crystallization temperature of 70°C, slightly above T_g. In case of PA 11, a molten film has been quenched ice water, to enforce homogeneous nucleation, and then heated to 160°C to allow coarsening of the initially low-temperature-formed structure for improved imaging. Note that the nucleation history is not destroyed by the high-temperature annealing step. Left image: Adapted from [145], Copyright (2012), with permission from Elsevier. Center image: Adapted from [115], Copyright (2017), with permission from Elsevier. Right image: Adapted with permission from [154]. Copyright (2013) American Chemical Society

embedded in the amorphous matrix. For all these polyamides, it has been proven by XRD that these nodules exhibit a mesomorphic structure (see, e.g., [69, 70, 77, 108, 115] or Figs. 7 and 8); however, with their size probably overestimated when analyzed by SPM, for iPP containing such mesomorphic nodules, the effect of the tip geometry on the determination of their size was demonstrated, providing clear evidence of smearing phenomena [155]. Transmission electron microscopy (TEM) [141] or small-angle X-ray scattering (SAXS) [156–158] reveals slightly smaller domain sizes. It is important to note that application-relevant properties are largely influenced by the different habit and arrangement of crystals, even if the crystallinity is similar; for example, non-spherulitic structures lead to higher ductility and reduced (visible) light scattering, compared to the spherulitically crystallized counterpart [159–167]. In more detailed investigations, even the crystal aspect ratio including thickness is considered, affecting the mechanical performance. In short, samples with non-lamellar crystals with a close-to-unity aspect ratio exhibit a modulus of elasticity/yield strength which is lower than in case of samples containing lamellae of high aspect ratio, fitting classical composite theories [168–172].

4 Shear-Induced Crystallization

PA 11 is commercially available as pellet or powder, allowing application of a large variety of melt-processing technologies to obtain semifinished or end-consumer products including extrusion, extrusion-blow molding, injection molding, injection-blow molding, or rotational molding [173]. Special grades with tailored rheology/viscosity as well as containing additives have been designed to fit the needs of the processing industry and of the end user. Though general information about processing parameters for the various processing technologies are provided for each grade/formulation, specific correlations between processing parameters, the supermolecular structure, and final application-relevant properties are hardly available.

For example, during injection molding, as a consequence of the combined effects of shear, pressure, and thermal fields, often skin/core morphologies with a layer-like or gradient structure with respect to the orientation of macromolecules and crystals, the crystal fraction, or the crystalline-amorphous superstructure develop [174–183]. It is obvious that such gradient- or layer-like microstructure has implications on the thermomechanical property profile, thus needing to be controlled by the molding conditions including temperature of the melt, injection pressure and injection time, or mold temperature, all affecting the skin/core morphology [174–183]. Whatsoever, specific reports about tailoring, e.g., the skin/core structure of injection moldings based on PA 11, are not available, being in contrast to other members of the polyamide family such as PA 6 and PA 66 [175, 176, 180–183]. Often it is found that the skin in injection moldings is featureless in POM, while the core shows spherulites that increase in size toward the center. Also, it was shown that the

thickness of the non-spherulitic skin layer decreased with increasing temperature of both the mold and melt. Because of the different cooling rate in the various parts of the molding, the crystalline component in the skin was rich in mesophase, while the core mainly contained crystals [176, 181, 182]. Research about the structure and properties of PA 66 injection moldings revealed that the cooling conditions are of great importance in thin-wall injection moldings and that slow cooling, enhanced by increasing the mold temperature, reduces or even fully inhibits the development of a surface layer. The crystallinity was analyzed by infrared spectroscopy along the cross section in the moldings, which in addition to the effect of the mold temperature/cooling rate also allowed identification of the effect of shearing the melt before its solidification [176], as in the shear zone a higher crystallinity was detected.

Shear-induced crystallization is an important phenomenon in processing of crystallizable polymers which is needed to be understood to gain further process in polymer engineering. Though numerous fundamental works have been performed in the past, to correlate shearing conditions and crystal nucleation [183–187], practical implementation of the findings seems rare as molding process typically is not designed considering such correlations. Moreover, research about shear-induced nucleation in polyamides, despite often processed by injection molding, is incomplete and underdeveloped; only recently a quantitative study, to obtain critical shearing conditions to promote crystal nuclei formation and to identify the temperature range in which such nuclei are effective, was performed for the case of PA 66 [188]. As one of the main results, it was found that increasing shear of the melt only leads to faster crystallization at high temperature, that is, in the temperature range of heterogeneous crystal nucleation; low-temperature crystallization, controlled by homogeneous nucleation, is not affected by previous shear flow. A further major finding is the observation that nuclei formed during shear only get destroyed by heating the melt above a critical temperature.

For PA 11, to date there is available only a single report about shear-induced crystallization [189]. In a broader study of the effect of the concentration of C7 short-chain branches, introduced by co-polycondensation of 11-aminoundecanoic acid with 11-heptylaminoundecanoic acid, on crystallization, it was found that addition of only low amount of 1 and 5 m% of comonomers, corresponding to 0.56 and 2.85 branches/1,000 C, led to distinct decreases of the crystallinity and the kinetics of crystallization of the quiescent melt. However, subjecting the melt at 180°C to relatively strong shear conditions and applying shear rates and strain up to 10 1/s and 60, respectively, had no effect on the nuclei density and spherulitic growth rate observed at identical temperature of 180°C, in both non-branched and branched PA 11. For illustration, in Fig. 13 is plotted the crystallization halftime as a function of the shear rate for the investigated linear and branched samples, revealing absence of any “substantial” [189] acceleration of the crystallization process.

The observed independence of the crystallization rate was expected since due to the molecular characteristics of polyamides, having rather low molar mass and low polydispersity, relaxation of the sheared melt occurs within a few seconds, as was estimated by analysis of the linear viscoelastic characteristics. The fast relaxation of

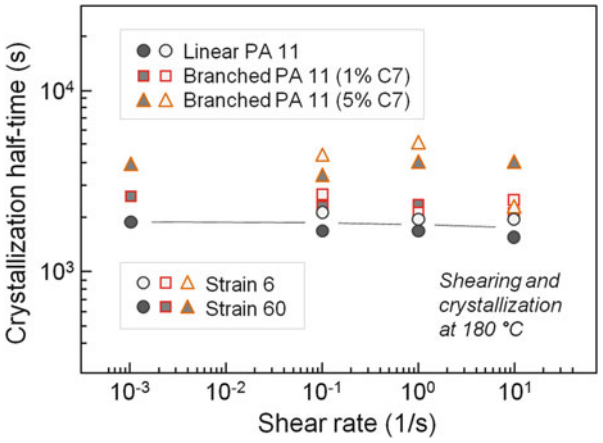

Fig. 13 Halftime of crystallization (measured by turbidity) as a function of the shear rate, for linear PA 11 and PA 11 containing 0.56 and 2.85 C7 branches per 1,000 C. Dark- and light-gray-filled symbols refer to strain values of 6 and 60, respectively. Data adapted from [189], Copyright (2005), with permission from Elsevier

the melt after cessation of shear was then compared with the long induction time of the crystallization process of few thousands seconds, argued being the reason for the insensitivity of shear at the selected crystallization temperature. Since insertion of the few branches into the polymer chain was not connected with a change of the viscoelasticity, for the copolymers also, no effect of shear on crystallization was observed [189].

With the presumption that shear-induced nucleation and crystallization during processing may play a less distinct role as, for example, in polyolefins, which typically exhibit a broad molar mass distribution and longer relaxation times after shearing the melt, a concept of prediction of the structure of injection moldings has been introduced and validated, focusing on the effect of the cooling conditions [68, 190]. This approach includes simulation of the cooling-rate profile in all regions of the molding as a function of the temperature of the melt and estimating temperatures of crystallization based on non-isothermal quiescent-melt crystallization experiments.

5 Thermomechanical Behavior

5.1 Temperature Dependence of Young's Modulus of PA 11 of Different Semicrystalline Morphology

Young's modulus of PA 11, similar as in the case of other semicrystalline polymers, is influenced by its semicrystalline morphology including the degree of crystallinity [191–193], the predominant crystal polymorph/packing density as demonstrated for the α/γ-crystal polymorphism of PA 6 [194–196] and PA 12 [197], the α/β-crystal polymorphism of iPP [198] or the Form I/II crystal polymorphism in isotactic polybutene-1 [199], and the crystal habit [162, 163], while the crystal superstructure

like size of spherulites has a stronger effect on large-deformation properties like yield strength and ductility [159]. A study of Young's modulus of PA 11 of different thermal history and with that semicrystalline morphology is reported in the literature [200]. Figure 14 shows at the top the modulus of elasticity of a specific PA 11 grade prepared by quenching extruded films (as-received, gray squares) and after additional annealing at 160°C for 60 min (red circles) as a function of temperature. The degree of crystallinity of the quenched sample, as analyzed by DSC, was about 26%, while it increased to about 30% after annealing. The rather minor increase of the crystallinity led to an increase of the modulus at ambient temperature, that is, in the glassy state, by about 10%, from 1.2 to 1.35 GPa. Besides the increased crystallinity as a result of annealing, the increase of the modulus may also be caused by a change of the predominant crystal polymorph as it is known that γ-mesophase converts to α-crystals on heating [77, 154]. Unfortunately there were not provided further information about the structure of the investigated samples.

In a further study, the temperature dependence of Young's modulus of well-characterized PA 11 was analyzed, exemplarily shown in the bottom part of Fig. 14. Samples of different structure were prepared by cooling the melt at different rate, as explained in detail on discussion of Fig. 11 [153]. The two curves represent data which were obtained on slowly cooled (red diamond symbols) and rapidly cooled samples (gray squares), labeled "1" and "5" in Fig. 11, respectively. The slowly cooled sample contains spherulitically grown lamellar α-crystals, while the rapidly cooled sample contains nodular mesophase domains without a higher-order superstructure; structural details were provided with the POM micrographs in the right part of Fig. 11 and the AFM images of Figs. 10 and 12 (right image), though the latter case are obtained on independent samples. Since the enthalpy-based

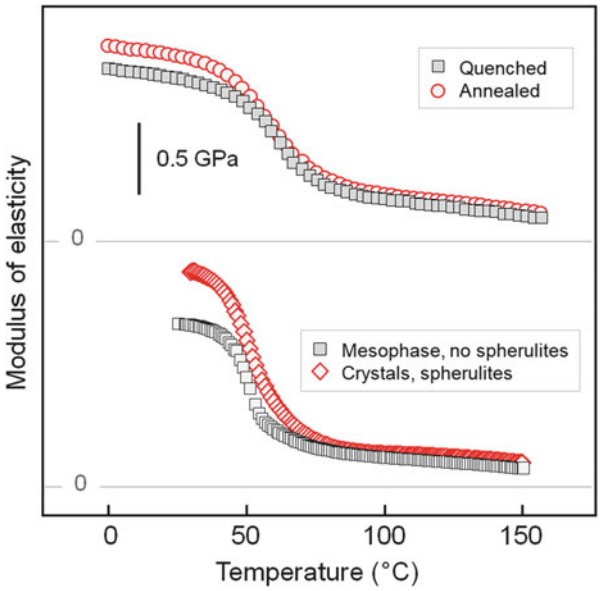

Fig. 14 Modulus of elasticity of PA 11 of different thermal history as a function of temperature. Top part adapted from [200], with kind permission from AIP Publishing [200]

crystallinity [201] of these samples is about identical, the higher modulus of the slowly cooled sample must be caused either by the different crystal symmetry/packing density or the different crystal shape, while in an independent study on iPP, it was demonstrated that the superstructure has no effect on the modulus [202].

5.2 *Thermomechanical Performance of PA 11-Based Nanocomposites*

The thermomechanical performance of polymers, in general, can efficiently be increased by addition of nanofillers with a high surface-to-volume ratio, to yield a polymer-based nanocomposite. There is an observed improvement of a number of properties compared to the neat polymer due to the addition of the nanofiller, including mechanical properties like Young's modulus and strength, thermal properties like heat resistance, barrier properties, flammability, or biodegradability in case of biodegradable polymers [203–206]. Regarding mechanical properties, for example, it has been shown that addition of 6.5 m% montmorillonite (MMT) in a PA 6 matrix leads to a doubling of the modulus of elasticity while there would be needed triple amount of glass fibers to obtain similar reinforcement (see Fig. 15). In addition to saving of weight, less deterioration in matrix properties like ductility or impact strength is encountered in addition to nanofillers instead of classical reinforcement components [206].

The nanofillers impart an improvement of properties according to composite theories [206–210], due to their specific own properties. Parameters which contribute to the reinforcement include their chemistry, concentration, their dimensions including the aspect ratio, or their coupling to the surrounding polymer matrix. In general it is predicted by composite theories that with increasing concentration of the nanofiller, Young's modulus and strength increase and the ductility and

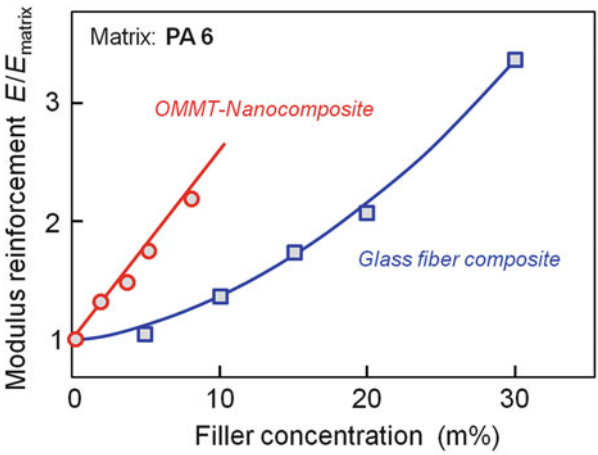

Fig. 15 Comparison of the reinforcement of PA 6 by glass fibers (blue squares) and by organically modified montmorillonite (OMMT) (red circles). The nanocomposite filler concentration is based on the m% inorganic montmorillonite [192–195]. Data adapted from [206], Copyright (2003), with kind permission from Elsevier [206]

impact strength decrease; however, often, it is observed that the reinforcing effect is leveling off at a loading of 5–10 m% since a perfect dispersion and distribution in the polymer matrix cannot be achieved anymore. Typical examples of the nanocomposite morphologies, demonstrating the effect of the content of organo-modified nanofiller on their dispersion during melt compounding in the PA 11 matrix, are shown in Fig. 16 [211]. The left and right TEM images were obtained on samples containing 2 and 8 m% organo-clay, respectively, revealing in both cases a homogeneous dispersion of the clay platelets in the polymer matrix. However, while in case of lower loading a disordered and exfoliated clay nanostructure was observed, the sample which contained 8 m% of the nanofiller showed ordered intercalated organo-clay morphology. Note that in both cases the characteristic organo-clay spacing of 2.5 nm was not observed anymore; however, loading with 8 m% organo-clay yielded a smooth shoulder with a gradual increase of the diffraction intensity at low angle, interpreted as being suggesting a complex structure with partial exfoliation and partial intercalation [211].

Despite imperfect exfoliation at higher nanofiller content, the impact of presence of nanofillers on mechanical properties is tremendous [29, 211–214], as is demonstrated by the huge increase of Young's modulus even on smallest loadings. Figure 17 shows data reported in different studies [29, 211–213], unanimously proving that the modulus of elasticity of PA 11 increases by a factor of about two in nanocomposites containing only 4 m% nanofiller. At high nanofiller concentrations, the reinforcing effect is then diminishing due to imperfect dispersion. Note that similar reinforcement has been achieved by layered silicates and fiber-like multi-walled carbon nanotubes (MWCNT).

Regarding the thermomechanical behavior of PA 11-based nanocomposites in the solid state, it was found that the increase of the modulus of elasticity (E) in addition to OMMT nanofiller is also maintained at temperatures higher than T_g, with the reinforcement factor ($E_{\text{nanocomposite}}/E_{\text{matrix}}$) approximately unchanged in the analyzed temperature range up to 100°C. However, it was noted that addition of the organo-clay led to a decrease of T_g, from about 63°C in neat PA 11 to about 51°C in

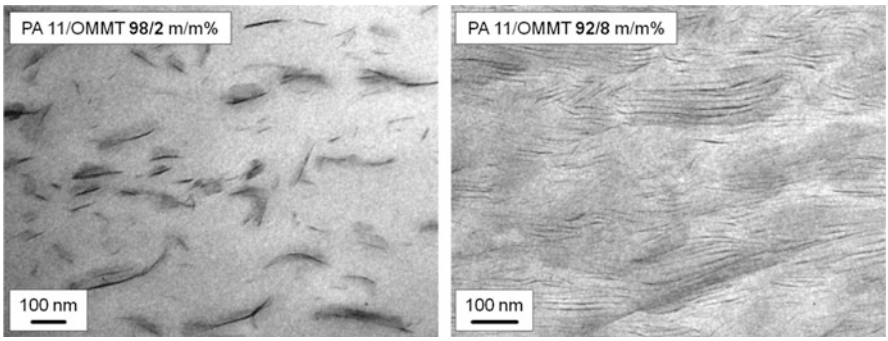

Fig. 16 Bright-field TEM images of PA/OMMT nanocomposites containing 2 (left) and 8 m% (right) nanofiller. Images adapted from [211], Copyright (2003), with kind permission from Elsevier [211]

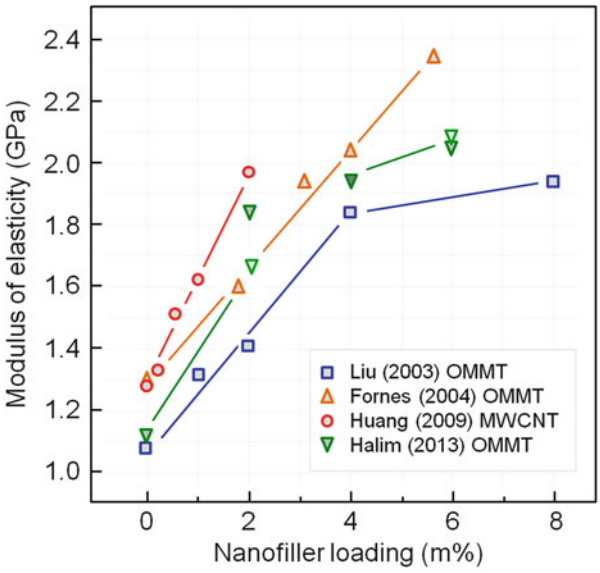

Fig. 17 Modulus of elasticity of PA 11 as a function of the concentration of OMMT and MWCNT nanofillers, as indicated in the legend. Data were adapted from the literature [29, 211–213]

a nanocomposite containing 8 m% nanofiller. This observation was explained by a plasticizing effect of the nanofiller surfactant within the organically modified clay [211]. Analysis of the melt rheology in both linear and non-linear response regions provided information that nanocomposites exhibit a much higher dynamic modulus and shear viscosity than neat PA 11 [215, 216]; similar as for the solid-state modulus (Fig. 17) aggregation and presence of ordered nanoclay stacks at higher loading (>5 m%) leads to abnormal effects.

Beneficial effects of nanofillers on properties may also be expected due to a possible nucleating effect on the crystallization process on the PA 11. In general, it is then expected that crystallization proceeds faster, that there develops a finer and more uniform spherulitic superstructure, and even that formation of specific crystal polymorphs may be favored. Crystallization studies on PA 11/MMT nanocomposites included analysis of the X-ray structure of as-extruded pellets [211] or injection-molded test bars [29]. In addition, analyses of halftimes of crystallization and of the cooling-rate dependence of the crystallization temperature by differential scanning calorimetry (DSC) were performed [133]. The X-ray analysis of injection-molded test bars solidified in a mold of temperature of 80°C and of as-extruded pellets revealed presence of α-crystals in both neat PA 11 and its nanocomposites with MMT [29, 211]. Halftimes of crystallization were measured at temperatures between 162 and 176°C, revealing acceleration of crystallization in the presence of the nanofiller; simultaneously it was found that the crystallization temperature during continuous cooling of the melt at rates between 2.5 and 20 K/min was increased, being connected with a decrease of the size of spherulites.

For demonstration of the effect of presence of nanofillers on crystallization at processing-relevant cooling conditions, often exceeding several hundred K/s [190, 191], in Fig. 18 are shown temperatures (top) and enthalpies of crystallization

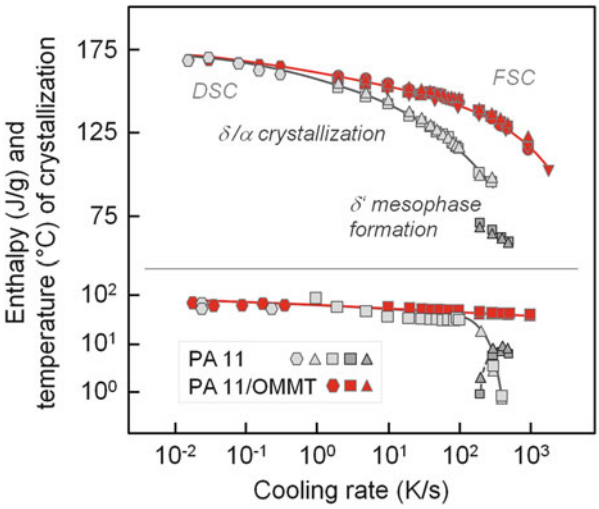

Fig. 18 Temperature (upper part) and enthalpy of crystallization/mesophase formation (lower part) of neat PA 11 (gray symbols) [154] and PA 11 in the presence of 5 m% OMMT (red symbols) as a function of the cooling rate. Data were obtained by DSC on cooling at rates lower than 1 K/s, otherwise by FSC. Figure adapted from [217] with kind permission from Springer Nature, Copyright (2013)

(bottom) of neat PA 11 (gray symbols)- and a PA 11-based nanocomposite containing 5 m% OMMT (red symbols) as a function of the cooling rate, spanning five orders of magnitude, from roughly 0.01 to 1,000 K/s [217]. Regarding the specific PA 11 grade used here, cooling slower than 100 K/s leads to crystallization in the high-temperature crystallization range, causing formation of α-crystals, while faster cooling causes δ′-mesophase formation at temperatures lower than 75°C; the data in the lower part of the figure reveal that cooling faster than 100 K/s is connected with a drastic decrease of the crystallinity in neat PA 11, and eventually, on cooling faster than 500 K/s, the melt completely vitrifies at T_g without any prior ordering. Presence of OMMT nanofiller has almost no effect on crystallization of the PA 11 matrix on slow cooling. In contrast, if the cooling rate is higher than 100 K/s, then crystallization of PA 11 is enhanced such that the high-temperature crystallization process can be detected even on cooling at a rate of 2,000 K/s, without a prior detrimental reduction of the crystal fraction.

The nucleating effect of OMMT nanofiller was in addition confirmed by isothermal analysis of crystallization, as shown in Fig. 19 [217]. However, the analysis of the nanocomposites was restricted to the temperature range from 145 to 180°C, since at lower temperatures the crystallization was simply too fast to be quantified with the particular FSC used (red data points). Crystallization peak times at high temperatures, assessable by DSC, again reveal an only negligible effect of the nanofiller on the PA 11 crystallization kinetics. However, with increasing supercooling of the melt, the crystallization-peak-time difference between neat PA 11 (gray symbols) and PA 11 containing 5 m% OMMT increases such that at a temperature of 145°C, the crystallization rate of the nanocomposite is more than one order of magnitude higher than in neat PA 11; similar decreases of the minimum characteristic crystallization time were observed, e.g., in PA 6/OMMT and PCL/MWCNT nanocomposites [138, 218].

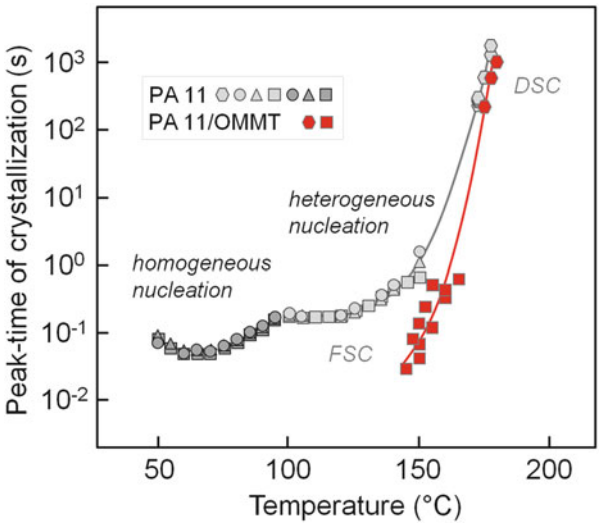

Fig. 19 Peak time of isothermal crystallization/ordering of neat PA 11 (gray symbols) [154] and PA 11 in the presence of 5 m% OMMT (red symbols) as a function of temperature. Data were obtained by DSC and FSC, as indicated. Figure adapted from [217] with kind permission from Springer Nature, Copyright (2013)

The above, with Figs. 18 and 19 described studies of the increase of the crystallization rate of PA 11 in the presence of nanofillers, was completed by analyses of the spherulitic superstructure, which suggested that the increase of the crystallization rate is caused by an increase of the number of heterogeneous nucleation sites but not an increase of the crystal growth rate [217]. As such, it was demonstrated that the addition of nanofiller into PA 11, besides the expected and intended variation of the property profile according to composite theories, also affects the crystallization behavior of the polymer matrix, in particular at conditions of melt solidification relevant in polymer processing. OMMT modification is connected with both an increase of the crystallinity on cooling faster than 100 K/s and simultaneously a decrease of the spherulite size, with well-known effects on mechanical properties [159–167].

6 Thermal Stability and Flame Retardancy of PA 11

6.1 Thermal Stability

Thermogravimetric analysis (TGA) is commonly used to assess the thermal stability of a material to permanent property changes caused by heat in combination with exposure to specific gaseous media. For polymers, the TGA decomposition onset temperature is often not well defined, and it is conventional to quantify the thermal stability by the temperature where a particular mass loss is reached, e.g., 5 or 10 m%. Figure 20a shows typical TGA mass-loss curves for PA 11 recorded in air and in an inert nitrogen atmosphere. The TGA curves for the neat polymer show gradual mass loss between 200 and 410°C. At this point the mass remaining is about 95 m%. Then

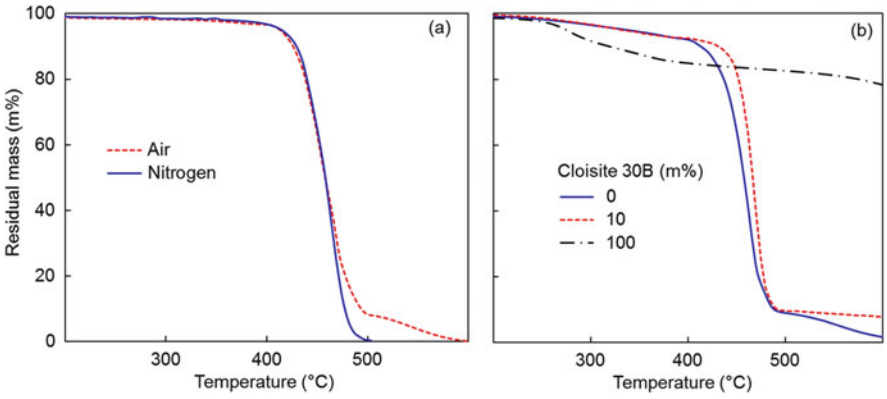

Fig. 20 Representative TGA traces: (**a**) PA 11 recorded in air and in nitrogen; (**b**) Neat PA 11 compared to neat Cloisite C30B organo-clay and its 10 m% nanocomposite

much more rapid mass loss occurs, and at 500°C the residue is negligible in nitrogen atmosphere. However, in air, a two-step mass-loss process is observed with a secondary plateau being reached at this temperature with about 8 m% remaining. This indicates a propensity for polyamide to char at elevated temperatures in the presence of air. However, as the temperature increases further, the char is progressively oxidized, and it slowly loses mass so that at a temperature of about 600°C, nothing remains.

Figure 20b shows TGA curves recorded in an air atmosphere for the neat PA 11, neat Cloisite 30B clay, and a nanocomposite containing 10 m% C30B clay. Noteworthy is the apparent improvement of the thermal stability of the nanocomposite compared to the neat polymer. This is actually caused by the diffusion barrier to oxygen ingress and to the release of volatile decomposition products posed by the impermeable clay platelets present in the nanocomposite.

6.2 Thermal Decomposition

The chemistry associated with the thermal decomposition of aliphatic polyamides, including PA11, was reviewed by [219]. The nature of the volatile products depends significantly on the temperature of pyrolysis [220]. At low temperatures the major components of the pyrolysis are hydrocarbons, C11 olefinic nitrile, and lactams [220]. At higher temperatures of pyrolysis, the lower lactams, acetonitrile and acrylonitrile, and cyclic ketones became more important at the expense of the C11-lactam and the olefinic nitrile [220]. The primary polyamide chain scission appears to occur either at the amide C(O)-NH or adjacent bonds, most likely at the alkyl-amide N(H)-CH_2 bond as it is relatively the weakest in the aliphatic chain [219]. The mechanisms depend on experimental conditions and include hydrolysis,

homolytic scission, intramolecular C-H transfer, and cis-elimination (a particular case of C-H transfer) [219]. Combined pyrolysis-gas chromatographic analysis showed that lactam was the first compound evolved and 10-undecenitrile was the second [221]. Monomer and dimer lactams form by an intramolecular exchange reaction [222, 223], and decomposition through a C-H hydrogen transfer reaction appears to occur as a secondary thermal process [222].

Time-resolved rheology studies, in combination with size-exclusion chromatography combined with multi-angle light scattering (SEC-MALS) and matrix-assisted laser desorption ionization/time-of-flight (MALDI-TOF) analyses of PA 11 in the melt at 215°C, indicated that post-condensation is the dominant degradation mechanism of PA 11 in inert N_2 atmosphere [224]. In contrast, three distinct thermo-oxidative processes take place in the presence of air, namely, post-condensation, chain scission, and cross-linking [224]. In both cases the number-average molar mass and the polydispersity increase over time.

Hydrolysis is the main mechanism for degradation of PA 11 in anaerobic environments such as the condition of underwater crude oil risers. The hydrolysis reaction follows a nucleophilic substitution (SN2) mechanism with water as the nucleophile in high-temperature water at near-neutral conditions [225]. The hydrolysis rate is also pH dependent, and three distinct regions of pH dependence exist though at near-neutral conditions the rate is insensitive to changes in pH. Estimates for the activation energies for base catalyzed, acid catalyzed, and water-assisted mechanisms for amide bond hydrolysis are 21, 31, and 99 kJ/mol, respectively [225]. In pH 7, water hydrolysis reactions lead to the formation of an equilibrium molecular weight of about 26 kg/mol [226]. This was attributed to a recombination reaction occurring in the solid state. Incorporating graphene oxide significantly reduces the hydrolytic degradation in PA 11 [227]. Short-term exposure to water is apparently not a problem as well-dispersed PA11/organo-modified clay nanocomposites were obtained using water-assisted melt compounding [228].

6.3 Thermo-oxidative Degradation

A striking feature of PA 11 thermo-oxidative degradation is the absence of an induction period, even at relatively low temperatures (<100°C) [229]. The consensus is that oxidative degradation commences by oxygen, first attacking the N-vicinal methylene group, leading to the formation of α-amino hydroperoxides (POOH) [229]. The inductive effect of the neighboring (electronegative) nitrogen atom is highly destabilizing so that, compared to polyolefins, the POOH concentration remains low; the activation energy of POOH decomposition, that is, of radical initiation for chain oxidation, is relatively low; and POOH decomposition occurs mainly by an unimolecular mode [229]. Propagation by hydrogen abstraction is fast and selective for attack on the α-methylenes as they are considerably more reactive than the other methylenes [229]. Termination by radical combination is also very fast owing to very efficient disproportionation processes. The main stable oxidation

products are imides, resulting from disproportionation processes. Other oxidation products arise from rearrangements of α-amino alkoxyls or α-amino hydroxyls, leading to β-scissions with terminal aldehydes or alcohols. Volatile nitriles, alkanes, and olefins are the products of thermo-oxidation, but no cyclic ketones are formed [220].

The chromophores responsible for the yellowing discoloration of nylons are attributed either to pyrrole-type structures, conjugated acrylamides, or conjugated azomethines [219]. Cross-linking in PA 11 is limited, and results from secondary reactions occur during thermo-oxidative decomposition [219]. PA 11 thermal decomposition into volatiles is catalyzed by strong mineral acids, strong bases, and some oxides or salts of transition metals. However, some fire-retardant additives promote secondary reactions that promote cross-linking and charring [219].

6.4 Flame Retardancy

Organic polymers such as PA 11 are highly flammable and can therefore result in undesirable fires. The combustion of polymers is a complex phenomenon that involves the solid phase, gaseous phase, as well as an interphase [230]. Characterizing the potential fire behavior attributes is difficult, and therefore several small-, medium-, and large-scale flammability tests are used. A simple test is the limiting oxygen index (LOI) method [231]. It provides a convenient numerical measure that quantifies the tendency of a material to sustain a flame. In this test, a sample is mounted inside a vertical glass tube and ignited at the top. A mixture of oxygen and nitrogen is passed through the tube from below. The LOI is defined as the percentage oxygen content in the mixture at which the sample barely continues to burn. Theoretically, samples with LOI < 21 should easily burn in air, and materials with $21 <$ LOI < 27 are conventionally classified as "slow burning" and those with LOI > 27 as "self-extinguishing."

The Underwriters Laboratory vertical UL 94 V test is another important small-scale fire test procedure to assess the flammability of polymer materials, often specified in electrical engineering and electronic applications [231]. In this test the same specimen is exposed to two successive gas flame applications. The material is classified into categories, depending on the performance with respect to the individual duration of burning for each specimen, the total duration of burning for all specimens, and the presence or absence of burning drips. For example, if it burns less than 5 s, then it is classified as V-O. If it burns and drips, and the burning drops fall on surgical cotton and ignite it, then it is classified as V-2. Generally, burning and dripping can remove both the flame and the heat from a sample but are likely to ignite the cotton. This means that the effects of melt flow and dripping are considered in the UL 94 test and to some extent crucial in deciding on the final classification. The gasification of fuel, charring, effective heat of combustion of the volatiles and flame inhibition, melt flow, and dripping are the most important phenomena determining the fire behavior of thermoplastics in the vertical UL 94 scenario.

The cone calorimeter [230, 232] is currently the preferred device for characterizing the combustion behavior of materials [233]. It is used to determine principal fire properties such as time to ignition, rate of heat release, and smoke obscuration, among others [234]. Sheetlike samples measuring 100 × 100 mm^2 and up to 50 mm thick are placed on top of a load cell. They are irradiated from above at a constant, preset heat flux (up to 100 kW/m^2) using a radiant electrical heater in the shape of a truncated cone. Ignition is assured by an intermittent spark igniter located 13 mm above the horizontal sample. The sample mass is continuously monitored during the test. Air is blown past the sample at a flow rate of 0.024 m^3/s. The heat release rate is calculated from the measured oxygen concentration in the exhaust stream. The instrument also allows characterization of smoke obscuration and the determination of the concentrations of other compounds, like CO or CO_2 in the exhaust gas. The cone calorimeter is often operated at heat flux values of either 35 or 50 kW as these reflect possible ranges for the heat generated in a well-developed fire [232]. Parameters reported include among others time to ignition (TTI in s), peak of heat release rate (PHRR in kW/m^2), and total heat release (THR in MJ/m^2) [234]. Figure 21 shows typical results of such cone calorimeter test for PA 11 and a nanocomposite containing 10 m% C30B, and Table 2 lists fire test performed on PA 11 compounds containing different fire-retardant additives for estimation of the flame retardancy. In Table 2, within the various shadowed sections, first, the unmodified PA 11 grade is listed, followed by data obtained on the same grade but modified for the purpose of investigating the effect of modification on the flame retardancy. Perusal of Table 2 indicates that excellent flame-retardant performance can be obtained for various PA 11 grades by adding 20–25 m% expandable graphite or aluminum phosphinates. However, this unfortunately comes at the cost of a loss in toughness of the material, i.e., reduced impact strengths.

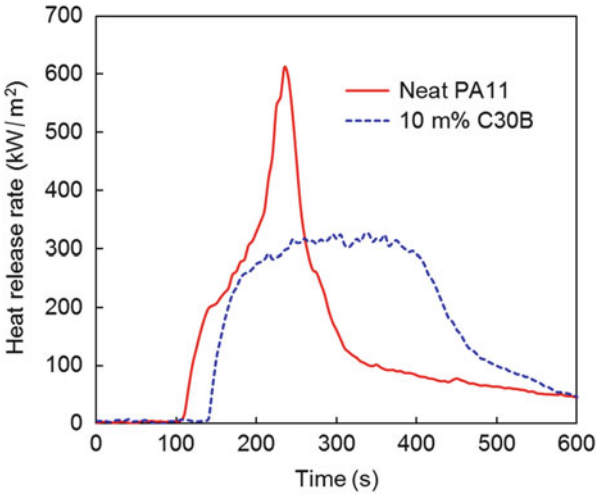

Fig. 21 Heat release rate (HRR) for neat PA 11 and its 10 m% Cloisite C30B nanocomposite during a cone calorimeter test conducted at a flux of 35 kW/m^2

Table 2 Fire test performance PA 11 compounds

PA 11 grade	Composition m%	LOI %	UL 94 V rating	TTI s	PHRR kW/m^2	THR MJ/m^2	Ref
Rilsan PCG LV	100		V-2				[235]
Rilsan PCG LV	72.5		V-0				
Exolit OP 1312[a]	25						
Halloysite nanotubes	2.5						
Rilsan BMNO TLD	100			83 (*)	971 (*)		[236]
Rilsan BMNO TLD	70			62 (*)	518 (*)		
Nanoboehmite	30						
RILSAN BESNO-TL	100	22.2	NR	45	1,366	124	[237]
RILSAN BESNO-TL	80	28.5	V-0	43	271	86	
Expandable graphite	20						
RILSAN BESNO-TL	80	24.6	V-0	39	760	111	
Melamine	20						
RILSAN BESNO-TL	80	32.3	V-0	40	279	77	
Expandable graphite	15						
Melamine	5						
Rilsan® PCG LV	100		V-2				[238]
Rilsan® PCG LV	80		V-0				
Exolit® OP 1230[b]	15						
Cloisite® 30B	2.5						
Carbon nanofibers	2.5						
Rilsan PCG LV	100		NR	59	653	101	[239, 240]
Rilsan PCG LV	75		V-0	52	147	92	
Exolit OP 1312[a]	20						
Carbon nanofibers	5						
Rilsan PCG LV	75		V-0	39	210	116	
Exolit OP 1312[a]	20						
Cloisite 30B	5						
Rilsan PCG LV	75		V-0				
Exolit OP 1230[b]	20						
Carbon nanofibers	5						
Rilsan PCG LV	72.5		V-0				
Exolit OP 1230[b]	20						
Cloisite 30B	7.5						

(continued)

Table 2 (continued)

PA 11 grade	Composition m%	LOI %	UL 94 V rating	TTI s	PHRR kW/m^2	THR MJ/m^2	Ref
Rilsan	100	23.0	V-1	69 (*)	679 (*)	93.2 (*)	[241]
Rilsan	80	31.5	V-1	107 (*)	460 (*)	79.4 (*)	
Exolit OP 1230[b]	20						
Rilsan	80	32.4	V-1	106 (*)	470 (*)	82.4 (*)	
Exolit OP 1230[b]	15						
Layered double hydroxide	5						
Rilsan Besno TL	100	22.2	NR	47	943	125	[242]
Rilsan Besno TL	75	29.2	V-0	38 (*)	177 (*)	44 (*)	
TiO_2	3						
AM-APP[c]	22						

Cone calorimeter tests were conducted at a heat flux of 35 or 50 kW/m^2 (*). Details about the tests and interpretation of data are available in the provided references

[a]Exolit OP 1312 is a non-halogenated flame retardant based on organic phosphinates [243]

[b]Exolit OP 1230 is a white, fine-grained powder based on an organic phosphinate [243]

[c]Adduct of melamine, p-aminobenzene sulfonic acid, and ammonium polyphosphate

7 Summary

PA 11 is an environment-friendly semicrystalline high-performance thermoplastic polymer with many specific applications in all fields of engineering but also as a biomaterial. It may not be a unique property or characteristics which favors the use of PA 11 for a particular application but often its balanced property profile in terms of thermal stability, mechanical behavior, and resistance to media. In this paper, comprehensive information about thermal properties is provided, aimed to further understand structure formation on cooling the melt as a prerequisite to design specific semicrystalline morphologies. As such, at first, information about thermodynamic functions of state of the melt and crystal phase are provided, permitting to predict equilibrium structural states at any temperature. This was followed by detailed description of the crystal polymorphism of PA 11 and explanation of different crystal-nucleation routes as a major tool to generate PA 11 of largely different semicrystalline morphology. Accordingly, it is possible to melt-process PA 11 such to obtain semicrystalline structures containing spherulitically grown crystal lamellae or non-spherulitically arranged mesophase domains of nearly identical phase fraction; even both morphologies can be combined with the available knowledge of the temperature dependence of prevailing nucleation mechanisms and crystallization rates. Naturally, such qualitatively different structures affect end-user properties, with detailed information hardly available in the literature. Few data about the effect of the crystallization history on the temperature

dependence of Young's modulus were presented in this review, including demonstration of the advantageous effect of modification with nanofillers; however, there remains need for further quantitative studies about processing-structure-property relations. Similarly, survey of the literature from point of view of obtaining information about the effect of deformation/shear of the melt during subsequent solidification revealed another field of missing knowledge, in particular since PA 11 is often processed by conventional melt-processing routes including extrusion and injection-molding, and since for many other crystallizable polymers, quantitative correlations between shearing conditions, the crystallization kinetics, and final morphology were already established. In the final chapter, the thermal stability and current efforts to increase the flame retardancy of this important polymer are summarized, with the latter information illustrating the efforts for development of new non-flammable PA 11 grades which certainly widen the area of application of this important thermoplastic polymeric material.

References

1. Arkema. Arkema celebrates the 70th birthday of its flagship Rilsan® polyamide 11 brand [Internet]. https://www.arkema.com/en/media/news/news-details/Arkema-celebrates-the-70th-birthday-of-its-flagship-Rilsan-polyamide-11-brand/. Assessed 17 Apr 2018
2. Starkweather Jr HW (1995) Transitions and relaxations. In: Kohan MI (ed) Nylon plastics handbook. Hanser, Munich, pp 139–150
3. Materials Database [Internet]. https://www.extrememateriales-arkema.com/en/materials-database/. Assessed 2 May 2018
4. Winnacker M, Rieger B (2016) Biobased polyamides: recent advances in basic and applied research. Macromol Rapid Commun 37:1391–1413
5. Arkema. Arkema announces a major investment project in the biosourced polyamide 11 chain in Asia [Internet]. https://www.arkema.com/en/media/news/news-details/Arkema-announces-a-major-investment-project-in-the-biosourced-polyamide-11-chain-in-Asia/. Assessed 30 Jul 2018
6. Ogunniyi DS (2006) Castor oil: a vital industrial raw material. Bioresour Technol 97:1086–1091
7. Mubofu EB (2016) Castor oil as a potential renewable resource for the production of functional materials. Sustain Chem Process 4:11. (12 pages)
8. Binder RG, Applewhite TH, Kohler GO, Goldblatt LA (1962) Chromatographie analysis of seed oils. Fatty acid composition of castor oil. J Am Oil Chem Soc 39:513–517
9. Genas M (1962) Rilsan (Polyamid 11), synthese und eigenschaften. Angew Chem 74:535–540
10. Arkema. Rilsan® polyamide 11 (PA11) - high performance bio based resins. https://www.extrememateriales-arkema.com/en/product-families/rilsan-polyamide-11-family/
11. Oliveira MJ, Botelho G (2008) Degradation of polyamide 11 in rotational moulding. Polym Degrad Stab 93:139–146
12. Sherman LM (2014) Additive manufacturing: materials for 'real-world' parts. Plast Technol 60:42–47
13. Bai J, Yuan S, Shen F, Zhang B, Chua CK, Zhou K, Wei J (2017) Toughening of polyamide 11 with carbon nanotubes for additive manufacturing. Virtual Phys Prototyping 12:235–240
14. Newman BA, Chen P, Pae KD, Scheinbeim JI (1980) Piezoelectricity in nylon 11. J Appl Phys 51:5161–5164
15. Scheinbeim JI (1981) Piezoelectricity in γ-form nylon 11. J Appl Phys 52:5939–5942

16. Mathur SC, Scheinbeim JI, Newman BA (1984) Piezoelectric properties and ferroelectric hysteresis effects in uniaxially stretched nylon-11 films. J Appl Phys 56:2419–2425
17. Balizer E, Fedderly J, Haught D, Dickens B, Dereggi AS (1994) FTIR and X-ray study of polymorphs of nylon 11 and relation to ferroelectricity. J Polym Sci Polym Phys 32:365–369
18. Williams JCL, Watson SJ, Boydell P (1995) Properties. In: Kohan MI (ed) Nylon plastics handbook. Hanser, Munich, pp 291–360
19. Holmes DR, Bunn CW, Smith DJ (1955) The crystal structure of polycaproamide: nylon 6. J Polym Sci 17:159–177
20. Evstatiev M (1997) Polyamides. In: Olabisi O (ed) Handbook of thermoplastics. Marcel Dekker, New York
21. Wunderlich B, Czornyj G (1977) A study of equilibrium melting of polyethylene. Macromolecules 10:906–913
22. Prevorsek DC, Butler RH, Reimschuessel HK (1971) Mechanical relaxations in polyamides. J Polym Sci Polym Phys 9:867–886
23. Gordon M, Taylor JS (1952) Ideal copolymers and the second-order transitions of synthetic rubbers. I. Non-crystalline copolymers. J Appl Chem 2:493–500
24. Manley TR, Martin CG (1973) The elastic modulus of nylons. Polymer 14:632–638
25. Ong ES, Kim Y, Williams HL (1986) Dynamic mechanical properties of some nylons and their blends. J Appl Polym Sci 31:367–383
26. Kawaguchi T (1959) The dynamic mechanical properties of nylons. J Appl Polym Sci 2:56–61
27. Schmieder K, Wolf K (1953) Mechanische relaxationserscheinungen an hochpolymeren. Kolloid-Z 134:149–189
28. Woodward AE, Deeley CW, Sauer JA, Kline DE (1957) Effect of irradiation on dynamic mechanical properties of 6-6 nylon. J Appl Phys 28:1124–1130
29. Fornes TD, Paul DR (2004) Structure and properties of nanocomposites based on Nylon-11 and -12 compared with those based on Nylon-6. Macromolecules 37:7698–7709
30. Gibbs JW On the equilibrium of heterogeneous substances, Trans Conn Acad. 3:108–248, 1876; 3:343–524, 1878. Reprinted in The Scientific Papers of J. Willard Gibbs, pp. 55–371, Longmans, Green, and Co, London 1906
31. Nylon 11 (NYLON11) Heat Capacity, Enthalpy, Entropy, Gibbs Energy: Datasheet from "The Advanced THermal Analysis System (ATHAS) Databank – Polymer Thermodynamics" Release 2014 in SpringerMaterials. http://materials.springer.com/polymerthermodynamics/docs/athas_0022
32. Wunderlich B (2005) Thermal analysis of polymeric materials. Springer, Berlin
33. Androsch R, Wunderlich B (2007) Scanning calorimetry. In: Matyjaszewski K, Gnanou Y, Leibler L (eds) Macromolecular engineering: precise synthesis, materials properties, applications, vol 3, pp 1827–1880
34. Xenopoulos A, Wunderlich B (1990) Heat capacities of solid polyamides. Polymer 31:1260–1268
35. Xenopoulos A, Wunderlich B (1990) Thermodynamic properties of liquid and semicrystalline linear aliphatic polyamides. J Polym Sci B Polym Phys 28:2271–2290
36. Wunderlich B (1995) The ATHAS database on heat capacities of polymers. Pure Appl Chem 67:1019–1026
37. Wunderlich B, Jones LD (1969) Heat capacities of solid polymers. J Macromol Sci Part B 3:67–79
38. Cheban YV, Lau SF, Wunderlich B (1982) Analysis of the contribution of skeletal vibrations to the heat capacity of linear macromolecules in the solid state. Colloid Polym Sci 260:9–19
39. Lau SF, Wunderlich B (1983) Calculation of the heat capacity of linear macromolecules from theta-temperatures and group vibrations. J Therm Anal Calorim 28:59–85
40. Pyda M, Bartkowiak M, Wunderlich B (1998) Computation of heat capacities of solids using a general Tarasov equation. J Therm Anal Calorim 52:631–656
41. Wunderlich B (1960) Study of the change in specific heat of monomeric and polymeric glasses during the glass transition. J Phys Chem 64:1052–1056
42. Wunderlich B (2003) Reversible crystallization and the rigid–amorphous phase in semicrystalline macromolecules. Prog Polym Sci 28:383–450

43. Schick C, Krämer L, Mischok W (1985) Der Einfluß struktureller Veränderungen auf den Glasübergang in teilkristallinem Polyethylenterephthalat I. Isotherme Kristallisation. Acta Polym 36:47–53
44. Schick C, Fabry F, Schnell U, Stoll G, Deutschbein L, Mischok W (1988) Der Einfluß struktureller Veränderungen auf den Glasübergang in teilkristallinem Poly (ethylenterephthalat) 2. Charakterisierung der übermolekularen Struktur. Acta Polym 39:705–710
45. Schick C, Wigger J, Mischok W (1990) Der Einfluß struktureller Veränderungen auf den Glasübergang in teilkristallinem Poly(ethylenterephthalat) 3. Der Glasübergang in den zwischenlamellaren Bereichen. Acta Polym 41:137–142
46. Androsch R, Wunderlich B (2005) The link between rigid amorphous fraction and crystal perfection in cold-crystallized poly(ethylene terephthalate). Polymer 46:12556–12566
47. Zia Q, Mileva D, Androsch R (2008) The rigid amorphous fraction in isotactic polypropylene. Macromolecules 41:8095–8102
48. Kolesov I, Androsch R (2012) The rigid amorphous fraction of cold-crystallized polyamide 6. Polymer 53:4070–4077
49. Chen H, Cebe P (2007) Investigation of the rigid amorphous fraction in Nylon-6. J Therm Anal Calorim 89:417–425
50. Di Lorenzo ML, Righetti MC (2008) The three-phase structure of isotactic poly (1-butene). Polymer 49:1323–1331
51. Righetti MC, Tombari E, Di Lorenzo ML (2008) Crystalline, mobile amorphous and rigid amorphous fractions in isotactic polystyrene. Eur Polym J 44:2659–2667
52. Schick C, Wurm A, Mohamed A (2001) Vitrification and devitrification of the rigid amorphous fraction of semicrystalline polymers revealed from frequency-dependent heat capacity. Colloid Polym Sci 279:800–806
53. Schick C, Wurm A, Mohammed A (2003) Formation and disappearance of the rigid amorphous fraction in semicrystalline polymers revealed from frequency dependent heat capacity. Thermochim Acta 396:119–132
54. Ma Q, Georgiev G, Cebe P (2011) Constraints in semicrystalline polymers: using quasi-isothermal analysis to investigate the mechanisms of formation and loss of the rigid amorphous fraction. Polymer 52:4562–4570
55. Lin J, Shenogin S, Nazarenko S (2002) Oxygen solubility and specific volume of rigid amorphous fraction in semicrystalline poly (ethylene terephthalate). Polymer 43:4733–4743
56. Olson BG, Lin J, Nazarenko S, Jamieson AM (2003) Positron annihilation lifetime spectroscopy of poly (ethylene terephthalate): contributions from rigid and mobile amorphous fractions. Macromolecules 36:7618–7623
57. Wunderlich B (1964) The melting of defect polymer crystals. Polymer 5:611–624
58. Wunderlich B (1980) Macromolecular physics, vol 3*:* crystal melting. Academic Press, New York
59. Zettlemoyer AC (1969) Nucleation. Dekker, New York
60. Volmer M (1938) Kinetik der Phasenbildung. Verlag von Theodor Steinkopff, Dresden
61. Wunderlich B (1976) Macromolecular physics, vol. 2, crystal nucleation, growth, annealing. Academic Press, New York
62. Mandelkern L (2004) Crystallization of polymers, vol 2, kinetics and mechanisms. Cambridge University Press, Cambridge
63. Strobl G (1996) The physics of polymers: concepts for understanding their structures and behavior. Springer, Berlin
64. Hoffmann JD, Davis GT, Lauritzen Jr JI (1976) The rate of crystallization of linear polymers with chain folding. In: Hannay HB (ed) Treatise on solid state chemistry, crystalline and noncrystalline solids, vol 3. Plenum, New York
65. Cheng SZD (2008) Phase transitions in polymers. Elsevier, Amsterdam
66. Wunderlich B (2012) Termination of crystallization or ordering of flexible, linear macromolecules. J Therm Anal Calorim 109:1117–1132
67. Zhang Q, Mo Z, Liu S, Zhang H (2000) Influence of annealing on structure of nylon 11. Macromolecules 33:5999–6005

68. Jariyavidyanont K, Williams JL, Rhoades AM, Kühnert I, Focke W, Androsch R (2018) Crystallization of polyamide 11 during injection molding. Polym Eng Sci 58:1053–1061
69. Schmidt GF, Stuart HA (1958) Gitterstrukturen mit räumlichen Wasserstoffbrückensystemen und Gitterumwandlungen bei Polyamiden. Z Z Naturforsch 13:222–225
70. Ziabicki A (1959) Über die mesomorphe β-form von polycapronamid und ihre Umwandlung in die kristalline form α. Koll Z Z Polym 167:132–141
71. Starkweather HW, Whitney JF, Johnson DR (1963) Crystalline order in nylon 66. J Polym Sci Polym Chem 1:715–723
72. Sandeman I, Keller A (1956) Crystallinity studies of polyamides by infrared, specific volume and X-ray methods. J Polym Sci Polym Chem 9:401–435
73. Auriemma F, Petraccone V, Parravicini L, Corradini P (1997) Mesomorphic form (β) of nylon 6. Macromolecules 30:7554–7559
74. Schroeder LR, Cooper SL (1976) Hydrogen bonding in polyamides. J Appl Physiol 47:4310–4317
75. Murthy NS (2006) Hydrogen bonding, mobility, and structural transitions in aliphatic polyamides. J Polym Sci Polym Phys 44:1763–1782
76. Illers KH (1978) Polymorphie, Kristallinität und Schmelzwärme von Poly (ε-caprolactam), 2. Kalorimetrische Untersuchungen. Macromol Chem Phys 179:497–507
77. Androsch R, Stolp M, Radusch HJ (1996) Crystallization of amorphous polyamides from the glassy state. Acta Polym 47:99–104
78. Kolesov I, Androsch R (2012) The rigid amorphous fraction of cold-crystallized polyamide 6. Polymer 53:4770–4777
79. Illers VKH, Haberkorn H (1971) Schmelzverhalten, Struktur und Kristallinität von 6-Polyamid. Macromol Chem Phys 142:31–67
80. Gurato G, Fichera A, Grandi FZ, Zannetti R, Canal P (1974) Crystallinity and polymorphism of 6-polyamide. Macromol Chem Phys 175:953–975
81. Mathias LJ, Powell DG, Autran JP, Porter RS (1990) ^{15}N NMR characterization of multiple crystal forms and phase transitions in polyundecanamide (nylon 11). Macromolecules 23:963–967
82. Pepin J, Miri V, Lefebvre JM (2016) New insights into the Brill transition in polyamide 11 and polyamide 6. Macromolecules 49:564–573
83. Brill R (1942) Über das Verhalten von Polyamiden beim Erhitzen. J Prakt Chem 161:49–64
84. Slichter WP (1959) Crystal structures in polyamides made from ω-amino acids. J Polym Sci Polym Chem 36:259–266
85. Little K (1959) Investigation of nylon "texture" by X-ray diffraction. Br J Appl Phys 10:225–230
86. Newman BA, Sham TP, Pae KD (1977) A high-pressure x-ray study of nylon 11. J Appl Phys 48:4092–4098
87. Radusch HJ, Stolp M, Androsch R (1994) Structure and temperature-induced structural changes of various polyamides. Polymer 35:3568–3571
88. Biangardi HJ (1990) Brill transition of polyamide 6.12. J Macromol Sci Phys 29:139–153
89. Jones NA, Atkins EDT, Hill MJ (2000) Comparison of structures and behavior on heating of solution-grown, chain-folded lamellar crystals of 31 even-even nylons. Macromolecules 33:2642–2650
90. Jones NA, Cooper SJ, Atkins EDT, Hill MJ, Franco L (1997) Temperature-induced changes in chain-folded lamellar crystals of aliphatic polyamides. Investigation of nylons 2 6, 2 8, 2 10, and 2 12. J Polym Sci Polym Phys 35:675–688
91. Yang X, Tan S, Li G, Zhou E (2001) Dependence of the Brill transition on the crystal size of nylon 10 10. Macromolecules 34:5936–5942
92. Morales-Gámez L, Soto D, Franco L, Puiggalí J (2010) Brill transition and melt crystallization of nylon 56: an odd–even polyamide with two hydrogen-bonding directions. Polymer 51:5788–5798
93. Ramesh C, Keller A, Eltink SJEA (1994) Studies on the crystallization and melting of nylon-6, 6: 1. The dependence of the Brill transition on the crystallization temperature. Polymer 35:2483–2487

94. Starkweather Jr HW (1989) Deconvolution of the excess heat capacity of the Brill transition in nylon 66. Macromolecules 22:2000–2003
95. Starkweather HW, Jones GA (1981) Crystalline transitions in powders of nylon 66 crystallized from solution. J Polym Sci B Polym Phys 19:467–477
96. Hirschinger J, Miura H, Gardner KH, English AD (1990) Segmental dynamics in the crystalline phase of nylon 66: solid state deuterium NMR. Macromolecules 23:2153–2169
97. Wendoloski JJ, Gardner KH, Hirschinger J, Miura H, English AD (1990) Molecular dynamics in ordered structures: computer simulation and experimental results for nylon 66 crystals. Science 247:431–436
98. Cooper SJ, Coogan M, Everall N, Priestnall I (2001) A polarised μ-FTIR study on a model system for nylon 6 6: implications for the nylon Brill structure. Polymer 42:10119–10132
99. Mathot VBF, Benoist L (1994) Calorimetry and thermal analysis of polymers. Hanser, Munich
100. Pijpers MFJ, Mathot VBF, Goderis B, Scherrenberg R, van der Vegte E (2002) High-speed calorimetry for the analysis of kinetics of vitrification, crystallization and melting of macromolecules. Macromolecules 35:3601–3613
101. Kolesov IS, Androsch R, Radusch HJ (2004) Non-isothermal crystallization of polyethylenes as function of cooling rate and concentration of short chain branches. J Therm Anal Calorim 78:885–895
102. Stuart HA, Kahle B (1955) Beobachtungen über die morphologische Struktur in Hochpolymeren. J Polym Sci Lett 18:143–147
103. Kahle B (1957) Über die Kristallisationskinetik in makromolekularen Substanzen. Z Elektrochemie. Ber Bunsenges Phys Chem 61:1318–1328
104. Liu S, Yu Y, Cui Y, Zhang H, Mo Z (1998) Isothermal and nonisothermal crystallization kinetics of Nylon-11. J Appl Polym Sci 70:2371–2380
105. Schick C, Mathot V (2016) Fast scanning calorimetry. Springer, Cham
106. Baeten D, Mathot VBF, Pijpers TFJ, Verkinderen O, Portale G, van Puyvelde P, Goderis B (2015) Simultaneous synchrotron WAXD and fast scanning (chip) calorimetry: on the (isothermal) crystallization of HDPE and PA11 at high supercoolings and cooling rates up to 200°C s^{-1}. Macromol Rapid Commun 36:1184–1191
107. Baeten D, Cavallo D, Portale G, Androsch R, Mathot V, Goderis B (2016) Combining fast scanning chip calorimetry with structural and morphological characterization techniques. In: Schick C, Mathot V (eds) Fast scanning calorimetry. Springer, Cham, pp 327–359
108. Rhoades AM, Wonderling N, Schick C, Androsch R (2016) Supercooling-controlled heterogeneous and homogenous crystal nucleation of polyamide 11 and its effect onto the crystal/mesophase polymorphism. Polymer 106:29–34
109. Hirami M (1984) SAXD studies on bulk crystallization of nylon 6. I. Changes in crystal structure, heat of fusion, and surface free energy of lamellar crystals with crystallization temperature. J Macromol Sci Phys B23:397–414
110. Brucato V, Piccarolo S, Titomanlio G (1993) Crystallization kinetics in relation to polymer processing. Macromol Symp 68:245–255
111. Cavallo D, Gardella L, Alfonso G, Portale G, Balzano L, Androsch R (2011) Effect of cooling rate on the crystal/mesophase polymorphism of polyamide 6. Colloid Polym Sci 289:1073–1079
112. Brucato V, Piccarolo S, La Carrubba V (2002) An experimental methodology to study polymer crystallization under processing conditions. The influence of high cooling rates. Chem Eng Sci 57:4129–4143
113. Rybnikař F, Burda J (1961) Temperaturabhängigkeit der Gitterstruktur von Poly-6-capronamid. Faserforschung und Textiltechnik 12:324–331
114. Haberkorn H, Illers KH, Simak P (1979) Molekülordnung und Kristallinität in Polyhexamethylenadipamid. Colloid Polym Sci 257:820–840
115. Gohn AM, Rhoades AM, Wonderling N, Tighe T, Androsch R (2017) The effect of supercooling of the melt on the semicrystalline morphology of PA 66. Thermochim Acta 655:313–318

116. Inoue M (1963) Studies on crystallization of high polymers by differential thermal analysis. J Polym Sci Polym Chem 1:2697–2709
117. Kawaguchi A, Ikawa T, Fujiwara Y, Tabuchi M, Monobe K (1981) Polymorphism in lamellar single crystals of nylon 11. J Macromol Sci Phys 20:1–20
118. Sasaki T (1965) Notes on the polymorphism in nylon 11. J Polym Sci Polym Lett 3:557–560
119. Androsch R, Rhoades AM, Stolte I, Schick C (2015) Density of heterogeneous and homogeneous crystal nuclei in poly (butylene terephthalate). Eur Polym J 66:180–189
120. Androsch R, Schick C (2017) Crystal nucleation of polymers at high supercooling of the melt. Adv Polym Sci 276:257–288
121. Long Y, Shanks RA, Stachurski ZH (1995) Kinetics of polymer crystallization. Prog Polym Sci 20:651–701
122. de Santis S, Adamovsky S, Titomanlio G, Schick C (2007) Isothermal nanocalorimetry of isotactic polypropylene. Macromolecules 40:9026–9031
123. Silvestre C, Cimmino S, Duraccio D, Schick C (2007) Isothermal crystallization of isotactic poly(propylene) studied by superfast calorimetry. Macromol Rapid Commun 28:875–881
124. Mileva D, Androsch R (2012) Effect of co-unit type in random propylene copolymers on the kinetics of mesophase formation and crystallization. Colloid Polym Sci 290:465–471
125. van Drongelen M, Meijer-Vissers T, Cavallo D, Portale G, Vanden Poel G, Androsch R (2013) Microfocus wide-angle X-ray scattering of polymers crystallized in a fast scanning chip calorimeter. Thermochim Acta 563:33–37
126. Rhoades AM, Williams JL, Androsch R (2015) Crystallization of polyamide 66 at processing-relevant cooling conditions and at high supercooling. Thermochim Acta 603:103–109
127. Pyda M, Nowak-Pyda E, Heeg J, Huth H, Minakov AA, di Lorenzo ML et al (2006) Melting and crystallization of poly(butylene terephthalate) by temperature-modulated and superfast calorimetry. J Polym Sci Polym Phys 44:1364–1377
128. Schawe JEK (2014) Influence of processing conditions on polymer crystallization measured by fast scanning DSC. J Therm Anal Calorim 116:1165–1173
129. Schick C, Androsch R (2016) New insights into polymer crystallization by fast scanning chip calorimetry. In: Mathot VBF, Schick C (eds) Fast scanning calorimetry. Springer, Cham
130. Toda A, Androsch R, Schick C (2016) Insights into polymer crystallization and melting by fast scanning chip calorimetry. Polymer 91:239–263
131. Schick C, Androsch R, Schmelzer JWP (2017) Homogeneous crystal nucleation in polymers. J Phys Condens Matter 29:453002. (35 pp)
132. Liu S, Yu Y, Cui Y, Zhang H, Mo Z (1998) Isothermal and nonisothermal crystallization kinetics of nylon-11. J App Polym Sci 70:2371–2380
133. Zhang Q, Yu M, Fu Q (2004) Crystal morphology and crystallization kinetics of polyamide-11/clay nanocomposites. Polym Int 53:1941–1949
134. Guo Y, Hu G, Wang Z, Li Y, Yang Y (2012) Isothermal crystallization kinetics and melting behavior of POE-g-mah compatibilized PA11/POE blends. J Wuhan Univ Technol Mater Sci Ed 27:702–707
135. Mollova A, Androsch R, Mileva D, Gahleitner M, Funari SS (2013) Crystallization of isotactic polypropylene containing beta-phase nucleating agent at rapid cooling. Eur Polym J 49:1057–1065
136. Androsch R, Monami A, Kucera J (2014) Effect of an alpha-phase nucleating agent on the crystallization kinetics of a propylene/ethylene random copolymer at largely different supercooling. J Crystal Growth 408:91–96
137. Schawe JE, Vermeulen PA, van Drongelen M (2015) A new crystallization process in polypropylene highly filled with calcium carbonate. Colloid Polym Sci 293:1607–1614
138. Zhuravlev E, Wurm A, Pötschke P, Androsch R, Schmelzer JW, Schick C (2014) Kinetics of nucleation and crystallization of poly (ε-caprolactone)–multiwalled carbon nanotube composites. Eur Polym J 52:1–11
139. Jariyavidyanont K, Focke W, Androsch R (2016) Crystallization kinetics of polyamide 11 in presence of sepiolite and montmorillonite nanofillers. Colloid Polym Sci 294:1143–1151
140. Zia Q, Androsch R, Radusch HJ, Piccarolo S (2006) Morphology, reorganization, and stability of mesomorphic nanocrystals in isotactic polypropylene. Polymer 47:8163–8172

141. Zia Q, Androsch R, Radusch HJ, Ingolič E (2008) Crystal morphology of rapidly cooled isotactic polypropylene: a comparative study by TEM and AFM. Polym Bull 60:791–798
142. Mileva D, Androsch R, Radusch HJ (2008) Effect of cooling rate on melt-crystallization of random propylene-ethylene and propylene-1-butene copolymers. Polym Bull 61:643–654
143. Hsu CC, Geil PH, Miyaji H, Asai K (1986) Structure and properties of polypropylene crystallized from the glassy state. J Polym Sci Polym Phys 24:2379–2401
144. Ogawa T, Miyaji M, Asai K (1985) Nodular structure of polypropylene. J Phys Soc Jpn 54:3668–3670
145. Mileva D, Androsch R, Zhuravlev E, Schick C (2012) Morphology of mesophase and crystals of polyamide 6 prepared in a fast scanning chip calorimeter. Polymer 53:3994–4001
146. Mileva D, Kolesov I, Androsch R (2012) Morphology of cold-ordered polyamide 6. Colloid Polym Sci 290:971–978
147. Magill JH (1969) Formation of spherulites in polyamides. IV. Even–odd polyamides and poly (ω-aminocarboxylic acids). J Polym Sci Polym Phys 7:123–142
148. Lindenmeyer PH, Holland VF (1964) Relationship between molecular weight, radial-growth rate, and the width of the extinction bands in polyethylene spherulites. J Appl Phys 35:55–58
149. Keith HD, Padden FJ (1996) Banding in polyethylene and other spherulites. Macromolecules 29:7776–7786
150. Barham PJ, Keller A, Otun EL, Holmes PA (1984) Crystallization and morphology of a bacterial thermoplastic: poly-3-hydroxybutyrate. J Mater Sci 19:2781–2794
151. Gránásy L, Pusztai T, Tegze G, Warren JA, Douglas JF (2005) Growth and form of spherulites. Phys Rev E 72:011605
152. Crist B, Schultz JM (2016) Polymer spherulites: a critical review. Prog Polym Sci 56:1–63
153. Jariyavidyanont K, Schick C, Androsch R (2019) Nucleation-controlled dual semicrystalline morphology of polyamide 11. Polym Int 68:263–270. https://doi.org/10.1002/pi.5606
154. Mollova A, Androsch R, Mileva D, Schick C, Benhamida A (2013) Effect of supercooling on crystallization of polyamide 11. Macromolecules 46:828–835
155. Zia Q, Androsch R (2009) Effect of atomic force microscope tip geometry on the evaluation of the crystal size of semicrystalline polymers. Meas Sci Technol 20:097003. (4 pp)
156. O'Kane WJ, Young RJ, Ryan AJ, Bras W, Derbyshire GE, Mant GR (1994) Simultaneous SAXS/WAXS and d.s.c. analysis of the melting and recrystallization behavior of quenched polypropylene. Polymer 35:1352–1358
157. Miyamoto Y, Fukao K, Yoshida T, Tsurutani N, Miyaji H (2000) Structure formation of isotactic polypropylene from the glass. J Phys Soc Jpn 69:1735–1740
158. Marega C, Causin V, Marigo A (2008) A SAXS-WAXD study on the mesomorphic-a transition of isotactic polypropylene. J Appl Polym Sci 109:32–37
159. Starkweather HW, Brooks RE (1959) Effect of spherulites on the mechanical properties of nylon 66. J Appl Polym Sci 1:236–239
160. Way JL, Atkinson JR, Nutting J (1974) The effect of spherulite size on the fracture morphology of polypropylene. J Mater Sci 9:293–299
161. Perkins WG (1999) Polymer toughness and impact resistance. Polym Eng Sci 39:2445–2460
162. Zia Q, Radusch HJ, Androsch R (2009) Deformation behavior of isotactic polypropylene crystallized via a mesophase. Polym Bull 63:755–771
163. Mileva D, Zia Q, Androsch R (2010) Tensile properties of random copolymers of propylene with ethylene and 1-butene: effect of crystallinity and crystal habit. Polym Bull 65:623–634
164. Mileva D, Androsch R, Radusch HJ (2009) Effect of the structure on light transmission in isotactic polypropylene and random propylene-1-butene copolymers. Polym Bull 62:561–571
165. Zia Q, Androsch R, Radusch HJ (2010) Effect of the structure at the micrometer and nanometer scales on the light transmission of isotactic polypropylene. J Appl Polym Sci 117:1013–1020
166. Kolesov I, Mileva D, Androsch R (2014) Mechanical behavior and optical transparency of polyamide 6 of different morphology formed by variation of the pathway of crystallization. Polym Bull 71:581–593

167. Menyhárd A, Gahleitner M, Varga J, Bernreitner K, Jääskeläinen P, Øysæd H, Pukánszky B (2009) The influence of nucleus density on optical properties in nucleated isotactic polypropylene. Eur Polym J 45:3138–3148
168. Halpin JC, Kardos JL (1972) Moduli of crystalline polymers employing composite theory. J Appl Phys 43:2234–2241
169. Kardos JL, Raisoni J (1975) The potential mechanical response of macromolecular systems – a composite analogy. Polym Eng Sci 15:183–190
170. Kardos JL, Piccarolo S, Halpin JC (1978) Strength of discontinuous reinforced composites: II. Isotropic crystalline polymers. Polym Eng Sci 18:505–511
171. Bédoui F, Diani J, Régnier G (2004) Micromechanical modeling of elastic properties in polyolefins. Polymer 45:2433–2442
172. Pukanszky B, Mudra I, Staniek P (1997) Relation of crystalline structure and mechanical properties of nucleated polypropylene. J Vinyl Addit Technol 3:53–57
173. Rilsan PA 11. Product information. http://www.rilsan.com/en/rilsan-pa11/pa11-product-information/. Accessed Nov 2016
174. Katti SS, Schultz M (1982) The microstructure of injection-molded semicrystalline polymers: a review. Polym Eng Sci 22:1001–1017
175. Russell DP, Beaumont PW (1980) Structure and properties of injection-moulded nylon-6. J Mater Sci 15:197–207
176. Drummer D, Meister S (2014) Correlation of processing, inner structure, and part properties of injection moulded thin-wall parts on example of polyamide 66. Int J Polym Sci 2014:718926. 8 pages
177. Housmans JW, Gahleitner M, Peters GW, Meijer HE (2009) Structure–property relations in molded, nucleated isotactic polypropylene. Polymer 50:2304–2319
178. Kantz MR, Newman HD, Stigale FH (1972) The skin-core morphology and structure–property relationships in injection-molded polypropylene. J Appl Polym Sci 16:1249–1260
179. Čermák R, Obadal M, Ponížil P, Polášková M, Stoklasa K, Lengálová A (2005) Injection-moulded α-and β-polypropylenes: I. Structure vs. processing parameters. Eur Polym J 41:1838–1845
180. Fornes TD, Paul DR (2003) Crystallization behavior of nylon 6 nanocomposites. Polymer 44:3945–3961
181. Murthy NS, Kagan VA, Bray RG (2002) Effect of melt temperature and skin-core morphology on the mechanical performance of nylon 6. Polym Eng Sci 42:940–950
182. Apichartpattanasiri S, Hay JN, Kukureka SN (2001) A study of the tribological behaviour of polyamide 66 with varying injection-moulding parameters. Wear 251:1557–1566
183. Yalcin B, Valladares D, Cakmak M (2003) Amplification effect of platelet type nanoparticles on the orientation behavior of injection molded nylon 6 composites. Polymer 44:6913–6925
184. Zhang R, Kennedy PK (2004) A model for post-flow induced crystallization: general equations and predictions. J Rheol 48:823–842
185. Sorrentino A, de Santis F, Titomanlio G (2007) Polymer crystallization under high cooling rate and pressure: a step towards polymer processing conditions. Lect Notes Phys 714:329–344
186. Janeschitz-Kriegl H (2003) How to understand nucleation in crystallizing polymer melts under real processing conditions. Colloid Polym Sci 281:1157–1171
187. Lamberti G (2014) Flow induced crystallization of polymers. Chem Soc Rev 43:2240–2252
188. Rhoades AM, Gohn AM, Seo J, Androsch R, Colby RH (2018) The sensitivity of polymer crystallization to shear at low and high supercooling of the melt. Macromolecules 51:2785–2795
189. Acierno S, van Puyvelde P (2005) Effect of short chain branching upon the crystallization of model polyamides-11. Polymer 46:10331–10338
190. Rhoades AM, Williams JL, Wonderling N, Androsch R, Guo J (2017) Skin/core crystallinity of injection-molded poly (butylene terephthalate) as revealed by microfocus X-ray diffraction and fast scanning chip calorimetry. J Therm Anal Calorim 127:939–946
191. Doyle MJ (2000) On the effect of crystallinity on the elastic properties of semicrystalline polyethylene. Polym Eng Sci 40:330–335

192. Humbert S, Lame O, Séguéla R, Vigier G (2011) A re-examination of the elastic modulus dependence on crystallinity in semi-crystalline polymers. Polymer 52:4899–4909
193. Crist B, Fisher CJ, Howard PR (1989) Mechanical properties of model polyethylenes: tensile elastic modulus and yield stress. Macromolecules 22:1709–1718
194. Shen L, Phang IY, Liu T (2006) Nanoindentation studies on polymorphism of nylon 6. Polym Test 25:249–253
195. Ito M, Mizuochi K, Kanamoto T (1998) Effects of crystalline forms on the deformation behaviour of nylon-6. Polymer 39:4593–4598
196. Dencheva N, Denchev Z, Oliveira MJ, Funari SS (2007) Relationship between crystalline structure and mechanical behavior in isotropic and oriented polyamide 6. J Appl Polym Sci 103:2242–2252
197. Dencheva N, Denchev Z, Oliveira MJ, Nunes TG, Funari SS (2008) Relationship between the crystalline structure and mechanical behavior in isotropic and oriented polyamide 12. J Appl Polym Sci 109:288–302
198. Labour T, Ferry L, Gauthier C, Hajji P, Vigier G (1999) α- and β-crystalline forms of isotactic polypropylene investigated by nanoindentation. J Appl Polym Sci 74:195–200
199. Azzurri F, Flores A, Alfonso GC, Sics I, Hsiao BS, Baltá Calleja FJ (2003) Polymorphism of isotactic polybutene-1 as revealed by microindentation hardness. Part II: correlations to microstructure. Polymer 44:1641–1645
200. Frübing P, Kremmer A, Gerhard-Multhaupt R, Spanoudaki A, Pissis P (2006) Relaxation processes at the glass transition in polyamide 11: from rigidity to viscoelasticity. J Chem Phys 125:214701
201. Mathot VBF, Pijpers MFJ (1989) Heat capacity, enthalpy and crystallinity of polymers from DSC measurements and determination of the DSC peak base line. Thermochim Acta 151:241–259
202. Zia Q, Tranchida D, Androsch R, Schönherr H (2012) Effect of crystal habit and superstructure on modulus of elasticity of isotactic polypropylene by AFM nanoindentation. J Mater Sci 47:3040–3045
203. Ray SS (2013) Clay-containing polymer nanocomposites: from fundamentals to real applications. Elsevier, Amsterdam
204. Thomas S, Joseph K, Malhotra SK, Goda K, Sreekala MS (2013) Polymer composites, nanocomposites. Wiley, Hoboken
205. Thomas S, Zaikov GE (2008) Polymer nanocomposite research advances. Nova Science, Hauppauge
206. Fornes TD, Paul DR (2003) Modeling properties of nylon 6/clay nanocomposites using composite theories. Polymer 44:4993–5013
207. Ahmed S, Jones FR (1990) A review of particulate reinforcement theories for polymer composites. J Mater Sci 25:4933–4942
208. Halpin JC, Kardos JL (1976) The Halpin-Tsai equations: a review. Polym Eng Sci 16:344–352
209. Tucker III CL, Liang E (1999) Stiffness predictions for unidirectional short-fiber composites: review and evaluation. Compos Sci Technol 59:655–671
210. Brune DA, Bicerano JU (2002) Micromechanics of nanocomposites: comparison of tensile and compressive elastic moduli, and prediction of effects of incomplete exfoliation and imperfect alignment on modulus. Polymer 43:369–387
211. Liu T, Lim KP, Tjiu WC, Pramoda KP, Chen ZK (2003) Preparation and characterization of nylon 11/organoclay nanocomposites. Polymer 44:3529–3535
212. Huang S, Wang M, Liu T, Zhang WD, Tjiu WC, He C, Lu X (2009) Morphology, thermal, and rheological behavior of nylon 11/multi-walled carbon nanotube nanocomposites prepared by melt compounding. Polym Eng Sci 49:1063–1068
213. Halim KAA, Farrell JB, Kennedy JE (2013) Preparation and characterisation of polyamide 11/montmorillonite (MMT) nanocomposites for use in angioplasty balloon applications. Mater Chem Phys 143:336–348

214. Hu Y, Shen L, Yang H, Wang M, Liu T, Liang T, Zhang J (2006) Nanoindentation studies on nylon 11/clay nanocomposites. Polym Testing 25:492–497
215. He X, Yang J, Zhu L, Wang B, Sun G, Lv P, Phang IY, Liu T (2006) Morphology and melt rheology of nylon 11/clay nanocomposites. J Appl Polym Sci 102:542–549
216. Zhang X, Yang G, Lin J (2006) Synthesis, rheology, and morphology of nylon-11/layered silicate nanocomposite. J Polym Sci Polym Phys 44:2161–2172
217. Kolesov I, Androsch R, Mileva D, Lebek W, Benhamida A, Kaci M, Focke W (2013) Crystallization of a polyamide 11/organo-modified montmorillonite nanocomposite at rapid cooling. Colloid Polym Sci 291:2541–2549
218. Mileva D, Monami A, Cavallo D, Alfonso GC, Portale G, Androsch R (2013) Crystallization of a polyamide 6/montmorillonite nanocomposite at rapid cooling. Macromol Mater Eng 298:938–943
219. Levchik SV, Weil ED, Lewin M (1999) Thermal decomposition of aliphatic nylons. Polym Int 48:532–557
220. Michal J, Mitera J, Kubát J (1981) Major pyrolysis and thermoxidative products from certain polyamides. Fire Mater 5:1–5
221. Sallet D, Mailhos-Lefievre V, Martel B (1990) Flame retardancy of polyamide 11 with a decabromodiphenyl-antimony trioxide mixture. A bromine-antimony-nitrogen synergism. Polym Degrad Stab 30:29–39
222. Ballistreri A, Garozzo D, Giuffrida M, Impallomeni G, Montaudo G (1989) Primary thermal decomposition processes in aliphatic polyamides. Polym Degrad Stab 23:25–41
223. Ohtani H, Nagaya T, Sugimura Y, Tsuge S (1982) Studies on thermal degradation of aliphatic polyamides by pyrolysis-glass capillary chromatography. J Anal Appl Pyrolysis 4:117–131
224. Filippone G, Carroccio SC, Mendichi R, Gioiella L, Dintcheva NT, Gambarotti C (2015) Time-resolved rheology as a tool to monitor the progress of polymer degradation in the melt state – part I: thermal and thermo-oxidative degradation of polyamide 11. Polymer 72:134–141
225. Duan P, Dai L, Savage PE (2010) Kinetics and mechanism of N-substituted amide hydrolysis in high-temperature water. J Supercrit Fluids 51:362–368
226. Meyer A, Jones N, Lin Y, Kranbuehl D (2002) Characterizing and modeling the hydrolysis of polyamide-11 in a pH 7 water environment. Macromolecules 35:2784–2798
227. Hocker SJ, Hudson-Smith NV, Smith PT, Komatsu CH, Dickinson LR, Schniepp HC, Kranbuehl DE (2017) Graphene oxide reduces the hydrolytic degradation in polyamide-11. Polymer 126:248–258
228. Stoclet G, Sclavons M, Devaux J (2013) Relations between structure and property of polyamide 11 nanocomposites based on raw clays elaborated by water-assisted extrusion. J Appl Polym Sci 127:4809–4824
229. Richaud E, Diogo OO, Fayolle B, Verdu J, Guilment J, Fernagut F (2013) Review: auto-oxidation of aliphatic polyamides. Polym Degrad Stab 98:1929–1939
230. Joseph P, Tretsiakova-McNally S, Zhang R (2016) Techniques for assessing the combustion behaviour of polymeric materials: some current perspectives and future directions. Macromol Symp 362:105–118
231. Kempel F, Schartel B, Marti JM, Butler KM, Rossi R, Idelsohn SR, Oñate E, Hofmann A (2015) Modelling the vertical UL 94 test: competition and collaboration between melt dripping, gasification and combustion. Fire Mater 39:570–584
232. Babrauskas V (1984) Development of the cone calorimeter – a bench-scale heat release rate apparatus based on oxygen consumption. Fire Mater 8:81–95
233. ASTM E 1354 (2004) Standard test method for heat and visible smoke release rates for materials and products using an oxygen consumption calorimeter. ASTM, Philadelphia
234. Schartel B, Hull TR (2007) Development of fire-retarded materials – interpretation of cone calorimeter data. Fire Mater 31:327–354

235. Hao A, Wong I, Wu H, Lisco B, Ong B, Sallean A, Butler S, Londa M, Koo JH (2015) Mechanical, thermal, and flame-retardant performance of polyamide 11-halloysite nanotube nanocomposites. J Mater Sci 50:157–167
236. Ferry L, Sonnier R, Lopez-Cuesta JM, Petigny S, Bert C (2017) Thermal degradation and flammability of polyamide 11 filled with nanoboehmite. J Therm Anal Calorim 129:1029–1037
237. Jin X, Chen C, Sun J, Zhang X, Gu X, Zhang S (2017) The synergism between melamine and expandable graphite on improving the flame retardancy of polyamide 11. High Perform Polym 29:77–86
238. Johnson B, Allcorn E, Baek MG, Koo JH, Lake CL, Lake P (2011) Combined effects of montmorillonite clay, carbon nanofiber, and fire retardant on mechanical and flammability properties of polyamide 11 nanocomposites. In: Annual international solid freeform application symposium
239. Lao SC, Koo JH, Moon TJ, Londa M, Ibeh CC, Wissler GE, Pilato LA (2011) Flame-retardant polyamide 11 nanocomposites: further thermal and flammability studies. J Fire Sci 29:479–498
240. Lao SC, Yong W, Nguyen K, Moon TJ, Koo JH, Pilato L, Wissler G (2010) Flame-retardant polyamide 11 and 12 nanocomposites: processing, morphology, and mechanical properties. J Compos Mater 44:2933–2951
241. Zhang S, Tang W, Gu X, Jiang P, Sun J, Sophie D, Bourbigot S, Casetta M (2016) Flame retardancy and thermal and mechanical performance of intercalated, layered double hydroxide composites of polyamide 11, aluminum phosphinate, and sulfamic acid. J Appl Polym Sci 133:43370
242. Jin X, Sun J, Zhang JS, Gu X, Bourbigot S, Li H, Tang W, Zhang S (2017) Preparation of a novel intumescent flame retardant based on supramolecular interactions and its application in polyamide 11. ACS Appl Mater Interfaces 9:24964–24975
243. Exolit® OP. https://www.clariant.com/de/Innovation/Innovation-Spotlight-Videos/Exolit. Assessed 28 Jul 2018

Adv Polym Sci (2019) 283: 189–218
https://doi.org/10.1007/12_2019_51

Published online: 22 August 2019

Thermal Properties of Biobased Polymers: Furandicarboxylic Acid (FDCA)-Based Polyesters

Nathanael Guigo, Emilie Forestier, and Nicolas Sbirrazzuoli

Contents

1 Introduction 190
2 PEF 192
2.1 Synthesis and Physical Properties of PEF 192
2.2 Thermal and Mechanical Properties of PEF 195
3 Other FDCA-Based Polyesters with Longer Aliphatic Chains 210
4 Conclusion 213
References 213

Abstract Furanic building blocks can be prepared by sugar conversion processes. Of these building blocks, 2,5-furandicarboxylic acid (FDCA) has strong potential for the preparation of biobased aromatic polyesters with both similarities and unique characteristics in comparison with terephthalic polyesters. This chapter aims to highlight the most significant breakthroughs on the thermal properties of FDCA polyesters. Poly(ethylene 2,5-furandicarboxylate), also referred as poly(ethylene 2,5-furanoate) or PEF, is a furandicarboxylic acid (FDCA) polyester with structural analogy to polyethylene terephthalate (PET). Thus, PEF synthesis, physical properties, thermal and mechanical properties, quiescent and strain-induced crystallization, glass transition, and molecular mobility are discussed. In addition, the thermal properties of PEF nanocomposites are also presented. Finally, the end of this chapter is dedicated to FDCA polyesters prepared with longer chain diols (i.e., containing from 3 to 12 methylene groups) as the flexibility and the consequent thermal properties of these FDCA polyesters are linked to the number of methylene units.

N. Guigo, E. Forestier, and N. Sbirrazzuoli (✉)
Université Côte d'Azur, Institut de Chimie de Nice, UMR CNRS 7272, Nice, Cedex 2, France
e-mail: nicolas.sbirrazzuoli@unice.fr; Nicolas.SBIRRAZZUOLI@univ-cotedazur.fr

Keywords Biobased polymers · FDCA polyesters · Furandicarboxylic acid (FDCA) · Hydroxymethylfurfural (HMF) · Lignocellulosic biomass · Poly(ethylene 2,5-furandicarboxylate) (PEF) · Poly(ethylene 2,5-furanoate) (PEF) · Thermomechanical properties

1 Introduction

In the development of engineering polymeric materials (e.g., fibers, films, etc.), aromatic polyesters are less sensitive to thermal hydrolysis than aliphatic polyesters. It is particularly interesting when melt processing is expected for material forming. Since the seminal works on polyethylene terephthalate (PET) in the 1940s [1], terephthalic polyesters have been broadly used in various commercial applications with, nowadays, optimized manufacturing and recycling technologies. However, the transition to a sustainable, biobased economy that is encouraged by new regulations is becoming a societal priority in recent times. In this context, the development of biobased polyesters is growing fast. The fermentation of sugars leads to aliphatic building blocks such as lactic acid, glycolic acid, and succinic acid, which can be further converted into aliphatic polyesters poly(lactic acid) (PLA), poly(glycolic acid) (PGA), poly(butylene succinate) (PBS), etc., by polycondensation. On the other hand, the preparation of aromatic polyesters from biobased aromatic building blocks offers fewer possibilities. Indeed, the routes for obtaining p-terephthalic acid (pTA) from carbohydrates are not direct since these sugars contain six carbons at most. The production of a C_8 pTA from C_6 sugars requires the addition of ethylene via Diel-Alder cycloaddition. The only subsequent way to yield a favorable mass balance, i.e., starting from a C_6 sugar (e.g., glucose or fructose) to produce C_6 aromatic building block, is to consider furanic molecules. Disubstituted furan-based molecules are very promising biobased platform molecules that can be obtained from non-food competitive carbohydrates. They have been referred to as "sleeping giants" because of their enormous market potential as attested by their presence in the US Department of Energy list of top 10 biobased products with high potential [2, 3]. These molecules have been known for a long time, but new (catalytic) processes allowing their production at an industrial scale have been recently optimized, thus paving the way for employing furanic compounds in various applications such as polyesters or biofuels [3]. Following the same analogy with the polyesters' synthesis from terephthalic acid (Fig. 1), the dicarboxylic acid in the furan family is furandicarboxylic acid (FDCA), which is obtained from controlled oxidation of 5-hydroxymethylfurfural (HMF) [4, 5]. HMF is produced from the triple dehydration of C_6 sugars such as fructose or glucose. FDCA polyesters can be then prepared through direct esterification and polycondensation of purified FDCA with diols. When monoethylene glycol (MEG) is employed for polycondensation with FDCA, it leads to poly(ethylene 2,5-furandicarboxylate), PEF, also referred as poly(ethylene 2,5-furanoate). This polyester can be viewed as a PET analogue bearing a furanic ring instead of a benzene ring (Fig. 1). PET is widely used

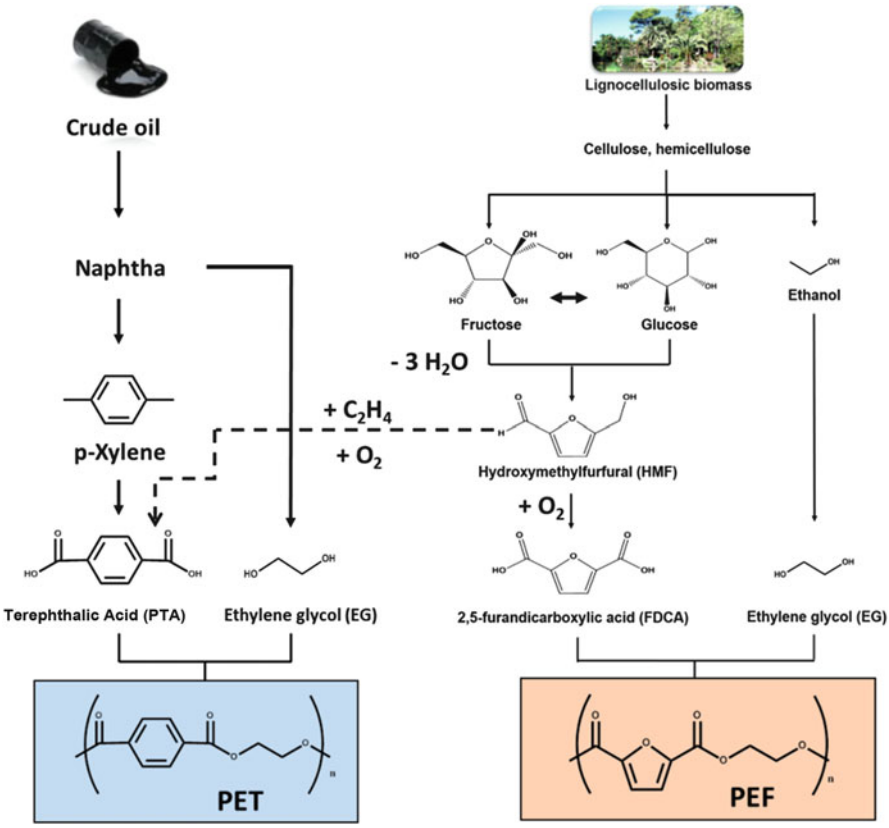

Fig. 1 Comparison of synthesis routes for oil-based PET and biobased PEF: from lignocellulosic biomass to PEF

because of its many useful properties, such as transparency, semicrystallinity, high rigidity, and barrier properties [6]. Therefore, the academic and commercial interest in PEF is increasing significantly, mainly for its potential as a biobased packaging material [7, 8]. This polyester can be employed for packaging use, fibers, films, and thermoformed articles. PEF has gained this increasing interest mainly due to its improved sustainability, intrinsically higher barrier properties, glass transition temperature, and modulus when compared to PET for amorphous materials.

In the context of developing new applications for biobased FDCA polyesters, increased knowledge and fine control of their thermal properties are of utmost importance, especially when compared with the existing thermal characteristics of the widely used terephthalic polyesters. The link between the thermal properties and the optimization of the process technology is crucial for considering and establishing application development and market implementation. The thermal properties of FDCA-based polyesters are driven by their structure and the peculiar local and global motions associated with the presence of the furan ring.

This chapter aims to highlight the most significant breakthroughs on the thermal properties of FDCA polyesters. The first section is dedicated to PEF, which is by far the most well-described FDCA polyester due to its structural analogy with PET. This section will start with some brief considerations about PEF synthesis and its physical properties and then the crystallization behavior of PEF and a description of the molecular mobility of the amorphous PEF chains. A subsequent section will be dedicated to preparation and thermal properties of PEF nanocomposites. Finally, this chapter will also expose some interesting features of FDCA polyesters prepared with longer chain diols.

2 PEF

2.1 Synthesis and Physical Properties of PEF

As for other polyesters, PEF synthesis is a step-growth polymerization that can proceed via two pathways, i.e., the direct esterification route with FDCA or the transesterification route employing dimethyl-2,5-furandicarboxylate (DMF). The first PEF synthesis was patented in 1946 by Derwitt and Lincoln in which melt polymerization was employed with a MEG/FDCA molar ratio of 1.6 [9]. Then, in the late 1970s, Gandini [10] and Moore and Kelly [11] reported PEF synthesis via the transesterification route. Direct esterification is intrinsically catalyzed by the FDCA carboxylic groups while a titanium catalyst is often used for increasing the transesterification rate. Both direct esterification and transesterification lead to the

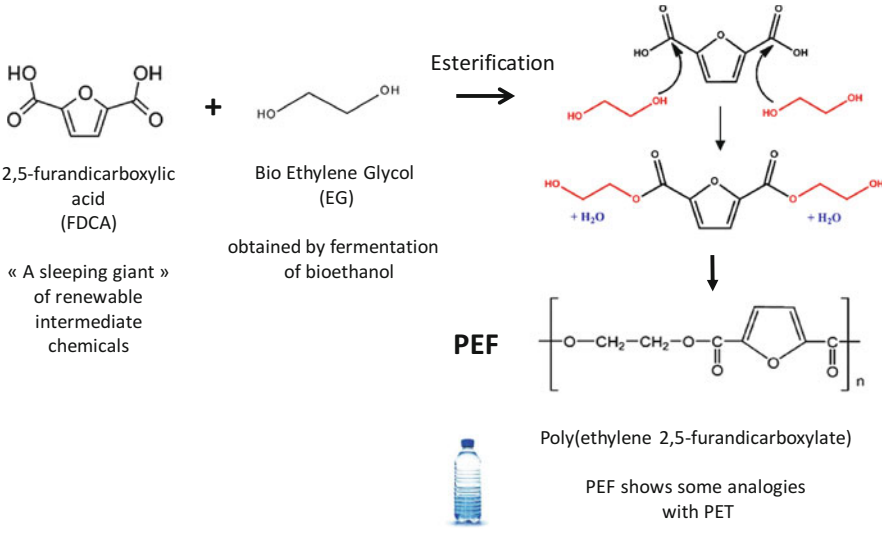

Fig. 2 PEF synthesis from FDCA

formation of bis(hydroxyethyl)-2,5-furandicarboxylate (BHEF) as shown in Fig. 2. Then, polycondensation of BHEF via a transesterification reaction occurs in the melt phase, often catalyzed by Sb_2O_3. As for PET, polycondensation releases ethylene glycol, which must be removed under vacuum in order to displace the equilibrium toward the formation of polyester [12]. An additional solid-state polymerization step is implemented to further increase the molecular weight. The purity of monomers is also an important issue, and it explains why the DMF route [10, 11, 13, 14] has been more frequently employed than direct FDCA esterification [15, 16] since it is easier to obtain pure DMF compared to FDCA. More details about PEF synthesis can be found in the recent review of Sousa et al. [5].

Although pTA and FDCA present some similarities (Fig. 1), there are some structural differences that are responsible for the distinctions between PET and PEF. From a structural point of view, the head to tail distance between the acid carboxylic groups is about 5.73 Å in pTA, whereas it is shorter in FDCA (4.83 Å) [17]. Moreover, pTA is a more linear molecule than FDCA. The angle between the carbonyl and the furan ring is equal to 130°, while the angle between the carbonyl and phenyl groups is 180°. FDCA differs from pTA by the presence of a furan ring instead of a benzene ring. The oxygen atom of the furan ring leads to a decrease in the aromaticity and of the orientation along the chain axis. As a result, the covalent strength along the chain is weaker, but the polarizability of the polymer is higher [5]. These structural differences between the furan and the benzene ring have an impact on the different properties of PEF and PET.

As already mentioned in the introduction, PEF has superior mechanical properties compared to PET [18] and much higher barrier properties to gas (e.g., O_2 and CO_2) or liquids (e.g., H_2O) than PET, which is beneficial for food and beverage packaging applications such as bottles. Amorphous PEF exhibits an 11× reduction in oxygen permeability, a 19× reduction in carbon dioxide permeability, and a 2.8× reduction in water permeability compared to amorphous PET [19–23]. PEF is not biodegradable but it is recyclable in the PET stream.

To explain the reduced gas permeability of PEF compared to PET, various authors have attributed these difference to a reduced PEF chain mobility associated with the lower bond angle of the carboxyl groups on the furan ring compared to the linear arrangement on the benzene ring [18, 24–27].

Both PEF and PET are thermoplastic polymers that can be deformed when heated above their glass transition. Glass transition temperature (T_g) and melting temperature (T_m) are key parameters for polymer processing. Below T_g, polymers are rigid (glassy state) and only small and local motions are possible. The glassy state is characterized by a small free volume that only allows for local motions of the chain segments. As the temperature rises, motions increase with increasing temperature and the material reaches a rubberlike state. The molecular motion intensifies and the free volume increases, initiating translational motion of the segments and eventually of the whole chain. This process requires a great degree of cooperativity between the chain segments. The glass transition temperature can be determined by differential scanning calorimetry (DSC). In dynamic mechanical analysis (DMA), it is associated with the main mechanical relaxation and called T_α. Because the glassy state is a

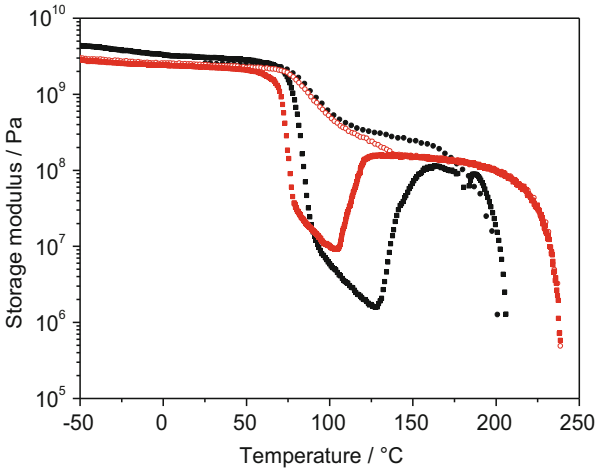

Fig. 3 Storage modulus (E') vs. temperature for amorphous and semicrystalline PEF (black) and PET (red) at 2 K min^{-1} (1 Hz). Amorphous PEF, black solid squares; semicrystalline PEF, black solid circles; amorphous PET, red solid squares; and semicrystalline PET, red open circles. Adapted and reproduced from [27] with permission from the Royal Society of Chemistry

non-equilibrium state, this temperature depends on experimental conditions. Nevertheless, under usual conditions, the T_g is around 76°C and the T_α is around 86°C for amorphous PET [18, 25], whereas for amorphous PEF the T_g is around 85°C and the T_α is around 98°C (Fig. 3).

The crystallization kinetics of PEF is lower than for PET. Cold crystallization of PEF does not occur at a heating rate of around 10 K min^{-1}, whereas it does occur for PET [18]. Heat capacity variation (Δc_p) at the glass transition results from a change of local vibrational motions to larger cooperative motions. Heat capacity variation is higher for PEF than for PET [18, 27]. The difference in the heat capacity and the temperature of glass transition can be explained by the spatial geometry of PEF for the first and a higher free volume for PEF than for PET for the second. Chain motions are more constrained in PEF, which leads to a higher glass transition temperature. The higher free volume in PEF results from the furan ring geometry and the presence of an oxygen atom with two doublets of non-binding electrons. These create more repulsions than in the benzene ring [27].

PEF presents a higher rigidity than PET. According to Knoop et al., PEF elastic modulus is 2,470 MPa, whereas it is about 2,000 MPa for PET at 25°C [14]. Figure 3 shows the elastic modulus evolution with temperature for amorphous and semicrystalline (with several levels of crystallinity) PEF and PET.

The higher rigidity of PEF can be explained by the absence of ring-flipping of the furan ring in PEF [18]. It leads to reduced mobility of the amorphous polymer chains, which require more energy for cooperative motions to occur. Thus, the reduced chain mobility induces a higher glass transition temperature in PEF compared to PET (Fig. 3).

The first PEF crystal structure proposed by Kazaryan et al. in 1968 was a triclinic cell for the α phase with the following parameters, $a = 5.75$ Å, $b = 5.35$ Å, $c = 20.10$ Å, $\alpha = 133.3°$, $\beta = 90°$, and $\gamma = 112°$, comprising two repeating units [28]. However, Mao et al. very recently proposed a monoclinic unit cell where

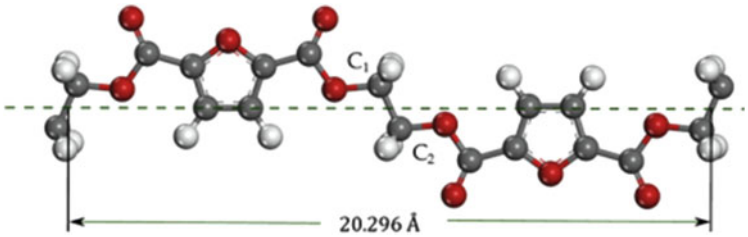

Fig. 4 PEF chain conformation with a one repeating unit; C_1 and C_2 are associated to the alkyl groups. Adapted and reprinted from [29] © 2016 Published by Elsevier Ltd

$a = 5.784$ Å, $b = 6.780$ Å, $c = 20.296$ Å and $\gamma = 103.3°$ [29]. Diffraction patterns of semicrystalline PEF have been reported in several studies [24–26]. In comparison, the crystal structure of PET has the following parameters, $a = 4.56$ Å, $b = 5.94$ Å, $c = 10.75$ Å, $\alpha = 98.5°$, $\beta = 118°$, and $\gamma = 112°$, comprising one repeating unit [24]. The crystal density is 1.455 g cm^{-3} for PET and 1.565 g cm^{-3} for PEF. Mao et al. found a density of 1.562 g cm^{-3} for PEF [29], yet even though their parameters were different from those found in 1968, they still measured the same crystal density. The volume of the unit cell, containing two chains, was 774.6 $Å^3$, which is twice as large as the triclinic cell volume used by Kazaryan and Medvedeva (388 $Å^3$). Figure 4 represents the PEF chain conformation with two repeating units [29].

Stoclet et al. have shown that PEF crystallizes into the α form for crystallization temperatures, T_c, above 160°C, while it crystallizes into a defective α' crystalline form below 160°C [26]. Regarding the crystal structure, the defective α' form does not present a diffraction peak at $2\theta = 19.5°$, and the peaks at $2\theta = 23.3°$ and $2\theta = 26.7°$ are shifted to lower values compared to the α form. Two main melting peaks were observed in DSC for crystallization temperatures lower than 170°C. The lower melting peak corresponds to the melting of the α' form (190–200°C), which recrystallizes into the α form [26]. In 2018, Maini et al. published refined results on the PEF crystal structure [30], concluding that the PEF chains adopted an almost planar configuration.

2.2 Thermal and Mechanical Properties of PEF

2.2.1 Quiescent Crystallization

In-depth understanding and control of the crystallization process from the melt and from the glassy state are of major importance from both the academic standpoint and with regard to manufactured products with desired properties, since fast crystallization from the glassy state is desired for solid-state polycondensation (SSP) and industrial reprocessing, whereas slow crystallization from the melt is desired for injection stretch blow molding of preforms for bottle blowing. Nuclei density of semicrystalline polymers determines the size and the shape of the crystals that are

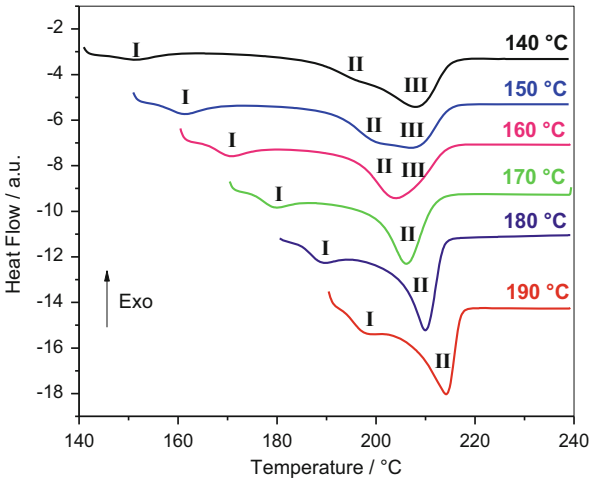

Fig. 5 DSC melting curves (10 K min^{-1}) after crystallization for 72 min at different temperatures. Adapted with permission from [24] Copyright © 2015, John Wiley and Sons

completely linked with the final thermal, optical, and mechanical properties of the material. In addition to this, crystallization can be too slow, and thus identifying a way to increase its rate is of great interest for industrial processing.

Isothermal crystallization was studied in [24, 26, 31]. Once crystallization has occurred, it is interesting to observe the subsequent melting. As for PET, several peaks are observed depending on the crystal nature. Figure 5 represents the melting obtained after 72 min during annealing at various temperatures [24]. The first peak is associated to the melting of unstable crystalline phases (Fig. 5, peak I). The second endotherm (Fig. 5, peak II) is the signature of the melting of more stable crystals. We note that the first and the second peaks are observed on every scan, contrary to the third peak that appears only under certain conditions. Indeed, the third peak (Fig. 5, peak III) is the result of the melting of a thicker crystal formed during recrystallization. This peak disappears for crystallization above 160°C [24].

Polarized optical microscopy (PLOM) observations by Papageorgiou et al. [25] revealed very small spherulites for PEF and a large nucleation density, even at high crystallization temperatures (Fig. 6). In contrast, PET forms larger spherulites.

The effect of polymerization catalysts on the isothermal crystallization of PEF has also been evaluated. It was found that $Ti(OPr)_4$ decreases the crystallization rate compared to catalyst-free PEF, while, on the other hand, $Ca(Ac)_2$ can lead to an acceleration of the crystallization.

Studies of nonisothermal crystallization of PEF have shown that crystallization upon heating of the glass can be described by the classical Hoffman-Lauritzen rate equation (theory of secondary crystallization), while melt crystallization shows an unexpected rate depression compared to the Hoffman-Lauritzen predictions. For the melt crystallization, it was shown that nucleation governs the process (this is reflected by negative increasing values of the apparent activation energy computed by an advanced isoconversional method). In this temperature domain, which can correspond to the temperature of injection molding (e.g., fabrication of parisons for

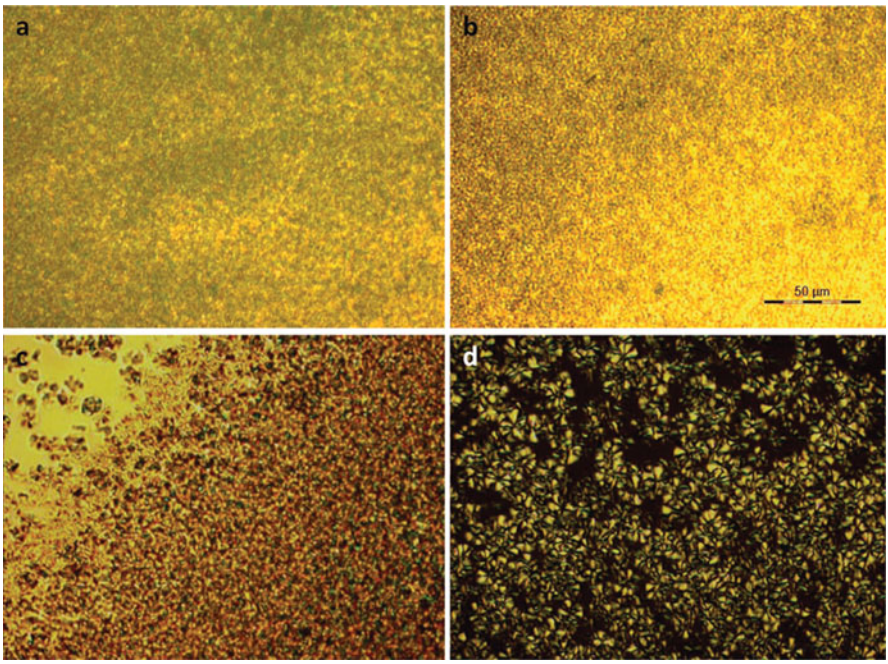

Fig. 6 PLOM photographs showing morphologies generated on isothermal crystallization: (**a**) PEF at 200°C, (**b**) PEF at 210°C, (**c**) PET at 220°C, (**d**) PET at 235°C. Reprinted with permission from [25]. Copyright © 2014, Royal Society of Chemistry

bottle blowing), more brittle materials with bigger crystals are obtained. In the cold crystallization region (crystallization from the glassy state), it was shown that diffusion governs the process and is the rate-limiting step for crystallization. This temperature region corresponds to the temperature conditions of the industrial processes such as solid-state polymerization (SSP) or pellet crystallization. Compared to melt crystallization, more ductile materials with smaller crystals are obtained during cold crystallization because a higher number of nuclei can develop at these temperatures. Computations were performed using DSC data of cold crystallization and melt crystallization, and a new kind of kinetic analysis of thermal data called advanced isoconversional analysis has highlighted new insights in crystallization kinetics and crystallization mechanisms [32]. An atypical depression of the crystallization rate for crystallization during cooling from the melt at $T < \sim 170°C$ has been demonstrated and was attributed to a change in the crystallization regime. This result was confirmed later by other authors who used isothermal DSC, small-angle X-ray diffraction (SAXS) and wide-angle X-ray scattering (WAXS) measurements and found that a defective crystalline form was induced upon isothermal crystallization at $T_c \leq 170°C$, while a more ordered one was induced above this critical T_c [26, 31]. The unexpected depression of the melt crystallization rate compared to the Hoffman-Lauritzen predictions was explained

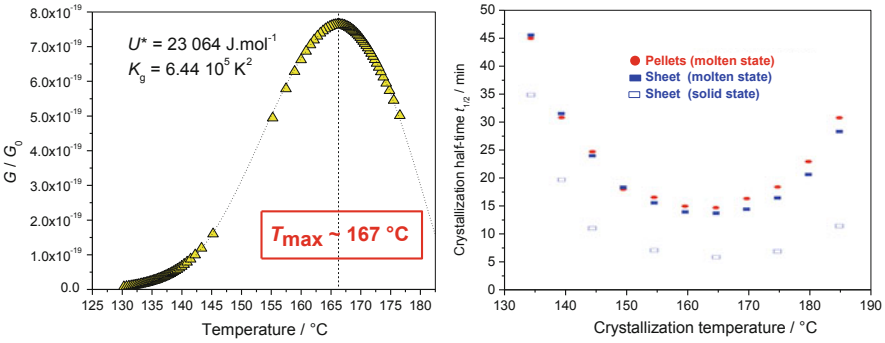

Fig. 7 Left: G/G_0 computed using the Hoffman-Lauritzen (HL) parameters vs. temperature (where G is the linear growth rate and G_0 the pre-exponential factor of the Hoffman-Lauritzen theory). Adapted with permission from [32] Copyright © 2014, John Wiley and Sons. Right: Crystallization half-time vs. crystallization temperature. Adapted with permission from [26] Copyright © 2015 Elsevier Ltd. All rights reserved

by transition to a regime where sporadic secondary nucleation limited the lateral growth rate. The faster crystallization rate found when PEF was crystallized from the glass suggests a more pronounced role of other mechanisms, such as primary nucleation, at lower temperatures.

The temperature at the maximum crystallization rate (around 167°C) was also estimated using advanced isoconversional analysis in association with the Hoffman-Lauritzen rate equation (Fig. 7). This result was also confirmed by other authors and isothermal DSC measurements [24, 26, 31]. Finally, it was concluded that PEF crystals formed from the glass or from the melt show similar structures but that the kinetics of crystal growth differs.

Nucleation of PEF was probed by fast scanning calorimetry (FSC) [33]. Firstly, the effect of different cooling rates on PEF crystallization upon heating of the glass was studied. It was demonstrated that both crystallization and nucleation were prevented at rates faster than 0.5–10 K s^{-1} (30–60 K min^{-1}). This was explained by the fact that at slow cooling rates ($<5 \times 10^{-1}$ K s^{-1}), a higher number of nuclei developed, which increased the number of growing crystals during the successive isothermal step (170°C). Secondly, the effect of low temperature annealing on crystallization upon heating of the glass was studied, with a special emphasis on the influence of nuclei created just above T_g. This point is also of great importance for industrial processing and future industrialization of PEF (crystallization from the glassy state). The studies have shown that nucleation may occur in the glassy state and that as the annealing time increases, the resulting crystallinity measured after an isothermal step at 170°C increases because a higher number of nuclei are created. When decreasing the annealing temperature, the resulting crystallinity measured after an isothermal step at 170°C increases to a lesser extent because the nucleation kinetics slows down due to a decrease in the mobility of the amorphous chain segments when the temperature becomes closer to the glass transition temperature. The limiting time after which a melting enthalpy was measured indicated that crystals were formed during annealing

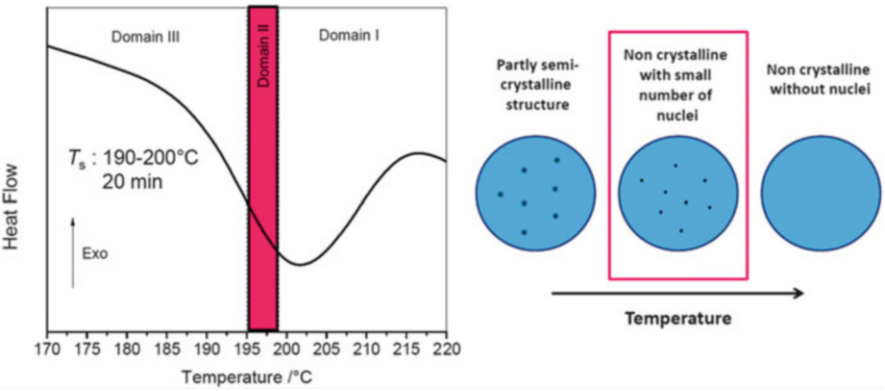

Fig. 8 PEF DSC melting endotherm and location of the self-nucleation domains. Left: Adapted and reprinted with permission from [33] Copyright © 2016, John Wiley and Sons. Right: Reprinted and adapted with permission from [34] Copyright © 2012, American Chemical Society

and not only nuclei, which was also determined for each annealing temperature. Finally, the effect of high-temperature annealing (190–200°C) on PEF crystallization upon heating of the glass was studied in order to highlight self-nucleation behavior. Depending on this annealing temperature (T_s), three different domains were found to exist (Fig. 8). If T_s was high (199–200°C, domain I), we observed a melting of all the crystals. Then, a second region would appear (195–198°C, domain II) where T_s was low enough to keep active self-nuclei. This promoted faster crystallization and subsequently increased the resulting crystallinity. This is an important result because, as crystallization of PEF is quite slow, this is a way to increase final crystallinity after crystallization from the melt without addition of any external nucleation agent, by self-nucleation. This phenomenon is explained by the fact that a higher number of active self-nuclei survive at lower temperatures, and the final crystallinity is enhanced as the temperature decreases within this temperature domain. Isothermal treatment at T_s between 190°C and 194°C also leads to crystallinity as a result of self-nucleation phenomena (domain III). A small high temperature melting peak appears in this case, and it becomes more important as T_s decreases. It corresponds to the melting of crystals that remained unmolten and underwent additional annealing at T_s. As T_s decreases, a higher proportion of unmolten crystals remain and are successively subjected to crystal thickening due to annealing, as is indicated by the increasing size of the high temperature melting peak. Finally, when T_s was low, we observed an annealing process (crystal thickening) of the unmolten crystals.

A new and very efficient method for modeling the nonisothermal crystallization kinetics of PEF was also proposed and was compared to more classical methods [35]. The equation that has been proposed is able to take into account for additional phenomena occurring at the end of crystallization upon heating of the glass, such as crystal thickening. These phenomena are not considered in the classical Hoffman-Lauritzen (HL) equation. Using this equation, it was possible to perfectly model the nonisothermal crystallization of PEF, both on heating from the glass and on cooling

from the melt, over the whole temperature range. It was also shown that model-free simulations made using an advanced isoconversional analysis gave very accurate results and constituted an alternative possibility to model crystallization data when the crystallization mechanisms are very complex and are not perfectly known. These results are very important for industrial processing of bottles and parisons.

2.2.2 Strain-Induced Crystallization

Generally, uniaxial and biaxial orientation induced by material processing promotes strain-induced crystallization (SIC), which may result in a noticeable improvement of mechanical and barrier properties. As different mechanisms are involved, the crystalline phase obtained by the stretching is different from the one induced by a heating treatment or by the one obtained after cooling. For PET it has been shown that under stretching, firstly, an extension and an orientation of the chains along the stretching direction will take place, followed by their spatial organization. This leads to some conformation changes: from *gauche* to *trans,* which is the conformation present in the crystal [36, 37]. From the mechanical standpoint, these microstructural modifications lead to a stress increase on the strain/stress curves as the result of the strain-hardening process. Along this phenomenon, the crystalline phase develops while the strain no longer evolves. When the stretching takes place at high temperature, there is always a competition between the mobility gain by the thermal energy supplied and the rearrangement of the chains in the stretching direction which leads to a more ordered structure. The post-stretching thermal treatment applied on a stretched sample can improve the microstructure defined by the stretching.

Uniaxial Stretching

Strain-induced structural evolution of PEF upon uniaxial stretching was studied by Stoclet et al. [38] by in situ SAXS-WAXS, using initial strain rates of 7.5×10^{-4} s^{-1} and 10^{-2} s^{-1}. PEF has been stretched at draw temperatures (T_d) between 65°C and 100°C. The stretching settings lead to two major microstructures. They concluded that during stretching PEF undergoes an ordered mesomorphic transition at low stretching temperatures (close to T_g), which result in a different structure from the strain-induced phase. This mesosphere is a smectic A type with macromolecules aligned along the stretching direction without interchain packing. A crystalline phase is formed at higher draw temperatures. Strain-induced crystallization was observed to a lesser extent for PEF than for PET. The mechanical behavior of PEF in the rubbery state is very sensitive to the draw temperature.

For stretching temperatures lower than T_g, the SAXS pattern obtained at a deformation of 40% reveals an intense and thin vertical streak associated with a fibrillar structure formation [38]. For such a deformation, WAXS shows a strong orientation, which was absent initially. The association of meridional diffractions arcs and broad equatorial spots on the diffraction patterns prove the orientation

initiation and development. Nevertheless, strain hardening remains very low. The meridional arcs are associated with the formation of a mesomorphic structure, whereas the spots are associated with the presence of an ordered phase. Accordingly, the low spot intensity found, thanks to azimuthal scattering, indicates that the crystalline fraction is very low. The mesophase is the dominant form with such experimental conditions: the temperature is too low for inducing crystallization. Therefore, chains are strongly oriented in the drawing direction but not laterally packed into a crystalline lattice.

For a higher drawing temperature (85°C), the material clearly exhibits strain-hardening. The equatorial spot apparition is correlated with the strain-hardening initiation. For a deformation of 350%, an intense amorphous halo is present as well as intense and diffuse equatorial spots. It reveals the presence of the mesomorphic form as well as a periodically organized phase. Finally, this structure continues to improve itself with the less diffuse spots and the occurrence of off-equatorial spots. These spots revealed the formation of a transversal order. For a final deformation of 700%, a fiber texture was observed, which is the signature of a well-organized structure. It appears that a precursor phase of crystallization was first developed. The level of organization in the sample was measured by azimuthal integration. Even though a strain-hardening was observed, the integrated profiles intensity was very low: the material had a good organization, but the crystallinity level was low. Moreover, when the stretching was performed at high temperatures (e.g., 100°C in this case), no mesomorphic or crystalline order was induced: chain mobility prevented the material from arranging macromolecules in an ordered structure.

A comparison of the strain-induced structure formed during stretching and the thermo-activated crystallized structure reveals many differences. The α and α' forms corresponded to the crystalline forms obtained for, respectively, quiescent crystallization above 160°C (more stable phase) and below 160°C (defective form). At a stretching temperature of 65°C, only two peaks corresponding to a meridional region were found, and the authors associated these peaks to the mesomorphic form. A periodic organization of the planes could be perpendicular to the macromolecular axis but without any regular packing. These two peaks did not appear on the thermally induced microstructure. For a stretching temperature of 85°C, more peaks were observable. The scatters were also different from the thermal induction as the orientation between the two modes of crystallization was different. Imposing a relaxation step after stretching at a temperature of 85°C leads to the crystalline phase enhancement, and the same phenomenon was observed with the mesomorphic phase. In PET during post-stretching relaxation, the mesomorphic phase quantity decreases as the crystalline phase increases. This has been measured by plotting the amorphous *trans* orientation and the crystallinity as a function of relaxation time depending on different initial orientation levels [39]. In PEF, mesophase seems to coexist with crystals.

In another recent publication [40], the PEF uniaxial deformation as well as its microstructural development under stretching has been investigated. PEF was stretched at 50 μm s^{-1} and at different temperatures (T_d = 90°C, 100°C, 110°C and 120°C), demonstrating a strain hardening of the material which became less

pronounced with the increase of the drawing temperature. This was the result of microstructural changes: even if a low quantity of crystal was attained with these conditions (around 5%), the chains had been strongly oriented.

To conclude this section, uniaxial stretching shows the importance of temperature and strain rate choice in strain hardening and crystalline structure development. Before crystallization, PEF seems to first orient its chain. Even if the crystallinity is low, chains can be highly oriented. The crystal obtained by stretching is significantly different to those that were induced thermally. Post-stretching thermal treatments above T_g stabilize the crystalline phase and increase its quantity.

Menager et al. [41] have shown that PEF can develop an organized crystalline-like microstructure under uniaxial stretching above its glass transition and can exhibit behavior close to that of PET. PEF mechanical behavior obeys the time/temperature superposition principle in the large deformation domain and can develop SIC in a rubberlike state involving crystallinity ratios up to 20%.

Biaxial Stretching

The biaxial stretching is closer to the injection stretch blow molding (ISBM) process used in bottle conception. This stretching can be equilibrated (the same draw ratio is applied in each direction) or not. With the use of a biaxial stretching, the chains are oriented along the two stretching directions (machine and transverse). The orientation behavior was studied for PEF in comparison with its chemical analogue, PET, after an equilibrated biaxial stretching [42]. The stretching was performed for areal stretch ratios between 3×3 and 5×5 at various temperatures. While PET exhibits a typical rubberlike behavior for all the stretching temperatures used, this is not the case for the three PEF stretching temperatures (Fig. 9). Indeed, in PET, linear behavior followed by a stress plateau leading to the strain-hardening zone was observed. For PEF, this comportment appeared when the stretching temperatures were above 95°C (100°C and 105°C). When the stretching occurred at 95°C, a yield point appeared after the stress linear increase: this is the signature of a plastic heterogeneous deformation. Because this temperature is too close to the PEF alpha relaxation, this bump can be associated to this transition and to the necking propagation along the specimen. In addition, the PEF rubber-plateau is broader than the PET one, and PEF can be stretched to higher areal draw ratio.

A DSC measurement at 10 K min^{-1} of the stretched samples shows a cold crystallization peak and its shift towards lower temperature as the areal stretch ratio increases. At this rate, the un-stretched samples are not able to crystallize because of the low PEF crystallization kinetic. This phenomenon is the result of the orientation initiated by the previous stretching: the chains already have a local organization and when the temperature is high enough, they start to organize themselves in a more ordered structure. In addition to the order made by the stretching (called SIC), an order made by the acquired thermal energy is also occurring. The separation of the thermal events is thus difficult to establish.

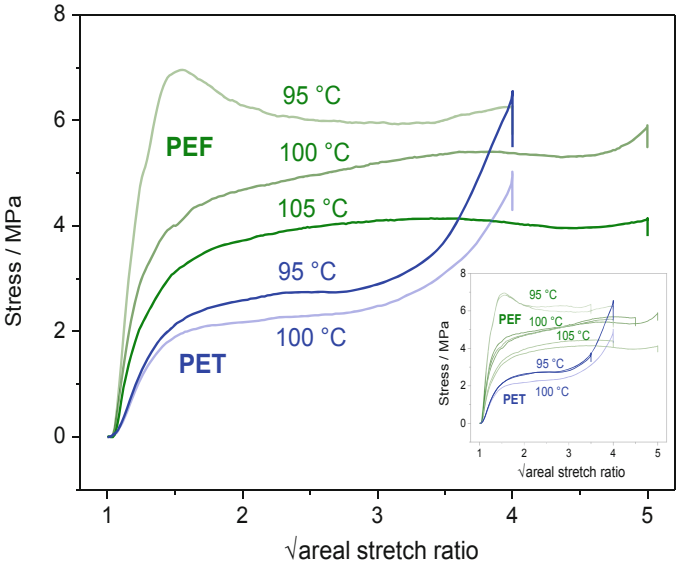

Fig. 9 Stress-strain curves during biaxial stretching of PEF (green line) and PET (blue line). The orientation temperature is indicated by each curve. Insert: overview of samples stretched at lower stretch ratios, indicating variation of the test. Reprinted with permission from [42] Copyright © 2018, John Wiley and Sons

Even if the amount of SIC in PEF increases as the areal stretch ratio increases, at equal draw ratio, the SIC quantity reached in PEF was lower than in PET. A correlation between the shrinkage and the SIC level has been established [42]. The shrinkage was related to the tendency of the oriented amorphous chains to disorient themselves toward their initial conformations. When the SIC increases, the shrinkage decreased at all the temperatures investigated. The PET shrinkage was lower than that of PEF, which can be explained by the higher free volume in PEF than in PET leading to more motion possibilities.

A DMA analysis led to an improved understanding of the orientation and the relaxation interplay processes (Fig. 10). For the stretched samples, the elastic modulus drop during the alpha relaxation was lower than for the unstretched. Indeed, because of the crystal presence, the amorphous chains cannot completely move without being disturbed. Moreover, the α-relaxation shown in the tan δ peak (Fig. 10) becomes broader when it reaches a higher stretch ratio, due to its very diverse microstructures including the amorphous phase, the oriented amorphous phase, and the crystalline one.

As for amorphous materials, permeability to oxygen and carbon dioxide is much lower in oriented PEF than in amorphous PET. From PET to PEF, the barrier improvement factor is about 10.4 for O_2 and 12.7 for CO_2 (median value) [42].

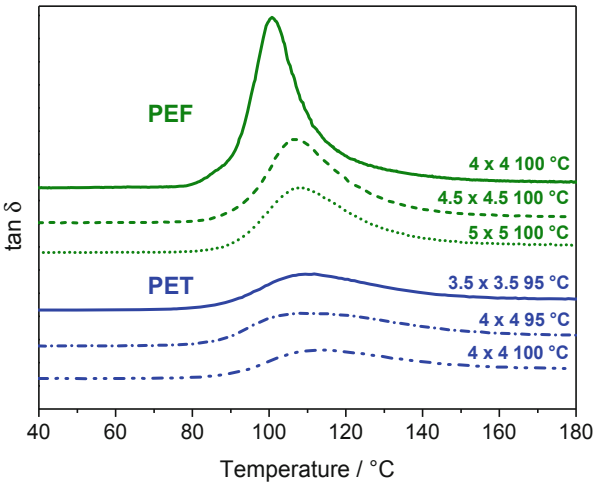

Fig. 10 DMA curves of tan δ vs. temperature for biaxially stretched PEF and PET. The areal-stretching ratio and temperature of orientation are indicated by each curve. Reprinted with permission from [42] Copyright © 2018, John Wiley and Sons

2.2.3 Glass Transition

The glass transition temperature is a very important parameter for polymer applications and processing. The glass transition and mobility of amorphous PEF was studied and compared to that of PET [27]. In particular, the influence of crystallites on the cooperative α-relaxation (glass transition) was highlighted. It was shown that the three-phase model that was used for PET also applied to PEF. This model describes two amorphous phases instead of one, where a fraction of the amorphous material is not undergoing regular Δc_p change during the α-relaxation because molecular motions are constrained due to their strong fixation to the crystal lamella. This phase is called the rigid amorphous fraction (RAF). The results of stochastically temperature-modulated DSC (TOPEM®) studies have shown that PEF presents a higher T_g (around 5°C) compared with PET, which was explained by the more constrained chain motions in PEF. PEF also presents a higher heat capacity variation ($\Delta {c_p}^{0\%}$) at the glass transition, which was explained by a higher free volume in PEF and less chain packing due to differences in chemical structure, in particular the presence of a dipole interaction and absence of linearity in PEF as compared with PET (Fig. 11).

The crystal phase fraction can be deduced from $X_c = \Delta H_{m,DSC}/\Delta {H_m}^0$ where $\Delta H_{m,DSC}$ is evaluated from the integration of the melting peak in DSC scans. The mobile amorphous fraction (MAF) is estimated using the formula $X_{MAF} = \Delta {c_p}^{x\%}/\Delta {c_p}^{0\%\ \text{crystallinity}}$ and the rigid amorphous fraction (RAF) using $X_{RAF} = 1 - X_c - X_{MAF}$. A study on the impact of crystals on the relaxation of MAF showed that for PEF the relaxation of MAF was less influenced by the crystals (Table 1). The T_g remained quasi-constant when the crystallinity increased, while an increase was observed for PET (around 8 K increase), whereas in PEF a lower amount of RAF develops (0–10% instead of 20–30% for PET).

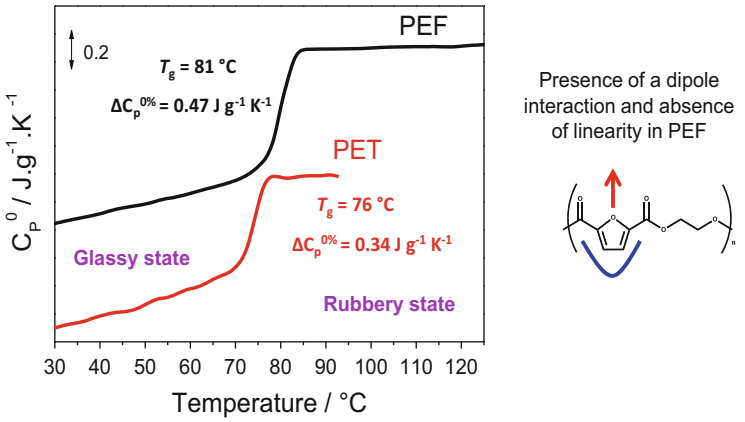

Fig. 11 Heat capacity (c_p) and Δc_p for amorphous PEF and PET obtained by stochastically temperature-modulated DSC (TOPEM®). Adapted and reproduced from [27] with permission from the Royal Society of Chemistry

Table 1 Results obtained from DSC measurements

Samples	X_c %	T_g °C	ΔC_p J.g^{-1}.K^{-1}	X_{MAF} %	X_{RAF} %	
PEF-am	0	81 ± 1	0.47	100	0	PEF
PEF-C0	20	82 ± 1	0.38	80 ± 3	0	
PEF-C1	31	82 ± 1	0.26	55 ± 4	7 ± 4	
PEF-C2	43	79 ± 2	0.24	51 ± 7	6 ± 7	
PET-am	0	76 ± 1	0.34	100	0	PET
PET-C1	34	84 ± 1	0.14	41 ± 3	25 ± 3	

Adapted and reproduced from [27] with permission from the Royal Society of Chemistry

In PEF, relaxation of MAF was less influenced by the crystals, and PEF exhibited a lower amount of RAF. These results were confirmed by DMA; Fig. 12.

As shown on the loss modulus curves, the α-relaxation temperature (marked by a peak) of semicrystalline PEF was slightly increased compared to amorphous PEF but to a lesser extent when compared to PET. This means that the cooperative motions in the amorphous phase are less affected by the presence of crystals.

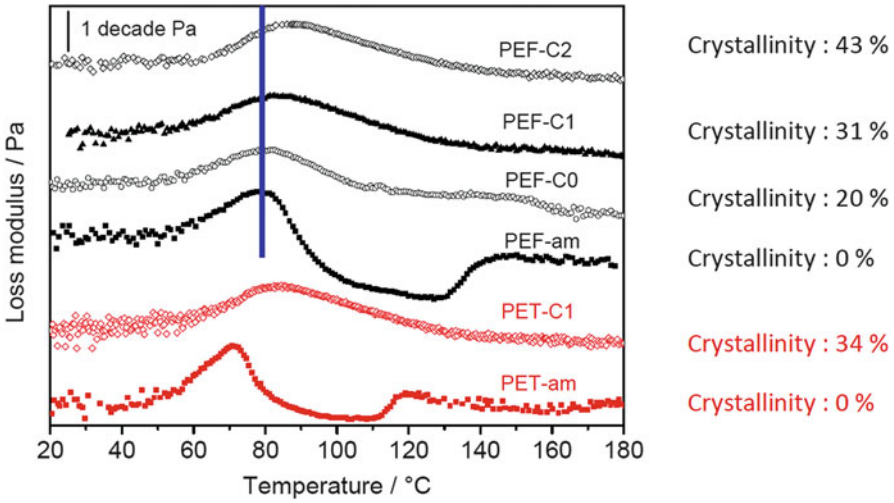

Fig. 12 Results obtained from DMA and DSC measurements. Adapted and reproduced from [27] with permission from the Royal Society of Chemistry

The temperature dependence of the normalized heat capacity $c_P{}^N$ for amorphous and semicrystalline PEF and PET samples is presented in Fig. 13. The glass transition temperature of amorphous PEF is higher than amorphous PET (81 vs. 76°C), while the glass transition temperature of semicrystalline PEF is lower than semicrystalline PET (82 vs. 84°C). The overshoot for amorphous samples is due to structural recovery (enthalpy relaxation). These values were used to compute the dependence of the effective activation energy E_α with the extent of conversion and with temperature [27, 43–47] (Fig. 14).

The variation in the effective activation energy (E_α) for both PET and PEF amorphous and semicrystalline samples as a function of temperature exhibit a decrease in the effective activation energy for all samples. This decrease can be interpreted in terms of the cooperative motion of the chain segments. In the glassy state, only local motions of the chain segments may occur because of the very low molecular mobility. As the temperature rises, the molecular motion intensifies and the translational motion of the segments and of the whole chain becomes possible. The mobility thus becomes higher, which allows the chain segments to relax more independently, i.e., with a lower degree of cooperativity. This results in decreased energetic constraints which is reflected in a decrease of the effective activation energy. For amorphous PET, the effective activation energy (E_α) values are higher and correspond to a lower temperature domain (65–77°C), while for semicrystalline PET, the values are perfectly consistent with the previous example, being lower and at higher temperature (77–105°C). The situation is very different for PEF: the values are very close for both amorphous and semicrystalline PEF, except for $T > 85$°C where the glass transition is finished for amorphous PEF. These results also confirm

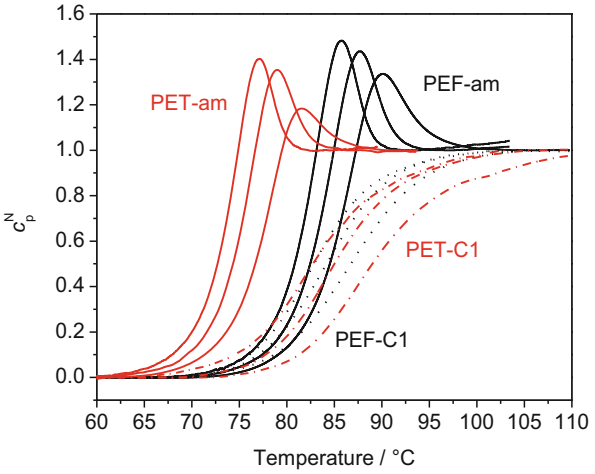

Fig. 13 Temperature dependence of the normalized heat capacity C_P^N determined for amorphous PEF (PEF-am, black lines), amorphous PET (PET-am, red lines), semicrystalline PEF (PEF-C1, black dotted lines, crystallinity ~31%) and semicrystalline PET (PET-C1, red dotted lines, crystallinity ~34%) at 10, 20, and 40 K min^{-1}. Adapted and reproduced from [27] with permission from the Royal Society of Chemistry

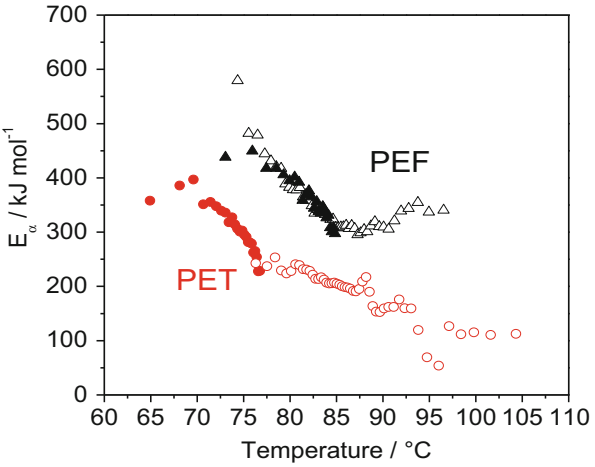

Fig. 14 Dependence of the effective activation energy E_α with temperature for amorphous PEF (black solid triangle), semicrystalline PEF (black open triangle, crystallinity ~31%), amorphous PET (red solid circle), and semicrystalline PET (red open circles, crystallinity ~34%). Adapted and reproduced from [27] with permission from the Royal Society of Chemistry

the hypothesis of reduced coupling between amorphous and crystal phases for PEF, which are mainly caused by the higher free volume of PEF.

2.2.4 Melt Viscosity and Mechanical Properties of PEF vs. PET

PEF melt viscosity is dependent on molecular weight, and analyses showed that this relationship required higher activation energies compared to PET. Similarly, the melt viscosity of PEF as function of shear rate showed earlier onset of shear thinning compared to PET. These results indicated that the PEF chain network is more loosely entangled compared to PET. Regarding tensile properties, PEF showed higher yield

stress and an increased tendency toward brittle behavior. Overall, the tensile behavior of PEF in the glassy state is comparable to PET with relatively high elongations at break. These features not only explain the entanglement density, but also suggest that the role of specific intermolecular interactions in PEF (such as dipole-dipole interactions) should be taken into account [48].

2.2.5 Nanocomposites Based on PEF

Preparation of nanocomposites has proven to be an efficient way to improve the thermomechanical properties of semicrystalline polyesters. PEF nanocomposites were developed for this purpose. Three types of nanofillers have been employed to prepare PEF nanocomposites, i.e., nanoclays, nanocellulose, and carbon nanotubes, with the objectives of increasing the thermomechanical performance of the polymer and understanding its capacity for interacting with other inorganic/organic compounds because the interfacial adhesion is exacerbated when nanofillers are employed.

Nanocomposites based on PEF and OMMT, i.e., montmorillonite modified with organophilic ammonium cations (dimethyl benzyl hydrogenated ammonium or octadecyl ammonium), were prepared either by a solvent casting method (employing 1,1,1,3,3,3-hexafluoro-2-propanol as solvent) [49] or by extrusion [50]. The morphology of the PEF/OMMT nanocomposites observed by transmission electron microscopy (TEM) and the WAXS patterns shows that PEF chains are intercalated within the OMMT galleries (Fig. 15).

Clays act as heterogeneous sites for PEF crystal nucleation, which resulted in a slight increase in the melt crystallization rate, producing higher crystallinity. The thermal stability of the PEF/OMMT nanocomposites in thermo-oxidative conditions was increased by around 20–30°C, which suggests that the clays acted as a barrier for the oxygen diffusion within the sample (Fig. 16). An advanced isoconversional kinetic analysis was performed in order to gain information on the thermal degradation mechanism and indicated that the degradation mechanisms were similar (similar activation energy and pre-exponential factor dependencies) but that the PEF thermal degradation was delayed in the presence of clay. Thus, it was concluded that thermal degradation is delayed by a purely physical effect, such as a shielding effect, without modifying the degradation mechanism.

The dispersed clay layers slow down the initial degradation of PEF, which could represent an advantage for processing and material forming at high temperature because PEF, as with other polyesters, can be affected by thermally induced hydrolysis during processing at high temperature. Similar conclusions were drawn for PEF/clay nanocomposites processed via the melt extrusion method. However, the increase in thermal stability was lower (16–21 K) than for solvent casted nanocomposites. This was explained by the partial degradation of the sample that may occur during the extrusion cycles, as evidenced by a decrease in the molecular weight.

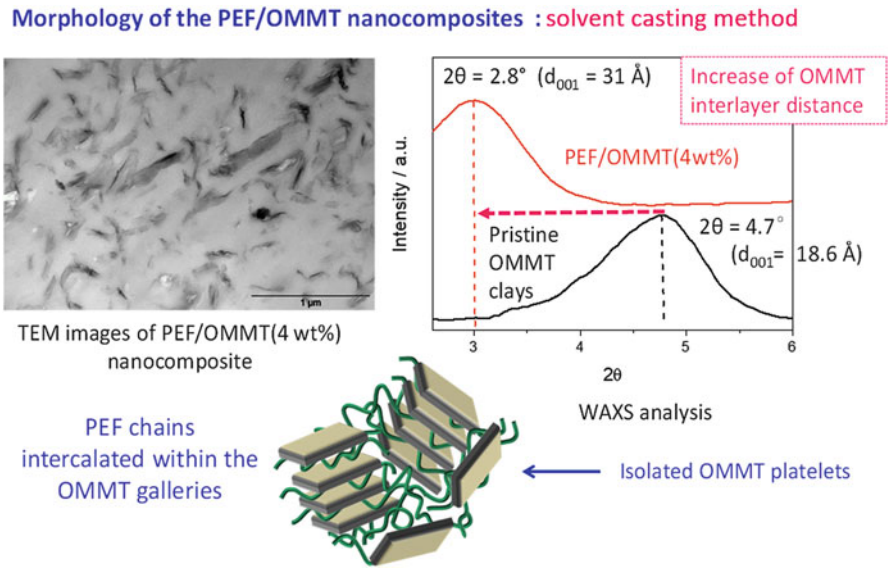

Fig. 15 TEM morphology of the PEF/OMMT nanocomposites (solvent casting method) and WAXS analysis. Adapted and reproduced from [49] with permission from the Royal Society of Chemistry

Following the same approach, cellulose-based PEF composites were prepared with nanocrystalline cellulose (NCC) via melt processing [51]. It appeared that a longer residence time during extrusion induced a more marked molecular weight reduction in the presence of cellulose, whereas this effect was avoided when a sufficiently short extrusion time was employed. Good interfacial adhesion was observed between PEF and cellulosic flakes of micrometric dimensions. Contrary to PEF/clay nanocomposites, the thermal degradation of PEF was not modified by cellulose. However, cellulose favorably modified the crystallization behavior. The crystallinity in the PEF/cellulose composite was two times those obtained in raw PEF. From a crystallization kinetic standpoint, the presence of cellulose accelerates the isothermal crystallization. For instance, the crystallization half time decreased by about 35% when cellulose was dispersed in PEF. On the other hand, PEF/cellulose composites were prepared with the solvent casting route which is considered to be an effective and simple method [52]. This is particularly attributed to the good dispersion that is commonly obtained and the absence of thermal treatment at high temperatures, which may contribute to polyester hydrolysis. Different sonication procedures were employed to, first, disperse cellulose nano-crystals in HFIP with equipment of increasing energies (ultra-sonic bath, ultra-sonication, and ultra-turrax). A low affinity between the solvent and the cellulose crystals was highlighted by TEM. Dissolved separately in the same solvent, the PEF was then poured into the cellulose suspension before casting. The composites showed dispersion of micron-sized cellulose agglomerates within the matrix. Fourier-transform infrared spectroscopy (FT-IR) investigation

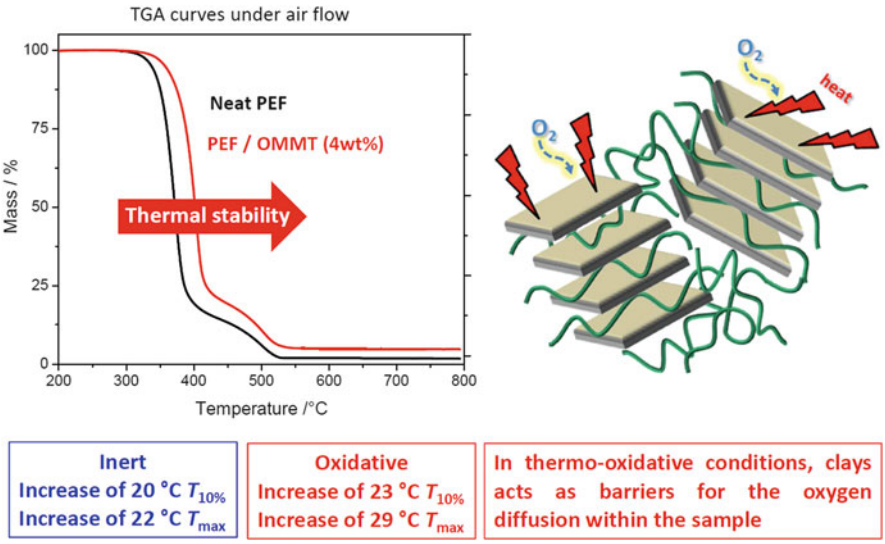

Fig. 16 Thermal stability by TGA of the PEF/OMMT nanocomposites. Adapted and reproduced from [49] with permission from the Royal Society of Chemistry

revealed that the signals from the hydroxyl end-groups in PEF broadened in the presence of cellulose due to interactions with the cellulosic hydroxyls. The same observation was also made for PEF hydroxyl end groups in the presence of nanoclays [50]. Despite their relatively low level of dispersion, the DSC scans showed a slight nucleating effect of cellulose in agreement with the conclusions made for PEF/cellulose composites prepared via extrusion [50].

Lotti et al. [53] have synthetized PEF nanocomposites containing 2.5 wt% multi-walled carbon nanotubes (MWCNTs), functionalized MWCNTs, or graphene oxide (GO) prepared by the melt polycondensation method. The nanocomposites showed faster crystallization rates and increased nucleation density, resulting in smaller spherulite sizes.

3 Other FDCA-Based Polyesters with Longer Aliphatic Chains

In addition to PEF, which attracts a lot of attention due to its similarities to the widely used PET, it is also possible to synthetize FDCA polyesters bearing longer alkyl chains. The presence of additional methylene will induce different properties compared to PEF where only two methylene groups are present. For example, the thermal properties and the rigidity are linked to the number of methylene groups

Table 2 Chemical formulas and characteristic temperatures of several furan-derived polyesters [15, 55–60]

	Name	Abbreviated name	Number of methylene units	T_g (°C)	T_m (°C)	Ref./ method
Odd	Pol(propylene furandicarboxylate)	PPF	3	58	–	[15]/DSC 10 K min^{-1}
	Poly(pentylene furandicarboxylate)	PPeF	5	19	92	[56]/DSC 20 K min^{-1}
	Poly(heptylene furandicarboxylate)	PHepF	7	5	82.5	[56]/DSC 20 K min^{-1}
	Poly(nonylene furandicarboxylate)	PNF	9	−5	94	[56]/DSC 20 K min^{-1}
Even	Poly(butylene furandicarboxylate)	PBF	4	35	169	[55]/DSC 10 K min^{-1}
	Poly(hexamethylene furandicarboxylate)	PHF	6	28.1	148.2	[15]/DSC 10 K min^{-1}
	Poly(octylene furandicarboxylate)	POF	8	21.8	148.6	[57]/ TMDSC 5 K min^{-1}
	Poly(decylene furandicarboxylate)	PDeF	10	1	112	[58, 59]/ TMDSC 5 K min^{-1}
	Poly(dodecylene furandicarboxylate)	PDoF	12	−5	111	[59, 60]/ TMDSC 5 K min^{-1}

of the specific glycol that is used and will decrease as the aliphatic chain increases [54]. This is the result of the increased chain flexibility. The color of the polymer is also dependent on the methylene group number: the higher this number, the darker the polymer. This is caused by the high temperatures that are required during the melt polycondensation procedure and the consequent degradation of the macromolecule [15]. All of the following polyesters that have been investigated present multiple melting peaks. The number of peak depends on the cold crystallization temperature and on the heating rate. These peaks are linked to the melting-recrystallization-remelting process and show different stabilities.

The even/odd chain nature is also important. The polymers with odd methylene group numbers such as poly(propylene furandicarboxylate), PPF; poly(pentylene furandicarboxylate), PPeF; poly(heptylene furandicarboxylate), PHepF; and poly (nonylene furandicarboxylate), PNF, are less ordered than the even ones like poly (butylene furandicarboxylate), PBF; poly(hexamethylene furandicarboxylate), PHF; poly(octylene furandicarboxylate), POF; poly(decylene furandicarboxylate), PDeF, and poly(dodecylene furandicarboxylate), PDoF. The reported thermal properties of these polyesters are listed in Table 2.

The following section presents the properties of these different polyesters in accordance with the even/odd nature of the aliphatic chain. Some of them are frequently compared to their terephthalate and naphthalene counterparts because of their many similarities.

(a) Furan-derived polyesters with odd methylene numbers: PPF, PPeF, PHepF, PNF.

All of these polyesters are composed of an odd-numbered aliphatic chain. They have lower melting points and can reach a lower degree of crystallinity. Because of their odd nature, it is complicated to arrange their chains in an ordered and periodic structure leading to a semicrystalline polymer. As the aliphatic chain increases, it becomes more and more difficult for these odd polymers to crystallize and thus to improve their thermal properties, which also results in increase the oxygen permeability. This leads to decreased barrier properties [61]. It has long been difficult to synthetize long furanoate (or furandicarboxylate) chains (PPeF, PHepF, PNF) because the corresponding diols were not readily available at sufficiently high purity. However, this goal is desirable because increasing the aliphatic chain length leads to the decrease of both the glass transition temperature and the melting temperature.

(b) Furan-derived polyesters with even methylene numbers: PBF, PHF, POF, PDeF, PDoF.

For these polyesters composed of an even methylene group number, crystallization is facilitated by the symmetry in the methylene chain and consequently their ability to create a spatial organization is improved. As PEF is supposed to replace its petroleum counterpart PET in packaging, the same issue is considered for PBT and PBF. Numerous articles address PBF and its thermal properties, as well as its good strength and ductility [62–66]. It has been reported that PBF is less thermally stable compared to PEF and PPF because of the higher number of methylene groups [62]. PBF can crystallize in two forms, either an α form or a less stable β form. It exhibits an intense recrystallization process compared to PBT and PBN and exhibits lower crystallinity [64].

For PHF, the high flexibility also enables spherulite growth and causes a lower nucleation density but a larger size of spherulites [67]. Tsanaktsis et al. have highlighted the decrease of the glass, melting and crystallization temperatures with the increasing number of methylene groups [68].

POF is a very fast crystallizing polymer because of its higher chain flexibility. This flexibility increases with the number of methylene groups leading to great difficulty in producing a fully amorphous polymer. As a matter of fact, FSC is frequently used for the characterization of polymers with a fast crystallization rate. Compared to regular DSC, this advanced thermoanalytical tool allows one to heat and cool the material at very fast rates and therefore to control the crystallization. In many cases, crystallization and nucleation can be avoided. The FSC was employed to characterize the crystallization behavior of POF [56], and cooling rate of more than 1,000 K s^{-1} was found to be necessary to avoid crystallization from the melt. Similarly, PDeF was found to be a very fast

crystallizing polyester with a large nucleation density and a rather small size of spherulite [57]. With a glass transition temperature around 1°C and a melting temperature at 112°C, PDeF exhibits mechanical properties that are very close to low-density polyethylene (LDPE). Finally, the FDCA polyester with the highest number of repeating methylene units is PDoF, which has been successfully prepared via a variation of the two-step polycondensation method [59].

4 Conclusion

The current developments and enthusiasm associated with FDCA also apply to the high potential for this furanic building block in preparing new biobased aromatic polyesters with both similarities and unique characteristics, in comparison to terephthalic polyesters. In the perspective of potential technological implementations, the thermal properties of FDCA polyesters are the first findings to highlight their peculiar behavior. The higher segmental rigidity of the furan ring, compared to the benzene ring, impacts the T_g value and the crystallization behavior (especially from glass) of FDCA polyesters. However, in PEF, the restriction of molecular mobility is compensated by its higher free volume compared to PET, which implies lower coupling with the crystal phases. The PEF chain network is also less entangled compared to PET, which necessitates, for instance, higher stretch ratios than PET to induce strain hardening. All these thermal features are also linked to the permeability of FDCA polyesters that is much lower in comparison with pTA polyesters. FDCA polyesters with longer aliphatic chains can present alternative properties such as fast crystallization or toughness.

Thanks to the recent emergence of FDCA polyesters, it is also an opportunity for the scientific community to further describe the behavior of terephthalic and naphthalic polyesters as the spectrum of aromatic polyesters becomes larger. Such background information will be important as the blending and the recycling of aromatic polyesters are taken into consideration, as these are key issues for a sustainable life cycle.

References

1. Whinfield JR, Dickson JT (1941) Improvements relating to the manufacture of highly polymeric substances. GB 578079
2. Bozell JJ, Petersen GR (2010) Technology development for the production of biobased products from biorefinery carbohydrates – the US Department of Energy's "Top 10" revisited. Green Chem 12:539–554
3. de Jong E, Dam MA, Sipos L, Gruter GJM (2012) Chapter 1. Furandicarboxylic acid (FDCA), a versatile building block for a very interesting class of polyesters. In: Biobased monomers, polymers and materials. ACS symposium series, vol 1105. American Chemical Societym, Washington, DC, pp 1–13

4. van Putten RJ, van der Waal JC, de Jong E, Rasrendra CB, Heeres HJ, de Vries JG (2013) Hydroxymethylfurfural, a versatile platform chemical made from renewable resources. Chem Rev 113:1499–1597
5. Sousa A, Vilela C, Fonseca A, Matos M, Freire C, Gruter G, Coelho J, Silvestre A (2015) Biobased polyesters and other polymers from 2,5-furandicarboxylic acid: a tribute to furan excellency. Polym Chem 6(33):5961–5983
6. Imhof P, van der Waal JC (2013) Catalytic process development for renewable materials. Wiley, Weinheim
7. Kriegel RM, Moffit RD, Schultheis MW, Shi Y, You X (2015) WO2015031907
8. Bouffand M, Colloud A, Reutenauer P (2014) WO2014032730
9. Drewitt JGN, Lincoln J (1946) Improvements in polymers. GB Patent 621971
10. Gandini A (1977) The behavior of furan derivatives in polymerization reactions. Adv Polym Sci 10:47–96
11. Moore JA, Kelly JE (1978) Polyesters derived from furan and tetrahydrofuran nuclei. Macromolecules 11:568–573
12. Rieckmann T, Völker S (2003) Chapter 2. Poly(ethylene terephthalate) polymerization – mechanism, catalysis, kinetics, mass transfer and reactor design, In: Scheirs J, Long TE (eds) Modern polyesters: chemistry and technology of polyesters and copolyesters. Wiley, Weinheim, pp 31–116
13. Gandini A, Silvestre AJD, Neto CP, Sousa AF, Gomes M (2009) The furan counterpart of poly (ethylene terephthalate): an alternative material based on renewable resources. J Polym Sci A Polym Chem 4:295–298
14. Knoop R, Vogelzang W, van Haveren J, van Es D (2013) High molecular weight poly(ethylene-2,5-furanoate); critical aspects in synthesis and mechanical property determination. J Polym Sci A Polym Chem 51(19):4191–4199
15. Jiang M, Liu Q, Zhang Q, Ye C, Zhou G (2012) A series of furan-aromatic polyesters synthesized via direct esterification method based on renewable resources. J Polym Sci A Polym Chem 50:1026–1036
16. Ma J, Pang Y, Wang M, Xu J, Ma H, Nie X (2012) The copolymerization reactivity of diols with 2,5-furandicarboxylic acid for furan-based copolyester materials. J Mater Chem 22:3457–3461
17. Wu J, Eduard P, Thiyagarajan S, van Haveren J, van Es DS, Koning CE, Lutz M, Fonseca Guerra C (2011) Isohexide derivatives from renewable resources as chiral building blocks. ChemSusChem 4(5):599–603
18. Burgess S, Leisen J, Kraftschik B, Mubarak C, Kriegel R, Koros W (2014) Chain mobility, thermal, and mechanical properties of poly(ethylene furanoate) compared to poly(ethylene terephthalate). Macromolecules 47(4):1383–1391
19. Burgess SK, Karvan O, Johnson JR, Kriegel RM, Koros WJ (2014) Oxygen sorption and transport in amorphous poly(ethylene furanoate). Polymer 55(18):4748–4756
20. Burgess SK, Mikkilineni DS, Yu DB, Kim DJ, Mubarak CR, Kriegel RM, Koros WJ (2014) Water sorption in poly(ethylene furanoate) compared to poly(ethylene terephthalate). Part 2: kinetic sorption. Polymer 55(26):6870–6882
21. Burgess SK, Mikkilineni DS, Yu DB, Kim DJ, Mubarak CR, Kriegel RM, Koros WJ (2014) Water sorption in poly(ethylene furanoate) compared to poly(ethylene terephthalate). Part 1: equilibrium sorption. Polymer 55(26):6861–6869
22. Burgess SK, Kriegel RM, Koros WJ (2015) Carbon dioxide sorption and transport in amorphous poly(ethylene furanoate). Macromolecules 48:2184–2193
23. Burgess SK, Wenz GB, Kriegel RM, Koros WJ (2016) Penetrant transport in semicrystalline poly(ethylene furanoate). Polymer 98:305–310
24. van Berkel JG, Guigo N, Kolstad JJ, Sipos L, Wang B, Dam MA, Sbirrazzuoli N (2015) Isothermal crystallization kinetics of poly (ethylene 2,5-furandicarboxylate). Macromol Mater Eng 300(4):466–474

25. Papageorgiou GZ, Tsanaktsis V, Bikiaris DN (2014) Synthesis of poly(ethylene furandicarboxylate) polyester using monomers derived from renewable resources: thermal behavior comparison with PET and PEN. Phys Chem Chem Phys 16:7946–7958
26. Stoclet G, Gobius du Sart G, Yeniad B, Lefebvre JM (2015) Isothermal crystallization and structural characterization of poly(ethylene-2,5-furanoate). Polymer 72:165–176
27. Codou A, Moncel M, van Berkel JG, Guigo N, Sbirrazzuoli N (2016) Glass transition dynamics and cooperativity length of poly(ethylene 2,5-furandicarboxylate) compared to poly(ethylene terephthalate). Phys Chem Chem Phys 18:16647–16658
28. Kazaryan LG, Medvedeva FM (1968) Vysokomolekulyarnye Soedineniya, Seriya B: Kratkie Soobshcheniya, pp 305–306
29. Mao Y, Kriegel RM, Bucknall DG (2016) The crystal structure of poly(ethylene furanoate). Polymer 102:308–314
30. Maini L, Gigli M, Gazzano M, Lotti N, Bikiaris DN, Papageorgiou GZ (2018) Structural investigation of poly(ethylene furanoate) polymorphs. Polymers 10(3):296
31. Tsanaktsis V, Papageorgiou DG, Exarhopoulos S, Bikiaris DN, Papageorgiou GZ (2015) Crystallization and polymorphism of poly(ethylene furanoate). Cryst Growth Des 15:5505–5512
32. Codou A, Guigo N, van Berkel J, de Jong E, Sbirrazzuoli N (2014) Nonisothermal crystallization kinetics of biobased poly(ethylene 2,5-furandicarboxylate) synthesized via direct esterification process. Macromol Chem Phys 215:2065–2074
33. Martino L, Guigo N, van Berkel J, Kolstad J, Sbirrazzuoli N (2016) Nucleation and self-nucleation of bio-based poly(ethylene 2,5-furandicarboxylate) probed by fast scanning calorimetry. Macromol Mater Eng 301(5):586–596
34. Wurm A, Zhuravlev E, Eckstein K, Jehnichen D, Pospiech D, Androsch R, Wunderlich B, Schick C (2012) Crystallization and homogeneous nucleation kinetics of poly(ε-caprolactone) (PCL) with different molar masses. Macromolecules 45:3816–3828
35. Guigo N, van Berkel J, de Jong E, Sbirrazzuoli N (2017) Modelling the non-isothermal crystallization of polymers: application to poly(ethylene 2,5-furandicarboxylate). Thermochim Acta 650:66–75
36. Picard M (2009) Evolution de la microstructure d'un PET lors du bi-étirage soufflage; corrélation au durcissement structural. PhD dissertation, Mines ParisTech, France
37. Cristea M, Ionita D, Simionescu B (2010) A new insight in the dynamo-mechanical behavior of poly(ethylene terephthalate). Eur Polym J 46(10):2005–2012
38. Stoclet G, Lefebvre JM, Yeniad B, Gobius du Sart G, de Vos S (2017) On the strain-induced structural evolution of poly(ethylene-2,5-furanoate) upon uniaxial stretching: an in-situ SAXS-WAXS study. Polymer 134:227–241
39. le Bourvellec G, Monnerie L, Jarry JP (1987) Kinetics of induced crystallization during stretching and annealing of poly(ethylene terephthalate) films. Polymer 28:1712–1716
40. Mao Y, Bucknall D, Kriegel R (2018) Synchrotron X-ray scattering study on amorphous poly (ethylene furanoate) under uniaxial deformation. Polymer 139:60–67
41. Menager C, Guigo N, Martino L, Sbirrazzuoli N, Visser R, Boyer S, Billon N, Monge G, Combeaud C (2018) Strain induced crystallization in biobased poly(ethylene 2,5-furandicarboxylate) (PEF); conditions for appearance and microstructure analysis. Polymer 158:364–371
42. van Berkel JG, Guigo N, Kolstad JJ, Sbirrazzuoli N (2018) Biaxial orientation of poly(ethylene 2,5-furandicarboxylate): an explorative study. Macromol Mater Eng 303(3):1700507
43. Vyazovkin S, Sbirrazzuoli N, Dranca I (2004) Variation of the effective activation energy throughout the glass transition. Macromol Rapid Commun 25(19):1708–1713
44. Vyazovkin S, Sbirrazzuoli N (2006) Isoconversional kinetic analysis of thermally stimulated processes in polymers. Macromol Rapid Commun 27:1515–1532
45. Vyazovkin S, Sbirrazzuoli N, Dranca I (2006) Variation in activation energy of the glass transition for polymers of different dynamic fragility. Macromol Chem Phys 207:1126–1130
46. Bosq N, Guigo N, Persello J, Sbirrazzuoli N (2014) Melt and glass crystallization of PDMS and PDMS silica nanocomposites. Phys Chem Chem Phys 16(17):7830–7840

47. Vyazovkin S (2015) Isoconversional kinetics of thermally stimulated processes. Springer, New York
48. van Berkel JG, Guigo N, Kolstad JJ, Sbirrazzuoli N (2018) Chain structure and molecular weight dependent mechanics of poly(ethylene 2,5-furandicarboxylate) compared to poly(ethylene terephthalate). Macromolecules 51(21):8539–8549
49. Martino L, Niknam V, Guigo N, van Berkel JG, Sbirrazzuoli N (2016) Morphology and thermal properties of novel clay-based poly (ethylene 2,5-furandicarboxylate) (PEF) nanocomposites. RSC Adv 6:59800–59807
50. Martino L, Guigo N, van Berkel JG, Sbirrazzuoli N (2017) Influence of organically modified montmorillonite and sepiolite clays on the physical properties of bio-based poly(ethylene 2,5-furandicarboxylate). Compos Part B Eng 110:96–105
51. Codou A, Guigo N, van Berkel JG, de Jong E, Sbirrazzuoli N (2017) Preparation and crystallization behavior of poly(ethylene 2,5-furandicarboxylate)/cellulose composites by twin screw extrusion. Carbohydr Polym 174:1026–1033
52. Codou A, Guigo N, van Berkel JG, de Jong E, Sbirrazzuoli N (2017) Preparation and characterization of PEF/nano-crystalline cellulose composite via solvent casting. J Polym Eng 37(9):869–878
53. Lotti N, Munari A, Gigli M, Gazzano M, Tsanaktsis V, Bikiaris DN, Papageorgiou GZ (2016) Thermal and structural response of in situ prepared biobased poly(ethylene 2,5-furan dicarboxylate) nanocomposites. Polymer 103:288–298
54. Papageorgiou GZ, Papageorgiou DG, Terzopoulou Z, Bikiaris DN (2016) Production of bio-based 2,5-furan dicarboxylate polyesters: recent progress and critical aspects in their synthesis and thermal properties. Eur Polym J 83:202–229
55. Pfister D, Storti G, Tancini F, Costa LI, Morbidelli M (2015) Synthesis and ring-opening polymerization of cycle butylene 2,5-furandicarboxylate. Macromol Chem Phys 216 (21):2141–2146
56. Tsanaktsis V, Terzopoulou Z, Nerantzaki M, Papageorgiou GZ, Bikiaris DN (2016) New poly (pentylene furanoate) and poly(heptylene furanoate) sustainable polyesters from diols with odd methylene groups. Mater Lett 178:64–67
57. Papageorgiou GZ, Guigo N, Tsanaktsis V, Papageorgiou DG, Exarhopoulos S, Sbirrazzuoli N, Bikiaris DN (2015) On the bio-based furanic polyesters: synthesis and thermal behavior study of poly(octylene furanoate) using fast and temperature modulated scanning calorimetry. Eur Polym J 68:115–127
58. Tsanaktsis V, Bikiaris DN, Guigo N, Exarhopoulos S, Papageorgiou DG, Sbirrazzuoli N, Papageorgiou GZ (2015) Synthesis, properties and thermal behavior of poly(decylene-2,5-furanoate): a biobased polyester from 2,5-furan dicarboxylic acid. RSC Adv 5:74592–74604
59. Fehrenbacher U, Grosshardt O, Kowollik K, Tübke B, Dingenouts N, Wilhelm M (2009) Synthese und Charakterisierung von Polyestern und Polyamiden auf der Basis von Furan-2,5-dicarbonsäure. Chem Ing Tech 81(11):1829–1835
60. Papageorgiou DG, Guigo N, Tsanaktsis V, Exarhopoulos S, Bikiaris DN, Sbirrazzuoli N, Papageorgiou GZ (2016) Fast crystallization and melting behavior of a long-spaced aliphatic furandicarboxylate biobased polyester, poly(dodecylene 2,5-furanoate). Ind Eng Chem Res 55:5315–5326
61. Vannini M, Marchese P, Celli A, Lorenzetti C (2015) Fully biobased poly(propylene 2,5-furandicarboxylate) for packaging applications: excellent barrier properties as a function of crystallinity. Green Chem 17:4162–4166
62. Tsanaktsis V, Vouvoudi E, Papageorgiou GZ, Papageorgiou DG, Chrissafis K, Bikiaris DN (2015) Thermal degradation kinetics and decomposition mechanism of polyesters based on 2,5-furandicarboxylic acid and low molecular weight aliphatic diols. J Anal Appl Pyrolysis 112:369–378
63. Ma J, Yu X, Xu J, Pang Y (2012) Synthesis and crystallinity of poly(butylene 2,5-furandicarboxylate). Polymer 53:4145–4151

64. Papageorgiou GZ, Tsanaktsis V, Papageorgiou DG, Exarhopoulos S, Papageorgiou M, Bikiaris DN (2014) Evaluation of polyesters from renewable resources as alternatives to the current fossil-based polymers. Phase transitions of poly(butylene 2,5-furan-dicarboxylate). Polymer 55:3846–3858
65. Zhu J, Cai J, Xie W, Chen PH, Gazzano M, Scandola M, Gross RA (2013) Poly(butylene 2,5-furan dicarboxylate), a biobased alternative to PBT: synthesis, physical properties, and crystal structure. Macromolecules 46:796–804
66. Soccio M, Martínez-Tong DE, Alegría A, Munari A, Lotti N (2017) Molecular dynamics of fully biobased poly(butylene 2,5-furanoate) as revealed by broadband dielectric spectroscopy. Polymer 128:24–30
67. Papageorgiou GZ, Tsanaktsis V, Papageorgiou DG, Chrissafis K, Exarhopoulos S, Bikiaris DN (2015) Furan-based polyesters from renewable resources: crystallization and thermal degradation behavior of poly(hexamethylene 2,5-furan-dicarboxylate). Eur Polym J 67:383–396
68. Tsanaktsis V, Papageorgiou GZ, Bikiaris DN (2015) A facile method to synthesize high-molecular-weight biobased polyesters from 2,5-furandicarboxylic acid and long-chain diols. J Polym Sci A Polym Chem 53:2617–2632

Adv Polym Sci (2019) 283: 219–256
https://doi.org/10.1007/12_2019_48

Published online: 21 August 2019

Nucleation and Crystallization in Bio-Based Immiscible Polyester Blends

Seif Eddine Fenni, Dario Cavallo, and Alejandro J. Müller

Contents

1 Introduction on Immiscible Blends of Semicrystalline Polymers 221
1.1 Morphological Features 222
1.2 Crystallization Behavior in Immiscible Blends 223
2 Crystallization in Different Immiscible Bio-Based Polyester Blends 229
2.1 Poly(Lactic Acid)/Poly(Butylene Succinate) Blends 229
2.2 Poly(Lactic Acid)/Poly(ε-Caprolactone) Blends 234
2.3 Poly(Butylene Succinate)/Poly(ε-Caprolactone) Immiscible Blends 244
2.4 Blends of Poly(Hydroxybutyrate) and Other Bio-Based Polyesters 245
3 Conclusions and Outlook 250
References 251

Abstract Bio-based thermoplastic polyesters are highly promising materials as they combine interesting thermal and physical properties and in many cases biodegradability. However, sometimes the best property balance can only be achieved by blending in order to improve barrier properties, biodegradability, or mechanical

S. E. Fenni
Laboratory of Physical-Chemistry of High Polymers (LPCHP), Process Engineering Department, Faculty of Technology, University of Ferhat ABBAS Sétif-1, Sétif, Algeria

Department of Chemistry and Industrial Chemistry, University of Genova, Genoa, Italy

D. Cavallo (✉)
Department of Chemistry and Industrial Chemistry, University of Genova, Genoa, Italy
e-mail: dario.cavallo@unige.it

A. J. Müller (✉)
POLYMAT and Polymer Science and Technology Department, Faculty of Chemistry, University of the Basque Country UPV/EHU, Donostia-San Sebastián, Spain

Ikerbasque, Basque Foundation for Science, Bilbao, Spain
e-mail: alejandrojesus.muller@ehu.es

properties. Nucleation, crystallization, and morphology are key factors that can dominate all these properties in crystallizable bio-based polyesters. Therefore, their understanding, prediction, and tailoring are essential. In this work, after a brief introduction about immiscible polymer blends, we summarize the crystallization behavior of the most important bio-based (and immiscible) polyester blends, considering examples of double-crystalline components. Even though in some specific blends (e.g., polylactide/polycaprolactone) many efforts have been made to understand the influence of blending on the nucleation, crystallization, and morphology of the parent components, there are still many points that have yet to be understood. In the case of other immiscible polyester blend systems, the literature is scarce, opening up opportunities in this environmentally important research topic.

Keywords Bio-based polyesters · Crystallization · Double-crystalline blends · Immiscible blends · Nucleation

Abbreviations

ATBC	Acetyl(tributyl citrate)
CNC	Cellulose nanocrystals
DCP	Dicumyl peroxide
DSC	Differential scanning calorimetry
EC-bp	Ethyl cellosolve-blocked polyisocyanate
FTIR	Fourier-transform infrared spectroscopy
G	Growth rate
GNP	Graphite nanoplatelets
GO	Graphene oxide
GOs	Graphene oxide nanosheets
iPP	Isotactic polypropylene
Lapol	Polyester plasticizer
LDI	L-Lysine-diisocyanate
LDPE	Low-density polyethylene
LIM	D-Limonene
LTI	L-Lysine-triisocyanate
MDs	Micro-domains
NPCC	Nano-sized calcium carbonate
NPs	Nanoparticles
P(LA-ran-CL)HMw	Poly(lactide-ran-caprolactone) high molecular weight
P(LA-ran-CL)LMw	Poly(lactide-ran-caprolactone) low molecular weight
PA	Polyamide
PA6	Polyamide-6
PBS	Poly(butylene succinate)
PBS-g-CNC	PBS-g-cellulose nanocrystal
PBS-g-MA	Maleic anhydride-grafted PBS

PBSL	Poly(butylene succinate-co-L-lactate)
PCL	Poly(caprolactone) or poly(ϵ-caprolactone)
PDLA	Poly(D-lactic acid)
PE	Polyethylene
PEG-PPG	Block copolymer of poly(ethylene glycol) and poly (propylene glycol)
PHB	Poly(hydroxybutyrate)
PHBV	Poly(hydroxybutyrate-co-hydroxyvalerate)
PLA	Poly(lactic acid)
PLA-b-PC	Poly(L-lactide-block-carbonate)
PLLA	Poly(L-lactic acid)
PLLA-g-MA	Maleic anhydride-grafted PLLA
PLLA-PCL-PLLA	Triblock PLLA-PCL-PLLA copolymer
PLOM	Polarized light microscopy
PMMA	Poly(methyl methacrylate)
POSS	Polyhedral oligomeric silsesquioxane
POSS-oib	Octaisobutyl polyhedral oligomeric silsesquioxane
PS	Polystyrene
PVDF	Poly(vinylidene fluoride)
rPBSL	Random poly(butylene succinate-co-lactic acid)
SB	Sodium benzoate
s-CNC	Surfactant-modified cellulose nanocrystals
Ta	Annealing temperature
Tc	Crystallization temperature
Tcc	Cold-crystallization temperature
TEM	Transmission electron microscopy
Tg	Glass transition temperature
TiO_2	Titanium dioxide
Tm	Melting temperature
WAXD	Wide-angle X-ray diffraction
wt%	Weight percentage
Xc	Crystallinity degree
XRD	X-ray diffraction
τ (50%)	Crystallization half time

1 Introduction on Immiscible Blends of Semicrystalline Polymers

Recently, much attention has been given to polyesters obtained from sustainable resources, biodegradable polymers, and their blends as their properties are comparable with those of polymers derived from petroleum resources, but they are more environmentally benign. Among these bio-based and biodegradable polymers,

poly(lactic acid) (PLA), poly(butylene succinate) (PBS), poly(caprolactone) (PCL), and poly(hydroxybutyrate) (PHB) are the most studied and employed.

Polymer blending has been extensively used to prepare new polymeric materials with an attractive combination of properties that combine those of the pure components. However, given that most polymers are immiscible, because of their unfavorable enthalpy of mixing, they form phase-separated systems. Depending on interfacial tension, composition, rheological properties, and processing conditions, immiscible polymer blends exhibit different morphologies, such as sea-island or co-continuous. Immiscible blends are characterized by poor mechanical properties coming from weak interfacial adhesion between the phases and stress concentrations at interface boundaries [1–4]. Several strategies have been employed to overcome this and improve blend compatibility, such as chemical modifications; addition of block copolymers, plasticizers, and nanofillers; and reactive blending [5–7].

If one or both components are semicrystalline, the superstructure and the crystallization behavior of each material may be affected by blending. The detailed knowledge of how blending impacts crystallization is important since most polymer properties, such as optical, thermal, mechanical, and barrier properties, will also be affected.

This chapter describes the general crystallization behavior of immiscible biodegradable polyester blends, with especial emphasis on the kinetics aspects. Several other aspects will also be highlighted, such as the influence of blending on nucleation, the phenomenon of fractionated crystallization, and the effects of composition on the morphology.

1.1 Morphological Features

The final morphology of immiscible blends is affected both by intrinsic features of the materials, such as interfacial tension between the two polymers and melt viscosity ratio, and by preparation method, i.e., shear rate and blend composition. The two most typical morphologies are (1) droplets of the minor component, with sizes between 0.1 and 10 μm, dispersed in a continuous matrix of the other polymer (i.e., a sea-island morphology), and (2) co-continuous morphology, usually obtained for symmetric compositions, characterized by two continuous phases with similar characteristic sizes that are strongly interpenetrated [1–4]. Co-continuous morphologies in immiscible polymer blends have many advantages in comparison with sea-island morphologies, in particular regarding synergy in the mechanical properties and selective permeability, which provide opportunities for a wide range of technological applications.

Clear relationships have been found between blend morphology and the crystallization of immiscible polymers [8–13]. We have selected an example from the literature, even if the reported blends are not bio-based or biodegradable, because it can clearly illustrate the large changes produced by different morphologies on the nucleation and crystallization of the phases.

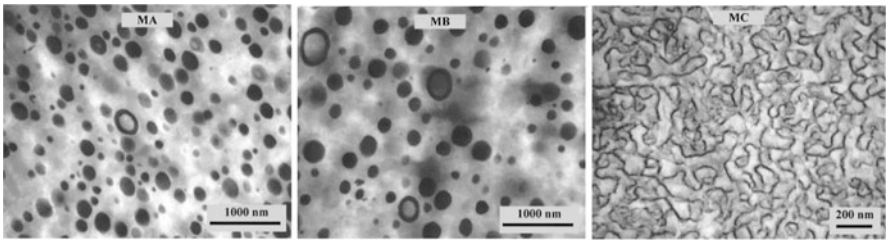

Fig. 1 TEM micrographs of three PE/PA blends prepared by reactive extrusion, showing sea-island (MA and MB) and co-continuous morphologies (MC). Adapted with permission from [9]

Figure 1 shows transmission electron microscopy (TEM) images of polyethylene/polyamide (PE/PA) blends prepared by reactive extrusion. Depending on the composition and compatibilizer content, it was possible to produce two types of morphologies: (1) droplets of polyamide in a polyethylene matrix (samples MA and MB in Fig. 1) and (2) co-continuous morphology of the two polymers (sample MC, Fig. 1) [9]. The kinetics of crystallization of PA in PE/PA immiscible blends changed from classical sigmoidal-type (typical of heterogeneously nucleated polymers with Avrami indexes of 3–4), in the blend with the co-continuous morphology, to first-order kinetics in the blends MA with sea-island morphology with submicron PA droplets (typical of a crystallization process initiated by surface nucleation or homogeneous nucleation [8, 9, 12]). In the MC blend, the nucleation was found to be heterogeneous at lower supercooling, while in MA and MB blends, the nucleation became homogeneous or induced by the polymer-polymer interface, and crystallization occurred at extremely large supercooling. On the other hand, crystallization of the PE phase was enhanced in all blends, due to the nucleation effect of the PA, previously crystallized at higher temperature [9]. The relationship between immiscible blend morphology and crystallization behavior of bio-based polyester blends will be analyzed in detail below.

1.2 Crystallization Behavior in Immiscible Blends

The polymers in an immiscible blend can be either amorphous or semicrystalline. Thus, amorphous/amorphous, crystalline/amorphous, or crystalline/crystalline final blends can be prepared.

In principle, phase separation of the components is expected; therefore, in the case of two semicrystalline components, the crystallization of each polymer takes place independently from one another. As such, the crystalline features (melting temperature (Tm), lamellar thickness, and growth rate (G)) are expected to be similar to the ones of pure components. The same does not obviously hold for miscible blends, where dilution effects on crystallization can be appreciated [10, 11, 13].

However, the crystallization kinetics of a given polymer in an immiscible blend can be substantially different from that of the pure component, since peculiar nucleation effects can arise. Nucleation could be enhanced and thus the overall crystallization kinetics is accelerated. Indeed, nucleation is commonly encountered at foreign surfaces, and it can thus be increased due to impurities/heterogeneities migration between the different phases during the blending process or to the presence of polymer-polymer interfaces [1, 2, 10, 13–17]. The opposite situation, i.e., a decrease of crystallization kinetics, is also commonly observed whenever the crystallizable polymers are separated in a "sufficiently high" number of individual domains. In these cases, the phenomenon is addressed as *fractionated crystallization*, as detailed in the following section.

1.2.1 Fractionated Crystallization

The term "fractionated crystallization" was introduced by Frensch et al. [18]. This crystallization mechanism is observed in polymer blends, when a minor crystallizable component is dispersed in droplets with very small average diameter. The fractionated crystallization appears when the number of droplets or micro-domains (MDs) is of the same order of magnitude, or larger, than the number of the active heterogeneities which act as primary nuclei for crystallization in the bulk polymer. For statistical reasons, different droplet ensembles will result, containing heterogeneities with varying nucleating ability or even free of foreign particles. Therefore, upon cooling from the melt, the different fractions of droplets will crystallize at distinct supercoolings, from low to high depending on the nucleating efficiency of the contained heterogeneities. Ideally, "clean" droplets will solidify at the maximum achievable supercooling (close to the glass transition temperature) by a homogeneous nucleation mechanism. Heterogeneity free droplets can also crystallize by interfacial nucleation at high supercoolings, but not as high as in the case of homogeneous nucleation, since the energy barrier for nucleation is lower when the interface between the two phases is able to nucleate the droplets. The different nucleation events are reflected in multiple exothermic peaks detected by a differential scanning calorimetry (DSC) cooling scan [10, 12, 13, 19–29].

The above outlined concept is described schematically in Fig. 2. The most active nucleating impurities are represented with the letter A, while B indicated less active heterogeneities. After blending, the heterogeneities will be randomly distributed among the droplets. The micro-domains containing type A heterogeneities crystallize at lower supercooling (exothermic peak 1 in the DSC of Fig. 2), while droplets with type B impurities nucleate at lower temperatures (DSC peak 2). Impurity-free polymer droplets reach the largest supercooling for the given cooling conditions (exothermic peak 3).

Figure 3 shows a real example of fractionated crystallization in immiscible blends and the effect of blend composition on its occurrence, for the system isotactic polypropylene/polystyrene. For a 70/30 wt% composition, isotactic polypropylene (iPP) droplets have an average diameter of 7–9 μm, and they mostly crystallize at

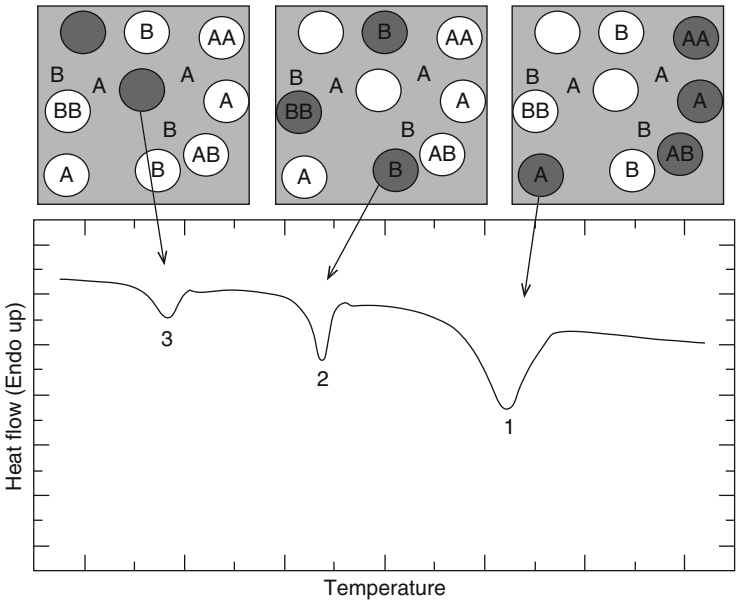

Fig. 2 A schematic illustration of the fractionated crystallization of polymer droplets dispersed in an immiscible polymer matrix, as measured by DSC. Reproduced with permission from [19]

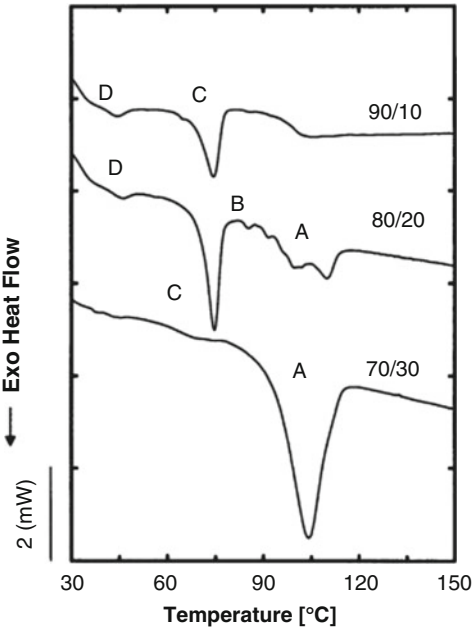

Fig. 3 DSC cooling curves at 10°C/min for PS/iPP blends with the indicated compositions. Reproduced with permission from [21]

low supercooling (peak A), while a small fraction of the droplets can be supercooled to a larger extent (peak C). By decreasing the amount of iPP to 20%, the average droplet size decreases to around 1–2 μm, and a clear fractionated crystallization is observed: since four distinct crystallization exotherms (A–D) are revealed. These correspond to different types of heterogeneities (A–C) and to nucleation at the interface with polystyrene (PS) or via a homogenous route in pure iPP droplets (D). When iPP content is only 10 wt%, the average droplet size is less than 1 μm. The concentration of droplets thus increases well above the content of the heterogeneities which cause nucleation at low supercoolings (peaks A through C). In fact, the high-temperature nucleation events (A and B) disappear, and the crystallization can only occur at lower temperatures, in exotherms C and D. If a compatibilizer is used in the blend, even smaller droplets are produced, and exotherm C disappears, indicating that the only event associated with heterogeneity-free droplets is the exothermic peak at maximum supercooling (D) which could be started by surface nucleation or homogeneous nucleation. As the glass transition temperature (Tg) of iPP is close to 0°C and the crystallization peak (D) is at around 40°C, it may be possible that a homogeneous nucleation process could have triggered the nucleation of these clean droplets [8, 10, 12, 21, 23, 24]. In general, the fractionated crystallization leads to lower crystallinity and slightly lower melting temperatures, due to the decrease of lamellar thickness at those supercoolings [8, 11, 13, 26, 27]. For more details on fractionated crystallization, the reader is referred to the reviews of Müller et al. [12, 21, 25].

1.2.2 Nucleation at Polymer-Polymer Interfaces

Several papers have reported the nucleation effect of one polymer on another in immiscible blends. The phenomenon is commonly indicated as interface-induced nucleation or interface-assisted crystallization and can be typically visualized directly by polarized light microscopy PLOM [30–37].

For example, Fig. 4 shows some PLOM micrographs of the area near the phase boundary between poly(L-lactide) (PLLA) and poly(vinylidene fluoride) (PVDF). The two polymers were sequentially crystallized for a suitable time at 150°C and 140°C. At 150°C, only the PVDF phase is able to crystallize within the given time (Fig. 4b), while after cooling to 140°C, PLLA can also crystallize. At 140°C, PLLA nucleates first at the interface with previously crystallized PVDF. A transcrystalline structure is produced due to the high (linear) nucleation density, which forces the spherulites to grow perpendicular to the interface (Fig. 4c, d). We can note that, during the same crystallization time, only few PLLA spherulites nucleate within the bulk phase, away from the PVDF interface [33].

In a similar experiment on PVDF/PCL blends, the nucleation of the PCL phase after isothermal crystallization of PVDF was shown to occur at the interface with PVDF crystals, giving rise again to a transcrystalline PCL layer. The nucleation effect of PVDF on PCL could also be detected by non-isothermal differential

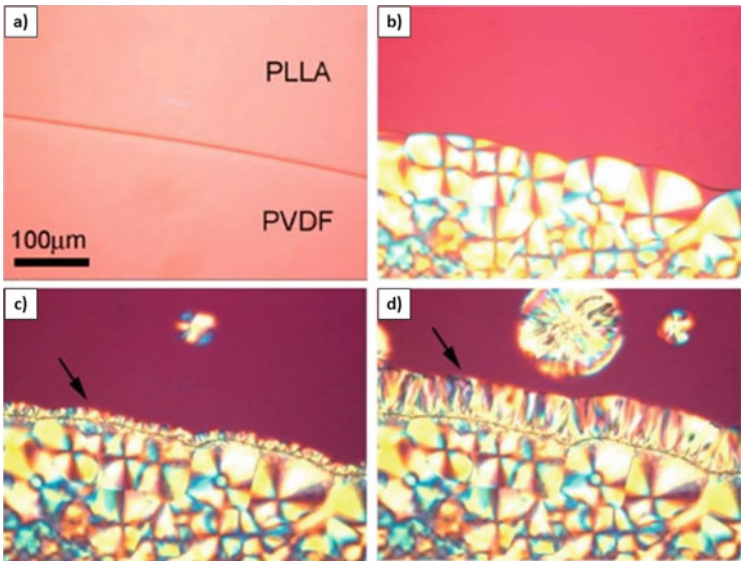

Fig. 4 PLOM micrographs of PLLA and PVDF near their interface, during a sequential crystallization at 150 and 140°C. The upper and lower sides of the micrographs are PLLA and PVDF, respectively. (**a**) 150°C, 0 min, (**b**) 150°C, 6 min, (**c**) 140°C, 10 min, and (**d**) 140°C, 30 min. Adapted with permission from [33]

scanning calorimetry, as a meaningful shift of PCL crystallization exotherm to higher temperature in a 70/30 wt% PVDF/PCL blend [34].

The nucleation of a given polymer on the surface of pre-existing crystals of a different polymer might not seem surprising and can be possibly attributed to the existence of epitaxial relationship between the two crystalline structures. However, even if less documented, the nucleation of a semicrystalline polymer at the interface with an amorphous polymer in their immiscible blend is also possible. Figure 5 shows polarized optical micrographs of isotactic polypropylene/poly(methyl methacrylate) (PP/PMMA) immiscible blend crystallized at 130°C. iPP transcrystalline growth layer around the PMMA domains can be observed. It should be noted that iPP crystallization takes place above the glass transition temperature of PMMA; thus, the nucleation effectively occurs at the interface with a viscous liquid [35].

1.2.3 Crystallization in Presence of Compatibilizers and Nanoparticles

Usually, the addition of small amounts of "compatibilizer" (i.e., block copolymers, graft copolymers, nanoparticles, etc.) results in a large decrease in the size of the dispersed phase, in comparison with the non-compatibilized blend. The addition of a copolymer-based compatibilizer, in general, has remarkable influence on the crystallization behavior of the blend components, because of the large effect on

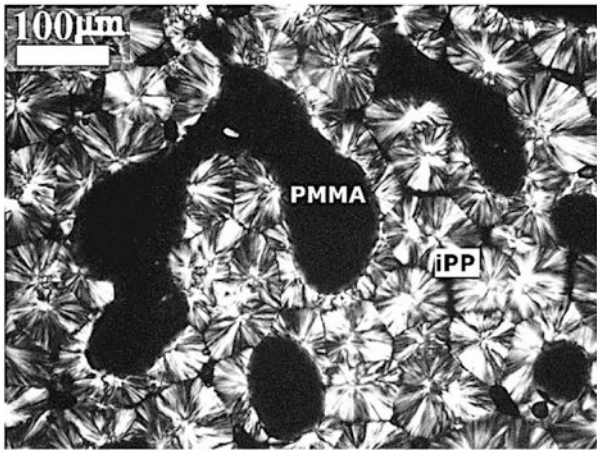

Fig. 5 PLOM micrograph for an iPP/PMMA blend after the sample was crystallized at 130°C for 30 min. Adapted with permission from [35]

the morphology of the system, which results either in a decrease in the size of the dispersed phase or in the formation of a percolated/co-continuous morphology [8, 13, 16, 38, 39]. Tol et al. [26] and Yordanov and Minkova [28] studied the reactive compatibilization of the immiscible blends polystyrene/polyamide-6 (PS/PA6) and low-density polyethylene/polystyrene (LDPE/PS), using different kinds of copolymer compatibilizers. They found a decrease in the droplet sizes and large increase in the droplet concentration. As a consequence, the nucleation mechanism of the crystalline polymer changed from heterogeneous to homogeneous/surface-induced. In the case of PA6, the increased supercooling favored the crystalline γ phase with respect to the α phase which develops in neat blends [26].

Another commonly used compatibilization method is "reactive blending," in which a molecule which can react with one or both phases is added during the extrusion process. During the reactive compatibilization, different kinds of interactions among the polymers can develop, leading to hydrogen, ionic, or covalent bonding, depending on the specific functional groups involved. Typically, a co-continuous morphology can be obtained. In the case of reactive compatibilization, when some specific reagent is employed, the crystallization behavior of the final blend can be affected as a result of chain scission or reduction of chain mobility due to cross-linking. In general, reactive compatibilization reduces the degree of crystallinity and induces fractionated crystallization [1, 2, 5, 11, 13, 21, 27, 28, 39–42].

Wang et al. [41] reported that the addition of dicumyl peroxide (DCP) at different concentrations to PLA/PBS 80/20 immiscible blend hinders the crystallization of both components, i.e., it decreases the crystallinity of both PBS and PLA and the cold-crystallization rate of PLA by reducing its nucleation density. Reactive blending in this case is creating new covalent bonds randomly distributed in between the two polymers. Such new covalent bonds interrupt the linear crystallizable sequences

creating molecular defects that need to be rejected to the amorphous phases, thereby reducing the crystallization ability of the components.

The addition of nanoparticles (NPs) or nanofillers to immiscible polymer blends can have an effect on the mechanical, thermal, optical, and gas properties. NPs in immiscible blends could be located at the interface between the components, dispersed preferentially in one component, or dispersed in nonequivalent way in both components. Generally, and depending on their locations, NPs affect the crystallization behavior of the crystallizable components by enhancing the primary nucleation, thus acting as heterogeneous nucleants [13, 43–45]. Examples can be found, for instance, for PLLA/PBS blends mixed with graphene oxide (GO) and cellulose nanocrystals (CNC) [44, 45].

2 Crystallization in Different Immiscible Bio-Based Polyester Blends

2.1 Poly(Lactic Acid)/Poly(Butylene Succinate) Blends

This section presents a short review on previous research about PLA/PBS blends in which the effect of addition of PBS on different properties of the PLA matrix is studied with the aim of improving mechanical properties, gas barrier behavior, etc. PLA is a bio-based polyester that has high rigidity, biocompatibility, and biodegradability. However, it presents slow crystallization and brittleness. PBS, on the other hand, is a biodegradable polyester with good processability. The commonly observed thermal transitions of the two materials are summarized in the following. PLA partially crystallizes on cooling around 100°C and vitrifies at the glass transition temperature ($Tg \approx 60°C$). Upon subsequent heating, it might show cold crystallization above Tg (typically at ≈100°C) and melting with a peak temperature of ≈170°C. On the other hand, PBS crystallizes on cooling at ≈75°C, has a low glass transition temperature (≈−35°C), and melts slightly above 116°C. We recall that for PLA, the crystallization and melting temperatures are controlled by the relative contents of D- and L-isomer of lactide in the chain [46–48].

Several authors investigated the effect of cooling and heating rates, blend composition, and addition of compatibilizers, nanoparticles, and nucleating agents on the thermal and crystallization behavior of PLA/PBS blends [6, 15, 41, 45, 49–55]. Both non-isothermal with varying cooling rates and isothermal crystallization behavior were investigated, using differential scanning calorimetry (DSC) and polarized optical microscopy (PLOM). The main works performed on PLA-/PBS-based systems are schematically summarized in Table 1.

In the case of PLA/PBS blends, the crystallization and melting temperatures of the two polymers in the blends remain in the same range of that of the pure components, confirming the immiscibility between the two polyesters. The melting processes are sufficiently apart to be distinguished upon heating.

Table 1 Reported experimental works on PLA-/PBS-based blends, with emphasis on the aspects related to nucleation and crystallization

Sample	Publication year	Composition wt%	Crystallization/ nucleation conditions and technics	*Tcc* of PLA (°C)	*Tc* of PLA (°C)	*Tc* of PBS (°C)	Crystallization/nucleation outcomes	Reference
PLLA/PBS	2006	Neat PLLA	Isothermal and non-isothermal DSC at various cooling rates	124.0	–	–	PBS accelerates the cold crystallization of PLA but is less effective in melt crystallization *Xc* increases with PBS content	[50]
		99/1		113.3	–	–		
		95/5		96.7	–	–		
		90/10		94.8	–	–		
PLLA/PBSL	2006	Neat PLLA	Non-isothermal DSC at various cooling rates; isothermal DSC	124.0	–	–	Molten PBSL enhances the isothermal and non-isothermal PLLA crystallization during the cooling process and accelerates *Tcc* during the heating process. *Xc* was found to increase with the addition of PBSL	[50]
		99/1		102	–	–		
		95/5		90.2	–	–		
		90/10		95.6	–	–		
PLA/PBS	2008	0–20 wt% of PBS.	DSC and PLOM : cooling from 180°C at 2°C/min	–	–	–	Addition of PBS accelerates the crystallization rate of PLA during both cooling and heating scans and the PBS domains act as nuclei for PLA	[49]
PLA/PBS/DCP	2009	Neat PLA	DSC non-isothermal crystallization PLOM isothermal crystallization X-ray diffraction	122.4	–	–	The addition of PBS accelerates the cold crystallization of PLA, while addition of DCP hinders both PLA and PBS crystallization. PBS acts as a nucleating agent for PLA, but the effect is reduced after reaction with DCP	[41]
		80/20		–	–	–		
		80/20/0.05		–	–	–		
		80/20/0.1		120.1	–	–		
		80/20/0.15		122.6	–	–		
		80/20/0.2		124.2	–	–		

PLLA/PBS	2012	Neat PLLA	DSC non-isothermal crystallization	132.5	–	–	Presence of PBS accelerates remarkably the cold crystallization of PLA, but no effect was recorded during the cooling process from the melt PLA domains does not affect the crystallization behavior of PBS	[51]
		Neat PBS		116.2	–	83.8		
		50/50		–	–	84.4		
		20/80		–	–	84.7		
PLA/PBS/PLLA-*g*-MA and PLA/PBS/PBS-*g*-MA	2014	0–100 wt% of PBS. With 0–4 wt% of PLLA-g-MA or PBS-g-MA	Non-isothermal DSC	–	–	–	PBS enhances the cold crystallization of PLA. The size and number of the dispersed PBS particles (droplets) have a significant influence on the crystallization rate of PLA (the smallest and highest number of dispersed PBS droplets resulted in higher nucleation effect). Addition of compatibilizer produced additional increases in the crystallinity of the blend	[52]
PLA/PBS/TiO_2 nanoparticles	2014	90/10	Non-isothermal DSC	95.7	–	–	DSC analysis showed that addition of TiO_2 promoted the crystallization of PLA. PBS has lower nucleating effect as compared with TiO_2	[53]
		90/10/1		96.8	–	–		
		90/10/2		98.4	–	–		
		90/10/3		107.9	–	–		
		90/10/5		94.7	–	–		
PLA/PBS	2015	0–100 wt% of PBS	DSC and PLOM non-isothermal crystallization at a scan rate of 10°C/min	–	–	–	After blending, crystallinity of both PLA and PBS increased Addition of 20 wt% of PBS gave the largest increase in the crystallinity of PLA	[15]

(continued)

Table 1 (continued)

Sample	Publication year	Composition wt%	Crystallization/ nucleation conditions and technics	*Tcc* of PLA (°C)	*Tc* of PLA (°C)	*Tc* of PBS (°C)	Crystallization/nucleation outcomes	Reference
PLA/PBS/ rPBSL	2016	80/20 wt% with 0–5 phr of rPBSL	DSC non-isothermal crystallization PLOM isothermal crystallization at 80°C	–	–	–	Addition of rPBSL to 80/20 PLA/PBS blend affects nucleation and crystallization, since the compound acts as a nucleating agent and plasticizer	[6]
PLA/PBS/ DCP/PBS-*g*-CNC	2016	70/70 wt% with DCP/PBS-g-CNC = 0/0, 0/2, 0.2/0, 0.2/0.5, 0.2/1 and 0.2/2	Non-isothermal DSC, WAXD	–	–	–	DCP and PBS-*g*-CNC have a strong contribution to the formation of PLA-α form and low effect on PBS crystallization. In addition, PBS-*g*-CNC increases the crystallinity degree of the PLA/PBS system and affects the crystal size of both PLA and PBS Addition of DCP restricts the crystallization	[54]
PLLA/PBS/GO	2018	Neat PLLA	DSC in isothermal and non-isothermal conditions	97	101.6	–	In the neat blend, fractionated crystallization of PBS phase and slight increase in *Tc* of PLLA were observed Addition of GOs enhances the crystallization rate of both PLA and PBS	[45]
		Neat PBS		–	–	77		
		70/30		91	105.2	73		
		70/30/0.1		–	103.7	92		
		70/30/0.3		–	105.5	92		
		70/30/0.5		–	105.5	92		

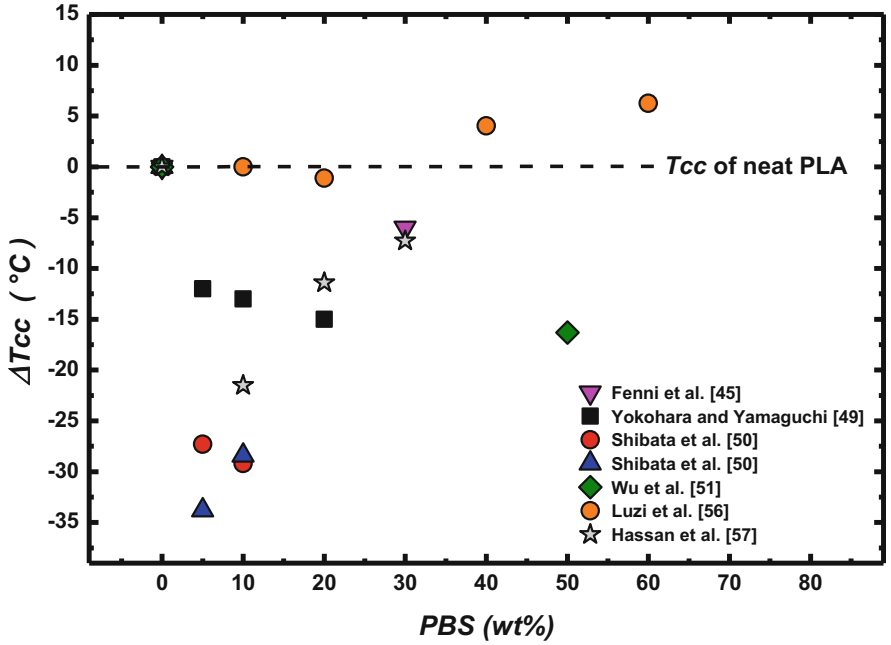

Fig. 6 Difference in cold-crystallization temperature between neat PLA and blended sample (ΔT_{cc}) as a function of PBS content in different PLA/PBS blends reported in literature

The crystallization rate of PLA is rather slow, so that often the structuring process is not completed during cooling and an exothermic cold-crystallization peak is usually observed during the second heating scan. Several works have reported an acceleration of PLA cold-crystallization rate by the addition of PBS [15, 41, 45, 49–54]. Figure 6 presents a collection of the reported cold-crystallization temperatures of PLA in its blends with PBS, as a function of PBS content. The data has been normalized by using the difference between the cold-crystallization temperature of neat PLA and of the PLA component in the blend. The more negative the value of ΔT_{cc} is, the larger the nucleation effect upon heating from the glassy state.

Notwithstanding the differences in the absolute values of cold-crystallization temperatures, which might be attributed to material (molar mass, D-lactide content) or measurement (heating rate) parameters, a clear shift of the cold-crystallization events toward lower temperature can be appreciated, especially upon the addition of a minor content of PBS (in the range 1–30 wt%). The largest nucleation effect can be approximately found for PBS content between 5 and 15 wt%. This is interpreted as the result of a decrease in the PBS droplet diameter, which leads to an increase in the PLA/PBS interfacial area.

Although several works attributed this change in cold-crystallization rate to a certain miscibility between PLLA and PBS [6, 56] at least on a local scale, this could not be sustained by any meaningful change in the glass transitions or morphology, while the growth rate is mostly unexplored. More probably, the enhancement of PLLA cold crystallization can be well described as a heterogeneous nucleation

phenomenon at the interface between the two polymer phases, thanks to the PBS crystals formed upon cooling. The possibility of impurity transfer between two melts cannot be ruled out but is not required to account for the observations.

On the other hand, only a limited number of works reported the effect of molten PBS in nucleating PLA during the cooling process or melt crystallization [15, 45, 49, 50]. For example, Yokohara and Yamaguchi [49] found that the addition of small amount of PBS largely increases the number of PLA nuclei, as observed by PLOM, and even enables the crystallization of the polymer during cooling at around 90°C. It should be noted that the melt crystallization of PLA necessarily occurs in a temperature range in which PBS is in the molten state. Therefore, the lower nucleating efficiency of the liquid-liquid contact surface could be expected.

Few studies have paid attention to the effect of the presence of PLA on PBS phase crystallization. Deng and Thomas [15] reported that blending PLA and PBS resulted in an increase in PBS crystallinity degree, which was tentatively attributed to a nucleating effect of PLA crystals. Differently, Hassan et al. [57] reported a decrease in the degree of crystallinity of PBS when it constitutes the minority phase in blends with PLA, as a consequence of fractionated crystallization and hindrance to the crystallization process exerted by the solidified PLA matrix. Fenni et al. [45] also reported the appearance of fractionated crystallization of PBS phase and a large slowing down of its crystallization kinetics compared to pure PBS in PLA/PBS 70/30 wt% immiscible blend.

Lastly, the effect of compatibilization, according to different strategies, on PLA/PBS blend crystallization can be analyzed. Wang et al. [41] employed dicumyl peroxide (DCP) with a content of 0–0.2 wt% to compatibilize an 80/20 wt% PLA/PBS blend. In the neat blend, PBS acted as a nucleating agent for PLA, both during the heating process and during isothermal conditions below its melting point. A reduction in PBS crystallization and PLLA cold-crystallization ability with increase of DCP content was observed and attributed to the increase in the viscosity of system. However, the interruption of crystallizable chain sequences was not considered. Also, the decrease in PBS crystallinity could be related to the decrease in domain size with increase of DCP content and the appearance of fractionated crystallization phenomena.

Supthanyakul et al. [6] used a random poly(butylene succinate-*ran*-lactic acid) (rPBSL) copolymer as compatibilizer between PLA and PBS 80/20 wt% blends. The random copolymer was partially miscible with PLA, as deduced from the plasticization effect, with the glass transition temperature dropping about 10°C for 5 phr of rPBSL (see Fig. 7a). The enhanced PLA mobility favored cold crystallization, which occurred much earlier on heating and lead to higher crystallinity (Fig. 7b, c). The interpretation of the accelerated crystallization to molecular mobility is supported by the measured increased in PLA growth rate and decrease in spherulite induction time with increasing rPBSL content.

2.2 Poly(Lactic Acid)/Poly(ε-Caprolactone) Blends

PLA/PCL immiscible blends have been extensively investigated, given the possible attractive combination of properties resulting from the mixture of these two

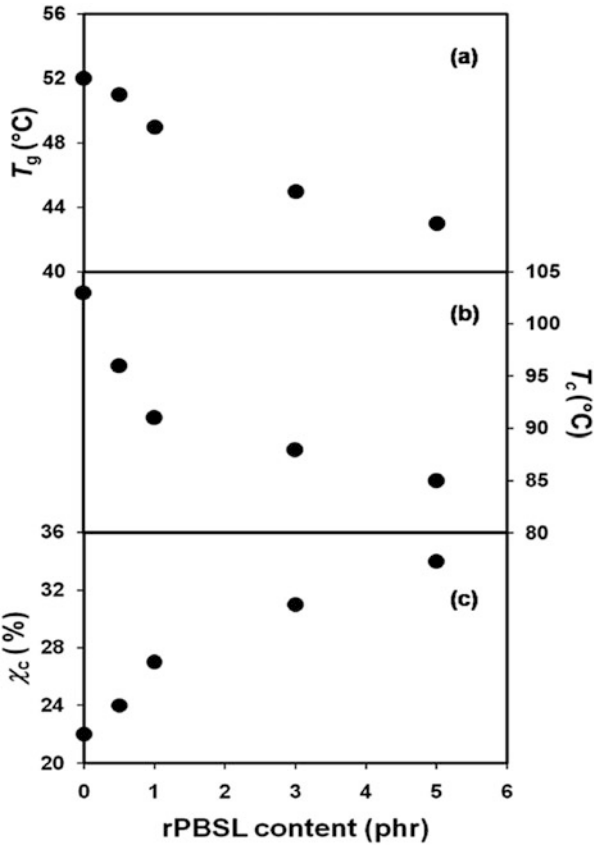

Fig. 7 Glass transition (**a**), cold-crystallization temperature (**b**), and crystallinity (**c**) of PLA in PLA/PBS (80/20) blends with different contents of rPBSL. Reproduced with permission from [6]

components. PCL is a biodegradable polyester with a very flexible chain, characterized by a low glass transition temperature (≈−60°C), although the melting and crystallization also occur in the low-temperature range at around 60 and 30°C, respectively. In this section, the main works dealing with the crystallization behavior of these blends, including the effect of composition and additives, are summarized [16, 31, 32, 36, 38, 58–77]. Table 2 provides a compendium of the related studies.

The crystallization of PLA as a major component in PLA/PCL blends will be considered first. A clear acceleration of PLA overall crystallization rate in the presence of 20 wt% PCL has been reported [16]. For example, the time to complete crystallization at 120°C is 1.5 min in the blend, with respect to 8 min in the pure PLA. A faster overall crystallization is consistently found for neat and compatibilized blends in a wider temperature range, as shown in Fig. 8 [38]. Considering the results of neat PLA and 80/20 uncompatibilized PLA/PCL blend, we can notice, besides the increase of the overall crystallization rate, a shift of the maximum rate toward a lower crystallization temperature and a substantial narrowing of the bell-shaped curve.

Table 2 Main experimental works on PLA-/PCL-based blend, with emphasis on the aspects related to crystallization and nucleation

Sample	Publication year	Composition wt%	Crystallization/nucleation conditions and technics	*Tcc* of PLA (°C)	*Tc* of PLA (°C)	*Tc* of PCL (°C)	Crystallization/nucleation outcomes	Reference
PLA/PCL/ PLLA-PCL-PLLA	2001	Neat PLA	PLOM isothermal crystallization; isothermal and non-isothermal DSC	115	–	–	Addition of PCL promotes the crystallization of PLA from the glassy state regardless of PCL and PLLA-PCL-PLLA content. The PLLA spherulitic growth rate kept constant in all compositions	[58]
		90/10		100	–	–		
		80/20		100	–	–		
		70/30		100	–	–		
PDLA/PCL	2006	0–100 wt% of PCL	DSC non-isothermal crystallization PLOM isothermal measurements	–	–	–	The crystallization of PDLA was enhanced by PCL resulting in an increase of PDLA *Xc* in the 80/20 PDLA/PCL	[62]
PLA/PCL/ talc	2010	Neat PLA	DSC non-isothermal crystallization	109	–	–	40/60 PLA/PCL blend: Increase in PCL T_c during cooling process and slight decrease in PLA T_{cc} during subsequent heating process. Addition of talc results in remarkable increase in both PCL and PLA crystallization temperature	[44]
		Neat PCL		–	–	30		
		40/60		106	–	39		
		70/30/1		–	110	36		
		Neat PCL		–	–	–		
		80/20		102.1	–	–		
		50/50		105.9	–	–		
		20/80		103.2	–	–		
		80/20		121.2	–	–		
		80/20/2.5		114.4	–	–		
		80/20/7.5		98.1	–	–		
PLA/PCL/ EC-bp	2013	Neat PLA	DSC non-isothermal crystallization. WAXD	126.8	–	–	Addition of PCL accelerates the cold crystallization of PLA and *Xc* increases EC-bp plays the role of cross-	[59]
		Neat PCL		–	–	–		
		90/10		121.6	–	–		
		80/20		119.6	–	–		

		70/30		115.5	–	–	linking agent, thus decreasing the crystallization rate of PLA	
		70/30/0.5		121	–	–		
		70/30/1		124.2	–	–		
		70/30/2		128.7	–	–		
		90/10		90.52	–	–		
		80/20		90.09	–	–		
		70/30		90.39	–	–		
PLA/PCL/POSS	2014	70/30 wt% with 2% of different kind of POSS	DSC non-isothermal crystallization	–	–	–	The addition of PCL and octaisobutyl-POSS results in slight changes in PLA crystallization. The presence of POSS limits PCL crystallization	[60]
PLA/PCL/TiO_2	2015	30–70 wt% of PCL with 1–5 wt% of TiO_2	DSC non-isothermal crystallization	–	–	–	PCL crystallinity kept constant and does not change in the blends (despite the presence of PLA, TiO_2, or PLA + TiO_2)	[61]
PLA/PCL/P(LA-ran-CL) LMw	2016	Neat PLA	PLOM isothermal crystallization of PLA, isothermal and non-isothermal DSC analysis	128.1	–	–	Fractionated crystallization of PCL phase, acceleration of PLA cold crystallization. The presence of copolymers causes an enhancement in the crystallization rate of both polymers	[38]
		Neat PCL		–	–	25.9		
		80/20		100.5/154	–	15.8/32.1		
		78.4/19.6/2		96.3/151.5	110.8	15.3/31.6		
PLA/PCL/P(LA-ran-CL) HMw	2016	78.4/19.6/2		93.4/152.2	95.8	34.7		
PLA/PCL	2016	Neat PLA	DSC non-isothermal crystallization	129	–	–	Fractionated crystallization of PCL phase has been observed in 70/30 PLA/PCL. Pure PLA is amorphous and the addition of PCL results in an increase of the PLA cold crystallization and *Xc*	[63]
		Neat PCL		–	–	–		
		70/30		125	–	–		
		50/50		124	–	–		
		30/70		122	–	–		

(continued)

Table 2 (continued)

Sample	Publication year	Composition wt%	Crystallization/nucleation conditions and technics	*Tcc* of PLA (°C)	*Tc* of PLA (°C)	*Tc* of PCL (°C)	Crystallization/nucleation outcomes	Reference
PLA/PCL	2016	0–100 wt% of PCL using three different PLA grades	DSC non-isothermal crystallization	–	–	–	Addition of PCL resulted in (1) large increase in the nucleation density and (2) faster PLA cold-crystallization kinetics. PCL crystallinity decreased with the increase in PLA content	[65]
PLA/PCL/ PLA-b-PC	2017	Neat PLA	Isothermal and non-isothermal DSC, PLOM isothermal analysis of PLA crystallization	129.1	–	–	Fractionated crystallization of PCL phase (20 wt%) during the cooling scan, and accelerated cold crystallization of PLA phase due to the nucleation effect of PCL (molten) droplets on glassy PLA	[16]
		Neat PCL		110.8	–	28.8		
		80/20		–	–	21.7/ 31.8		
		80/20/2		–	119.2	4.6/ 23.1		
PLA/PCL/ PC	2017	80/20/2		–	93 0.1	12/ 19.7		
PLA/PCL	2018	0–50 wt% of PCL	DSC non-isothermal crystallization; DSC and PLOM isothermal crystallization of PCL	–	–	–	Overall isothermal crystallization kinetics revealed that the presence of 20–40 wt% of PLA enhances the crystallization ability of PCL. Growth rate of PCL found to be independent of PLA content	[64]

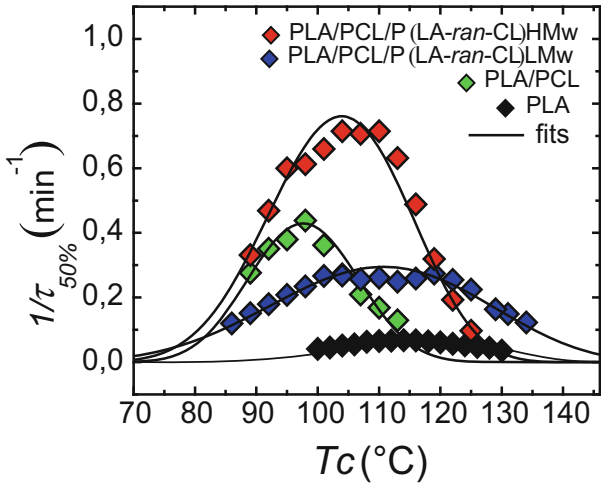

Fig. 8 Overall crystallization rate ($1/\tau_{50\%}$) as a function of isothermal crystallization temperature *Tc* in neat PLA and blends with PCL 80/20. Results for blends compatibilized with poly(lactide-ran-caprolactone) (P(LA-ran-CL)) of different molecular weights are also included. The solid lines represent a guide to the eye. Reproduced with permission from [38]

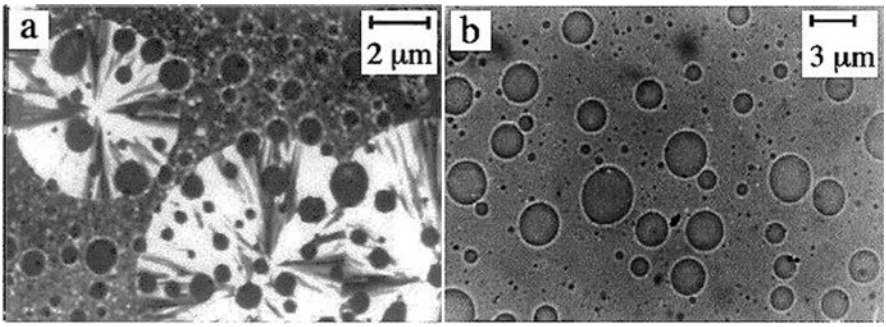

Fig. 9 Optical micrographs of 80/20 PLLA/PCL blend (**a**) at 125°C and (**b**) in the melt state. Adapted with permission from [58]

In order to account for the change in the temperature dependence of the overall crystallization rate (shape of the curve in Fig. 8), the effect of PCL on the different stages of the crystallization process, i.e., primary nucleation and growth, should be considered.

Given the immiscibility of the polymers, a change in the growth rate of PLA by blending is not expected. In Fig. 9, we can see optical micrographs of 80/20 PLLA/PCL blend at 125°C (Fig. 9a) and in the molten state (Fig. 9b) [58].

The phase separation is evident, and the PCL droplets, which are molten at 125°C, are not interfering with the growth of PLA spherulites, which simply proceed with their engulfment. The invariance of PLA growth rate between neat polymer and

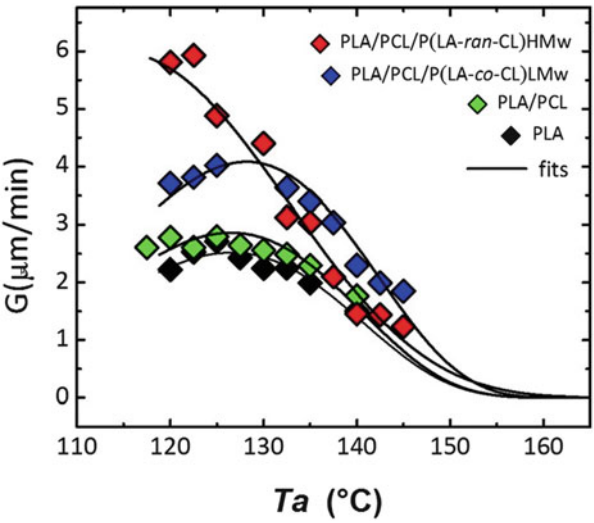

Fig. 10 Spherulitic growth rate *G* as a function of isothermal crystallization temperature (*Tc*) for neat PLA and 80/20 PLA/PCL blends, with or without P (LA-ran-CL) copolymers as compatibilizing agents. The solid lines are a guide to the eye. Reproduced with permission from [38]

uncompatibilized PLA/PCL blend was quantitatively confirmed, as shown in Fig. 10 [38]. No meaningful changes in the PLA spherulitic growth rate (*G*) can be detected in the blend, in the whole crystallization temperature range, unless compatibilizing copolymers were added to the systems.

Therefore, it seems apparent that the increase in PLA overall crystallization rate with the presence of PCL (Fig. 8) can be explained only as a nucleation effect, either by the interface between the molten polymers or by some heterogeneity transferred to the PLA phase from the PCL bulk during the mixing process.

Similarly to the case of PLA/PBS blends, a distinct effect of PCL on the crystallization of PLA from the glassy state in their immiscible blend has also been extensively reported [38, 44, 58, 59, 61, 65, 68–70]. A literature-based collection of PLA cold-crystallization temperatures as a function of PCL content is presented in Fig. 11, according to the same normalization method employed in Fig. 6. Despite differences among the systems are large, depending on the specific polymer grade, a clear reduction of ΔTcc values is observed when PCL is added to PLA. While the trend as a function of composition is not so clear, the nucleating effect of the PCL component on PLA, for most values reported in the literature, is pronounced for most systems.

It should be noted, however, that a fundamental difference exists between PCL and PBS, at the typical temperatures of PLA cold crystallization. Indeed, while in PLA/PBS immiscible blend the devitrified PLA is in contact with semicrystalline PBS droplets, in the case of PLA/PCL blend, the nucleating effect might originate from a molten PCL phase. Alternatively, it could be hypothesized that nucleation of PLA occurs during the cooling stage, upon PCL crystallization, even though the PLA matrix is already in the glassy state (at $T_{c,PCL}$). Note that this possibility is not contemplated for PLA/PBS blend, since poly(butylene succinate) crystallizes above the glass transition of polylactide. In order to better understand the peculiar

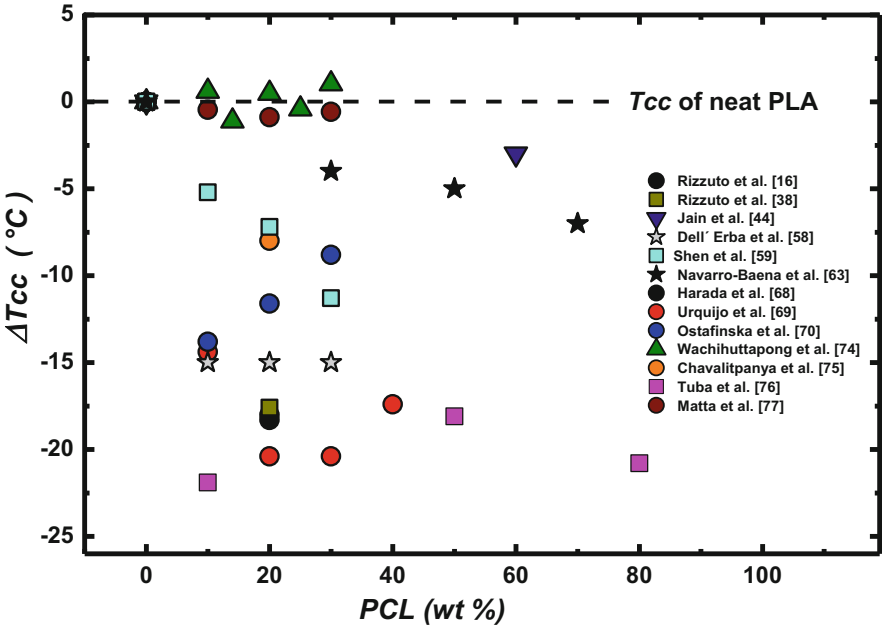

Fig. 11 Difference in cold-crystallization temperature between neat PLA and blended sample (ΔT_{cc}) as a function of PCL content in different PLA/PCL blends reported in literature

nucleation mechanism upon cold crystallization of PLA in its immiscible blend with PCL, a purposely designed thermal history has been applied by Müller et al. [16].

According to this protocol, the samples were quenched below $T_{g,PLA}$ and annealed at progressively lower temperatures for a fixed time, before reheating to measure PLA cold-crystallization temperature and PCL crystallinity (by its melting enthalpy). The relevant results are reported in Fig. 12 [16].

Crystallization of PCL occurs in a rather broad temperature range, from about 45 to 20°C. Concomitantly with the increase of PCL crystallinity obtained by lowering the annealing temperature, the cold-crystallization temperature of PLA decreases smoothly from 135 to 115°C, indicating a nucleation effect of the developing PCL crystals on the glassy PLA matrix. It should be noted that a similar acceleration of PLA cold crystallization is not observed in pure PLA, when annealed for the same time in the same temperature range (see Fig. 12). If the blend is compatibilized, resulting in smaller PCL droplets and higher PLA/PCL interfacial area, a higher nucleating efficiency of PCL crystals on PLA cold crystallization can be found [16]. Although it is now well established that PLA can nucleate at temperatures below its glass transition [78, 79], despite the extremely low mobility, the presence of PCL crystals seems to accelerate this process. The exact mechanism of nucleation in this peculiar situation has not been established, but a role of the stresses developing at the interface between the two polymers, upon PCL crystallization, can be speculated.

The effect of the addition of a third polymeric component to PLA/PCL immiscible blend on the crystallization of PLA was reported in a number of works [16, 38,

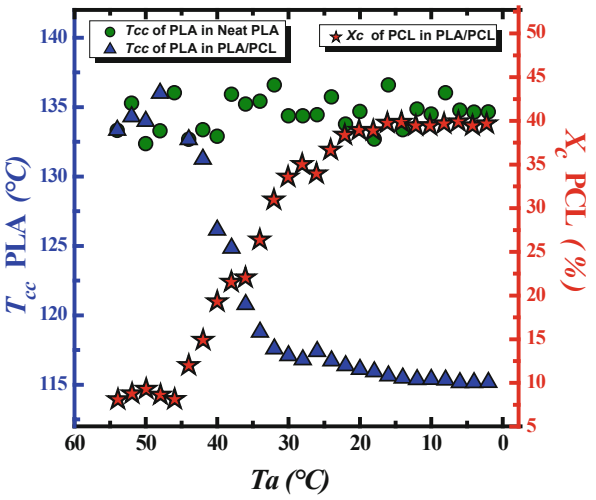

Fig. 12 Cold-crystallization temperature of PLA (T_{cc}) and crystallinity degree of PCL (Xc) as a function of the annealing temperature Ta. Data related to neat PLA and PLA/PCL 80/20 blend are shown. Adapted with permission from [16]

58, 74, 75]. In general, an acceleration of PLA crystallization kinetics can be observed, although the exact origin of this effect depends on the balance between the miscibility of the additive with the PLA matrix and its compatibilizing action.

Rizzuto et al. [16] have investigated the crystallization behavior of PLA/PCL 80/20 wt% with the addition of 2 wt% of poly(L-lactide-*block*-carbonate) copolymers with different compositions. A large effect on the morphology, with the formation of submicron PCL droplets in the best case, was detected, together with a minor decrease in PLA glass transition temperature. Given that PLA spherulitic growth rate was not affected, the measured enhancement of overall crystallization kinetics with respect to the neat blend in the presence of the block copolymer was attributed to a nucleating effect of the PCL interfaces. On the other hand, when the added third polymer is partially miscible, plasticization effects can arise, causing higher PLA chain mobility and faster crystal growth rates. This is the case, for instance, of the already mentioned P(LA-ran-CL) copolymers [38] (see Fig. 10) or Pluronic (PEG-PPG-PEG) triblock copolymers [74]. In this latter system, despite the block chain architecture, a partial miscibility exists, and it results in a faster PLA cold and melt crystallization. Figure 13 indeed shows that, upon cooling a 85/15 PLA/PCL blend, larger spherulites develop when few percent of Pluronic block copolymer is added.

A relatively small number of works reported on the crystallization of the PCL components of immiscible PLLA/PCL blends. Opposite effects are observed, depending on the specific morphology. Few studies [38, 44, 64] have reported an enhancement of PCL crystallization during cooling upon the addition of PLA. This is a consequence of the nucleation at the interface with the previously crystallized PLA phase, as shown in the PLOM micrographs of Fig. 14. A 32/68 PLLA/PCL immiscible blend is first crystallized at 120°C and subsequently cooled to 35°C. At 120°C (Fig. 14a), only PLA is able to crystallize, whereas the PCL is molten and dispersed in between the PLA spherulites (see as an example the white oval marker in Fig. 14a, where molten PCL is shown). By quenching to 35°C (Fig. 14b), the PCL

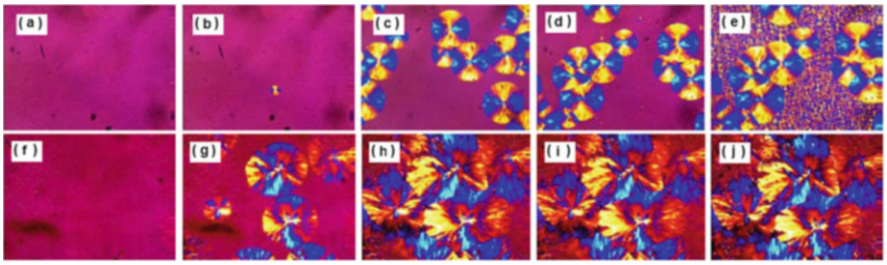

Fig. 13 PLOM images during crystallization of 85/15 PLLA/PCL blends either neat (**a**–**e**) or with 5 wt% Pluronic copolymer (**f**–**j**). Pictures are taken during stepwise crystallization at (**a**, **f**) 141°C, 0 min; (**b**, **g**) and (**g**) 141°C, 30 min; (**c**) and (**h**) 141°C, 90 min; (**d**, **i**) 127°C; and (**e**, **j**) 37°C. Reproduced with permission from [74]

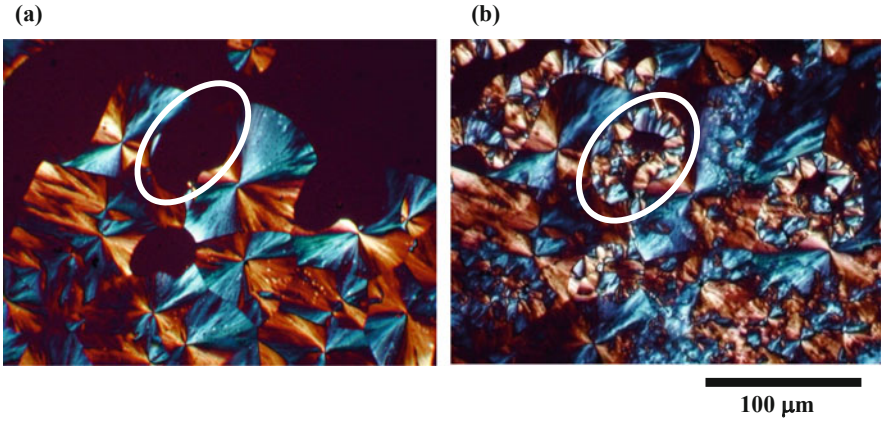

Fig. 14 Optical micrographs of 32/68 PLLA/PCL immiscible blends during crystallization (**a**) at 120°C and (**b**) at 35°C. Figure adapted with permission from [46]

crystallization starts clearly at the interface with crystalline PLA, developing a transcrystalline morphology clearly visible within the white oval region depicted [46].

On the other hand, when PCL is the minority phase dispersed in small domains within the PLA matrix, fractionated crystallization and a decrease in PCL crystallinity were found [16, 38, 60, 63, 76]. As an example, the DSC cooling traces of PLA, PCL, and 80/20 PLLA/PCL blends containing different kinds of compatibilizing agents poly(L-lactide-block-carbonate) (PLA-b-PC) are shown in Fig. 15. In neat PLA/PCL blends, two different populations of droplets are present. The majority of them crystallize at the same temperature as bulk PCL (32°C), indicating that they still contain most of the heterogeneities present in the original PCL sample. A minority of PCL droplets contains less efficient nucleating impurities and solidifies about 10°C lower. Upon addition of PLA-b-PC compatibilizer, droplet size is decreased and the larger fraction of droplets crystallizes at even lower temperatures, possibly nucleated at the interface with glassy PLA [16].

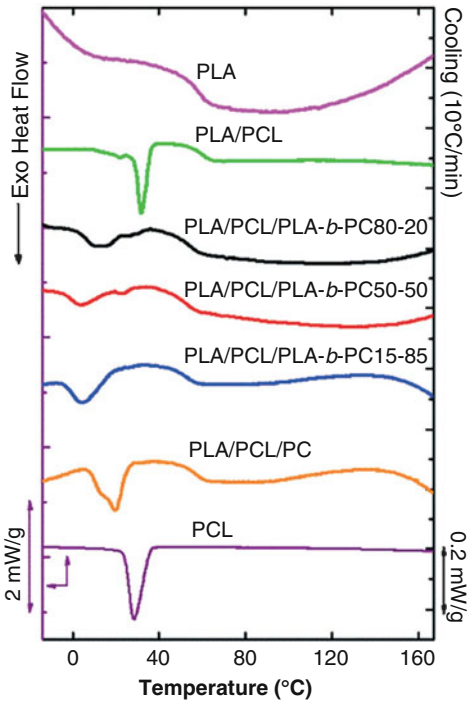

Fig. 15 DSC cooling curves at 10°C/min, of neat PLA, neat PCL, PLA/PCL blends, and PLA/PCL/compatibilizer blends. Adapted with permission from [16]

2.3 *Poly(Butylene Succinate)/Poly(ε-Caprolactone) Immiscible Blends*

Blends of poly(butylene succinate) and poly(ε-caprolactone) are interesting because of the good mechanical properties shown by the two parent homopolymers, both of which are constituted by flexible chains. This notwithstanding, only very few works focused on the study of PBS/PCL blends, either neat or compatibilized [80–82].

Qiu et al. [81] explored the effect of composition on crystallization and melting behavior of PBS/PCL blends. Figure 16 shows the DSC cooling curves of all samples at a cooling rate of 5°C/min.

On the PBS-rich part of the composition range, no significant effect of PCL addition on the crystallization of the major component was noticed. On the other hand, a minor content (<40 wt%) of PBS causes at first the increase in PCL crystallization rate, i.e., an upward shift of the crystallization peak temperature. The same effect was reported for an 80/20 PBS/PCL blend, with an increase of $T_{c,PCL}$ of about 10°C and the invariance of $T_{c,PBS}$ [81]. The enhanced PCL crystallization was attributed to a nucleation effect of the interfaces with previously crystallized PBS. When PCL becomes the minority phase, a large depression of the crystallization temperature is observed, and multiple crystallization events, i.e., fractionated crystallization, are also evident. Fractionated crystallization is

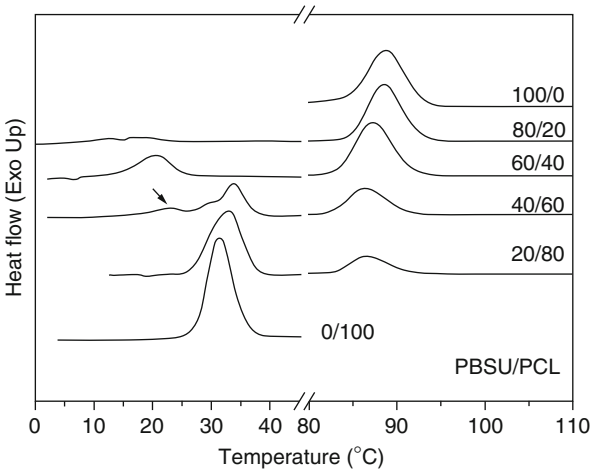

Fig. 16 Non-isothermal crystallization from the melt of PBS/PCL blends with different compositions at a cooling rate of 5°C/min. Reproduced with permission from [81]

particularly clear in the 60/40 PBS/PCL blend [81], which is an unusual composition for the phenomenon. However, a detailed morphological analysis that could explain the observation has not been carried on.

Fractionated crystallization and finer dispersion of PCL phase at lower contents are also associated with a substantial decrease of its crystallinity, indicating a hindrance of the crystallized matrix on PCL structuring.

2.4 Blends of Poly(Hydroxybutyrate) and Other Bio-Based Polyesters

Poly(hydroxybutyrate) (PHB) is a biodegradable thermoplastic polyester which can be obtained via a biotechnological process by means of selected bacteria. PHB is a highly crystalline polymer with high stiffness and a melting and glass transition temperatures of around 170 and 5°C, respectively.

Blends of PHB with PLA have been investigated, with the aims of reducing PHB crystallinity (detrimental for some applications) on one side and improving the properties of PLA (e.g., gas barrier properties for food packaging application) on the other side. The degree of compatibility between the PLA and PHB in their blends affects the crystallization behavior of the two components [43, 61, 83–96]. This section presents a summary of previous research on PLA/PHB blends in which the authors discussed, at least in part, the crystallization behavior. The results are summarized in Table 3.

It should be noted that PLA/PHB can be miscible in the melt state if PLA of low molecular weight is employed [86, 96]. Crystallization from a miscible melt can give rise to concomitant formation of PHB and PLA crystals at the same isothermal crystallization temperature and with similar kinetics [86]. Each phase crystallizes in

Table 3 Main experimental works on PHB/PLA blends, with emphasis on nucleation and crystallization

Sample	Publication year	Composition wt%	Crystallization/nucleation conditions and technics	*Tcc* of PLA (°C)	*Tc* of PLA (°C)	*Tc* of PHB (°C)	Crystallization/nucleation outcomes	Reference
PLA/PHB	2006	50/50	FTIR spectroscopy; stepwise isothermal crystallization of the two polymers	–	–	–	Crystallization mechanism of PLA not affected by PHB presence, but kinetics is retarded. Possible dilution effect. PHB crystallization rate after solidification of PLLA is depressed due to segregation/confinement of the polymer in the interfibrillar or interlamellar region of PLA spherulites	[83]
PLA/PHB	2011	0–100 wt% of PHB	PLOM; DSC non-isothermal crystallization; WAXD; FTIR	–	–	–	PHB acts as a nucleating agent for PLA, leading to an enhancement in PLA cold-crystallization rate and crystallinity The crystallization rate of PHB during cooling is also accelerated	[90]
PLA/PHB/Lapol	2012	Neat PLA	DSC non-isothermal crystallization; XRD	115	–	–	No meaningful effect of PHB on the crystallization behavior of PLA. The addition of Lapol (plasticizer) increases PLA crystallinity	[95]
		75/25		115	–	–		
		75/25/7		120	–	–		
PLA/PHB/talc	2013	90/10	DSC non-isothermal and isothermal crystallization; FT-IR; PLOM	86.3	–	–	PHB acted as a nucleating agent for PLA. Further increases in PLA crystallization kinetics were found by addition of talc PLOM revealed that addition of 10 wt% PHB resulted in large increase in PLA nucleation density. A further increase in PLA nucleation density was found with the addition of talc PHB crystallization was inhibited by the presence of PLA and talc	[43]
		90/10/0.5		86.2	–	–		
		90/10/1		76.5	–	–		
		90/10/2		83.3	–	–		
		90/10/5		76.6	–	–		

PLA/ PHB/ CNC	2014	Neat PLA	XRD F-TIR, DSC non-isothermal crystallization	82.5	–	–	Addition of PHB, CNC, or CNCs resulted in a faster PLA cold-crystallization rate. While addition of binary PHB/CNC or PHB/CNCs resulted in increase of T_{cc} of PLA due to lower chain mobility	[92]
		75/25		66.4	–	–		
		71.25/23.75/5		70.9	–	–		
PLA/ PHB/ CNCs	2014	71.25/23.75/5		72.1	–	–		
PLA/ PHB/ ATBC/ CAT	2014	Neat PLA	DSC non-isothermal crystallization; XRD analysis	118.1	–	–	Addition of PHB results in lowering the crystallization rate of PLA; thus, the PLA T_{cc} shifted to higher temperatures. PLA T_{cc} decreases upon addition of 15 wt% of ATBC due to its plasticizing effect Presence of catechin increased PLA T_{cc}, due to specific intermolecular interactions	[93]
		75/25/0/0		130	–	–		
		63.6/21.2/15/0		106.3	–	–		
		71.1/23.7/0/5		150	–	–		
		60/20/15/5		126	–	–		
PLA/ PHB/ LIM	2014	Neat PLA	DSC non-isothermal crystallization; PLOM; FT-IR	123.3	–	–	After blending, PHB play the role of nucleating agent for PLA. Further increase in PLA crystallinity was found in PLA/PHB/LIM blend due to the plasticizing effect of LIM	[94]
		75/25		96.9	–	–		
		63.75/21.25/15		77.4	–	–		
PLA/ PHBV/ TiO_2	2015	30–70 wt% of PHBV with 1–5 wt% of TiO_2	DSC non-isothermal crystallization	–	–	–	Addition of PHBV resulted in a faster cold crystallization of PLA due to a plasticizing effect, which provides more mobility to PLA	[61]
PLA/ PHB/ ATBC/ CNC	2015	Neat PLA	XRD; FT-IR; DSC non-isothermal crystallization	82.5	–	–	PHB works as a nucleating agent for the PLA phase CNCs and ATBC have a synergic effect on PLA crystallization	[91]
		75/25		66.4	–	–		
		63.75/21.25/15		75.5	–	–		
		60/20/15/5		67.2	–	–		
		60/20/15/5		95.8	–	–		

a distinct type of spherulite, which interpenetrates when their growth front meets, due to the continued growth of one kind of lamellae in the interlamellar region of the other spherulites [96].

In the case of immiscible high molecular weight polymer, the effect of PHB addition on PLA crystallization is not so well studied. Isothermal melt crystallization of the PLA phase in a PLA/PHB 90/10 wt% shows a large acceleration effect, with half crystallization times decreasing more than twice with respect to neat PLA. By means of PLOM measurement, the enhanced crystallization rate was correlated with an increase in PLA nucleation density [43]. On the other hand, Zhang et al. studied the isothermal crystallization of PLLA in the immiscible 50/50 PLLA/PHB blend and observed a substantial depression of the crystallization rate [86]. This decrease in crystallization rate was attributed to a dilution effect, i.e., the PHB melt lowers the PLLA growth rate by reducing the amount of PLA chains in the growth front of the spherulite. Similarly, opposite effects of PHB on PLA cold crystallization have been found. Several researchers reported an enhancement of the cold-crystallization rate of PLA upon addition of small amounts of PHB [43, 61, 90–92]. In analogy, with what has been already discussed for PLA/PBS blends, the decrease of PLA T_{cc} can be attributed to an interfacial nucleation effect on the crystalline PHB domains. On the contrary, Arrieta et al. [95] found that a 25 wt% of PHB in PLA/PHB blend caused a large increase in PLA cold-crystallization temperature from 118.1°C to 130°C. This peculiar effect was ascribed to the possible occurrence of transesterification reactions between PHB and PLA during the blending step.

Ternary systems containing immiscible PLA/PHB blend and various additives have also been investigated. Often, an acceleration in the crystallization rate of PLA is seen, typically due to (1) additional heterogeneous nucleation, for example, from talc [43], cellulose nanocrystals (CNC), and surfactant-modified cellulose nanocrystals (CNCs) [91, 92], and/or (2) increase in the PLA chain mobility by a plasticizing effect of small soluble molecules such as acetyl(tributyl citrate) (ATBC) [91, 93] and limonene (LIM) [94]. Interestingly, a delayed cold crystallization is observed for blends containing catechin, probably as a result of hydrogen bond formation with PLA chains [93].

Concerning the crystallization of the PHB phase in the presence of PLA as a major blend component, a strong depression of its kinetics – or even the complete suppression of crystallization in the adopted conditions – is always reported [43, 90]. These results have been generally interpreted as a confinement effect imposed by the crystalline PLA matrix, because upon PLA spherulitic crystallization at higher temperatures, the amorphous PHB chains are segregated to the interlamellar/interfibrillar regions of PLA superstructures [97, 98]. Such intimate contact between the phases usually arises when some degree of partial miscibility exists between the chains in the melt state [99].

Few works have also investigated the phase behavior and crystallization of PHB blends with other biodegradable polymers, namely, PBS and PCL [100–102]. Ma et al. [100] prepared PHB/PBS blends in the entire composition range, with the aim of improving the crystallizability of PHB by the addition of the second component. The blends were immiscible with typical sea-island morphology for

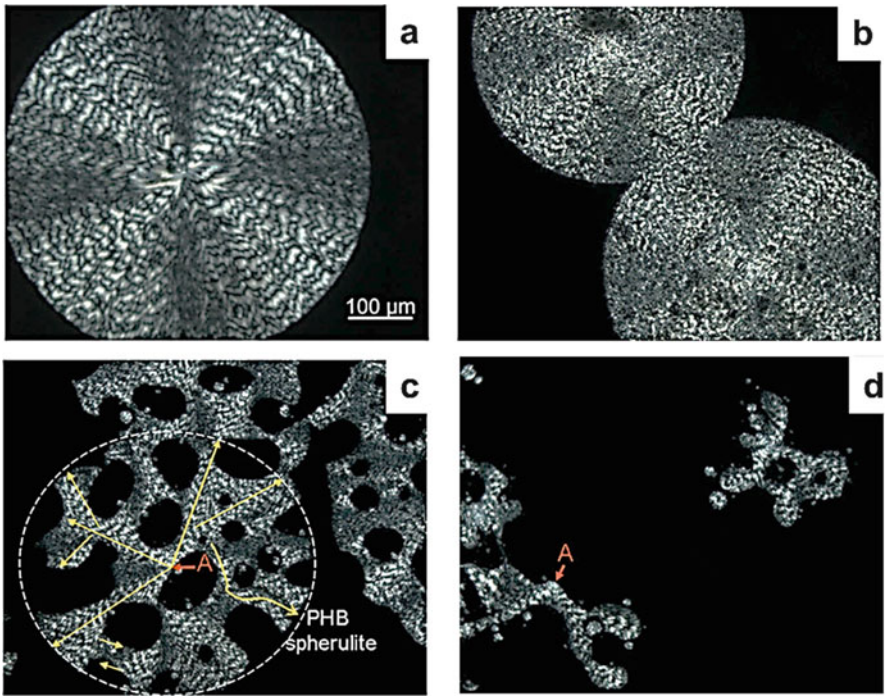

Fig. 17 Polarized light optical microscopy during crystallization of PHB/PBS blends with various compositions at 120°C. The PBS content in the blend is (**a**) 0%, (**b**) 30%, (**c**) 50%, and (**d**) 70% by weight. The development of PHB spherulite in (**c**) is indicated by the arrow and the nucleation point by the letter "A." Adapted with permission from [100]

asymmetric compositions and co-continuous PHB/PBS phases at 50/50 wt%. Non-isothermal crystallization revealed a clear increase in $T_{c,PHB}$ of up to 30°C with PBS content. The crystallization of PBS is instead depressed when the polymer is the minor component. Ma et al. interpreted this result as a consequence of confinement by the crystalline PHB matrix, but it could also be due to changes in nucleation induced by impurity transfer phenomena. The increase of PHB crystallization rate in the presence of PBS was also noticeable in isothermal conditions, with half crystallization times which decreased more than five times in the blends with respect to the neat polymer, independently from the composition. This acceleration of crystallization kinetics was attributed to a nucleation effect of the interfaces with molten PBS domains, as supported by PLOM measurements during isothermal crystallization above the PBS melting point (Fig. 17).

It can be seen that neat PHB (Fig. 17a) crystallized in banded spherulites with very low nucleation density. Upon addition of 30 wt% PBS, the morphology is still spherulitic with dark molten domains of PBS engulfed in it. When the PHB content in the blend becomes 50% or less, the crystals are forced to grow around the molten PBS domains, and the spherulitic structure becomes branched-like. However, the

persistence of the banded motif allows one to identify the nucleation points (highlighted by the letter A in Fig. 17c, d), at the interface with molten PBS domains. Moreover, nucleation of smaller molten PHB domains by contact with crystallizing PHB in larger droplets was also observed. It should be noted that a small reduction of PHB growth rate is measured and attributed to the hindrance of molten PBS to the crystal development, although a limited miscibility between PHB and PBS has also been suggested [101].

Poly(hydroxybutyrate)/poly(ε-caprolactone) exhibits a molecular weight-dependent miscibility. Lovera et al. [102] investigated the crystallization, morphology, and degradation behavior of PHB/PCL blends upon varying PCL molecular weight.

PHB/high molecular weight PCL blend was found to be immiscible. Analysis of the crystallization behavior after blending revealed fractionated crystallization of the PCL minor phase, with a depression of crystallization temperature of around 30°C. Blends with low molecular weight PCL were also biphasic, but the PHB-rich phase exhibited a partial miscibility with PCL, as inferred by the measured depression in the PHB melting and glass transition temperatures and by the increase in the spherulitic growth rate close to T_g. A decrease of PHB nucleation density in the partially miscible blend has also been reported, probably caused by impurity transfer between the two phases during blending.

3 Conclusions and Outlook

In this review, we have concentrated on immiscible and mostly double-crystalline thermoplastic polyester blends. The nucleation and crystallization of these complex materials greatly depend on their morphology, as determined by their composition, processing conditions, and thermal history.

As far as the nucleation of double-crystalline polyester blends is concerned, the component that crystallizes at higher temperatures can nucleate (a) on existing heterogeneities which were either present in the parent homopolymer or transferred during melt blending from the second blend component or (b) on the interface between the two molten components. Notice than in the second case, or case (b) above, no epitaxial mechanism can be invoked to explain the heterogeneous nucleation that has been clearly documented by PLOM and DSC. Hence other causes must be found that could be related to secondary interactions between the immiscible phases, interfacial free energy differences, or other unknown factors that clearly need more future research.

If the blend above with two crystallizable components is further cooled, after the first blend component has already crystallized, then the second polymer can be nucleated (a) by existing heterogeneities which were either present in the parent homopolymer or transferred during blending from the second melt component or (b) on the interface between the previously crystallized blend component and the melt of the second component. In this second case, epitaxial nucleation is a

possibility. In many cases, nucleation effects of the previously crystallized component on the second phase of the blend (that crystallizes at lower temperatures) have been reported. More peculiar effects like the nucleation of PCL droplets on glassy PLA matrices deserve more research in order to find how the nucleation can occur in the glassy state by interfacial contacts with crystalline polymeric droplets.

Another common occurrence is fractionated crystallization. This is a general process that has been found in many immiscible blends when a highly dispersed phase is produced and has been extensively studied and reviewed before; therefore, it has not been the subject of extensive discussion in this review.

There are many more studies dealing with non-isothermal nucleation and non-isothermal crystallization of immiscible polyester blend components than isothermal studies. In the cases where the blends are immiscible, the spherulitic growth rates are clearly not affected, unless compatibilizers or plasticizers are employed. Hence, the overall isothermal crystallization kinetics of immiscible polyester blends is determined by the nucleation effects of one blend component on the other.

It is clear that future studies are needed in order to fully comprehend the solidification of these important bio-based and in many cases bio-degradable materials, as such understanding can clearly lead to tailoring their properties for applications where they can substitute traditional nondegradable plastic materials.

Acknowledgments The authors would like to acknowledge funding by the BIODEST project ((RISE) H2020-MSCA-RISE-2017-778092).

References

1. Utracki LA, Wilkie C (eds) (2014) Polymer blends handbook. Springer, New York
2. Utracki LA (ed) (2002) Polymer blends handbook, vol 2. Kluwer Academic, Dordrecht
3. Paul DR, Barlow JW (1979) A brief review of polymer blend technology. In: Cooper SL, Estes GM (eds) Multiphase polymers. Advances in chemistry. ACS, Washington, pp 315–335
4. Paul DR, Barlow JW (1980) Polymer blends (or alloys). J Macromol Sci Rev Macromol Chem Phys 18:109–168
5. Cor K, Martin VD, Christophe P, Robert J (1998) Strategies for compatibilization of polymer blends. Prog Polym Sci 23:707–757
6. Supthanyakul R, Kaabbuathong N, Chirachanchai S (2016) Random poly(butylene succinate-co-lactic acid) as a multi-functional additive for miscibility, toughness, and clarity of PLA/PBS blends. Polymer 105:1–9
7. Dhibar AK, Kim JK, Khatua BB (2011) Cocontinuous phase morphology of asymmetric compositions of polypropylene/high-density polyethylene blend by the addition of clay. J Appl Polym Sci 119:3080–3092
8. Tol RT, Mathot VBF, Reynaers H, Groeninckx G (2006) Relationship between phase morphology, crystallization, and semicrystalline structure in immiscible polymer blends. In: Harrats C, Thomas S, Droeninchx G (eds) Micro- and nanostructured multiphase polymer blend systems phase morphology and interfaces. Taylor & Francis, Boca Raton, pp 391–420
9. Cordova ME, Lorenzo AT, Müller AJ, Gani L, Tence-Girault S, Leibler L (2011) The influence of blend morphology (co-continuous or sub-micrometer droplets dispersions) on the nucleation and crystallization kinetics of double crystalline polyethylene/polyamide blends prepared by reactive extrusion. Macromol Chem Phys 212:1335–1350

10. Pracella M (2013) Crystallization of polymer blends. In: Piorkowska E, Rutledge GC (eds) Handbook of polymer crystallization. Wiley, Hoboken, pp 287–325
11. Jabarin SA, Ardakani KM, Lofgren EA (2016) Crystallization and melting behavior in polymer blends. In: Isayev AI (ed) Encyclopedia of polymer blends. Structure, vol 3. Wiley, Weinheim, pp 135–189
12. Michell RM, Müller AJ (2016) Confined crystallization of polymeric materials. Prog Polym Sci 54–55:183–213
13. Tien ND, Prud'homme RE (2017) Crystallization behavior of semicrystalline immiscible polymer blends. In: Thomas S, Arif PM, Gowd B, Kalarikkal N (eds) Crystallization in multiphase polymer systems. Elsevier, Amsterdam, pp 181–212
14. Bartczak Z, Galeski A (1990) Homogeneous nucleation in polypropylene and its blends by small-angle light scattering. Polymer 31:2027–2038
15. Deng Y, Thomas NL (2015) Blending poly(butylene succinate) with poly(lactic acid): ductility and phase inversion effects. Eur Polym J 71:534–546
16. Rizzuto M, Marinetti L, Caretti D, Mugica A, Zubitur M, Müller AJ (2017) Can poly (ε-caprolactone) crystals nucleate glassy polylactide? CrstEngComm 19:3178
17. Ma P, Cai X, Wang W, Duan F, Shi D, Lemstra PJ (2014) Crystallization behavior of partially crosslinked poly(b-hydroxyalkonates)/poly(butylene succinate) blends. J Appl Polym Sci 131:41020
18. Frensch H, Harnischfeger P, Jungnickel BJ (1989) Fractionated crystallization in incompatible polymer blends. In: Utracky LA, Weiss RA (eds) Multiphase polymers: blends and ionomers. American Chemical Society, Washington, pp 101–125
19. Müller AJ, Michell RM (2016) Differential scanning calorimetry of polymers. In: Guo Q (ed) Polymer morphology: principles, characterization, and processing. Wiley, Hoboken, pp 72–99
20. Morales RA, Arnal ML, Müller AJ (1995) The evaluation of the state of dispersion in immiscible blends where the minor phase exhibits fractionated crystallization. Polym Bull 35:379–386
21. Arnal ML, Matos ME, Morales RA, Santana OO, Müller AJ (1998) Evaluation of the fractionated crystallization of dispersed polyolefins in a polystyrene matrix. Macromol Chem Phys 199:2275–2288
22. Arnal ML, Müller AJ (1999) Fractionated crystallisation of polyethylene and ethylene/a-olefin copolymers dispersed in immiscible polystyrene matrices. Macromol Chem Phys 200:2559–2576
23. Schick C, Androsch R, Schmelzer JWP (2017) Homogeneous crystal nucleation in polymers. J Phys Condens Matter 29:453002
24. Santana OO, Müller AJ (1994) Homogeneous nucleation of the dispersed crystallizable component of immiscible polymer blends. Polym Bull 32:471–477
25. Michell RM, Blaszczyk-Lezak I, Mijangos C, Müller AJ (2013) Confinement effects on polymer crystallization: from droplets to alumina nanopores. Polymer 54:4059–4077
26. Tol RT, Mathot VBF, Groeninckx G (2005) Confined crystallization phenomena in immiscible polymer blends with dispersed micro- and nanometer sized PA6 droplets, part 2: reactively compatibilized PS/PA6 and (PPE/PS)/PA6 blends. Polymer 46:383–396
27. Tol RT, Mathot VBF, Groeninckx G (2005) Confined crystallization phenomena in immiscible polymer blends with dispersed micro- and nanometer sized PA6 droplets, part 3: crystallization kinetics and crystallinity of micro- and nanometer sized PA6 droplets crystallizing at high supercoolings. Polymer 46:2955–2965
28. Yordanov C, Minkova L (2005) Fractionated crystallization of compatibilized LDPE/PA6 blends. Eur Polym J 41:527–534
29. Anstey A, Codou A, Misra M, Mohanty AK (2018) Novel compatibilized nylon-based ternary blends with polypropylene and poly(lactic acid): fractionated crystallization phenomena and mechanical performance. ACS Omega 3:2845–2854
30. Huo H, Guo C, Zhou J, Zhao X (2014) The combination of fluctuation-assisted crystallization and interface-assisted crystallization in a crystalline/crystalline blend of poly(ethylene oxide) and poly(ε-caprolactone). Colloid Polym Sci 292:971–983

31. Qiaolian L, Wu D, Xie H, Peng S, Chen Y, Xu C (2016) Crystallization of poly (3-caprolactone) in its immiscible blend with polylactide: insight into the role of annealing histories. RSC Adv 6:37721
32. Sakai F, Nishikawa K, Inoue Y, Yazawa K (2009) Nucleation enhancement effect in poly(L-lactide) (PLLA)/poly(ε-caprolactone) (PCL) blend induced by locally activated chain mobility resulting from limited miscibility. Macromolecules 42:8335–8342
33. Pan P, Shan G, Bao Y (2014) Enhanced nucleation and crystallization of poly(L-lactic acid) by immiscible blending with poly(vinylidene fluoride). Ind Eng Chem Res 53:3148–3156
34. Kong Y, Ma Y, Lei L, Wang X, Wang H (2017) Crystallization of poly(ϵ-caprolactone) in poly(vinylidene fluoride)/poly(ε -caprolactone) blend. Polymers 9:42
35. Shi W, Chen F, Zhang Y, Han CC (2012) Viscoelastic phase separation and interface assisted crystallization in a highly immiscible iPP/PMMA blend. ACS Macro Lett 1:1086–1089
36. Wu D, Lin D, Zhang J, Zhou W, Zhang M, Zhang Y, Wang D, Lin B (2011) Selective localization of nanofillers: effect on morphology and crystallization of PLA/PCL blends. Macromol Chem Phys 212:613–626
37. Yu C, Han L, Bao J, Shan G, Bao Y, Pan P (2016) Polymorphic crystallization and crystalline reorganization of poly(L-lactic acid)/poly(D-lactic acid) racemic mixture influenced by blending with poly(vinylidene fluoride). J Phys Chem B 120(32):8046–8054
38. Rizzuto M, Mugica A, Zubitur M, Caretti D, Müller AJ (2016) Plasticization and anti-plasticization effects caused by poly(L-lactide-ran-caprolactone) addition to double crystalline poly(L-lactide)/poly(ε- caprolactone) blends. CrstEngComm 18:2014
39. Wei Q, Chionna D, Pracella M (2005) Reactive compatibilization of PA6/LDPE blends with glycidyl methacrylate functionalized polyolefins. Macromol Chem Phys 206:777–786
40. Garcia-Garcia D, Rayon E, Carbonell-Verdu A, Lopez-Martinez J, Balart R (2017) Improvement of the compatibility between poly(3-hydroxybutyrate) and poly(e-caprolactone) by reactive extrusion with dicumyl peroxide. Eur Polym J 86:41–57
41. Wang R, Wang S, Zhang Y, Wan C, Ma P (2009) Toughening modification of PLLA/PBS blends via in situ compatibilization. Polym Eng Sci 49:26–33
42. Liu NC, Xie HQ, Baker WE (1993) Comparison of the effectiveness of different basic functional groups for the reactive compatibilization of polymer blends. Polymer 34:4680–4687
43. Tri PN, Domenek S, Guinault A, Sollogoub C (2013) Crystallization behavior of poly(lactide)/poly(β-hydroxybutyrate)/talc composites. J Appl Polym Sci 129:3355–3365
44. Jain S, Reddy MM, Mohanty AK, Misra M, Ghosh AK (2010) A new biodegradable flexible composite sheet from poly(lactic acid)/poly(e-caprolactone) blends and micro-talc. Macromol Mater Eng 295:750–762
45. Fenni SE, Monticelli O, Conzatti L, Doufnoune R, Stagnaro P, Haddaoui N, Cavallo D (2018) Correlating the morphology of poly(L-lactide)/poly(butylene succinate)/graphene oxide blends nanocomposites with their crystallization behavior. Express Polym Lett 12:58–70
46. Müller AJ, Avila M, Saenz G, Salazar J (2014) Crystallization of PLA-based materials. In: Jiménez A, Peltzer M, Ruseckaite R (eds) Poly(lactic acid) science and technology: processing, properties, additives and applications. The Royal Society of Chemistry, Cambridge, pp 66–98
47. Di Lorenzo ML, Androsch R (2015) Crystallization of poly(lactic acid). In: Fakirov S (ed) Biodegradable polyesters. Wiley, Weinheim, pp 109–130
48. Androsch R, Schick C, Di Lorenzo ML (2017) Kinetics of nucleation and growth of crystals of poly(l-lactic acid). Advances in polymer science, vol 279. Springer, Basel, pp 235–272
49. Yokohara T, Yamaguchi M (2008) Structure and properties for biomass-based polyester blends of PLA and PBS. Eur Polym J 44:677–685
50. Shibata M, Inoue Y, Miyoshi M (2006) Mechanical properties, morphology, and crystallization behavior of blends of poly(L-lactide) with poly(butylene succinate-co-L-lactate) and poly (butylene succinate). Polymer 47:3557–3564

51. Wu D, Yuan L, Laredo E, Zhang M, Zhou W (2002) Interfacial properties, viscoelasticity, and thermal behaviors of poly(butylene succinate)/polylactide blend. Ind Eng Chem Res 51:2290–2298
52. Persenaire O, Quintana R, Lemmouchi Y, Sampson J, Martin S, Bonnaud L, Dubois P (2014) Reactive compatibilization of poly(L-lactide)/poly(butylene succinate) blends through polyester maleation: from materials to properties. Polym Int 63:1724–1731
53. Buasri A, Buranasing G, Piemjaiswang R, Yousatit S, Loryuenyong V (2014) Effect of titanium dioxide nanoparticles on mechanical and thermal properties of poly(lactic acid) and poly(butylene succinate) blends. Adv Sci Tech 96:33–38
54. Zhang Z, Zhang Y (2016) Reinforcement effect of poly(butylene succinate) (PBS)-grafted cellulose nanocrystal on toughened PBS/polylactic acid blends. Carbohydr Polym 140:374–382
55. Harada M, Ohya T, Iida K, Hayashi H, Hirano K, Fukuda H (2007) Increased impact strength of biodegradable poly(lactic acid)/poly(butylene succinate) blend composites by using isocyanate as a reactive processing agent. J Appl Polym Sci 106:1813–1820
56. Luzi F, Fortunati E, Jiménez A, Pugliaa D, Pezzolla D, Gigliotti G, Kenny JM, Chiralt A, Torre L (2016) Production and characterization of PLA PBS biodegradable blends reinforced with cellulose nanocrystals extracted from hemp fibres. Ind Crop Prod 93:276–289
57. Hassan E, Wei Y, Jiao H, Muhuo Y (2013) Dynamic mechanical properties and thermal stability of poly(lactic acid) and poly(butylene succinate) blends composites. J Fiber Bioeng Inform 6:85–94
58. Dell'Erba R, Maglio G, Malinconico M, Migliozzi A (2001) Immiscible polymer blends of semicrystalline biocompatible components: thermal properties and phase morphology analysis of PLLA/PCL blends. Polymer 42:7831–7840
59. Shen T, Lu M, Liang L (2013) Modification of the properties of polylactide/polycaprolactone blends by incorporation of blocked polyisocyanate. J Macromol Sci Part A Pure Appl Chem 50:547–554
60. Monticelli O, Calabrese M, Gardella L, Fina A, Gioffredi E (2014) Silsesquioxanes: novel compatibilizing agents for tuning the microstructure and properties of PLA/PCL immiscible blends. Eur Polym J 58:69–78
61. Mofokeng JP, Luyt AS (2015) Dynamic mechanical properties of PLA/PHBV, PLA/PCL, PHBV/PCL blends and their nanocomposites with TiO2 as nanofiller. Thermochim Acta 613:41–53
62. Lopez-Rodriguez N, Lopez-Arraiza A, Meaurio E, Sarasua JR (2006) Crystallization, morphology, and mechanical behavior of polylactide/poly(-caprolactone) blends. Polym Eng Sci 46:1299–1308
63. Navarro-Baena I, Sessini V, Dominici F, Torre L, Kenny JM, Peponi L (2016) Design of biodegradable blends based on PLA and PCL: from morphological, thermal and mechanical studies to shape memory behavior. Polym Degrad Stab 132:97–108
64. Han W, Liao X, He B, Yang Q, Li G (2018) Disclosing the crystallization behavior and morphology of poly(ε-caprolactone)/within poly(ε-caprolactone)/poly(L-lactide) blends. Polym Int 67:566–576
65. Derakhshandeh M, Noroozi N, Schafer LL, Vlassopoulos D, Hatzikiriakos SG (2016) Dynamics of partially miscible polylactide-poly(ε-caprolactone) blends in the presence of cold crystallization. Rheol Acta 55:657–671
66. Cabedo L, Feijoo JL, Villanueva MP, Lagaron JM, Gimenez E (2006) Optimization of biodegradable nanocomposites based on a PLA/PCL blends for food packaging applications. Macromol Symp 233:191–197
67. Bouakaz BS, Habi A, Grohens Y, Pillin I (2017) Organomontmorillonite/graphene-PLA/PCL nanofilled blends: new strategy to enhance the functional properties of PLA/PCL blend. Appl Clay Sci 139:81–91

68. Harada M, Iida K, Okamoto K, Hayashi H, Hirano K (2008) Reactive compatibilization of biodegradable poly(lactic acid)/poly(ε-caprolactone) blends with reactive processing agents. Polym Eng Sci 48:1359–1368
69. Urquijo J, Guerrica-Echevarrıa G, Eguiazabal JI (2015) Melt processed PLA/PCL blends: effect of processing method on phase structure, morphology, and mechanical properties. J Appl Polym Sci 42641:1–9
70. Ostafinska A, Fortelny I, Nevoralova M, Hodan J, Kredatusova J, Slouf M (2015) Synergistic effects in mechanical properties of PLA/PCL blends with optimized composition, processing, and morphology. RSC Adv 5:98971
71. Bai H, Huang C, Xiu H, Gao Y, Zhang Q, Fu Q (2013) Toughening of poly(L-lactide) with poly(ε-caprolactone): combined effects of matrix crystallization and impact modifier particle size. Polymer 54:5257–5266
72. Bai H, Xiu H, Gao J, Deng H, Zhang Q, Yang M, Fu Q (2012) Tailoring impact toughness of poly(L-lactide)/poly(ε-caprolactone) (PLLA/PCL) blends by controlling crystallization of PLLA matrix. ACS Appl Mater Interfaces 4:897–905
73. Na YH, He Y, Shuai X, Kikkawa Y, Doi Y, Inoue Y (2002) Compatibilization effect of poly (ε-caprolactone)-b-poly(ethylene glycol) block copolymers and phase morphology analysis in immiscible poly(lactide)/poly(ε -caprolactone) blends. Biomacromolecules 3:1179–1186
74. Wachirahuttapong S, Thongpin C, Sombatsompop N (2016) Effect of PCL and compatibility contents on the morphology, crystallization and mechanical properties of PLA/PCL blends. Energy Procedia 89:198–206
75. Chavalitpanya K, Phattanarudee S (2013) Poly(lactic acid)/polycaprolactone blends compatibilized with block copolymer. Energy Procedia 34:542–548
76. Tuba F, Olah L, Nagy P (2011) Characterization of reactively compatibilized poly(D, L-lactide)/poly(ε-caprolactone) biodegradable blends by essential work of fracture method. Eng Fract Mech 78:3123–3133
77. Matta AK, Rao RU, Sumana KNS, Rambabuc V (2014) Preparation and characterization of biodegradable PLA/PCL polymeric blends. Procedia Mater Sci 6:1266
78. Androsch R, Di Lorenzo ML (2013) Kinetics of crystal nucleation of poly(L-lactic acid). Polymer 54:6882–6885
79. Di Lorenzo ML, Androsch R (2013) Crystal nucleation in glassy poly(L-lactic acid). Macromolecules 46, 6048–6056
80. Liu Q, Zhou XM (2015) Preparation of poly(butylene succinate)/poly(ϵ-caprolactone) blends compatibilized with poly(butylene succinate-co-ϵ-caprolactone) copolymer. J Macromol Sci Part A Pure Appl Chem 52:625–629
81. Qiu Z, Komura M, Ikehara T, Nishi T (2003) Miscibility and crystallization behavior of biodegradable blends of two aliphatic polyesters. Poly(butylene succinate) and poly (1-caprolactone). Polymer 44:7749–7756
82. Gumede TP, Luyt AS, Müller AJ (2018) Review on PCL, PBS, and PCL/PBS blends containing carbon nanotubes. eXPRESS Polym Lett 12:505–529
83. Zhang J, Sato H, Furukawa T, Tsuji H, Noda I, Ozaki Y (2006) Crystallization behaviors of poly(3-hydroxybutyrate) and poly(L-lactic acid) in their immiscible and miscible blends. J Phys Chem B 110:24463–24471
84. Sato H, Nakamura M, Padermshoke A, Yamaguchi H, Terauchi H, Ekgasit S, Noda I, Ozaki Y (2004) Thermal behavior and molecular interaction of poly(3-hydroxybutyrate-co-3-hydroxyhexanoate) studied by wide-angle X-ray diffraction. Macromolecules 37:3763–3769
85. Sato H, Murakami R, Padermshoke A, Hirose F, Senda K, Noda I, Ozaki Y (2004) Infrared spectroscopy studies of $CH^{\cdots}O$ hydrogen bondings and thermal behavior of biodegradable poly(hydroxyalkanoate). Macromolecules 37:7203–7213
86. Zhang L, Xiong C, Deng X (1996) Miscibility, crystallization and morphology of poly (P-hydroxybutyrate)/poly(d,l-lactide) blends. Polymer 37:235–241

87. Arrieta MP, Samper MD, Aldas M, Lopez J (2017) On the use of PLA-PHB blends for sustainable food packaging applications. Materials (Basel) 10(9). pii: E1008. doi: https://doi.org/10.3390/ma10091008
88. Arrieta MP, Lopez J, Rayon E, Jimenez A (2014) Disintegrability under composting conditions of plasticized PLA-PHB blends. Polym Degrad Stab 108:307–318
89. Armentano I, Fortunati E, Burgos N, Dominici F, Luzi F, Fiori S, Jimenez A, Yoon K, Ahn J, Kang S, Kenny JM (2015) Processing and characterization of plasticized PLA/PHB blends for biodegradable multiphase systems. eXPRESS Polym Lett 9:583–596
90. Zhang M, Thomas NL (2011) Blending polylactic acid with polyhydroxybutyrate: the effect on thermal, mechanical, and biodegradation properties. Adv Polym Technol 30:67–79
91. Arrieta MP, Fortunati E, Dominici F, Lopez J, Kenny JM (2015) Bionanocomposite films based on plasticized PLA-PHB/cellulose nanocrystal blends. Carbohydr Polym 121:265–275
92. Arrieta MP, Fortunati E, Dominici F, Rayon E, Lopez J, Kenny JM (2014) Multifunctional PLA-PHB/cellulose nanocrystal films: processing, structural and thermal properties. Carbohydr Polym 107:16–24
93. Arrieta MP, Castro-Lopez MDM, Rayon E, Barral-Losada LF, Lopez-Vilarino JM, Lopez J, Gonzalez-Rodriguez MV (2014) Plasticized poly(lactic acid)-poly(hydroxybutyrate) (PLA-PHB) blends incorporated with catechin intended for active food-packaging applications. J Agric Food Chem 62:10170–10180
94. Arrieta MP, Lopez J, Hernandez A, Rayon E (2014) Ternary PLA-PHB-limonene blends intended for biodegradable food packaging applications. Eur Polym J 50:255–270
95. Abdelwahab MA, Flynn A, Chiou BS, Imam S, Orts W, Chiellini E (2012) Thermal, mechanical and morphological characterization of plasticized PLA-PHB blends. Polym Degrad Stab 97:1822–1828
96. Blumm E, Owen AJ (1995) Miscibility, crystallization and melting of poly (3-hydroxybutyrate)/poly(L-lactide) blends. Polymer 36:4077–4081
97. Xu J, Bao J, Guo BH, Ma H, Yun TL, Gao L, Chen GQ, Iwata T (2007) Imaging of nonlinear optical response in biopolyesters via second harmonic generation microscopy and its dependence on the crystalline structures. Polymer 48:348–355
98. Ohkoshia I, Abe H, Doi Y (2000) Miscibility and solid-state structures for blends of poly[(S)-lactide] with atactic poly[(R,S)-3-hydroxybutyrate]. Polymer 41:5985–5992
99. Schultz JM (ed) (2001) Polymer crystallization: the development of crystalline order in thermoplastic polymers. American Chemical Society, New York
100. Ma P, Hristova-Bogaerds DG, Zhang Y, Lemstra PJ (2014) Enhancement in crystallization kinetics of the bacterially synthesized poly(β-hydroxybutyrate) by poly(butylene succinate). Polym Bull 71:907–923
101. Qiu Z, Ikehara T, Nishi T (2003) Poly(hydroxybutyrate)/poly(butylene succinate) blends: miscibility and nonisothermal crystallization. Polymer 44:2503–2508
102. Lovera D, Marquez L, Balsamo V, Taddei A, Castelli C, Müller AJ (2007) Crystallization, morphology, and enzymatic degradation of polyhydroxybutyrate/polycaprolactone (PHB/PCL) blends. Macromol Chem Phys 208:924–937

Index

A
Alginates, 12–13

B
Bio-based polyesters
  and biodegradable polymers, 121
  crystallization (*see* Crystallization)
  immiscible polymers, 222
  PHAs, 120
  thermoplastics, 88
Biobased polymers
  biodegradable, 2
  cellulose, 3–5
  chitin, 8–10
  chitosan, 8–10
  classification, 3
  FDCA (*see* Furandicarboxylic acid (FDCA))
  fossil-based materials, 24
  lignin, 7–8
  NR, 10–12
  starch, 5–6
  vulcanization, 2
Biodegradability
  bio-based, 121
  enzymatic, 21
  N-acetylglucosamine, 8
  and non-biodegradable polymers, 3
  NR, 11
  PHAs, 15
  PLA, 95
  plant-based, 38
  polyesters, 71, 235
  polymers, 2
Bio-polyamides, 22
Bio-polyethylene (Bio-PE), 21
Branching, 63–66

C
Caoutchouc, 10
Cellulose, 3–5, 7, 10, 17, 19, 209, 210, 248
Collagen, 12
Copolymerization
  α-amino acid, 62–63
  2-hydroxyalkanoic acid, 56–62
  stereo (*see* Stereo copolymerization)
Copolymers
  heterogeneous, 12
  3-hydroxybutyrate, 17
  L-form-rich, 89
  molecular structures, 39
  PLA (*see* Poly(lactic acid) (PLA))
  polymer chains, 62
  SA, 24
Crystallization
  compatibilizers, 227–229
  copolymerization (*see* Copolymerization)
  flow-induced, 93–95
  fractionated, 224–226
  growth rate, 90
  molecular weight, 43–45
  nanoparticles, 227–229
  nucleation, 71–73, 90–91
  polymer-polymer interfaces, 226–227
  SCs, 66–71
  shear, continuous, 101
  solution, 77–78
  stereocomplex, 91–93

Crystallization (*cont.*)
terminal group effects, 47–49
Crystal polymorphism, 42, 48, 53, 154–157, 164, 165, 176
Cylindrites, 95, 96, 99, 100, 103

D
Double-crystalline blends, 250

F
Fillers, 11, 18, 23, 103–105
Flame retardancy, 173–176
Flow-induced crystallization (FIC)
generalities, 93–96
non-isothermal
shear, 101
Shish-Kebab microstructure, 100–101
nucleation rate, 96–99
PLA processing
additive/fused filament deposition modeling, 110–111
extrusion casting, 109–110
foam injection molding, 109
injection molding, 106–109
melt spinning, 110
related processes, 106–109
SC, 101–102
Furandicarboxylic acid (FDCA)
aliphatic chains, 210–213
applications, 191
dicarboxylic acid, 190
furan derivative, 22
PEF synthesis, 192
polyesters, 192
aliphatic chains, 210–213
applications, 191
esterification, 190
5-hydroxymethylfurfural, 190
oil-based PET, 191

G
Galactomannans, 14–15
Glass transition, 204–207
amorphous fraction, 133
heating, 129
PEF, 194
PHB melting, 250
PLLA, 41
polylactide, 240
systematic effect, 147
temperature, 4, 148, 227

H
2-Hydroxyalkanoic acid, 39, 50, 56–62
Hydroxymethylfurfural (HMF), 190

I
Immiscible blends
crystallization behavior, 222–223
PBS/PCL blends, 244–245
PCL/PLA, 234–244
PHB, 245–250
PLA/PBS blends, 229–234
Incorporated polymers
amorphous, 74
crystallizable, 74–77
India rubber, 10
Isoprene rubber (IR), 11

L
Lactide (LA)
cyclic dimer, 50
PLA (*see* Poly(lactic acid)/poly(lactide) (PLA))
PLLA (*see* Poly(L-lactic acid) (PLLA))
Lignin
added-value applications, 7
chemical structure, 8
monolignols, 7
natural polymer, 7
phenol, 23
TPS, 6
Lignocellulosic biomass, 19, 191

M
Mechanical properties
alginate gels, 12
aliphatic polyamides, 147
biodegradable bio-based polyesters, 16
PEF, 166
PLA fiber, 96
thermal degradation, 121
TPS, 6
Young's modulus, 166
Melt viscosity, 207–208

Molecular structures, 11, 39, 40, 45, 54, 75
Molecular weight
and chain branching, 103
crystallization, 81
D-lactide, 90
effects, 43–45
homopolymers, 64
LLA units, 55
PDLA, 67
PHB/high molecular weight, 250
PLLAs, 47, 49
structures, 39
water hydrolysis reactions, 172
Morphology
crystallization behavior, 101
cylindrite, 103
glass transitions, 233
low shear deformation, 95
melt-recrystallizable nucleation, 71
PEF/OMMT nanocomposites, 209
PHB crystals, 122–125
PLA, 39
POM micrographs, 72
and properties, 5
relationships, 222
semicrystalline, 157, 164–167
spherulites, 50
transcrystalline, 243

N
N-acetylglucosamine (2-acetamido-2-deoxy-β-D-glucopyranose), 8
Nanocomposites, 208–210
Natural rubber (NR), 2–3, 10–12, 175, 176
Nucleating agent
crystallization, 68, 71
fillers effects, 103–105
and plasticizers, 17
time and production cost, 66
Nucleation
chain length, 45
density/rate, 129
FIC, 96–99
heterogeneous, 123
homogeneous, 223
melt-quenching process, 39
polymer-polymer interfaces, 226–227
quiescent, 90–91
rate, 96–99
semicrystalline morphologies, 157–162
stress-induced, 110
supercoolings, 226

O
Oscillatory shear injection molding (OSIM), 105, 106, 109

P
Pectins, 3, 5, 6, 14
Phase structure, 132, 149, 151
Polarized optical microscopy (POM), 90, 91, 95, 101, 103, 123, 124, 159–162
Polyamide 11 (PA 11)
applications, 146
comparison, 146–149
flame retardancy, 173–176
heat capacity, 149–154
history, 144
properties, 146
structure, 146
synthesis, 145
thermal
decomposition, 171–172
stability, 170–171
thermodynamic functions, 149–154
thermo-oxidative degradation, 172–173
Poly(butylene succinate) (PBS)
cold-crystallization temperature, 233
concentrations, 228
cooling process, 234
immiscible blends
and PCL, 244–245
and PLA, 229–234
polarized light optical microscopy, 249
polymers, 25
reported experimental works, 230–232
semicrystalline polymer, 18
thermoplastic polyester, 17
Poly(ε-caprolactone) (PCL)
biodegradable polyesters, 71
cold-crystallization, 241
crystallization and nucleation, 236–239
MWCNT nanocomposites, 169
PLOM images, 243
PVDF, 226
Polyethylene (PE), 21, 47, 159, 223
Poly(ethylene 2,5-furandicarboxylate)/poly(ethylene 2,5-furanoate) (PEF)
nanocomposites, 208–210
vs. PET, 207–208
physical properties, 192–195
quiescent crystallization, 195–200
SIC, 195–204
synthesis, 192–195
Poly(ethylene terephthalate) (PET), 20–22, 25, 190–197, 200–208, 212, 213

Polyhydroxyalkanoates (PHAs), 2, 3, 15–17, 120
Poly(lactic acid)/poly(lactide) (PLA)
  assessing methods, 95
  chain branching, 103
  commercial bio-based, 88
  copolymers-based materials, 38
  crystallization (*see* Crystallization)
  FIC (*see* Flow-induced crystallization (FIC))
  immiscible blends
    nucleation density, 228
    and PBS, 229–234
    and PCL, 234–244
    PHB phase, 248
  incorporation, polymers (*see* Incorporated polymers)
  molecular
    structures, 39
    weight, 103
  parameters, 39–42
  thermal properties, 78–81
Poly(L-lactic acid) (PLLA)
  homopolymers, 43, 49
  L-form homopolymer, 39
  melt-crystallization, 52
  molecular weight, 47
  orthorhombic γ-phase, 20
  photomicrographs, 62
  POM micrographs, 72
  WAXD profiles, 58
Poly[(R)-3-hydroxybutyrate] (PHB), 71, 72, 121
  amorphous fraction, 129–133
  crystallization kinetics, 121, 126–129
  crystal structure, 122–125
  global dependence, 120
  melting crystals, 133–136
  morphology, 122–125
  and PHAs, 120
  thermal stability, 121
Pullulan, 13–14

R
Ricinoleic acid, 22, 145
Rigid amorphous fraction (RAF), 204
  amorphous PHB, 129, 130
  crystallization temperature, 132
  crystal phase, 129
  devitrification, 130
  glass transition, 133
  MAF, 133
  PEF, 205
  phase, 204
  in PHB, 132
  temperature, 151
  time evolution, 131
  vitrification, 126, 130

S
Semicrystalline polymers
  crystallinity level, 18, 164
  morphological features, 222–223
Shear-induced crystallization, 103, 105, 162–164
Shish-kebab structures, 94–96, 100–101, 103
Spherulites
  crystallization, 17
  density, 69
  growth rate, 20, 44, 55, 76
  PHB, 123, 127
  PLA, 95
  polarized photomicrographs, 46, 65
Starch, 3, 5–6, 10, 16, 18, 19, 21, 22, 24
Star-shaped polymers, 21
Stereocomplexs (SCs)
  crystallization, 38, 91–93
  flow-induced crystallization, 101–102
  PLLA and PDLA, 89, 102
  unsubstituted and substituted, 66–71
Stereo copolymerization
  alternates, 54–55
  block, 55–56
  random, 50–54
Strain-induced crystallization (SIC)
  β-form, 17
  para-crystalline structure, 122
  phase, 200
  stretching
    biaxial, 202–204
    uniaxial, 200–202
Supermolecular structure
  crystal polymorphism, 154–157
  nucleation-controlled, 157–162
  semicrystalline morphologies, 157–162
  thermal-pathway-controlled, 154–157

T
Terminal group, 45–49
Thermal properties, 78–81
  crystalline structure, 8
  FDCA (see Furandicarboxylic Acid (FDCA))

PA 11 (*see* Polyamide 11 (PA 11))
PHAs, 16
PLLA, 20
Thermomechanical properties
melt viscosity, 207–208
nanocomposites, 208–210
PA 11-based nanocomposites, 166–170
PLA matrix, 229
quiescent crystallization, 195–200
SIC, 200–207
Young's Modulus, 164–166
Thermoplastic starch (TPS), 6
Thermosetting bio-materials, 23–24

Y
Young's Modulus, 107, 109, 164–166, 177

Z
Zero-entropy, 153, 155